

(NASA-CR-196533) RESEARCH REPORTS:
1994 NASA/ASEE SUMMER FACULTY
FELLOWSHIP PROGRAM Final Report
(Alabama Univ.) 302 p

N95-18967
--THRU--
N95-19016
Unclas

112552

G3/80 0030890

352653

NASA CONTRACTOR REPORT

NASA CR- 196533

**RESEARCH REPORTS - 1994 NASA/ASEE SUMMER FACULTY
FELLOWSHIP PROGRAM**

The University of Alabama
Tuscaloosa, Alabama
and
The University of Alabama in Huntsville

October 1994

Final Report

Prepared for NASA, George C. Marshall Space Flight Center, Marshall Space
Flight Center, Alabama 35812

RESEARCH REPORTS

1994 NASA/ASEE SUMMER FACULTY FELLOWSHIP PROGRAM

George C. Marshall Space Flight Center

**The University of Alabama
Tuscaloosa, AL**

and

The University of Alabama in Huntsville

EDITORS:

**Dr. L. Michael Freeman
Associate Professor of Aerospace Engineering
The University of Alabama**

**Dr. Charles R. Chappell
Associate Director for Science
Marshall Space Flight Center**

**Dr. Frank Six
University Affairs Officer
Marshall Space Flight Center**

**Dr. Gerald R. Karr
Professor and Chairman of Mechanical and Aerospace Engineering
The University of Alabama in Huntsville**

NASA CR-196533

TABLE OF CONTENTS

- I. Amin, Ashok T.
University of Alabama in Huntsville
MSFC Institutional Area Network and ATM Technology
- II. Anderson, Richard
University of Missouri-Rolla
A Comparison Between Using Incoherent or Coherent Sources to Align and Test
an Adaptive Optical Telescope
- III. Antar, Basil N.
The University of Tennessee Space Institute
Bubble Formation in Microgravity
- IV. Benn, Karen P.
Oakwood College
The Assessment of Virtual Reality for Human Anatomy Instruction
- V. Bernstein, Edward L.
Alabama A&M University
Residual Stresses in Welded Plates
- VI. Bucinell, Ronald B.
Union College, Schenectady, NY
Foreign Body Impact Event Damage Formation in Composite Structures
- VII. Campbell, C. Warren
The University of Alabama in Huntsville
A Finite Element Code for Electric Motor Design
- VIII. Cariapa, Vikram
Marquette University
Concept of Using a Benchmark Part to Evaluate Rapid Prototyping Processes
- IX. Chu, Tsuchin
Southern Illinois University at Carbondale
Composite Structures for Magnetosphere Imager Spacecraft
- X. Clark, John H.E.
The Pennsylvania State University
Implications of Summertime Marine Stratocumulus on the North American
Climate

- XI. DeBrunner, Linda S.
The University of Oklahoma
Performance Evaluation of the Engineering Analysis and Data System (EADS) II
- XII. Feikema, Douglas A.
The University of Alabama in Huntsville
Optical Measurements in Rocket Engine Liquid Sprays
- XIII. Gerth, Richard J.
The Ohio University
Data Driven Propulsion System Weight Prediction Model
- XIV. Greenway, R. Bryan, Jr.
University of Kansas
Real-Time Thickness Measurement of MCC Ablator Material
- XV. Gross, R. Steven
Auburn University
Steady and Unsteady Blade Stresses Within the SSME ATD/HPOTP Inducer
- XVI. Gudimetla, V.S. Rao
Oregon Graduate Institute
Special Relativity Effects for Space-Based Coherent Lidar Experiments
- XVII. Howard, Thomas G.
Northwest-Shoals Community College
Surface Roughness Measurements
- XVIII. Isaac, Bryan J.
Catawba College
Probing the Chemistry of Nickel / Metal Hydride Battery Cells Using
Electrochemical Impedance Spectroscopy
- XIX. Jackson, Jeff
The University of Alabama
A Hypertext-Based Internet-Assessable Database for the MSFC Technology
Transfer Office
- XX. Jenkins, Rhonald M.
Auburn University
A Preliminary Analysis of Low Frequency Pressure Oscillations in Hybrid Rocket
Motors

- XXI. Jones, Kenneth M.
North Carolina A&T State University
Development of CFD Model for Augmented Core Tripropellant Rocket Engine
- XXII. Landrum, D. Brian
The University of Alabama in Huntsville
Computational Simulation of Liquid Fuel Rocket Injectors
- XXIII. Lindsey, Patricia F.
East Carolina University
Development of Microgravity, Full Body Functional Reach Envelope Using 3-D
Computer Graphic Models and Virtual Reality Technology
- XXIV. Lo, Chor P.
The University of Georgia
A GIS Approach to Urban Heat Island Research: The Case of Huntsville, AL
- XXV. Luxemburg, Leon A.
Texas A&M University
Neural Networks Applications to Control and Computations
- XXVI. Mahanta, Kamala
The State University of New York College at Oneonta
A CMC Database for Use in the Next Generation Launch Vehicles (Rockets)
- XXVII. Main, John A.
Vanderbilt University
Lean Spacecraft Avionics Trade Study
- XXVIII. Matthys, Donald R.
Marquette University
MANN - A Program to Transfer Designs for Diffractive Optical Elements to a
MANN Photolithographic Mask Generator
- XXIX. Mazzoleni, Andre P.
Texas Christian University
Design of High Pressure Waterjet Nozzles
- XXX. Moriarity, Debra M.
The University of Alabama in Huntsville
Concentration and Temperature Effects on Ovostatin Activity
- XXXI. Noble, Viveca K.
Tuskegee University
Error Coding Simulations in C

- XXXII. Olivier, Philip D.
Mercer University
A New Piston Control Strategy for Segmented Mirrors
- XXXIII. Pearson, Earl F.
Western Kentucky University
Growth of Thin Films of Dicyanovinylanisole on Quartz and Teflon-Coated Quartz
by Physical Vapor Transport
- XXXIV. Phanord, Dieudonné D.
University of Wisconsin at Whitewater
Two Space Scatterer Formalism Calculation of Bulk Parameters of Thunderclouds
- XXXV. Santi, L. Michael
Christian Brothers University
Evaluation of SSME Test Data Reduction Methods
- XXXVI. Schonberg, William P.
The University of Alabama in Huntsville
Cracking Characteristics of a Habitable Module Pressure Wall Following Orbital
Debris Penetration
- XXXVII. Schreur, Barbara
Texas A&M University - Kingsville
Evaluation of the Efficiency and Reliability of Software Generated by Code
Generators
- XXXVIII. Smith, Willard A.
Tennessee State University
A Report of Work Activities on the NASA Spacelink Public Electronic Library
- XXXIX. Solakiewicz, Richard
Chicago State University
Scattering of Point Source Illumination by an Arbitrary Configuration
- XL. Talia, George E.
The Wichita State University
Microstructural Analysis of Cracks Generated During Welding of 2195 Aluminum-
Lithium Alloy
- XLI. Tawfik, Hazem
State University of New York at Farmingdale
Quality Optimization of Thermally Sprayed Coatings Produced by the JP-5000
(HVOF) Gun Using Mathematical Modeling

- XLII. Taylor, Charles R.
Pacific University
Prism Project Optical Instrument
- XLIII. Temple, Enoch C.
Alabama A&M University
The Probability of Flaw Detection and the Probability of False Calls in
Nondestructive Evaluation Equipment
- XLIV. Walsh, Daniel W.
California Polytechnic State University
The Effect of Fabrication on Corrosion in Aluminum 2195: Environmental and
Microstructural Considerations
- XLV. Wang, Jai-Ching
Alabama A&M University
Numerical Formulation of Composition Segregation at Curved Solid-Liquid
Interface During Steady State Solidification Process
- XLVI. Wang, Francis C.
The University of Alabama in Huntsville
Effects of Vibration (G-JITTERS) on Convection in Micro-gravity
- XLVII. Williams, George O., Jr.
Calhoun Community College
Capillary Electrophoresis: Biotechnology for Separation of DNA and
Chromosomes
- XLVIII. Wilson, Lori J.
East Tennessee State University
Salt-Induced Aggregation of Lysozyme: Implications for Crystal Growth
- XLIX. Wohlman, Richard A.
Western Carolina University
A Technique for Determining Cloud Free vs. Cloud Contaminated Pixels in
Satellite Imagery

112553

N95-18968

352663

P.7

1994

NASA/ASEE SUMMER FACULTY FELLOWSHIP PROGRAM

MARSHALL SPACE FLIGHT CENTER
THE UNIVERSITY OF ALABAMA

MSFC INSTITUTIONAL AREA NETWORK AND ATM TECHNOLOGY

Prepared By: Ashok T. Amin

Academic Rank: Associate Professor

Institution and Department: The University of Alabama in Huntsville
Computer Science Department

NASA/MSFC:

Laboratory: Information Systems Office
Division: Systems and Integration Engineering

MSFC Colleagues: Alan Forney
Michael Savage

1. INTRODUCTION

The New Institutional Area Network (NEWIAN) at Marshall supports over 5000 end users with access to 26 file servers providing Work Presentation Services. It comprises of some 150 Ethernet LANs interconnected by bridges/routers which are in turn connected to servers over two dual FDDI rings. The network supports various higher level protocols such as IP, IPX, AppleTalk (AT), and DECNet. At present IPX and AT protocols packets are routed, and IP protocol packets are bridged, however work is in progress to route all IP packets. We examine the impact of routing IP packets on the network operation.

Broadband Integrated Services Data Network (BISDN), presently at various stages of development, is intended to provide voice, video, and data transfer services over a single network. BISDN will use Asynchronous Transfer Mode (ATM) as a data transfer technique which provides for transmission, multiplexing, switching, and relaying of small size data units called cells. Limited ATM Wide Area Network (WAN) services are offered by Wiltel, AT&T, and Sprint and others. NASA is testing a pilot ATM WAN with a view to provide Program Support Communication Network services using ATM. ATM supports wide range of data rates and quality of service requirements. It is expected that ATM switches will penetrate campus networks as well. However, presently products in these areas are at various stages of development and standards are not yet complete. We examine development of ATM to help assess its role in the evolution of NEWIAN.

2. ROUTING VERSUS BRIDGING OF IP IN THE NEWIAN

The Internet Protocol (IP) is the network layer protocol of the TCP/IP suite of protocols. The unit of the data transferred between network layer entities is called a packet. A host on the Internet has a globally unique 32-bit IP address and is typically written in the form $X_3.X_2.X_1.X_0$, where for $i = 0,1,2,3$ the value of X_i is between 0 and 255. The IP addresses are organized in hierarchical fashion in the form of (class, net-id, host-id), where the class is A, B, or C. The Class A addresses are intended for a small number of large size networks while the Class C addresses are intended for a large number of small size networks. An IP address of a network layer entity is globally unique and the net-ids are centrally administered. For example, Marshall with medium size network has a Class B net-id with address 128.158.0.0. Often it is the case, as with the NEWIAN, that host-ids within a network are organized by the network administrator so that the higher order bits of the host-id represent the subnet-id. A host on an Internet needs to know the IP address of the remote host to be able to send a packet to it. For transmission over an Ethernet, an IP packet is encapsulated in an Ethernet frame as shown in Figure 1.

LANs may be interconnected by Bridges at the link level or by Routers at the network level. A bridge/router, called Brouter, permits bridging of some protocols while routing of other protocols. In the NEWIAN a Brouter is used with two types of ports- an Ethernet port, and a FDDI port. A Brouter is connected to a number of 10Mbps Ethernets, and the Brouters are interconnected over one or two dual 100Mbps FDDI

rings. The file servers are connected to one of the FDDI ring and the end user devices are connected to Ethernets. Thus, all the end users are one or at most two Routers away from the servers.

2.1 Bridging of IP in the NEWIAN

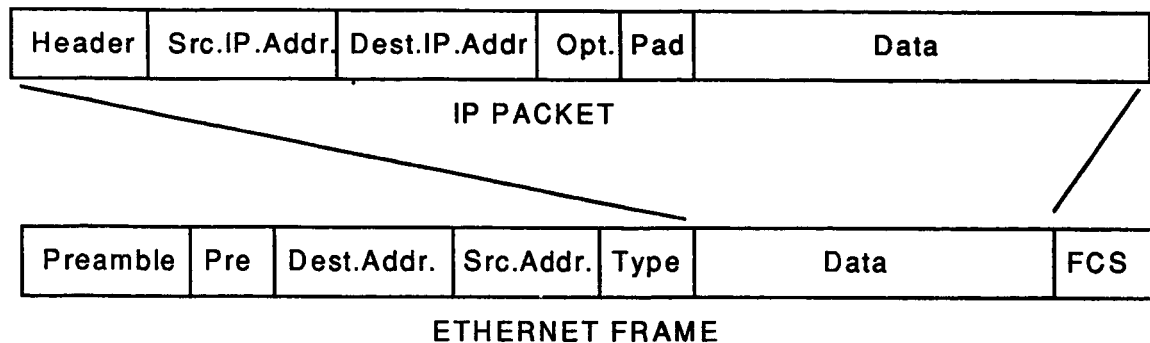
Two or more Ethernets may be connected at the MAC layer by a *Bridge* to create what we will call an *Extended LAN*. Each LAN connects to a port on a Bridge. The Bridge receives frames from all the LANs connected to it. A routing table is maintained in the Bridge which associates with the MAC address of each end user on every LAN in the NEWIAN one of its ports. The action taken by the Bridge upon receipt of a frame is as follows. If the destination MAC address of the frame is associated with same port on which it was received, then the frame is discarded; otherwise, the frame is routed on the port associated with the destination MAC address on the frame in the routing table. When the LAN on which a frame is received is of different type than on which the frame is to be routed, a frame translation is performed at the Bridge. A broadcast frame or a frame with destination MAC address not in the forwarding table is forwarded on all other ports of the bridge.

Since bridging is independent of higher level protocols, it supports multiple higher level protocols in the network. It is seen that a broadcast frame on a LAN will be forwarded to every LAN in the network. This often creates much unnecessary traffic referred to as 'broadcast storm', unless some additional 'filtering' capability is provided in the bridge. Further, in a bridged network, a user must know the MAC address of the remote entity on the network to communicate. This creates a situation with IP packets which results in undesirable broadcast traffic. Suppose a source host on a LAN has to transmit a IP packet to a destination host, on the network, whose IP address is known but the MAC address is not known. The problem of mapping a given IP address to associated MAC address is referred to as the Address Resolution Problem. Address Resolution Protocol (ARP) permits a source host to obtain the MAC address of the destination host from the IP address of the destination host. An ARP packet broadcast is received by all the hosts on the network, and the destination host will respond to the ARP packet and send its MAC address to the source host. A recent occurrence of the following rather peculiar situation on the NEWIAN indicates how the effect of the broadcasts can be compounded. An X-terminal transmits a broadcast message to locate a server to setup an X-connection. A number of servers responding to the broadcast send ARP broadcast to determine the MAC address of the X-terminal, resulting in multiple broadcasts.

2.2 Routing of IP Packets in the NEWIAN

A Router is a device rooted in the TCP/IP view of the communication subnet as consisting of interconnected networks (Internet) in which routing between networks is provided by Routers connecting two or more networks. A Router port connecting to a network has a unique IP address on that network. A host on a network can send IP packet directly to another host on the same network, however a packet to a host on

another network is sent to a nearest Router on the same network. A Router maintains a table which associates one or more IP addresses of Routers with each network-id. A packet with destination net-id of a network connected to the Router is sent directly to the destination host, otherwise it is routed to an appropriate Router based on the routing table. A Router also provides segmentation when routing a packet over a network with maximum packet size is smaller than the received packet size. A Router provides the functionality's of the lower three layers of the ISO model, namely, the network, the link, and the physical layers. Earlier literature on TCP/IP refers to a Router as a Gateway. However, the term Gateway refers to a device which provides functionality's of all seven layers of the ISO Model.



An IP Packet Encapsulated in an Ethernet Frame
Figure 1.

Two or more Ethernets may be interconnected at the network layer by a *Router* to create a subnetwork. A Router port connected to a LAN has a unique MAC address associated with that port as well a unique IP address. A Router maintains a routing table associating MAC address and the port-id with the IP address of each Router on the NEWIAN and of each IP host in the subnet defined by the Router. Routing of packets from source host to destination host on the network is based on the destination host-id contained in the packet header. A Router receives only those frames on a port that are addressed to it. A received frame is processed and the packet is routed based on the destination IP address on the packet. Routing a packet over a LAN requires encapsulation of the IP packet in an Ethernet frame as shown in Figure 1. A packet with destination net-id other than that of MSFC is routed to the PSCN Router. A packet is routed directly to the destination host over associated port if the destination subnet-id is the same as the of the receiving Router, otherwise it is routed to the Router with the same subnet-id as its destination subnet-id.

2.3 A Comparison of Bridging versus Routing of IP in the NEWIAN

A comparison of routing and bridging of IP packets is presented with respect to its impact on processing requirements, network traffic, and network operations.

- 1) In a bridged network, to send a packet, a source host needs to know the MAC address of the destination host; while in a routed network a source host needs to know only the MAC address of the subnet Router.

- 2) A broadcast frame on a LAN will be broadcast on every LAN on the NEWIAN in a bridged network, while a broadcast frame will be restricted to that LAN only in a routed network.
- 3) An ARP request will be broadcast on every LAN for a bridged network, while for a routed network the ARP request will be routed to the Router of the subnetwork where the destination host resides. The ARP may have to broadcast to all LANs on the subnetwork only if the Router can not respond to the ARP from its routing table.
- 4) Both a Bridge and a Router provide for store and forward of frames and packets, respectively. A Bridge needs to forward /discard each frame on each of the LANs connected to it. A Router, on the other hand, receives only frames addressed to it on each of its LANs, however, a Router will have to process each received frame and route the packet based on the destination host-id contained in the packet header.
- 5) When an end user WS/PC is moved from one LAN to another, in a bridged network the MAC address of its Ethernet interface remains unchanged but is now associated with different port of the same or different Bridge in the network. This requires all the bridges to update their forwarding tables, however this is not a problem since the bridges are learning bridges which update the forwarding tables based on the source MAC address of frames it receives on its ports. When a end user WS/PC is moved from one LAN to another, in a routed network its IP address needs to be changed only if the new LAN is connected to a different Router (and hence is a host in a different subnetwork). This would have required power-down of the Router, but with the new generation of the Wellfleet Routers which are being installed this can be done on-line.

3. ATM TECHNOLOGY AND EVOLUTION OF THE NEWIAN

The ATM WAN services in a limited form are available from a number of carriers. However use of ATM switches in campus networks is found only in experimental networks. This is in part due the lack of standards for Private Network-to-Network Interfaces (P-NNI) and for LAN emulation, however they are expected to be completed by the end of 1994 [5]. The LAN emulation standards will facilitate development of Adapters for Ethernet-ATM conversion as an integral module in an ATM switch and as a stand-alone module such as Synoptics Ether-Cell. And P-NNI standard will make ATM switches from different vendors inter-operable. With the ATM backbone network, high speed 100-155Mbps full-duplex ATM adapters for the Servers will be needed. These are either already available or are in testing for various machines such as SUN, Silicon Graphics, HP7000, DEC Turbochannel, and IBM RS6000. ATM adapters are expected for PCI bus widely used in 486 and Pentium systems, and for DEC Alpha PC's. While ATM adapters and drivers are available for TCP/IP, drivers for Novell Netware are in testing, and drivers for Windows NT and Windows Workgroups are expected soon.

The connections of end user's devices (PC/) to the Servers can take one of many forms. A number of single user Ethernets can be connected to an Ether-Cell which in turn connects through it's ATM port to the backbone ATM switch. An Ethernet frame is switched either to the ATM port (with Ethernet-ATM conversion) or another Ethernet port on the Ether-Cell. This permits a PC 10Mbps bandwidth and direct access to the

backbone ATM switch without requiring adapters and drivers for the PC. It should be noted that for a Switched Ethernet with Servers either directly connected to the switch or through a FDDI will provide the similar capability. Thus, with or without ATM in the backbone, one can provide 10Mbps bandwidth to end users. Thus, the applications which justify ATM capabilities are those that require bandwidth over 10Mbps range such as required in real time analysis/display of high density images, or multimedia application such as personal video-conferencing.

Experimental ATM networks are presently at various stages of development at a number of universities [2,4]. The primary application for these networks appears to be high speed transfer of medical images for instructional or diagnosis purposes. In addition, these also serve as test bed for products developed by vendors or by the universities and thereby help the development of the ATM technology. As standards are developed, cost of equipment come down, and most importantly new applications emerge, use of ATM is expected to gain momentum. Among expected benefits of ATM deployment are 1) it enables new applications, 2) it leads to lower operational costs, and 3) it appears to be a long term solution. At the same among concerns expressed by users include 1) incomplete standards, 2) lack of interoperable products and services, and 3) high equipment costs.

4. CONCLUSION

The NEWIAN network is undergoing updating with new generation Routers and routing of IP protocols. While routing entails increased processing over bridging, it also results in reduced traffic by limiting broadcast within a LAN and limiting an ARP to at most a subnet. The current activities with Switched Ethernet and ATM pilot Network will yield valuable experience to guide the future development of NEWIAN and especially help determine the role ATM in it.

REFERENCES

- [1] D. Comer, Inter-networking with TCP/IP: Principles, Protocols, and Architecture, Prentice Hall, 1988.
- [2] . R. Cox, M. E. Gaddis, and J. S. Turner, "Project Zeus", IEEE Network, March 1993, pp.20-30.
- [3] R. P. Davidson and N. J. Muller, Inter-networking LANs: Operation, Design, and Management, Artech House, 1992.
- [4] R. G. Foldvik and W. Walling, "Distance Learning and ATM: a Trial at the University of Minnesota", Proc. of 18th Conf. on Local Computer Networks, September 1993, pp.77-80.
- [5] R. Jeffries, "ATM to the Desktop: Prospects and Probabilities", Telecommunications, April 1994, pp.25-32.
- [6] W. Stallings, Handbook of Computer Communication Standards, volume 2: Local Area Network Standards, MacMillan, 1990.
- [7] H. Lee Thomas, "NEWIAN Response Time Issues", MITRE, Contract No. NAS9-18057, June 1994, A working paper.

112554

382665

P. 7

1994

NASA/ASEE SUMMER FACULTY FELLOWSHIP PROGRAM

MARSHALL SPACE FLIGHT CENTER
THE UNIVERSITY OF ALABAMA

A COMPARISON BETWEEN USING INCOHERENT OR COHERENT SOURCES TO
ALIGN AND TEST AN ADAPTIVE OPTICAL TELESCOPE

Prepared By:	Richard Anderson
Academic Rank:	Professor Emeritus
Institution and Department:	University of Missouri-Rolla Department of Physics

NASA/MSFC:

Laboratory:	Astrionics
Division:	Optics and Radio Frequency
Branch:	Optical Fabrication

MSFC Colleague:	Robert Rood
-----------------	-------------

INTRODUCTION

A segmented mirror adaptive optics telescope called the phased array mirror extendable large aperture telescope (Pamela)¹ was designed by Kaman Aerospace Corporation, delivered to Marshall Space Flight Center, and is under study. This telescope has a spherical mirror of radius of curvature of 1.5227 m and consists of 36 segments forming a telescope 0.5 m in diameter. It is a prototype for a planned 12 m telescope having 144,000 segments. This proposed telescope will be used for laser power beaming and may also be used for imaging. A secondary mirror forming a catadioptric element corrects for spherical aberration. An additional lens system renders the emergent beam parallel. A portion of the emergent beam is deflected with a beamsplitter into an imaging CCD detector array. The remainder of the beam is sampled by a Hartmann wavefront sensor (WFS)² which has a detector element corresponding to each mirror segment and the detectors are lateral effect diodes (LEDD)³. These elements measure the tilt produced by atmospheric turbulence. In correcting for atmospheric turbulence a point source beacon is used, which may be a star or artificially produced guide star⁴ and these are incoherent sources. The atmosphere distorts the spherical wave-front from the beacon and the amount of phase (tilt) distortion is measured using the WFS. This distortion is removed using the adaptive optics telescope and the laser power beam is transmitted after this correction. The mirror must be corrected and the laser beam must be transmitted in less than 10 ms which is the approximate atmospheric coherence time so all intensity measurements are considered instantaneous.

Additional optics are required to align the telescope and these are a Wyko interferometer for segment tilt adjustment and a white light interferometer to adjust the pitch across the segment boundaries. Finally, a spatial filtered, expanded, collimated HeNe laser beam is used after alignment to record the central position of the 36 beams in the 36 LEDDs. In test experiments an aberrator is placed in this HeNe laser arm after the collimator and the closed-looped WFS-actuator-computer control system can be tested under various distortion conditions.

The concept in the initial alignment of the telescope is to produce an optical transfer function (OTF) which closely approximates the diffraction limited value⁵ which would correspond to a system pupil function that is unity over the aperture and zero outside⁶. In some experiments an additional computer calculates the OTF. When the system is aligned, the WFS is calibrated by recording the spot position on each detector element. When an atmospheric distorted wave-front is intercepted by the telescope pupil plane, the WFS measures the wave-front phase distortion by noting the change in spot positions and the segment actuator-control computer returns the spot on each WFS LEDD to the position it had for the aligned telescope by adjusting mirror segments. The atmosphere-instrument system is represented by an atmosphere-instrument OTF and the actuator-control computer system adjusts segments to remove any wave-front error and reproduce the original aligned telescope OTF.

There are differences in the theory of intensity measurements between coherent and incoherent radiation. As a result, some of the classical quantities which describe the performance of an optical system for incoherent radiation can not be defined for a coherent field. The most important quantity describing the quality of an optical system is the OTF and for a coherent source the OTF is not defined. Instead a coherent transfer function (CTF)⁶ is defined.

THEORY

A. Theory For An Incoherent Source

Consider the telescope is in the alignment mode and an incoherent plane wave-front is incident on it. After alignment the telescope receives a signal from a distant incoherent point source called a beacon. In alignment the telescope is adjusted to give a system OTF which closely approximates the diffraction limited value. For a distant incoherent beacon the incident wave-front is plane and spatially coherent before distortion is produced by atmospheric turbulence. The WFS and actuator-control computer system attempt to correct the mirror to its aligned OTF. In the case of Pamela each WFS element is masked and measures the atmospheric phase (tilt) distortion for a single segment of the telescope with no overlap between segments. As a result, each sensor detector element has a pupil function which exits over the extent of the segment and goes to zero outside the segment. An OTF can be associated with each mirror segment and system has the total OTF which is the sum of these segment OTFs. The entire telescope should be corrected so this discussion will refer to the OTF of the entire telescope for this is what is sensed by the imaging CCD array.

In the alignment mode an incoherent plane wave is incident on the telescope. The pupil function of the telescope at point \bar{r} of coordinates (x,y) in the detector's pupil plane is $h_o(\bar{r})$ and the system point spread function (PSF) is $o_o(\bar{r})$. The real image intensity⁷ $i(\bar{r})$ in the pupil plane of the detector is

$$i(\bar{r}) = o_o(\bar{r}) \otimes i_s(\bar{r}) = |h_o(\bar{r})|^2 \otimes i_s(\bar{r}) \quad (1)$$

where $i_s(\bar{r})$ is the source or object intensity distribution projected to the real image plane and is the magnified image of the object and \otimes is the convolution operator. If the Fourier transform⁸ is taken of equation (1), the image intensity in spatial frequency space \bar{u} is

$$I(\bar{u}) = O_o(\bar{u}) I_s(\bar{u}) = [H_o(\bar{u}) \odot H_o^*(\bar{u})] I_s(\bar{u}) \quad (2)$$

where the capital letters correspond to the Fourier transformed values of the corresponding small letters in the previous equation and \odot is the autocorrelation operation. The quantity $I(\bar{u})$ is the real image spectrum, $I_s(\bar{u})$ is the object spectrum, $O_o(\bar{u})$ is the OTF of the aligned telescope, $H_o(\bar{u})$ is the instrument pupil function spectrum. The data from the WFS are recorded after alignment and if it is desired, the data from the WFS can be Fourier transformed to yield $I(\bar{u})$ and if the incident wave-front is plane, its amplitude is constant so $I_s(\bar{u})$ can be measured and removed from equation (2) and the instrument OTF can be evaluated.

If an incoherent point source a large distance (effectively infinite) from the telescope is imaged through the atmosphere, the image in the pupil plane of the telescope is

$$i_a(\bar{r}) = o_a(\bar{r}) \otimes i_s(\bar{r}) = |a(\bar{r}) \otimes h_o(\bar{r})|^2 \otimes i_s(\bar{r}) \quad (3)$$

where $i_s(\bar{r})$ is the atmospheric turbulence distorted image and $o_a(\bar{r})$ is the atmosphere-

instrument PSF. The PSF is the absolute value squared of the product of an atmospheric turbulence term convoluted into the instrument pupil function. In Fourier space the signal is

$$I_a(\bar{u}) = O_a(\bar{u}) I_s(\bar{u}) = [A(\bar{u})H_o(\bar{u})] \odot [A(\bar{u})H_o(\bar{u})]^* I_s(\bar{u}) \quad (4)$$

where capital letters are the Fourier transformed values. The OTF is the autocorrelation of the term $[A(\bar{u})H_o(\bar{u})]$. In an adaptive optics system the WFS and actuator-control computer try to restore the system to the original instrument OTF, $[H_o(\bar{u}) \odot \check{H}_o(\bar{u})]$.

B. Theory For A Coherent Source

For a laser's Gaussian beam profile a collimated beam can not be obtained using a lens system⁹. There are two definitions of collimation of Gaussian beams. One is the divergence angle is made as small as possible and the other is the next beam waist is made at the maximum distance from the lens system collimating the beam. This means the emerging beam from the collimator is a truncated Gaussian beam and it remains a truncated Gaussian in both the real and spatial frequency space. The HeNe laser used to align Pamela exhibits an approximate 20% fall-off at its input to the WFS. The beam is a spatially and temporally coherent truncated Gaussian function. For a coherent source the field can be calculated at any point along the beam path and the detector measures the intensity at that point. In the alignment mode for a coherent beam the field at a point \bar{r} in the pupil plane of the detector is

$$e_c(\bar{r}) = h_o(\bar{r}) \otimes e_{sc}(\bar{r}) \quad (5)$$

where $e_c(\bar{r})$ is the calculated field in the pupil plane of the detector, $e_{sc}(\bar{r})$ is the object field in this plane, and $h_o(\bar{r})$ is the pupil function of the telescope in this plane. The intensity⁷ in the pupil plane of the detector is

$$i_c(\bar{r}) = [h_o(\bar{r}) \otimes e_{sc}(\bar{r})] [h_o^*(\bar{r}) \otimes e_{sc}^*(\bar{r})]. \quad (6)$$

In the Fourier plane the intensity becomes

$$I_c(\bar{u}) = [H_o(\bar{u}) E_{sc}(\bar{u})] \odot [H_o^*(\bar{u}) E_{sc}^*(\bar{u})]. \quad (7)$$

The intensity is the autocorrelation of the product of the Fourier transformed pupil function and the spatial dependent transformed field and it is not the autocorrelation of just the transformed pupil function which is the classical definition of the OTF. If the field in the real plane at each WFS element exhibits a measurable lateral spatial coordinate dependence (coordinates perpendicular to the direction of propagation of the beam), the recorded calibration position for the aligned telescope will be in error. If at the CCD the Fourier transformed field exhibits spatial frequency dependence, this dependence can not be removed from the autocorrelations in equation (7) and the instrument OTF can not be correctly evaluated.

A laser source beacon at a large distance from the telescope has been proposed to phase-up the adaptive system for the effects of atmospheric turbulence. Assume the coherent laser is

operating in the TEM₀₀ mode to simplify the theory¹⁰, then the radial or lateral spatial dependence of the laser field is

$$E(r) = E_o \omega_o / \omega(z) \exp\{-r^2[1/\omega^2(z) + jk/2R(z)]\}, \quad (8)$$

$$\omega^2(z) = \omega_o^2[1 + z^2/z_o^2], R(z) = z[1 + z_o^2/z^2], \text{ and } z_o = \pi\omega_o^2 n/\lambda$$

where λ is the laser wavelength and ω_o is the beam waist. The range is the distance from the beacon to the telescope and if $z = R$ goes to infinity, then the field at the telescope is independent of r so the field at the telescope is approximately

$$E(R) = E_o \omega_o^2 / \lambda R \exp[-jkr^2/2R] = E_o \omega_o^2 / \lambda R. \quad (9)$$

The transformed fields are also independent of the coordinates \bar{r} and \bar{u} in the real and Fourier planes.

In the case of the distant laser beacon traversing the atmosphere the field in the pupil plane of the detector is

$$e_c(\bar{r}) = a(\bar{r}) \otimes h_o(\bar{r}) \otimes e_{sc}(\bar{r}). \quad (10)$$

The intensity measured by the detector is

$$i_c(\bar{r}) = [a(\bar{r}) \otimes h_o(\bar{r}) \otimes e_{sc}(\bar{r})] [a^*(\bar{r}) \otimes h_o^*(\bar{r}) \otimes e_o^*(\bar{r})]. \quad (11)$$

The intensity in spatial frequency space is

$$I_c(\bar{u}) = [A(\bar{u})H_o(\bar{u})E_{sc}(\bar{u})] \odot [A^*(\bar{u})H_o^*(\bar{u})E_{sc}^*(\bar{u})] \quad (12)$$

but since the distant laser field can be assumed independent of the lateral position coordinate \bar{u} , the field may be removed from the autocorrelation integrals and equation (12) has the same form as in the incoherent light case or

$$I_s(\bar{u}) = [A(\bar{u})H_o(\bar{u})] \odot [A^*(\bar{u})H_o^*(\bar{u})] I_{sc}. \quad (13)$$

CONCLUSIONS

The main conclusion of the paper is that an incoherent collimated source and not a collimated laser source is preferred to calibrate the WFS of an aligned adaptive optical system. A distant laser source can be used with minimum problems to correct the system for atmospheric turbulence. The collimation of the HeNe laser alignment source can be improved by using a very small pin hole in the spatial filter so only the central portion of the beam is transmitted and the beam from the filter is nearly constant in amplitude. The size of this pin hole will be limited by the sensitivity of the LEED elements.

REFERENCES

1. Phased Array Mirror Extendable Large Aperture Telescope, Phase III, Pamela Program, Kaman Aerospace Corporation, Contract # DASG 60-90-0022, 1993.
2. Lane, R.G. and Tallon, M., Wave-Front Reconstruction Using a Shack-Hartmann Sensor, Applied Optics, Vol. 31, pp 6902-6907, 1992.
3. Kelley, B.O. and Nemhauser, R.I., Technique for Using the Position Sensitivity of Silicon Photodetectors to Provide Remote Machine Control, 21st Annual IEEE Machine Tool Conference, paper C73970-1IA, Hartford, Conn., October 29-31, 1973.
4. Happer, W., MacDonald, G.J., Max, C.E., and Dyson, F.J., Atmospheric-Turbulence Compensation by Resonant Optical Backscattering from the Sodium Layer in the Upper Atmosphere, Journal of the Optical Society of America, Vol. A11, pp 263-276, 1994.
5. Roggemann, M.C. and Meinhardt, J.A., Image Reconstruction by Means of Wave-Front Sensor Measurement in a Closed-Loop Adaptive-Optics Systems. Journal of the Optical Society of America, Vol. A10, pp 1996-2007, 1993.
6. Goodman, J.W., Introduction to Fourier Optics, McGraw-Hill, ISBN 0-07-023776-X, pp 111-115, 1968.
7. Mavroidis, T., Dainty, J.C., and Northcott, M.J., Imaging Coherently Illuminated Objects Through Turbulence: Plane-Wave Illumination, Journal of the Optical Society of America, Vol. A7, pp 348-355, 1990.
8. Gaskill, J.D., Linear Systems, Fourier Transforms, and Optics, John Wiley & Sons, ISBN 0-471-29288-5, pp 313-317, 1978.
9. O'Shea, D.C., Elements of Modern Optical Design, John Wiley & Sons, ISBN 0-471-07796-8, pp241-245, 1985.
10. Yariv, A., Optical Electronics, Saunders College Publishing, ISBN 0-03-04744-2, pp 47-48, 1991.

112555

N95-18970

352666

1994

P. 7

NASA/ASEE SUMMER FACULTY FELLOWSHIP PROGRAM

**MARSHALL SPACE FLIGHT CENTER
THE UNIVERSITY OF ALABAMA**

BUBBLE FORMATION IN MICROGRAVITY

Prepared by:	Basil N. Antar, Ph.D.
Academic Rank:	Professor
Institution and Department:	The University of Tennessee Space Institute Department of Engineering Science and Mechanics
NASA/MSFC:	
Laboratory:	Space Science
Division:	Microgravity Science and Applications
Branch:	Biophysics
MSFC Colleague:	Dale M. Kornfeld

INTRODUCTION

A well known problem that has plagued microgravity materials processing and bioprocessing experiments for a very long time is the formation of undesired bubbles during procedures involving liquid transfer and mixing. It is conjectured that often bubble appearance is not due to simple mechanism leakage or lack of proper liquid degassing, but due to a phenomenon associated with microgravity environment. In a number of reported incidents, liquid handling operations performed on flight hardware in 1-g result in no bubble formation, while bubbles were observed when the same operations were performed in microgravity.

As an example, in the recent USML-1 shuttle mission a number of fluid experiments were adversely affected by unexpected and unexplained bubble formation. The Nucleation of Crystals from Solution (NCS) experiment experienced bubble formation in its solution reservoir which greatly interfered with the transfer of solution to the nucleation chamber both by agglomerating in the transfer line and by forming voids in the nucleation chamber. These bubbles appeared to have been generated at the end of the fill line, and sufficient number of bubbles were present in the cell to prevent initiation of nucleation on the first experiment run. An exceptional effort was required by the crew to accomplish a successful second run.

The Onset of Oscillatory Thermocapillary Flow Experiment (OTFE) also had problems with bubbles that were formed in the bottom of the heated liquid chamber. However, in this case the bubbles only interfered with the observations of the flow patterns and did not affect the experiment itself.

In the Protein Crystal Growth Glovebox (PCGG) experiment unexplained bubble formation was observed while extruding solutions from syringes and filling syringes for the experiments. During filling process, these bubbles appeared on the walls of initially dry syringes and were removed by manually centrifuging the syringes. This procedure wasted valuable time. During extrusion of solutions from syringes, bubbles appeared at the exits of the syringes. They were suppressed by greatly slowing the extrusion rate, which again wasted valuable time. This problem was especially serious during the solution mixing process required to initiate crystal nucleation due to the excessive time required to perform the procedure slow enough to avoid bubble formation. In another instance bubbles were observed to form during stirring of PCG solution in a polysulfone container with a needle. When the needle tip accidentally scrapped the surface of the container small bubbles were observed. However, upon repeating the same procedure in terrestrial conditions no bubbles were observed.

In all of the USML-1 examples cited above, bubbles appeared to be associated with the flow of liquids in tubes or through orifices, and occurred in of preflight degassing procedures. The specific examples were discussed in post-flight crew debriefing and subsequent personal communications. It is abundantly clear from these examples that formation of undesired bubbles can arise unexpectedly and with great frequency when transferring liquids in microgravity environment.

PROBLEM DEFINITION

The basic difficulties encountered with bubble formation during the low gravity experiments described above are due to the lack of specific procedures for dealing with bubbles. For example, any bubble generated during filling of an empty container with a liquid solution in terrestrial environment will eventually migrate to the top of the liquid where it will finally break the liquid/gas surface. In this instance buoyancy force works to ensure that the liquid bulk remains bubble free. Thus no special considerations need be adopted in this case to inhibit bubble generation during the filling procedure. In low gravity environment on the other hand, any bubble formed during filling will remain stationary within the liquid host and thus negatively impact the experimental procedure. Such a response of the bubbles is typically due to the absence or diminution of gravity induced buoyancy force. It is clear that the liquid transfer procedures involved in the experiments described above will have to be modified when performed in low gravity environment in order to ensure that bubbles are not formed.

Once bubbles are generated within a liquid host their subsequent development and motion in low gravity environment cannot be easily predicted. This difficulty is essentially due to the absence of the buoyancy force in such an environment. Furthermore, thermocapillary effects cannot be exploited for effecting liquid/gas separation in most of protein crystal growth processes due to the absence of the necessary temperature gradients in the liquid solutions. Thus the most desirable option for dealing with bubbles in this case is to prevent their formation in the first place. In order to ensure that bubbles are not generated requires developing special liquid handling procedures. Such procedures will involve both new fluid transfer protocols as well as novel container designs.

Gas bubbles are formed within liquid bulks in either one of two ways. Either by gas entrainment into the liquid through the gas/liquid free surface or by nucleation and diffusion of the dissolved gases within the liquid bulk. Bubbles may be formed by gas whenever a free gas/liquid interface is broken such as might happen when developed waves on the interface are amplified and subsequently broken. This may occur during filling of an empty container with liquid from a supply tank. Bubbles can also develop by nucleation from a vapor pocket seed through either homogenous or heterogeneous nucleation. In the homogeneous nucleation case the vapor seed is formed due to random molecular action within the liquid under the proper thermodynamic conditions. Homogeneous nucleation may occur whenever the pressure within the liquid falls below the vapor pressure or the temperature rises above the saturation temperature. Heterogeneous nucleation is usually initiated by trapped gas pockets in crevices at solid walls which are in contact with the bulk liquid.

When transferring liquid to an empty container under adiabatic conditions and without large variations in pressure, bubbles are most likely formed by entraining gas through the liquid/gas interface. It is necessary in this case to keep the free surface stable and free from waves during the filling process. These requirements may be accomplished by optimizing the liquid injection rate, as well as by the proper design of the inlet nozzle and the geometry of the receiving container.

When using a syringe to transfer liquids, either through injecting liquid into a host bulk or by withdrawing liquid from a bulk, bubbles may be formed through homogeneous or heterogeneous nucleation processes. In the injection case a cavitation bubble may form in the vicinity of the needle tip where the pressure conditions are extreme and crevices may be present in the external or internal walls of the needle. In the liquid suction case the adiabatic expansion within the syringe piston could reduce the pressure well below the vapor pressure and thus allow bubbles to form. In addition since the volume of some of the liquid bulks is small, the possibility could exist for the needle to break the liquid bulk surface allowing gas to be entrained into the syringe. This is possible in low gravity environment since the liquid bulk inside the vessel may not always be in contact with the vessel wall.

APPROACH

In order to understand the fundamental physics in bubble formation in microgravity a number of experiments were designed to study this phenomenon under controlled conditions. Specifically, a number of tests were designed to be performed onboard the NASA KC-135 airplane for the purpose of understanding the conditions that lead to bubble formation during microgravity liquid transfer. The KC-135 airplane provides approximately 40 parabola each of 30 seconds duration with a gravity level of $10^{-2} g_0$ per flight day. Normally, 4 days are available for testing during a flight campaign.

The first flight in this effort took place on March 14 - 18, 1994. In that flight three types of low gravity experiments were performed. In the first set of experiments water with PEG solution was injected, at various flow rates, through different needle diameters into a group of empty containers configured to duplicate the NCS experiment that was carried onboard USML-1. The purpose of these tests is to investigate bubble formation due to breakdown of the liquid/gas interface as the test cell is being filled with liquid. In the second set water with PEG solution was injected into liquid filled container of unique design to investigate cavitation phenomenon for submerged jets. Different needle sizes were used in these tests as well as different flow rates. In third set a number of "scratch tests" were performed by scrapping a needle with a sharp tip over various plastic surfaces that were submerged in water or PCG type solutions. These tests were intended to duplicate specific incidents reported to occur during the Glovebox PCG experiments.

All of the test chambers were constructed from transparent material such as plexiglass in order to allow for visual recording of the fluid motion within the test cells. High speed motion picture cameras were used to record all of the tests. In addition, both temperature and pressure data were collected for the submerged jet cavitation tests. Two pressure transducers were used in that test, one located at the entrance to the jet inlet line, and another at the inner wall of the chamber to record the background pressure. For each experiment a sequence of individual tests were designed and fitted within a test matrix. All of the items in the test matrices for these experiments were successfully conducted during the four flight of the campaign. All of the movie record-

ings were performed at a speed of 400 frames per second to allow for reasonable resolution of the events. fifteen rolls of films were used during that flight. The analysis of the films was conducted at 30 frames per second which was recorded on video tapes for convenience.

The NCS filling tests yielded the most dramatic images. For the high inflow rates the exiting liquid was seen to spread along two paths. One path is along the floor of the cell in the form of a very thick liquid film with a front advancing radially from the exit corner. The second path of the liquid is along the two side walls adjacent to the exit nozzle (the exit nozzle in all of these tests was located at the bottom corner of the test cell). In this case the liquid took the configuration of growing drops along the cell sidewall. Also the liquid was observed to climb along the inlet tube in the cell corner and spread along the top surface. Eventually, the liquid for these tests took a shape similar to an hourglass form. Needless to say that for such a complex liquid configuration the liquid engulfed a large number of bubbles and finally was full of bubbles. In the low flow rate tests as the liquid exited the nozzle it took a spherical form which expanded outwards in the radial direction. The spherical shape become more symmetrical with decrease in the flow rate. A spherical shape for the liquid/gas interface is the theoretical limit for zero gravity. The number of engulfed bubbles in all of these tests decreased with decrease in the flow rate.

The submerged jet cavitation tests did not show any bubbles forming at the jet exit nozzle. This was expected since the hardware design criteria, i.e. jet diameter and jet exit speed, were well below the critical values for cavitation to take place. These tests were repeated in the second flight campaign in which the jet conditions were brought closer to the critical values.

Careful analysis of the scratch tests have lead to the conclusion that the the gas bubbles observed during the shuttle experiments must have been entrained through the gas/liquid free surface with the assistance of the needle. This conclusion was made after the films were slowed down to 6 frames per second and then down to a single frame observations. In other words, the entrainment mechanism occurred extremely fast. Single frame analysis shows very clearly that a fast oscillation of the needle tend to engulf gas from the downstream side of the needle at the liquid/gas interface and then down into the liquid bulk along the needle axis. The gas is initially entrained in the form of a cloud surrounding the submerged portion of the needle which subsequently breaks up into bubbles. The bubbles will then spread throughout the liquid bulk along the motion streamlines of the liquid. There are two characteristic feature of these tests, one is that there exists a lower limit of the needle oscillation speed below which gas is not entrained. The other feature is the speed with which gas is entrained. the gas cloud appears in single frame advance indicating that it occurs in under 2.5 milliseconds.

These tests are far from being complete and further experiments are planned in order to advance the tests to the point of establishing a final conclusion on bubble formation in microgravity fluid handling processes. Also the results from all the tests will indicate the optimum design criteria for microgravity hardware for liquid handling.

CONCLUSIONS

Two KC-135 flight campaigns have been conducted to date which have specifically dedicated to study bubble formation in microgravity. The first flight was conducted during March 14-18, 1994; and the other during June 20-24, 1994. The results from the June 1994 flight have not been analyzed yet, while the results from the March flight have been partially analyzed. Thus the conclusions detailed in here are based on the results from first flight.

In the first flight three different experiments were performed, one with the specific aim at determining whether or not cavitation can take place during any of the fluid handling procedures adopted in the shuttle bioprocessing experiments. The other experiments were concerned with duplicating some of the procedures that resulted in bubble formation namely the NCS filling procedure and the needle scratch of a solid surface. The results from this set of experiments suggest that cavitation did not take place during any of the fluid handling procedures. The results clearly indicate that almost all the were generated as result of the breakup of the gas/liquid interface. This was convincingly demonstrated in the scratch tests as well as in the liquid fill tests.

112556

N95-18971

1994

352667

NASA/ASEE SUMMER FACULTY FELLOWSHIP PROGRAM *P.S.*

MARSHALL SPACE FLIGHT CENTER
THE UNIVERSITY OF ALABAMA

THE ASSESSMENT OF VIRTUAL REALITY
FOR
HUMAN ANATOMY INSTRUCTION

Prepared By: Karen P. Benn, M.S.

Academic Rank: Instructor/Director
Allied Health Program

Institution and Department: Oakwood College
Department of
Chemistry, Biochemistry
& Allied Health

NASA/MSFC:

Laboratory: Mission Operations
Division: Operations Engineering
Branch: Crew Systems
Engineering

MSFC Colleague: Joseph P. Hale

INTRODUCTION

Virtual reality is the computer graphics creation of an environment which allows its participants to physically interact with objects within an electronic environment. A virtual reality applications program has been under development at the Marshall Space Flight Center (MSFC) since 1989. The MSFC VR systems consists of VPL Research, Inc. Eyephones (Models 1 and LX), DataGloves, and software (Swivel 3D, Body Electric, and ISAAC), Polhemus Isotrak and Fastrak spatial tracking systems, two Macintosh IIfx computers and two Silicon Graphics Inc. graphics computers (4D/310VGX and 4D/320VGXB). The objectives of the MSFC VR applications program are to develop, assess, validate, and utilize VR in hardware development, operations development and support, mission operations training, and science training.

This research project seeks to meet the objective of science training by developing, assessing and validating VR as a human anatomy training medium. Current anatomy instruction is primarily in the form of lectures and usage of textbooks. In ideal situations, anatomic models, computer-based instruction, and cadaver dissection are utilized to augment the traditional methods of instruction. At many institutions, lack of financial resources limits anatomy instruction to textbooks and lectures. However, human anatomy is three-dimensional, unlike the one-dimensional depiction found in textbooks and the two-dimensional depiction found on the computer. Virtual reality is a breakthrough technology that allows one to step through the computer screen into a 3-D artificial world. This technology offers many opportunities to enhance science education. Therefore, a virtual testing environment of the abdominopelvic region of a human cadaver was created to study the placement of body parts within the nine anatomical divisions of the abdominopelvic region and the four abdominal quadrants.

RESEARCH PLAN

The development of the VR training medium consisted of the following objectives: creation of a static three-dimensional model of the abdominopelvic region of a human cadaver utilizing RB2 Swivel software, creation of the behavioral relationship between objects in the virtual environment via Body Electric software and establishment of the communications between the two software packages- RB2 Swivel and Body Electric. Completion of these objectives resulted in the creation of a three-dimensional computer graphics model of the human body in which one is able to enter, "fly" around, grab and rearrange organs (see Figure 1). The

hypothesis of the research project is that an immersive learning environment affords quicker anatomic recognition and orientation and a greater level of retention in human anatomy instruction. Based on this hypothesis, the study will attempt to determine the most appropriate time to augment traditional human anatomy instruction with virtual reality training.

The proposed research study will be assessed and validated during the institutional cycle at Oakwood College and will utilize a cohort design with treatment partitioning. Two groups will exist- experimental and control. The purpose of the design will be to test whether the two groups differ. In the control group, students will be exposed to the traditional non-immersive learning environment. In the experimental group, students will be exposed to the non-traditional VR immersive learning environment. Comparisons of these two groups will be made with the ultimate goal of determining if there were quicker uptake and longer retention in the group exposed to the immersive non-traditional VR learning environment. Both groups will be given pre- and post- paper tests to validate the efficacy of VR as a teaching modality for human anatomy instruction.

The respondents will be partitioned into one of three groups based on the extent of their experience. This will be done to strengthen the internal validity of the cohort design. These groups will include the following: students who are enrolled in Medical Terminology, students who are repeating Medical Terminology, students who have been exposed to Anatomy & Physiology at the undergraduate level and students who have been exposed to Anatomy & Physiology at the high school level.

In the experimental group, students will be further subdivided into one of three groups: pre-VR training, concurrent VR training and post-VR training. All students will be given a paper pre-test one week prior to VR immersion and subsequently lectured on the placement of body parts in the nine anatomical divisions of the abdominopelvic region and the four abdominal quadrants. Students in the pre-VR training group will utilize the human anatomy VR training modality one day prior to the lecture. Students in the concurrent VR training group will utilize the human anatomy VR training modality one day after the lecture. Students in the post-VR training group will utilize the human anatomy VR training modality three days after the lecture. All students will be given a post-paper test one week and six weeks post-VR immersion.

For the control group, archival records from the previous year's class will be obtained because it is reasonable to assume that the background characteristics of this group will be similar to those of the experimental group at the same institution. This cohort design will allow the drawing of causal 'quasi-comparability' inferences between the cohorts that do and do not receive VR training.

In conclusion, the assessment and validation of virtual reality as a tool for human anatomy instruction will determine the extent to which an artificial computer graphics simulation of the human body augments traditional modes of instruction.

I would like to thank my MSFC Colleague, Joseph Hale, for his support and guidance. In addition, I would like to thank Michael Flora for his technical assistance in the development of this project.

REFERENCES

1. Aukstakalnis, Steve and David Blatner. Silicon Mirage: The Art and Science of Virtual Reality. CT: Peachpit Press, Inc., 1992.
2. Helsel, Sandra K. and Judith P. Roth. Virtual Reality Theory, Practice and Promise. CT: Meckler Publishing, 1991.
3. Kalawsky, Roy. The Science of Virtual Reality and Virtual Environments. England: Addison-Wesley Publishing Co., 1993.
4. Merril, Jonathan R., Rakesh Raju and Rita T Roy. "VR Applications in Medical Education," *Virtual Reality Special Report* , Premier Issue, pp 61-64, 1994.
5. Merril, Jonathan R. "Virtual Reality for Medical Training and Trade Show 'Fly-Paper'," *Virtual Reality World*, Vol. 1, nos 3-4, pp. 34-38.
6. Pimentel, Ken and Kevin Teixdeira. Virtual Reality: Through the New Looking Glass. New York: McGraw-Hill, Inc, 1993.
7. Rheingold, Howard. Virtual Reality. New York: Simon & Schuster, 1991.

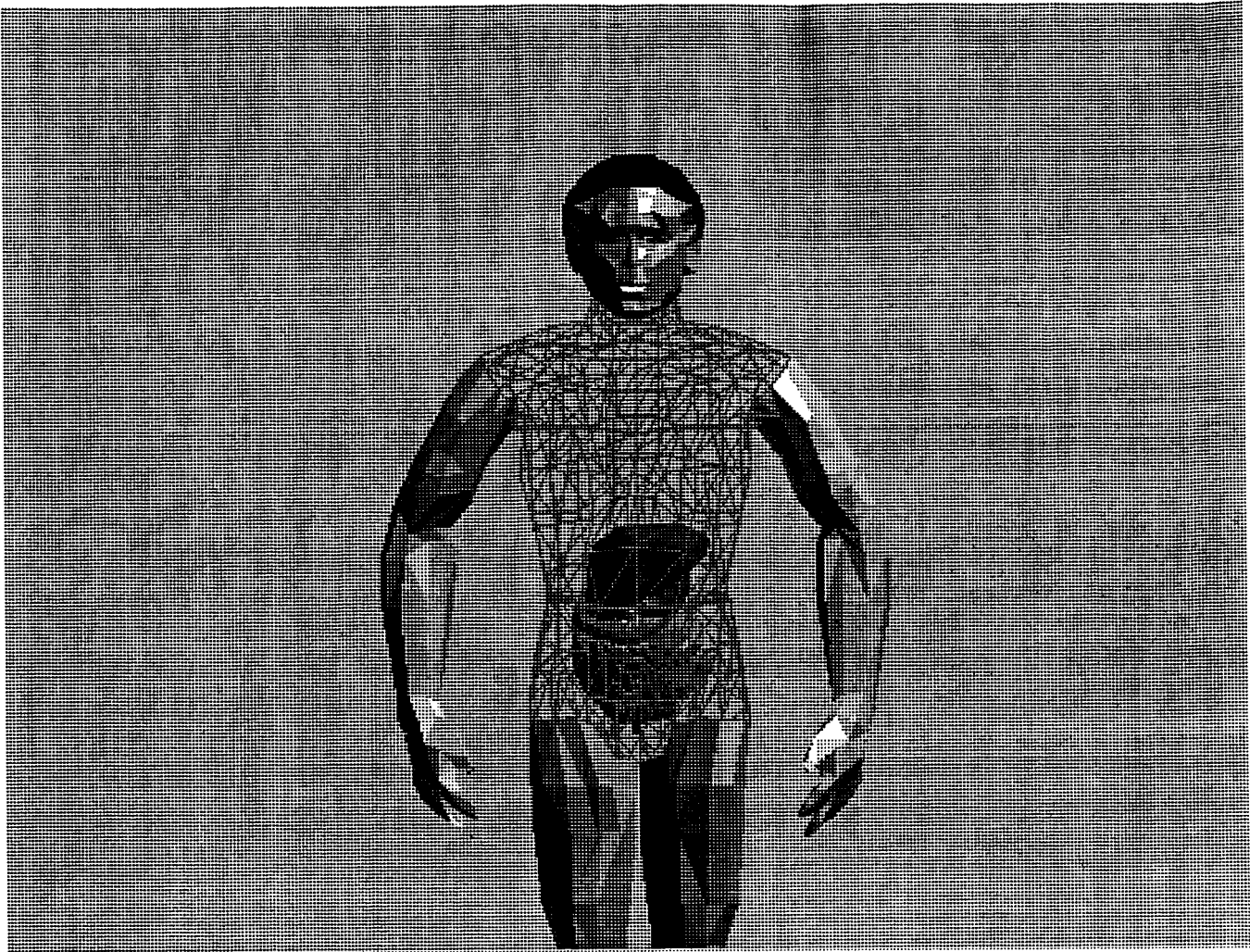


FIGURE 1

112557

1994

N95-18972

NASA/ASEE SUMMER FACULTY FELLOWSHIP PROGRAM

352668

**MARSHALL SPACE FLIGHT CENTER³
THE UNIVERSITY OF ALABAMA**

P.7

RESIDUAL STRESSES IN WELDED PLATES

Prepared By: Edward L. Bernstein
Academic Rank: Assistant Professor
Institution and Department: Alabama A&M University
Department of Engineering Technology

NASA/MSFC:

Laboratory: Materials and Processes
Division: Metallic Materials and Processes
Branch: Metallurgy Research

MSFC Colleague: Arthur Nunes

INTRODUCTION

Residual stresses are stresses that remain in a body after all external stresses are removed. They may either lower the usable strength, or may be beneficial and raise the strength. Residual stresses can arise from manufacturing processes or from non-uniform temperature changes. They result from stress levels causing plastic deformation of the material, which is then elastically unloaded, but prevented from returning to its initial state by interior or exterior structural restraints. The welding process, in particular, creates residual stresses. These stresses have been related to cracking in repair welds which has been observed in Al 2195, the lightweight aluminum-lithium alloy to be used in the Light Weight Space Shuttle Tank.

The mechanism that results in residual stresses in the welding process starts with the deposition of molten weld metal which heats the immediately adjacent material. After the solidification of weld material, normal thermal shrinkage is resisted by the adjacent, cooler material. When the thermal strain exceeds the elastic strain corresponding to the yield point stress, the stress level is limited by this value, which decreases with increasing temperature. Cooling then causes elastic unloading which is restrained by the adjoining material. Permanent plastic strain occurs, and tension is caused in the region immediately adjacent to the weld material. Compression arises in the metal farther from the weld in order to maintain overall static equilibrium. Subsequent repair welds may add to the level of residual stresses.

The level of residual stress is related to the onset of fracture during welding. Thus, it is of great importance to be able to predict the level of residual stresses remaining after a weld procedure, and to determine the factors, such as weld speed, temperature, direction, and number of passes, which may affect the magnitude of remaining residual stress. The purpose of this project was to develop a simple model which could be used to study residual stress. It was hoped to use traditional analytical modeling techniques so that it would be easier to comprehend the effect of these variables on the resulting stress. This approach was chosen in place of finite element methods so as to facilitate the understanding of the physical processes. The accuracy of the results was to be checked with some existing experimental studies giving residual stress levels found from X-ray diffraction measurements.

THE MODEL

The structure which was modeled was a thin plate of infinite width. It was considered to have a weld of uniform thickness deposited along a central line. The plate was assumed to have uniform thickness and uniform physical properties, although the yield stress, elastic constants, and coefficient of thermal expansion vary with temperature. The coordinate system is shown in Figure 1. The x-coordinate is along the width of the plate perpendicular from the weld, y is the weld direction, and z is the thickness direction.

The analysis of the mathematical model was composed of a thermal analysis to determine the temperature distribution, and a subsequent stress analysis, using the resulting temperature distribution.

THERMAL ANALYSIS

The heat supplied by a welding arc produces complex thermal cycles in the weld zone. It was assumed that the heat source was a point source, and all losses were by conduction into the plate. The temperature was assumed to be unchanged at a large distance from the weld. The basic equation is:

$$\frac{\partial T}{\partial t} = \kappa \left(\frac{\partial^2 T}{\partial x^2} + \frac{\partial^2 T}{\partial y^2} + \frac{\partial^2 T}{\partial z^2} \right)$$

where

$\kappa = \text{thermal diffusivity} = \lambda/c\rho$, $\lambda = \text{thermal conductivity}$, $c = \text{specific heat}$

It was assumed that the temperature distribution varied only in the x-direction so that the equation could be further simplified to

$$\frac{\partial T}{\partial t} = \kappa \left(\frac{\partial^2 T}{\partial x^2} \right)$$

This equation was solved by a finite difference formulation:

$$\frac{T_{ij+1} - T_{ij}}{\Delta t} = \frac{\kappa}{\Delta x} \left(\frac{T_{i+1j} - T_{ij}}{\Delta x} - \frac{T_{ij} - T_{i-1j}}{\Delta x} \right)$$

or

$$T_{ij+1} = \kappa \frac{\Delta t}{\Delta x^2} (T_{i+1j} - 2T_{ij} + T_{i-1j}) + T_{ij}$$

where the subscript j represents a time increment and i represents a spatial nodal increment in the x-direction. The model is shown in Figure 1.

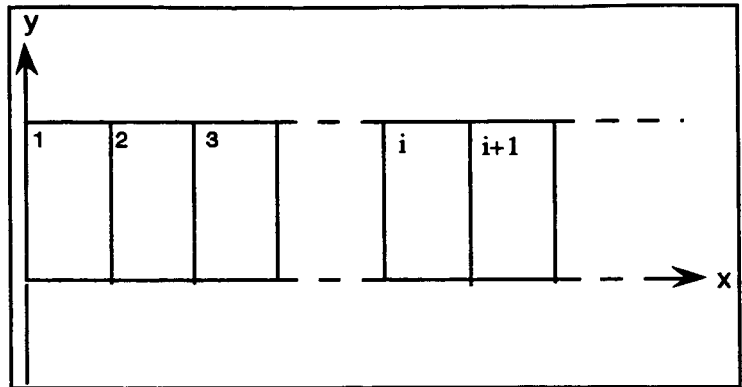


Figure 1. Finite Difference Model of Plate

Initially, the temperature at the central node was set at 600° C, the approximate melting temperature of aluminum, and the other nodes set to 20° C ambient temperature. The above equation was used to calculate heat flow over enough time intervals until an approximately uniform distribution was reached across the plate. This formulation will approximate the temperature states passed through by a welded plate. A total of 27 nodes were used, representing symmetric nodes on each side of the center weld. The nodes were spaced at $x = \text{weld width} = \text{thickness of plate} = 1/4"$. A time increment was chosen corresponding to

a weld speed of $v = 8 \text{ in/min}$. Then $\Delta t = \Delta y/v = 1/8"/8 \text{ in/min} = 1/64 \text{ min}$ or approximately 1 second. However, it was found that a time interval of 0.1 second was required for convergence. A value of $\kappa = 53 \text{ mm}^2/\text{sec} = .08 \text{ in}^2/\text{sec}$ for 2219 Al was used. The MATLAB program was used to solve the equations, and it was found that an approximately uniform distribution was reached after 76 time iterations or 7.1 seconds when the change in temperature at the middle of plate from one time interval to the next was less than 5%. The temperature distribution for eight time intervals is shown in Figure 2. These values were used for the initial values in the following stress analysis.

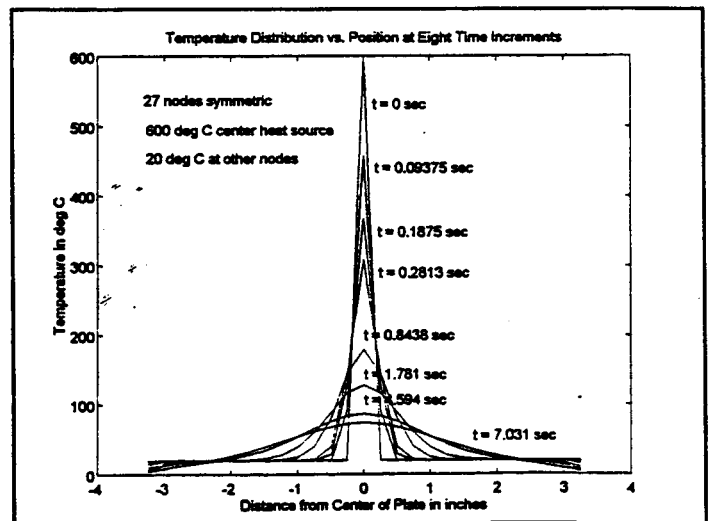


Figure 2. Results of Thermal Analysis

STRESS ANALYSIS

Residual stresses were calculated using a model which represents the plate as a series of unconnected bars, undergoing only axial strain. Eight time intervals were selected, and each bar was assigned a temperature distribution based on the thermal analysis above. The mechanical properties were assumed to vary with temperature, and values for yield stress, coefficient of thermal expansion, and modulus of elasticity were used for 2219 aluminum alloy based on Ref.2

It was assumed that an idealized stress-strain relationship holds, with a constant yield stress for each temperature level. Time intervals were taken close together near the onset of welding and further apart as the time approached the state of uniform temperature distribution. The effects of transverse stress were ignored and uniform longitudinal strain across the plate was assumed.

The solution procedure was based on one developed in Ref 1 and is as follows: At time 0 the thermal stress for the i -th axial element is calculated from $\sigma_{yi} = E_i \alpha_i \Delta T_i$, where E_i is the modulus of elasticity, α_i is the coefficient of thermal expansion, and ΔT_i is the temperature change from the previous time interval (or the initial temperature for the first time interval). The axial force over the entire width of the plate is then calculated and averaged to produce an average stress in each element. In order to maintain static equilibrium, this stress is then subtracted from the thermal stress to produce a net stress level. If this value exceeds the yield stress, it is lowered to that value. A new axial force is then calculated over the width, and an check for static equilibrium performed. If static equilibrium is not satisfied to within a predetermined tolerance, a new average axial stress is calculated and the process repeated until static equilibrium is attained. Then, the temperature distribution for the next time interval is applied, and the calculation process begun again, adding the stresses resulting from the previous time increment, before matching them against the yield stress level. At the conclusion of the process, the final stress level at the last time increment is the residual stress in the plate.

The results of the analysis are shown in Figure 3.

A maximum value of 48.5 ksi tensile is found at the weld centerline, with a compressive value of -6.0 ksi seen at the edge of the weld. The compressive stress then decreases as the distance from the weld increases.

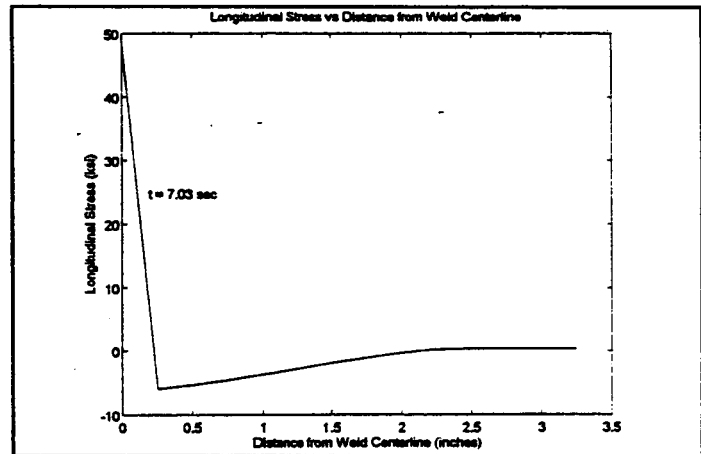


Figure 3. Results of Stress Analysis

Comparison with Experimental Results

These results were compared with X-ray diffraction residual stress measurements previously made on 2195 aluminum alloy. These results are shown in Figure 4. They reveal a maximum tensile stress of 39.7 ksi at a distance of 0.42 in from the weld centerline, and a maximum compressive stress of -16.7 ksi at a distance of 1.08 in from the centerline. They also show a reduction of tensile stress within the weld to almost zero at the centerline. The analytical model gives a

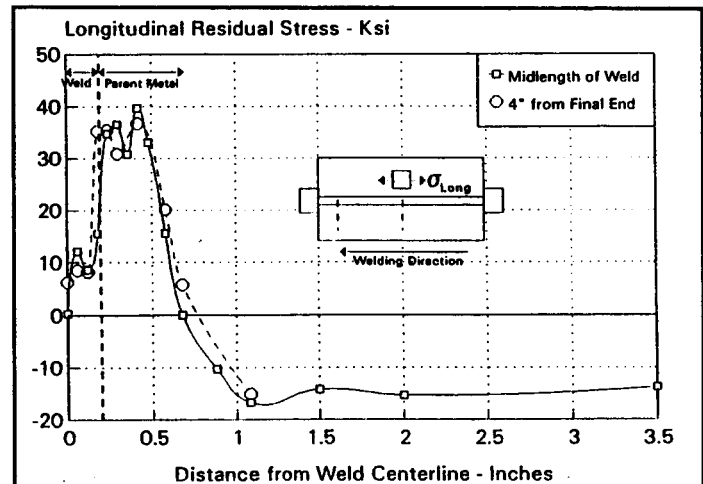


Figure 4. Residual Stress Measurements

maximum tensile stress of 48.7 ksi at the centerline and a maximum compressive stress of -6.0 ksi at a distance of 0.5 inches from the centerline. These results compare reasonably well in magnitude, although the experimental results show stress maxima to be located farther away from the centerline. The analytical results show the same shape of stress distribution.

While this correlation is encouraging for the simple model used, it was hypothesized that an improved model, incorporating the effects of transverse stress, might show the decrease in tensile stress within the weld seen in the experimental study. It also would provide a value for the transverse stress, which may be related to the onset of fracture observed in repair welds. The supposition was that as the weld area shrinks, a restraint to transverse contraction is provided by the adjacent cooler material. This restraint causes a transverse tensile stress which is associated with a longitudinal compressive stress, through the Poisson effect. This stress would tend to lower the tensile longitudinal stress previously modeled.

STRESS ANALYSIS INCLUDING TRANSVERSE STRESS

Each of the elements in Figure 1 is assumed to be in a state of plane stress. It is assumed that the longitudinal strain ϵ_{yi} and the transverse stress σ_{xi} is constant across all elements i . The stress strain relations in the i -th element are (Ref. 3)

$$\epsilon_{xi} = \frac{1}{E_i} [\bar{\sigma}_x - \nu_i \sigma_{yi}] + \alpha_i T_i + \epsilon_{xi}^p + \Delta \epsilon_{xi}^p$$

$$\bar{\epsilon}_y = \frac{1}{E_i} [-\nu_i \bar{\sigma}_x + \sigma_{yi}] + \alpha_i T_i + \epsilon_{yi}^p + \Delta \epsilon_{yi}^p$$

where ϵ_{xi} is the transverse strain, $\bar{\epsilon}_y$ is the constant longitudinal strain, ϵ_{xi}^p and ϵ_{yi}^p are the plastic strains which accumulated prior to the current time interval, $\Delta \epsilon_{xi}^p$ and $\Delta \epsilon_{yi}^p$ are the incremental plastic strains developed in the current time interval, $\bar{\sigma}_x$ is the constant transverse stress, σ_{yi} is the constant longitudinal stress, and ν_i is Poisson's ratio. Static equilibrium across the width of the plate is given by the equation

$$\sum \sigma_{yi} \Delta x_i = 0$$

and the condition restricting the total transverse displacement to zero is given as

$$\sum \epsilon_{xi} \Delta x_i = 0$$

where the summations are over all the elements, and Δx_i is the width of the i -th element. These equations can be written as a series of linear equations in the unknown quantities $\bar{\sigma}_x$, σ_{yi} , ϵ_{xi} , $\bar{\epsilon}_y$. At the first time interval, $t = 0$ the right-hand side of these equations contains the known quantities $\alpha_i T_i$, where T_i are again taken from the thermal stress analysis. Elastic strains are assumed, so that the plastic strain terms ϵ^p and $\Delta \epsilon^p$ are zero. The equations are then solved, and if a stress level exceeds the yield stress, it is equated to the yield stress. The equations are then solved again, but the yield stress for that element is now known, and a plastic strain is now introduced as an unknown, replacing the role of the elastic stress component. The solution of this set of equations yields the plastic strain increment for the first time interval. At the next time period the previous plastic strain increment becomes the ϵ^p term and is placed on the right hand side of the equations. The procedure is repeated for each time interval. The solution at the final time interval provides the residual stresses in the plate. The results are shown in Figure 5.

They show a similar distribution to the previous analysis. The maximum tensile stress was reduced about 30% to 34 ksi and compares more closely to the experimental results. The compressive stress level of -6 ksi is comparable to the previous result. A transverse compressive stress of -4.5 ksi was calculated, and can be compared to an experimental result varying from -4.6 to -13.1 ksi located from 1 in to 3 1/2 inches from the weld centerline.

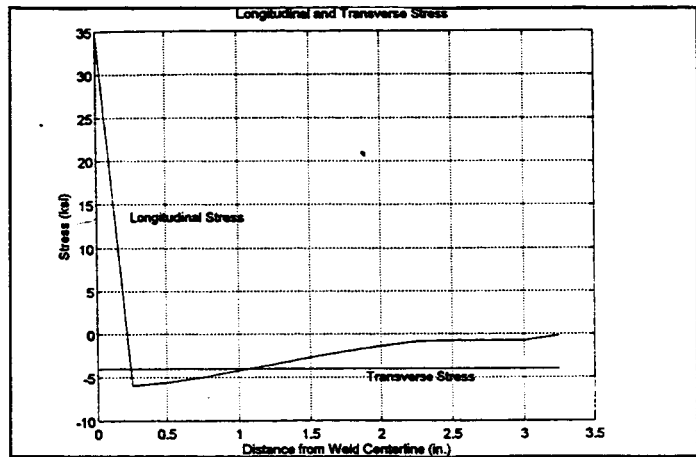


Figure 5. Results of Transverse Stress Analysis

Future Directions

This project did succeed in reproducing qualitative residual stress characteristics similar to expected and observed results. The maximum value of tensile residual stress agreed within 12% of the experimental values, while the compressive stress levels were approximately 1/2 of the experimental results. The dip in tensile values in the interior of the weld was not reflected in the model. The following areas for further research in this area should be pursued:

1. The thermal analysis can easily be coupled with the stress analysis for greater computational efficiency. In this way a solution would flow directly from the assumed temperature distribution to the final residual stresses.
2. Refinement of the model within the weld area should be made to include smaller elements and changed properties reflecting the changed metallurgical characteristics of the solidified weld material.
3. A more realistic thermal model reflecting the continuous heat input of a moving line heat source would could have a large effect on the residual stresses.
4. The transverse stress model should be improved. The plastic strain portion of the solution should be analyzed more carefully, possibly using the Prandtl-Reuss flow rule.
5. Critical stress values should be correlated to fracture of welded plates and to further experimental results which should be tied to analytical models.

References

1. Tall, L., "Residual Stresses in Welded Plates - a Theoretical Study," *Welding Journal*, Vol. 43, pp.10s-23s, 1964.
2. *Metals Handbook*, 10th edition, American Society for Metals, 1989
3. Mendelson, A., *Plasticity: Theory and Applications*, Macmillan, London, 1968.
4. Rosenthal, D., "The Theory of Moving Sources of Heat and its Application to Metal Treatments," *Transactions of the ASME*, Vol. 68, 1946.

112558

N95-18973

1994

NASA/ASEE SUMMER FACULTY FELLOWSHIP PROGRAM

352681

**MARSHALL SPACE FLIGHT CENTER
THE UNIVERSITY OF ALABAMA**

**FOREIGN BODY IMPACT EVENT DAMAGE
FORMATION IN COMPOSITE STRUCTURES**

Prepared By: Ronald B. Bucinell, Ph.D.
Academic Rank: Assistant Professor
Institution and Department: Union College, Schenectady, NY
Department of Mechanical Engineering

NASA/MSFC:

Laboratory: Materials and Processes
Division: Nonmetallic Materials and Processes
Branch: Polymers and Composites

MSFC Colleagues: Alan T. Nettles

INTRODUCTION

The use of composite materials in structural applications is becoming more widely accepted. The success of composites on the Delta and Titan solid rocket motor programs clearly indicates that composite materials can be used reliably in launch vehicle hardware. Even with this success, there is still concern related to the effect of foreign body impact events on the integrity of composite structures. The manufacturing, storage, transportation, and service environments are filled with foreign body impact event scenarios. Some of these scenarios can severely degrade the integrity of the composite structure; however, many will have little or no effect at all on structural integrity. A methodology for determining the severity and residual effects of foreign body impact events on composite structures has yet to be developed and accepted by the composite materials community. As a result, current flight hardware that is knowingly subjected to a significant impact event is removed from service.

This overly conservative approach to dispositioning composite structures subjected to impact events was recently used to remove a TOS-2 Kevlar motor case from service. This incident refocused NASA MSFC's attention on the need to develop a methodology for assessing the extent and effect of impact related damage on composite structures. The RTOP entitled *Filament Wound Composite Pressure Vessel Damage Tolerance Program* was conceived in March 1992 and funded in July 1992 at NASA MSFC to address this need. The scope of this RTOP includes development of Non-Destructive Evaluation (NDE) techniques, subscale testing, and analytical model development.

One aspect of the analytical model development task is the development of an analytical methodology that can be used to evaluate the experimental data, predict damage formation and modes, and predict the residual properties of an impacted composite structure. Several methodologies have successfully predicted the response of composite structures to impact events [1,2,3,4] and the scaling of impact events up to the point of damage initiation [5,6,7]. However, methodologies for predicting damage formation [8,9] to date have been either empirical or material specific.

The remainder of this report will discuss a methodology that can be used to assess the effect of foreign body impacts on composite structural integrity. The described effort focuses on modeling the effect of a central impact on a 5 3/4" filament wound test article. The discussion will commence with details of the material modeling that was used to establish the input properties for the analytical model. This discussion is followed by an overview of the impact assessment methodology. Finally, the progress on this effort to date will be reviewed along with a discussion of tasks that have yet to be completed.

MATERIAL PROPERTIES

The success of modeling the 5 3/4" bottle shown in Figure 1 is dependent on the accuracy of the material properties input to the models. The bottle configuration contains four different types of materials: rubber liner, inert propellant, steel boss, and composite outer layer. The material properties for the liner, propellant, and boss are summarized in Table 1. These materials are all isotropic and, for the loading being considered, behave in a linear-elastic

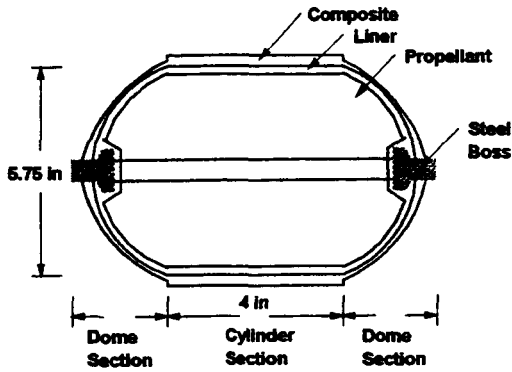


Figure 1: Illustration of 5 3/4" bottle

Table 1: Isotropic material properties for 5.75" bottle

	E (psi)	ν
Steel Boss	$30(10^6)$	0.3
Liner	1,440	0.49
Inert Propellant	800	0.49

manner. The composite outer layer is the primary load bearing component of the bottle. The composite constituent materials used are IM7 fibers embedded in 8553-45 matrix material.

To fully model the response of the bottle to a central impact event and evaluate its residual properties, material properties of the composite layer at the constituent, lamina, and laminate level are required. Effective constituent properties were determined using vendor supplied unidirectional property data and micro-mechanics models. Micro-mechanics, variational principals, and lamination theory were employed to compute the properties of the composite laminate in the cylinder and dome sections of the bottle. In the cylinder section of the bottle the laminate is filament wound into a $[90_2/\pm 11.5/90_2/\pm 11.5]$ configuration. The resulting orthotropic material properties are:

$$\begin{array}{lll}
 E_a = 12.7 \text{ Msi} & \nu_{a\theta} = 0.002 & G_{a\theta} = 9.55 \text{ Msi} \\
 E_\theta = 13.6 \text{ Msi} & \nu_{\theta r} = 0.345 & G_{\theta r} = 5.32 \text{ Msi} \\
 E_r = 1.34 \text{ Msi} & \nu_{r\theta} = 0.345 & G_{r\theta} = 4.95 \text{ Msi}
 \end{array}$$

where the coordinate directions are defined as a-axial (along the length of the bottle), θ -circumferential direction, and r-radial direction.

The complex laminate configuration in the dome section of the bottle is a result of the polar wind used to fabricate the bottles. As a result the laminate configuration and thickness change continuously from the top of the dome (at the cylinder/dome intersection) to the bottom of the dome (at the boss). Thus the material properties in this region are continually changing as shown in Figure 2 and become extremely anisotropic. For modeling purposes the three dimensional anisotropic material properties for the dome were computed at discrete increments along the curvature of the dome. The laminate configuration at discrete increments were computed using a contractor

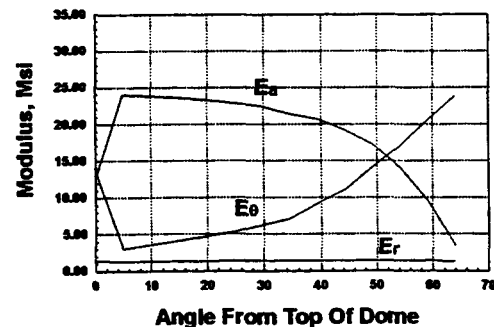


Figure 2: Variation of dome properties

supplied model. The discrete increments were chosen to correspond to the location of element center points in the finite element model used to predict the impact response.

MODEL DEVELOPMENT

The modeling of the 5 3/4" bottle shown in Figure 1 requires a systematic simplification of the complex phenomenon associated with the impact event. Because of the relatively high ratio of the impactor mass to effective bottle mass, the effect of the higher order vibration modes can be ignored enabling the use of a static analysis [3]. The static analysis employed involves various levels of modeling starting at the global or full structural level and ending at the micro-mechanics level. This step wise approach is taken in order to facilitate the determination of fiber and matrix phase averaged stresses in the composite layer that result from the impact event while at the same time making efficient use of computer resources. The phase averaged stresses in the composite are used to predict damage and eventually residual properties of the bottle.

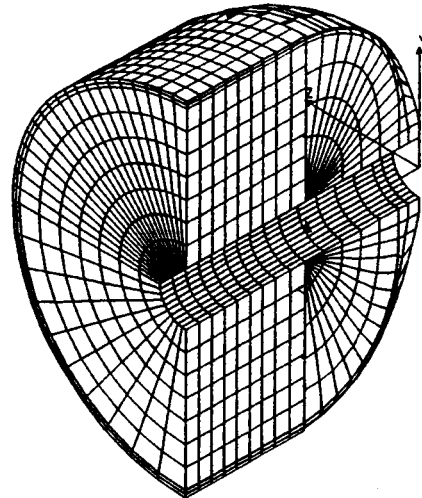


Figure 3: Global finite element mesh of bottle

The global or full structural model employs the use of the finite element technique. The finite element mesh used in this investigation is shown in Figure 3. At this level the composite is modeled as a single layer of homogeneous material. The finite element model takes advantage of the symmetry associated with the bottle geometry. On the symmetric surfaces the displacements normal to the surface and rotations parallel to the surfaces are constrained from movement. In addition, a constraint representing the cradle used to hold the bottle is also imposed. This constraint restricts radial displacements in the cylinder section of the bottle along a 1/2" wide strip that adjoins the dome and circumferentially starts at the bottom of the bottle and ends half way up the bottle's side. The purpose of this model is to define displacements along a boundary region that is local to the impact event. Because this region will be chosen away from the actual impact event a point load is used to represent the force of the impactor tup on the bottle at the top intersection of the symmetric surfaces. As a result of this loading condition a maximum displacement of 0.1" is produced at the point of impact. Figure

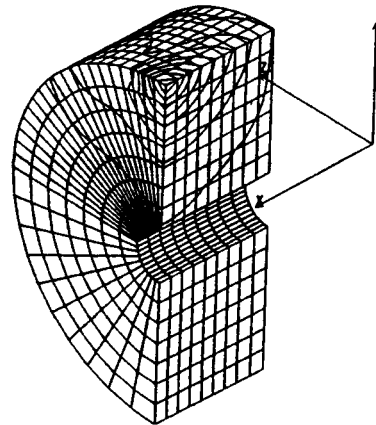


Figure 4: Displacement contours in bottle resulting from the impact event.

4 illustrates the displacement contours for the impact event that was produced using the above described model.

The second step in the modeling process models the region local to the impact event using a finer finite element mesh. At this level each layer of the composite is modeled as a unidirectional ply. The displacements calculated using the global finite element analysis are used as the boundary conditions for the local finite element mesh. Since the local mesh will have more nodal points along all of the boundaries, polynomials are fit through the results of the global analysis in order assist in the estimation of the proper nodal constraints on the boundary surfaces of the local finite element mesh. The load resulting from the impact event in this model is modeled as a elliptical pressure distribution [10]. The resulting stress distributions in the individual plies are then calculated. These results are then used by a micro-mechanical analysis that computes the phase (constituent) averaged stresses. Knowing the phase averaged stresses, damage in the constituent phases are predicted. These predictions are then used to degrade the material properties in the damage regions in order to calculate the residual properties of the bottle.

PROGRESS, TASKS REMAINING, RECOMMENDATIONS

The above described effort has made significant progress this summer. The modeling of all the materials in the bottle has been completed. Some of the material properties were experimentally verified. The global finite element analysis has also been completed and the displacements in the region of the impact event have been determined. Currently, the construction of the local finite element model is in progress. The micro-mechanical models that will be used to predict the constituent phased averaged stress using the results of the local finite element model have already been constructed. The 5 3/4" bottles were impacted earlier this year at NASA MSFC. Correlations between the model predictions and the observed damage remain to be made.

As a result of this summers efforts the following recommendations are made to help improve NASA MSFC's capability to predicting the response of composite structures to foreign impact events:

- 1) The current model for the geometry of the composite in the dome requires modification to account for tow width and the use of helical winds.
- 2) A user subroutine needs to be developed that will allow the local finite element code to have direct access to the micro-mechanical models. This will enable progressive damage analysis of impact events to be performed.
- 3) An effort should be initiated to develop a model that will predict the residual properties of the composite bottles after they have been impacted.
- 4) The 18" bottles that are slated for testing in FY '95 should be modeled using the above methodology to verify the approach taken.

REFERENCES

- 1) Greszczuk, L.B., "Damage in composite materials due to low velocity impact," *Impact Dynamics*, Wiley, New York, 1982.
- 2) Cairns, D.S., Lagace, P.A., "Transient response of graphite/epoxy and Kevlar/epoxy laminates subjected to impact," Proceedings of the AIAA/ASME/ASCE/AMS 29th Structures, Structural Dynamics, and Materials Conference, 18-20 April 1988, Williamsburg, VA, Paper No. 88-2328.
- 3) Bucinell, R.B., Nuismer, R.J., Koury, J.L., "Response of composite plates to quasi-static impact events," *Composite Materials: Fatigue and Fracture (third Volume)*. ASTM STP 1110, T.K. O'Brien, Ed., American Society for Testing and Materials, Philadelphia, 1991, pp.528-549.
- 4) Olsson, R., "Impact response of orthotropic composite plates predicted by a one-parameter differential equation," FFA TN 1989-07, The Aeronautical Research Institute of Sweden, (1989).
- 5) Morton, J., "Scaling of impact loaded carbon fiber composites," Proceeding of the 28th Structures, Structural Dynamics and Materials Conference, Part I, Paper 87-0867, (1987), pp. 819-826.
- 6) Bucinell, R.B., Madsen, C.B., Nuismer, R.J., Benzinger, S.T., Morgan, M.E., "Experimental investigation of scaling impact response and damage in composite rocket motor cases," Proceedings of the JANNAF Composite Motor Case and Structures and Mechanical Behavior Meeting, Jet Propulsion Laboratory Anaheim, CA, (1989).
- 7) Qian, Y, Swanson, S.R., Nuismer, R.J., Bucinell, R.B., "An experimental study of scaling rules for impact damage in fiber composites," *Journal of Composite Materials*, 24(1990), pp. 559-570.
- 8) Sun, C.T., Chen, J.K., "On the impact of initially stressed composite laminates," *Journal of Composite Materials*, 19(1985), pp.490-504.
- 9) Beckwith, S.W., Morgan, M.E., Knapp, J.R., Anderson, P.G., "Damage tolerance/fracture control approach to graphite/epoxy filament wound case (FWC) for space shuttle motors," Proceedings of 32th International SAMPE Symposium and Exhibition, Anaheim, CA, (1987), pp. 1528-1543.
- 10) Goldsmith, W., *Impact, the Theory and Physical Behavior of Colliding Solids*, Edward Arnold Ltd., London, 1960.

112559

N95-18974

1994

NASA/ASEE SUMMER FACULTY FELLOWSHIP PROGRAM

352734

**MARSHALL SPACE FLIGHT CENTER
THE UNIVERSITY OF ALABAMA**

A FINITE ELEMENT CODE FOR ELECTRIC MOTOR DESIGN

Prepared By:

C. Warren Campbell, Ph.D., P.E.

Academic Rank:

Associate Professor

Institution and Department:

The University of Alabama in Huntsville
Department of Civil & Environmental Engineering

NASA/MSFC:

Laboratory:

Propulsion

Division:

Component Development

Branch:

Control Mechanisms

MSFC Colleague:

Rae Ann Weir

INTRODUCTION

NASA is studying the replacement of rocket engine hydraulic systems with electro-mechanical actuators (EMAs). Repairing and refurbishing hydraulic systems is one of the major costs of preparing the Space Shuttle for flight. Previously, EMAs could not match the weight, volume, and performance characteristics of hydraulic systems, but new rare earth magnet technology makes EMAs competitive.

Motor design technology has improved recently with the development of finite element methods for magnetic analysis¹⁻³. Codes are available to do the analysis, but these codes are either costly or run on relatively unfriendly main frames. Furthermore, the codes are usually general purpose codes that solve a variety of problems (structural, thermal, dynamic, etc.). They are relatively costly, do not allow access to source codes, nor to all the variables that are required for the analysis. Furthermore, priorities for upgrades to the codes are determined by the marketplace. For these reasons, a NASA code that runs on user friendly PCs is desirable.

FEMOT PHILOSOPHY

The specifications for FEMOT were as follows:

1. Provide nonlinear solutions to the magnetostatic problem
2. Able to solve problems up to 15,000 nodes
3. Run on PCs
4. Requires a minimum of commercial software
5. Allow run time access to every variable in the code

FEMOT as implemented will run on a PC. The only commercial software required is Borland C/C++. The version used was 3.1. Version 4 is now available for less than \$150. A spline interpolation function from *Numerical Recipes in C*⁴ was the only other piece of software used. The spline routine can be obtained free from Internet. These requirements satisfy specification 4. Borland C/C++ has a symbolic debugger that permits stepping line by line through the code and allows access to every variable in the code during run time. This feature is useful for debugging the code as well as debugging motor runs on FEMOT. Hence, specification 5 is satisfied.

Memory is the greatest restriction to running on a PC. The code was developed on a 386 PC with 16 M RAM. To minimize the memory required, the code should store and solve linear systems using only the nonzero elements of the coefficient matrix. Using only the nonzero elements also reduces the number of calculations required. If a 10,000 node problem is to be solved, the full coefficient matrix will be 10,000 x 10,000 or 10⁸ words of storage. Hence, sparse matrix technology must be applied.

FEMOT DATA STRUCTURES

The data structure adopted for this effort is a modification of the method used by Kundert⁵ for nonsymmetric matrices. FEMOT generates positive definite, symmetric coefficient matrices so that Kundert's method could be simplified. The basic structure for the first three rows of a 7x7 matrix are shown in Figure VII-1.

SYMMETRIC SPARSE MATRIX STORAGE SCHEME

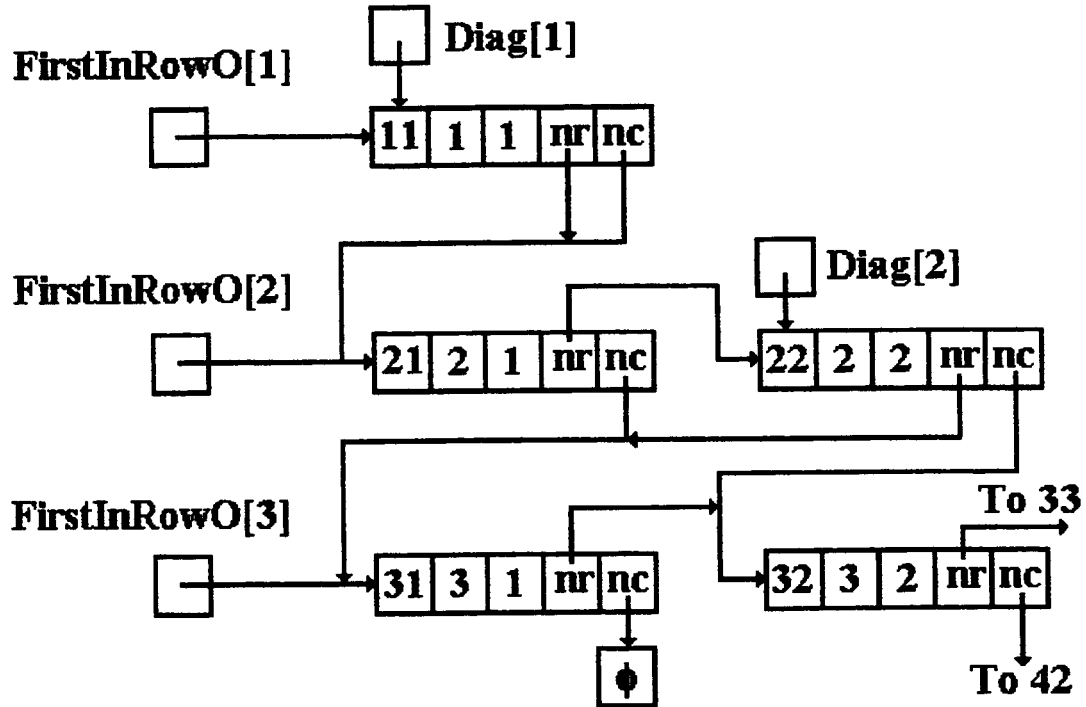


Figure VII-1. FEMOT Coefficient matrix data structure.

In this storage scheme, each matrix element is stored in a structure containing the element value, the row index i , the column index j , a pointer to the next element in the same row, and a pointer to the next element in the same column. If the element is on the main diagonal ($i = j$), the pointer to the next element in the row points to the first element in the next row. If the matrix contains no nonzero elements in the remainder of the column, the pointer points to the NULL pointer.

To overcome the problem of sequential access, two additional pointer arrays are

used. FirstInRowO[i] points to the first element in row i, and Diag[i] points to the diagonal element. This is a slight modification of Kundert's method which used an additional pointer array to point to the first element in each column. For a symmetric matrix, the first element in each column is the diagonal element so that this pointer would be redundant with Diag.

This linked list permits dynamic memory allocation while the two pointer arrays increase the speed of linear equation solutions.

DATA INPUT AND MATRIX STRUCTURE

FEMOT uses the triangular, first order, Newton nonlinear element. Newton's method is used for fast solution of the nonlinear problem. The first version of FEMOT will update the coefficient matrix at each iteration, but this may be changed in a later version to speed the solution.

Figure VII-2 shows a simple example that illustrates the data input.

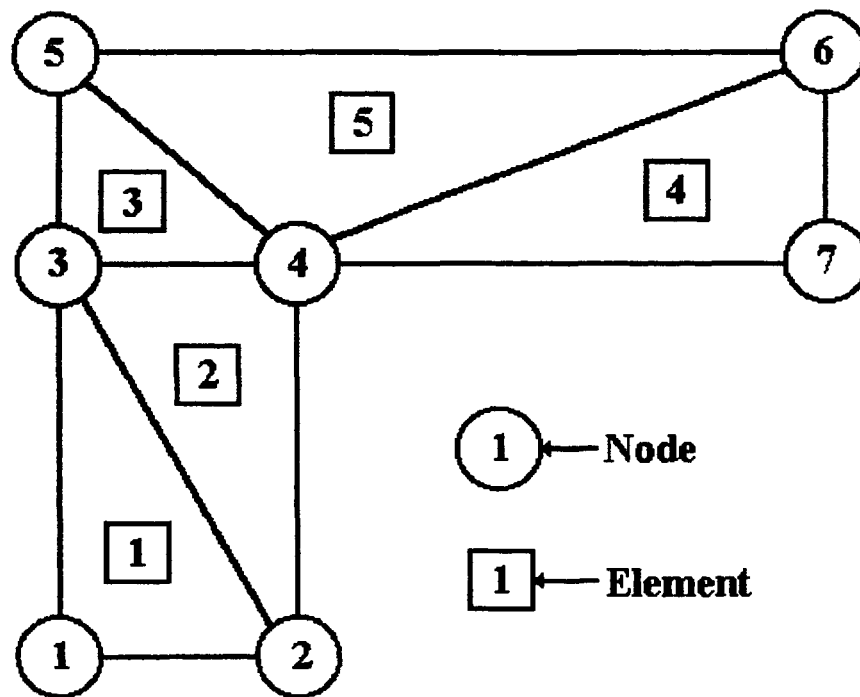


Figure VII-2 A simple finite element example.

The data structure for this example are given in Figure VII-3. For the simple geometry above, The top box in the figure gives the node number, x and y coordinates,

whether or not the node is a fixed potential node (1 = yes) or not, and if the node potential is fixed, its value. Node zero at the bottom is a flag indicating that the node list is finished. The second box is the element list. From Figure VII-2, element 1 contains nodes 1, 2, 3 and element 2 contains nodes 2, 4, and 3. Each line of the element input gives the element number, the vertices of the element (nodes i, j, and k), the nodal sources (current densities), and the material number of the element. Because nodal sources are input, the current density has a linear variation in x and y across the element.

INPUT DATA

Node Data

Node	x	y	Fixed?	Potential
1	0.0	0.0	0	0.0
2	1.0	0.0	0	0.0
3	0.0	4.0	0	0.0
4	1.0	4.0	0	0.0
5	0.0	4.5	0	0.0
6	3.0	4.5	1	0.0
7	3.0	4.0	1	0.0
0	0.0	0.0	0	0.0

Element Data

Element No.	Node i	Node j	Node k	Source i	Source j	Source k	Material No.
1	1	2	3	1.0	1.0	1.0	1
2	2	4	3	1.0	1.0	1.0	1
3	3	4	5	0.0	0.0	0.0	2
4	4	7	6	0.0	0.0	0.0	2
5	4	6	5	0.0	0.0	0.0	3

Figure VII-3 Sample data input.

Figure VII-4 shows the coefficient matrix structure corresponding to Figures VII-2 and VII-3. The stars represent nonzero elements. The circled x is an element that is initially zero, but becomes non-zero during factorization. Since the matrix is symmetric, only the lower triangular part is shown.

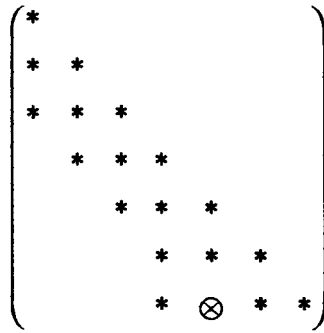


Figure VII-4. Coefficient matrix structure

SUMMARY

FEMOT is a finite element program for solving the nonlinear magnetostatic problem. This version uses nonlinear, Newton first order elements. The code can be used for electric motor design and analysis. FEMOT can be embedded within an optimization code that will vary nodal coordinates to optimize the motor design. The output from FEMOT can be used to determine motor back EMF, torque, cogging, and magnet saturation. It will run on a PC and will be available to anyone who wants to use it.

REFERENCES

1. Silvester, P. P., Cabayan, H. S., and Browne, B. T., "Efficient Techniques for Finite Element Analysis of Electric Machines," *IEEE Transactions on Power App. and Syst.*, Vol. PAS-92, 1973, pp. 1274-1281.
2. Chari, M. V. K., and D'Angelo, J., "Finite Element Analysis of Magneto-Mechanical Devices," Fifth International Workshop in Rare Earth-Cobalt Permanent Magnets and their Applications, Roanoke, VA, 7-10 June, 1981, Paper No. VI-1.
3. Anderson, O. W., "Transform Leakage Flux Program Based on the Finite Element Method," *IEEE Transactions on Power App. and Syst.*, Vol. PAS-92, No. 2, 1973.
4. Press, William H., et al., *Numerical Recipes in C*, Cambridge University Press, New York, 1990.
5. Kundert, Kenneth S., "Sparse Matrix Techniques," in *Circuit Analysis, Simulation, and Design*, ed. by A. E. Ruehli, Elsevier Science Publishing Company, Inc., New York, 1986.

112560

N95-18975

1994

NASA/ASEE SUMMER FACULTY FELLOWSHIP PROGRAM 352795

**MARSHALL SPACE FLIGHT CENTER
THE UNIVERSITY OF ALABAMA**

p 7

**CONCEPT OF USING A BENCHMARK PART TO EVALUATE
RAPID PROTOTYPING PROCESSES**

Prepared by: Vikram Cariapa, Ph.D., P.E.

Academic Rank: Associate Professor

Institution and Department: Marquette University
Department of Mechanical
and Industrial Engineering

NASA/MSFC:

Laboratory : Materials and Processes

Division : EH31/ Non- Metallic
Materials

Branch : EH34/ Ceramics and Coatings

MSFC Colleagues : Floyd E. Roberts III

INTRODUCTION

In this fast changing modern global economy, companies that generate prototypes quickly can finalise designs and penetrate markets earlier than the competition. These advantages motivated the development of many computer based rapid prototyping processes(4). Such processes are based on a computer generated solid model of the part that is being prototyped. Proprietary software then sections this drawing into layers. Then the rapid prototyping machine builds the prototype from the bottom layer upwards. For example, in stereolithography a laser beam is focussed on a vat of photosensitive resin. Then the beam traverses across the cross section of the layer that is being processed. This causes the resin to polymerise and a layer of solidified material is created. In this manner the prototype is built from the bottom upwards with layers being bonded to each other.

Different rapid prototyping processes that are currently available use different raw materials and different energy sources. For example, the materials range from photosensitive liquid resins to powdered metals. Some processes are fully automated while others require manual interaction to complete the part. Such diversity makes it difficult to compare to the capabilities of the various rapid prototyping processes.

The objective of this research is to develop a tool that can verify the purported capabilities of any rapid prototyping process. This tool is a benchmark part which is designed to have unique product details and features . The extent to which a rapid prototyping process can reproduce these features becomes a measure of the capability of the process. Since rapid prototyping is a dynamic technology, this benchmark part should be used to continuously monitor process capability of existing and developing technologies. Development of this benchmark part will therefore be based on an understanding of the properties required from prototypes and characteristics of various rapid prototyping processes and measuring equipment that is used for evaluation.

PROTOTYPE PROPERTIES

Current rapid prototyping processes produce three distinct types of prototype products: show and tell products, form and fit products and

functional products. The properties and expectations from each type are different. For example, show and tell products are used to establish the overall design of a product and obtain feedback from product managers and customers. In addition, the product design can be evaluated for potential manufacturing and inspection problems and can be used for materials and allied planning activities. Form and fit products are more precise products that additionally allow assembly and tooling strategies to be established. Functional products are most desired as they can be field tested and thus provide useful and timely information to the designer and potential user. The goal of any rapid prototyping process is to generate such functional products in the quickest possible manner. However at present, most rapid prototyping processes can produce prototypes that are either show and tell products or form and fit products. Characteristics of the more widely used rapid prototyping processes are described herewith.

RAPID PROTOTYPING PROCESS CHARACTERISTICS

At present, the laser based rapid prototyping processes are the most widely used. These include stereolithography (3), selective laser sintering (1), and laminated object manufacturing (4). Processes based on the ink jet droplet deposition principle such as three dimensional printing (3) are gradually becoming more widely accepted. Processes that involve deposition of molten beads of material such as fused deposition modelling process (4) is also discussed. A brief description of these processes is given herewith:

- a) **Stereolithography.** The basic process has been described earlier. After part build is over in the stereolithographic machine, the part is manually cleaned and further cured in an ultra violet light chamber.
- b) **Selective laser sintering.** The process also utilises a vertical axis computer controlled laser beam. But this beam raster scans the surface of a bed of plastic or metal powder, across the section of the part that is being built. The laser fuses the powder upon contact and the part is built from the bottom upwards. Upon completion of the build the part is removed from the powder bed, excess powder is dusted off and the part is considered complete.
- c) **Laminated object manufacturing.** Adhesive backed film is initially pressed to a flat reference plate. A vertical computer controlled laser then cuts this film along the periphery of the section of the part

that is being processed. A fresh layer of film is then bonded over this recently cut contour and the contour corresponding to this new layer is then cut. The process then continues until the part is completed.

d) Inkjet processes. There are two different processes based on the ink jet principle. The first process deposits a binder on a bed of ceramic powder across the section being processed. Successive layers are thus created until a "green" part is fully built. This "green" part is then sintered to produce the completed part.

A second process uses two ink jets. One jet deposits a plastic layer that follows the part section and the second deposits a low temperature wax that is used as a support. After the build is over the wax is dissolved to leave behind the completed plastic part.

e) Fused deposition modelling. A wax or nylon wire is fed through a liquefier that melts this material. This molten material is then forced through a jet that traverses across the section of the product. The product is built up of layers of molten material that fuse to the already deposited layers.

In summary, there are some important commonalities between these rapid prototyping processes. All processes are initiated with a computer solid model of the desired part and the actual rapid prototyping process is computer controlled. The parts are always built up in layers which are created by raster scanning a laser or ink jet deposition system across the section of the part.

A wide range of materials are used in these processes and the processing techniques vary widely. The control of the various process parameters to obtain consistent parts is still under development. Some processes require manual interaction for cleaning and post processing operations, such as curing or sintering.

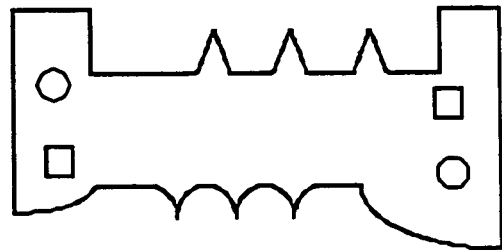
These process characteristics are different from conventional manufacturing processes. In addition, prototypes are made in miniscule quantities and of such differing geometries that conventional statistical techniques for control and prediction cannot be used efficiently. Thus there is a need to develop new techniques to evaluate the process capability of these different processes. The benchmark part is a tool that will satisfy this need.

CONCEPT OF BENCHMARK PART

The benchmark part is a reference tool that will be used to continuously upgrade the precision of parts made by rapid prototyping technologies. It will be designed with two major objectives: the first is that it will be utilised by a rapid prototyping process developer to continuously evaluate the dimensional improvements that are made to the process and the second is enable a user to evaluate the dimensional process capability of various rapid prototyping processes.

A planar benchmark part design is proposed for those rapid prototyping processes that do not utilise post processing operations and those that do not need supports. Thus two conditions are such that the product is completely dependent on the characteristics of the process alone and are not dependent on any manual intervention. Since parts are fully supported by inherent process features, any layer that is generated should be a representative of all the layers. Fig.1 depicts the details of the first concept of this benchmark part.

This benchmark part shown on the right has a uniform thickness and contains features with linear and curvilinear dimensions, small grooves and holes. The linear dimensions allow one to assess the capabilities of a process in the x or y axes. The curvilinear dimensions allow one to assess the ability of the process to produce nonlinear details. Positional errors are evaluated by measuring the location of holes. The ability to generate details is assessed by the precision with which the triangular and curved projections are created.



The rapid prototyping processes that require supports or post processing will be evaluated with a benchmark part that has vertical walls in the xz and yz planes, in addition to the existing details that are available on the planar reference part. These walls will magnify any deleterious effects caused by the post processing or manual operations.

JUSTIFICATION OF DETAILS ON BENCHMARK PARTS

A rapid prototyping process is highly dependent on process parameters. For example, the length of time that a laser spends on a spot will determine the strength and stability of that a spot. This period of time is dependent on the ability of the machine to maintain a correct scan speed throughout the process. Thus linear dimensions enable one to assess the single axis control of the machine, curvilinear dimensions allow a two axis control to be assessed and the triangles and curvilinear details allow the precision of the process to be established.

All these dimensional details are dependent on the ability of the measuring instruments to assess the error . Ideally, these parts should be measured on a non contact system such as a laser system. However, from a practical viewpoint a coordinate measuring machine can be used. Further, a benchmark part should be made for each set of materials that is processed and also if the density or strength of the part is changed.

SUMMARY AND CONCLUSION

A conceptual benchmark part for guiding manufacturers and users of rapid prototyping technologies is proposed . This is based on a need to have some tool to evaluate the development of this technology and also assist the user in judiciously selecting a process. The proposed part is designed to provide both short and long range feedback and so should be readily accepted by the rapid prototyping community.

REFERENCES

1. Girouard,D., "Molds for Low Temperature Molding Process using Rapid Prototyping", Proceedings of the Fourth International Conference On Rapid Prototyping, Dayton, June 14-17, 1993, pp 61-66.
2. Jacobs,P.F., " Fundamentals of Stereolithography" ,SME Press(1992).
3. Michaels,S.,Sachs,E.,Cima,M. ,"Metal Parts Generation by Three Dimensional Printing", Proceedings of the Fourth International Conference On Rapid Prototyping, Dayton, June 14-17, 1993, pp 25-31.
- 4 . Proceedings of the International Conference On Rapid Prototyping, Dayton, June ,1990.

112561

N95-18976

1994

352802

NASA/ASEE SUMMER FACULTY FELLOWSHIP PROGRAM

P. 7

MARSHALL SPACE FLIGHT CENTER
THE UNIVERSITY OF ALABAMA

COMPOSITE STRUCTURES
FOR MAGNETOSPHERE IMAGER SPACECRAFT

Prepared By:

Tsuchin Chu, Ph.D.

Academic Rank:

Assistant Professor

Institution and Department:

Southern Illinois University at Carbondale
Department of Mechanical Engineering
and Energy Processes

NASA/MSFC:

Directorate:

Program Development

Office:

Advanced Spacecraft & Payload Systems

Office:

Space Science & Applications

MSFC Colleagues:

Les Johnson/PS02
Susan Spencer/PD22

INTRODUCTION

For the past thirty years, scientists were only able to obtain incomplete spacecraft *in situ* measurements of the magnetospheric fields and particles. In order to obtain simultaneous measurements at different wavelengths and with energetic neutral atoms to provide a global view of the magnetosphere, NASA initiated a Science Definition Team (SDT) to define the rationale and scope of the Inner Magnetosphere Imager (IMI, now called MI) mission. Marshall Space Flight Center (MSFC) was given the responsibility to define the mission and to conduct the conceptual and preliminary design studies [1].

The spacecraft will be a spin-stabilized one with an orbit of 4800 km perigee by 7 Re apogee. Due to the constraint of the cost ceiling, only three core instruments will be installed on the MI spacecraft. These instruments include hot plasma imager, plasmasphere imager (He⁺304), and FUV imager. The baseline launch vehicle is Taurus S which is capable of boosting 330 kg of payload to the designated orbit.

The MI mission is now a part of the Sun/Earth Connection Program. To qualify for this category, new technology and innovative methods to reduce the cost and size have to be considered. The assessment from the preliminary study results in several new technology options for MI. These include using gallium-arsenide solar cells and adopting solid state data recorders. To further reduce the weight and cost of the structure and fully utilize the new material technology, carbon fiber reinforced composites has been considered for replacing aluminum structures.

A study has been conducted to address the issues and benefit in using composites for MI spacecraft design. The results of the composite option trade study are presented in the following sections.

WHAT IS COMPOSITE?

A composite is a combination of a reinforcement material in a matrix or binder material. Composites are light weight, high strength, and high stiffness materials. Low coefficient of thermal expansion (CTE), as well as directional strength and stiffness, can be tailored into composites to meet special spacecraft design requirements. Additionally, with innovative manufacturing processes, the composite materials can be used to provide cost savings and reduced part count.

Reinforcements for composites can be fibers, particles, or whiskers. Fibers are the most common reinforcements in composites. Matrix materials include polymer, ceramic, and metal. The matrix is usually served as a binder to hold the reinforcements together. It provides load transfer between reinforcements, creates formability of the structure, protects the reinforcements from environmental effects, and lend desirable physical characteristics to the composites.

Fiber Reinforced Plastics (FRP) is the largest subgroup of composites. The matrix of FRP is either a polymer or plastics and the reinforcement is a fiber. Epoxy resin is the most common matrix material for FRP. Fibers can be glass, organic (aramid or Kevlar by trade), carbon, or graphite. Advanced composite materials generally refer to composites with high modulus fibers (elastic modulus $E > 200,000$ MPa) and no less than 50% reinforcement fibers in volume.

Advantages and Disadvantages of Composites

The major advantage of using composites to replace metals in aerospace industry is their high strength and high stiffness to weight ratio. In addition, composites offer new design flexibilities, improved corrosion and wear resistance, increased fatigue life, and low coefficient of thermal expansion (CTE). Some specific benefits in using composites over metals are:

- Specific tensile strength (ratio of tensile strength to density) of composites is four to six times greater than that of steel or aluminum.
- Specific modulus of composites is three to five times greater than steel or aluminum. Some newly developed ultra high modulus fibers can provide even higher specific modulus.
- Composites have higher fatigue endurance limits.
- Composites can be tailored to low or zero CTE in a desired direction.
- Some ultra high modulus carbon fibers have higher thermal conductivity than that of metals.
- Composites have high directional strength and modulus.
- Use flexible and innovative manufacturing processes on composites can reduce the cost.

The general disadvantages of composites are their high cost, lack of well-defined design rules, lack of automated manufacturing processes, and susceptible to environmental effects such as moisture and temperature. However, by choosing the proper combination of fibers and matrix materials, many deficiency can be overcome. Additionally, with the development of ultra high modulus graphite fibers and low water absorption resins, more composites are now available for spacecraft design.

Carbon/Graphite Fibers

The demand of high strength and high modulus reinforcements for composites has led to the development of carbon or graphite fibers. Although the graphite fiber has higher carbon contents and is stronger than carbon fiber, the terms have been used interchangeably. Carbon fibers can be manufactured by using polyacrylonitrile (PAN), rayon, and petroleum pitch. Rayon based carbon fibers are mainly used for making nozzles. Pitch-based fibers have a higher degree of graphite structure than to PAN-based fibers. Pitch fibers have high elastic moduli (480-830 GPa) but reduced tensile strength (up to 2.4 GPa). However, for small spacecraft, such as MI, the stiffness (elastic modulus) is more important than the strength of the material. Additionally, high modulus fibers are also high thermal conductors. The excess heat generated by electronic equipments and batteries can be dissipated to heat sink or radiator through these fibers in the composites. Amoco has developed some high modulus graphite fibers such as P75, P100, and P120, which have thermal conductivities comparable to those of metals. Table 1 shows some of the thermal conductivities of these materials [2,3].

Fiber or Metal	Supplier	Thermal Conductivity (W/m-K)
P75	Amoco	185
P100	Amoco	520
P120	Amoco	640
T300	Amoco	10
Copper		450
Aluminum		200

Table 1. Comparison of Thermal Conductivity of Some Carbon Fibers

STRUCTURAL DESIGN FOR MI

Three major factors have been considered for the Magnetosphere Imager (MI) spacecraft structural design, namely the stiffness, excess heat dissipation, and ease of manufacturing and assembly. The baseline design, as shown in Figure 1, includes twelve side panels and the top and bottom decks mounted on a frame structure. The spacecraft is 1.3 m high and 1.3 m in diameter. All panels and decks are made of aluminum honeycomb sandwiches. Electronic boxes and instruments are mounted directly around the center of the panels for efficient dissipation of excess heat generated from electronic instruments and batteries to the radiator. Power for the spacecraft will be supplied by the gallium-arsenide solar cells mounted on the panels and decks.

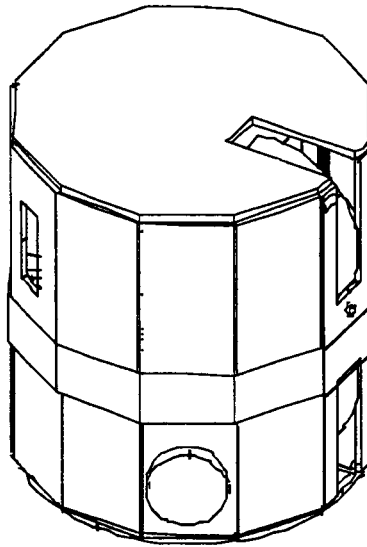


Figure 1. MI Spacecraft Conceptual Design [4]

Composite Design Configuration

Composite materials in general are more expensive than aluminum alloy. However, the high stiffness and high strength to weight ratio of composites along with innovative manufacturing methods can dramatically reduce the overall cost of using composite structures for spacecraft design. The composite design configuration includes replacing the aluminum face sheets of the honeycomb sandwich panels with graphite/cyanate composites as well as using composite longerons and brackets. Another option utilizes the light weight and high stiffness composite isogrid panels for the two decks.

Replacing the aluminum face sheets (skins) in the baseline design by composites can reduce the skin weight by approximately 30% to 40%. The aluminum honeycomb core should be used for heat conduction through the thickness of the sandwich panel. Various options and design guidelines can be considered for MI spacecraft design using composite sandwich panels and composite isogrid panels:

- Co-cure all panels to form the body of the spacecraft. Upper and lower decks can be attached to the body with potted insert fasteners. They can also be fastened to the co-bonded brackets at the ends of the panels. This design eliminates all longerons and the fasteners required to attach the panels, thus reduces the weight and the assembly cost.

The only disadvantage is that difficulties may arise for installing and uninstalling the instruments and cables.

- Co-cure two to three panels to form sections. Longerons can be co-bonded and co-cured to the edges of each section of two to three panels. Deck attachment is the same as above mentioned design. This option can reduce one half to two-thirds of the longerons and fasteners. However, since the body is formed by four to six sections, installing and uninstalling the instruments will no longer be a problem.
- Use rib stiffened composite panels (isogrid) for upper and lower decks. The composite ribs are arranged in an isogrid configuration and are secondary bonded to the composite skin to replace the honeycomb core in a panel. This composite isogrid panel can further reduce the weight of the panels [5].
- Brackets for installing instruments and batteries can be co-cured and co-bonded to the skin of the panels.
- Local doublers can be incorporated in high shear and high stress concentration areas to maintain overall panel stiffness and local skin strength. These doublers can be imbedded within the panel skins or bonded to the exterior of the panel skins.
- The exterior of the spacecraft will be covered by solar cells except for the middle of the body which will be covered by the radiator. Since the graphite fibers are good electrical conductors along the fiber direction, the skin of the panels should be insulated from the solar cells by nonconductive films. These films can be co-cured with or secondary bonded to the composite panel skin.

These options can dramatically reduce the number of parts to be assembled, reduce the number of fasteners, and reduce the weight. With less human touch and automated manufacturing process, the cost can also be reduced.

Material Selection

For small spacecraft design using composite materials, such as MI, high or ultra high modulus graphite fibers should be used for reinforcements to make high stiffness composite structures or components. Some of the newly developed ultra high modulus graphite fibers are also very good heat conductors. Some of these fibers have thermal conductivity values comparable or even higher than that of pure coppers (450 W/m-K). Since the thermal conductivity of polymeric resin is very low, the overall thermal conductivity of a composite laminate is linearly proportional to the fiber volume content. Nysten and Issi have conducted some measurements on the thermal conductivity of carbon fiber reinforced composites [6]. The best composite measured (45% P120 fibers) showed a thermal conductivity value of 245 W/m-K which is higher than that of pure aluminum (200 W/m-K).

The space environment effects, such as radiation, outgassing, and atomic oxygen exposure, should also be carefully considered in choosing the proper type of matrix materials. The polycyanate resin is a specially developed matrix material for spacecraft applications due to its low water absorption and desorption, low dielectric properties, improved resistance to microcracking and resistance to UV radiation. ICI Fiberites, Hexcel, YLA, Dow Chemical, Ciba Geigy, and Bryte Technologies are the major sources of the polycyanate resins.

Analysis of Composite Structures

The above mentioned composite sandwich panels are plates with stiff, thin face sheets supported by soft, thick honeycomb cores. The Kirchoff assumptions for analyzing solid plates are made across the thickness of the sandwich plate. However, the soft honeycomb cores are flexible in shear. Thus the transverse shear effects should be included in the sandwich plate theory. For symmetrical face sheets, the laminate theory for composites can be greatly simplified. The light-weight soft core has negligible in-plane stiffness. The total stiffness is simply the sum of the face sheet stiffness. The forces acting on the sandwich plates are controlled by the in-plane stress resultants acting on the face sheets. The total in-plane and flexural loads can be defined from these resultants. The simplified theory is very useful in design. The error introduced by this approach is small provided that the face sheets are thin [7].

There are many micromechanics theories for composite analysis. None of them are entirely correct. However, the micromechanics formulas are still useful in predicting the material property variations in conjunction with the empirical data. Composite analysis using the elasticity theory often result in boundary value problems or optimization of functions. For practical spacecraft design, numerical approximations are necessary for finding the solutions. Numerical tools such as finite difference method and finite element analysis (FEA) are some of the useful tools. Commercial packages for finite element analysis, such as NASTRAN, ANSYS, and PAL/2 are available for composites structures.

REFERENCES

1. Johnson, C.L., and Herrmann, M., "Inner Magnetosphere Imager Mission: A New Window on the Plasma Universe," *Optical Engineering*, Vol. 33, No. 2, pp. 329-334, Feb. 1994.
2. Supplier's Data from Amoco Performance Products, Inc.
3. TRW, "Composite Spacecraft Design Guide," Preliminary Draft of NASA Contractor's Report, April 25, 1994.
4. Drawing prepared by S. Hincle.
5. Kim, T.D., et al, "Continuous Fiber Composite Isogrid For Launch Vehicle Applications," *Composite Properties and Application*, Proceedings of ICCM/9, Vol. VI, pp. 101-107, July, 1993.
6. Nysten, B. and Issi, J-P, "Composites Based on Thermally Hyperconductive Carbon Fibers," *Composites*, Vol. 21, No. 4, pp. 339-343, July 1990.
7. Tsai, S.W., *Theory of Composite Design*, Think Composites, 1992.

112562

N95-18977

1994

352804

NASA/ASEE SUMMER FACULTY FELLOWSHIP PROGRAM

**MARSHALL SPACE FLIGHT CENTER
THE UNIVERSITY OF ALABAMA**

~~510-47~~
~~30900~~
P. 7
P. 6

**IMPLICATIONS OF SUMMERTIME
MARINE STRATOCUMULUS ON
THE NORTH AMERICAN CLIMATE**

Prepared By:

John H.E. Clark

Academic Rank:

Associate Professor

Institution and Department:

**The Pennsylvania State University
Department of Meteorology**

NASA/MSFC:

Laboratory:

Space Sciences

Division:

Earth Science & Applications

Branch:

Climate Processes & Modeling

MSFC Colleague:

Franklin R. Robertson

INTRODUCTION

The advent of global satellite coverage has triggered renewed interest in monitoring the atmosphere for evidence of climate change. While it is suspected that the atmosphere is susceptible to warming because of increasing CO₂ concentrations, there is considerable doubt as to the magnitude (and even sign) of the resulting temperature change (Lindzen, 1990). This uncertainty mainly arises because of our lack of understanding of the response of cloud cover to increasing CO₂ (Lindzen, 1990). Cloud can have either a positive or negative feedback on global temperature changes. For instance, Randall et al. (1984) showed that a mere 4% increase in global cloud cover by low-level stratiform cloud could more than offset the predicted 2-4 K global warming due to a doubling of CO₂.

Even though the dominant cloud type at mid- and high latitudes is low-level stratiform, there has been little study of the effect of semi-permanent areas of this cloud on intra- and inter-annual climate variability. Much more effort has been focused on the effects of cumulus cloud, which dominates at equatorial latitudes. For instance, it is known that changes in deep convective cloud over the western Pacific warm pool impact climate anomalies over North America (Wallace and Gutzler, 1981). However, the climatic impact of alterations in the semi-permanent stratiform cloud deck off the west coast are not known. Because of its proximity compared to western Pacific convective cloud, the North American climate could be much more sensitive to eastern Pacific stratocumulus cloud.

This study focuses on the effects of summertime stratocumulus over the eastern Pacific. This cloud is linked to the semi-permanent sub-tropical highs that dominate the low-level circulation over the Pacific and Atlantic. Subsidence on the eastern flank of these highs creates an inversion based about 800 m above sea level that caps moist air near the surface. This air overlies cool waters driven by upwelling along the coastal regions of North America. Strong surface north-westerlies mix the boundary layer enough to saturate the air just below the capping inversion. Widespread stratocumulus is thus formed.

All calculations were carried out using the GENESIS general circulation model that was run at MSFC. Among the more important properties of the model is that it includes radiative forcing due to absorption of solar radiation and the emission of infrared radiation, interactive clouds (both stratocumulus and cumulus types), exchanges of heat and moisture with the lower boundary. Clouds are interactive in the sense that they impact the circulation by modifying the fields of radiative heating and turbulent fluxes of heat and moisture in the boundary layer. In turn, clouds are modified by the winds through the advection of moisture.

In order to isolate the effects of mid- and high-latitude stratocumulus, two runs were made with the model: one with and the other without stratocumulus. The runs were made for a year, but with perpetual July conditions, i.e., solar forcing was fixed. The diurnal solar cycle, however,

was allowed for. The sea surface temperature distribution was fixed in both runs to represent climatological July conditions. All dependent variables were represented at 12 surfaces of constant $\sigma = p/p_0$, where p is pressure and p_0 surface pressure. To facilitate analysis, model output was transformed to constant pressure surfaces. Structures no smaller in size than 7.5 degrees longitude and 4.5 degrees in latitude were resolved. Smaller features of the circulation were parameterized. The model thus captures synoptic- and planetary-scale circulation features.

RESULTS

Cloud effects were isolated by comparing features of the runs with and without stratocumulus present. All dependent variables, i.e., temperature (T) and wind components (u, v, ω), were divided into time mean and deviations at each location. Thus, for example, $T(x, y, p, t) = \bar{T}(x, y, p) + T'(x, y, p, t)$, where \bar{T} is the mean and $\bar{T}' = 0$. First, changes in the time-mean summertime circulation over North America were considered. Next, properties of the cloud-generated transient or time-dependent part of the circulation were studied. Finally, the interaction of transients and the time-mean circulation are studied by separately looking at how transients are generated from the mean flow and how the transients feed back onto the mean flow.

A broad range of frequencies make up the transients, spanning periods from a few days to six months. It was convenient to break up this spectrum into two broad regimes:

<u>RANGE</u>	<u>PERIODS</u>
Low frequency	10 to 90 days
High frequency	2.5 to 6 days

Low-pass and bandpass filters, Blackman and Lau (1980), were applied to the daily anomaly fields, u', v', T' etc., to isolate the low and high frequency bands respectively. Transient behavior and structures sharply contrast between these ranges.

CLOUD EFFECTS ON MEAN CIRCULATION

A preliminary check was made on the model-generated time-mean summertime circulation to ensure that it matched observations. Agreement was surprisingly good considering some of the crude parameterizations that were used. For example, the fractional cloud cover due to stratocumulus closely matched the marine climatological cloud cover data of Hanson (1991).

Model-generated time-mean states with and without stratocumulus will now be compared so that the consequences of stratocumulus can be isolated. Important findings are:

1. by reflecting more incoming solar radiation back to space, stratocumulus can decrease the net solar radiation absorbed by the atmosphere by up to 60 W/m^2 over regions of high cloud fraction such as off the coast of California,
2. lower troposphere temperatures are decreased everywhere by the stratocumulus especially over marine areas,
3. over central Canada where there is very little summertime stratocumulus, there was a large region of cloud-induced cooling of up to 4C ,
4. the effects of stratocumulus were clearly not localized to the region of large cloud fraction,
5. everything else being equal, cooling due to stratocumulus was larger at high latitudes than at low latitudes because increased solar reflection was more effective where the day length is largest,
6. the zonally-averaged north-south temperature gradient was increased by cloud especially in the latitude belt from 45N to 60N ,
7. the semi-permanent Pacific and Atlantic anticyclones were weakened by the cloud (this is quite unexpected),
8. subsidence that normally occurs on the eastern flank of the Pacific anticyclone was weakened by the stratocumulus (this is another unexpected result),
9. an approximately barotropic (structure independent of height) stationary wave was forced by the cloud, and
10. this wave was approximately out of phase with the climatological mean wave pattern such that the ridge (trough) over the west (east) coast of North America was slightly weakened by the cloud.

Items 8. contradicts conventional thinking about the response of a stably stratified atmosphere subjected to a diabatic cooling perturbation as with the marine stratocumulus. The cooling is normally compensated for by compressional heating due to enhanced subsidence. Model results indicate suggest the opposite: adiabatic cooling in the eastern Pacific upward motion anomaly supplements the cloud radiative cooling. It turns out that a horizontal warm air advection anomaly balances the radiative plus adiabatic cooling. Northwesterly surface winds off the California coast are associated with cold air advection since the flow is directed from the cool marine regions toward the considerably warmer inland areas over California. Since, according to item 7., stratocumulus weakens the anticyclone, the northwesterly wind speeds also decrease. A warm air advection anomaly results over the offshore region and thermal balance is maintained.

TRANSIENT EFFECTS OF STRATOCUMULUS

As mentioned in items 3. and 4. above, the effects of marine stratocumulus near North America are not just localized to the coastal regions. Properties of synoptic-scale transients triggered by the cloud are now considered. Their structure, propagation characteristics, and interaction with the time-mean tropospheric flow are of interest.

BAROCLINIC INSTABILITY

Stratocumulus increased the zonally-averaged north-south temperature gradient and, as verified, the corresponding vertical shear of the mean tropospheric westerlies. The baroclinic instability of the time-mean summertime could be enhanced thus facilitating the generation of baroclinic waves. The above-mentioned non-local effects of marine stratocumulus might be accounted for. The background stability was measured by calculating the associated maximum growth rate according to the Eady model: $\nu = 0.31fU_z/N$ where f is the Coriolis parameter, U_z the vertical wind shear, and the buoyancy frequency $N^2 = (g/\theta_0)\partial\theta/\partial z$. The e-folding time, $1/\nu$, did indeed decrease due to the cloud-induced enhanced vertical shear. The change, however, was small $\sim O(0.01)$ days) compared to typical values of a few days. Thus the stratocumulus does not impact the stability of the summertime westerlies.

STRUCTURE OF CLOUD-INDUCED WAVES

The lag-correlation technique, Blackmon and Lau (1980), was applied to the transient part of the daily 500 and 850 mb temperature fields, thereby revealing the spatial and temporal scales of propagating disturbances triggered by stratocumulus. Important findings are:

1. cloud-triggered eastward propagating high frequency disturbances occur at 500 mb in the region of strong westerlies over Alaska (horizontal wavelength ~ 4000 km), and
2. the cloud also triggered a smaller-scale high frequency disturbance over the Gulf of Alaska (wavelength ~ 2500 km) at both 500 and 850 mb that propagated southeastward approximately parallel to the west coast of North America.

FEEDBACK OF CLOUD-FORCED TRANSIENTS ON MENA FLOW

The divergence of the E-vector, Trenberth (1986), quantifies how the transient eddies are forcing the time-mean winds at any location. Low-frequency transients tended to weaken the mean westerlies over Alaska and the eastern U.S.A. thus dampening the barotropic stationary long-wave pattern. High-frequency propagating waves triggered by the cloud had negligible feedback on the mean flow.

Summertime stratocumulus off the west coast of North America had small but not negligible *in situ* as well as downstream continental effects. The cloud was shown to enhance the contrast between the warm continental regions and adjacent offshore regions. In spite of this increased continentality, the stationary wave pattern over North America is weakened by the cloud. Simple linear stationary wave theory cannot explain this finding. This study reveals that low-frequency disturbances triggered by the cloud feedback through nonlinear effects on the standing wave pattern to weaken it. This feedback is mostly driven by barotropic processes. High frequency propagating baroclinic waves are also triggered by the cloud. The process responsible for these waves is not known; enhanced baroclinic instability over their Alaskan source region was ruled out.

Results from this study suggest the stratocumulus is coupled to regional summertime climate fluctuations over North America. It would be interesting to examine linkages between eastern Pacific stratocumulus global-scale mechanisms involving inter-annual climatic fluctuations. Then it might be possible to relate regional climate anomalies such as the 1993 mid-west flooding to global climate anomalies.

REFERENCES

- Blackmon, M.L. and N.-G. Lau, 1980: Regional characteristics of the Northern Hemisphere Wintertime Circulation: A Comparison of the Simulation of a GFDL General Circulation Model with Observations. *J.Atmos.Sci.*, 37, 497-514.
- Lindzen, R.S., 1990: Some coolness concerning global warming. *Bull. Amer. Meteor. Soc.*, 71, 288-299.
- Randall, D.A., J.A. Coakley, Jr., C.W. Fairall, R.A. Kropfli, and D.H. Lenschow, 1984: Outlook for research on subtropical marine-stratiform clouds. *Bull.Amer.Meteor.Soc.*, 65, 1290-1301.
- Trenberth, K.E., 1986: An Assessment of the Impact of Transient Eddies on the Zonal Flow during a Blocking Episode Using Localized Eliassen-Palm Diagnostics. *J.Atmos.Sci.*, 43, 2070-2087.
- Wallace, J.M. and D.S. Gutzler, 1981: Teleconnections in the geopotential height field during the Northern Hemisphere winter. *Mon. Wea. Rev.*, 109, 784-812.

112563

511-32

N95-18978

1994

352802

P 7

NASA/ASEE SUMMER FACULTY FELLOWSHIP PROGRAM

**MARSHALL SPACE FLIGHT CENTER
THE UNIVERSITY OF ALABAMA**

**PERFORMANCE EVALUATION OF THE
ENGINEERING ANALYSIS AND DATA SYSTEM (EADS) II**

Prepared By: Linda S. DeBrunner, Ph.D.

Academic Rank: Assistant Professor

Institution and Department: The University of Oklahoma
School of Electrical Engineering

NASA/MSFC:

Laboratory: Information Systems Office
Division: Systems Development and Implementation Division
Branch: Computer Systems Branch

MSFC Colleagues: Ellen Williams
Amy Epps

INTRODUCTION

The Engineering Analysis and Data System (EADS) II [1] was installed in March 1993 to provide high performance computing for science and engineering at Marshall Space Flight Center (MSFC). EADS II increased the computing capabilities over the existing EADS facility in the areas of throughput and mass storage. EADS II includes a Vector Processor Compute System (VPCS), a Virtual Memory Compute System (VMCS), a Common File System (CFS), a Common Output System (COS), as well as Image Processing Stations, Mini Super Computers, and Intelligent Workstations. These facilities are interconnected by a sophisticated network system. This work considers only the performance of the VPCS and the CFS. The VPCS is a Cray YMP. The CFS is implemented on an RS 6000 using the UniTree Mass Storage System.

To better meet the science and engineering computing requirements, EADS II must be monitored, its performance analyzed, and appropriate modifications for performance improvement made. Implementing this approach requires tool(s) to assist in performance monitoring and analysis. In Spring 1994, PerfStat 2.0 was purchased to meet these needs for the VPCS and the CFS. PerfStat[2] is a set of tools that can be used to analyze both historical and real-time performance data. Its flexible design allows significant user customization. The user identifies what data is collected, how it is classified, and how it is displayed for evaluation. Both graphical and tabular displays are supported.

We evaluated the capability of the PerfStat tool, suggested and implemented appropriate modifications to EADS II to optimize throughput and enhance productivity, and observed the effects of the modifications on system performance. In this paper, we briefly describe the PerfStat tool, then outline its use with EADS II. Next, we describe the evaluation of the VPCS, as well as modifications made to the system. Finally, we draw conclusions and outline recommendations for future work.

THE PERFSTAT PERFORMANCE ANALYSIS TOOL

The software architecture of PerfStat is shown in Figure 1. Data collectors are run on the Systems Under Study to collect metrics. More than one data collector may be run on a particular System Under Study (SUS). This data is collected directly from operating system counters and is extracted from system logs.

The data is transferred from each SUS to the Archive Workstation where it is stored. The specific data to be collected from a SUS is determined by a metrics pool and a selection list. The metrics pool defines which metrics can be collected by data collectors on the SUS. The selection list for a particular data collector identifies which of the metrics in the metrics pool will be collected.

After or during data collection, User Interface Workstations may be used to display the data either graphically or in a tabular format. The User Interface Workstation may be located on the same physical computer as the Archive Workstation. Many people may display data simultaneously through the use of multiple user interfaces. The user may classify data in many ways. For example, data may be classified by user id or by level of memory usage. A more

complicated classification might combine user id and level of memory usage to identify processes associated with a particular user id that require more than 4 Mwords of memory.

USE OF PERFSTAT WITH EADS II

PerfStat is used with EADS II to study two systems: the VPCS and the CFS. A single Archive Workstation is implemented on a separate workstation. The workstation used as the Archive Workstation also serves as a User Interface Workstation. In addition, several other User Interface Workstations are being used.

The Common File System is implemented by a Maximum Strategy Disk Array and robotic tape storage systems controlled by an RS 6000 workstation. UniTree file management software is used. To monitor the CFS, a customized metrics pool that extracts data from the UniTree log files, as well as collecting data from the operating system was provided.

The VPCS is a Cray-YMP supercomputer running UNICOS 6.1. We customized the metrics pool provided to collect information of particular interest. The data is derived from operating system log files and counters.

Several graphs were developed to regularly monitor the CFS and the VPCS. Additional graphs are easily created to investigate new situations.

EVALUATION AND TUNING OF THE VPCS

After observing the VPCS, several areas were identified for possible improvement. Of these areas, two were selected for implementation during the period of this work. Coincidentally, a previously planned hardware change was implemented to increase system capacity. On July 14, 2 CPUs were added to increase the number of CPUs from 6 to 8. On July 20, several changes were made to the ldcache structure. Then, on July 27, the structure of the Network Queuing System was changed for weekends.

As shown in Figure 2, the addition of CPUs appears to have resulted in a decrease in CPU utilization, as expected. During the same time period, CPU utilization decreased because of a significant workload decrease related to contractor layoffs. This workload decrease is expected to be temporary as the work is shifted to other personnel. In addition, users from the Cray-XMP are being shifted to the Cray-YMP. Weekends are easily identifiable on the graph in Figure 2.

Figure 3 shows the memory requirements for the Cray-YMP. Again, weekends appear as decreases in memory requirements. This graph shows that the current memory of 128 Mwords is adequate for the current situation since the system is not significantly over-subscribed.

The ldcache structure was changed for the /wrk file system. The big file allocation size was set to match the block size. This change should reduce fragmentation[3]. In addition, we eliminated the ldcache for the /bin file system since its re-use ratio was low (analyzed using PerfStat). Third, we increased the number of hash table entries to improve the performance of the ldcache. The effects of these changes were not expected to be evident for several weeks. They will continue to be monitored. Figure 4 shows the re-use ratio for the /wrk file system. In addition, a script was

prepared to measure the disk fragmentation indirectly by allocating a file on each partition of the /wrk file system.

The increase in system idle time, particularly on weekends, led us to investigate the Network Queuing System (NQS) structure. Using PerfStat, we observed jobs ready to run on the weekends, even though the system was taking idle time. To improve system throughput, we increased user limits and queue limits for the weekends. These changes affect system utilization (Figure 1) and queue backlog (Figure 5). PerfStat can be easily used to identify appropriate modifications to the NQS structure as the system workload changes.

CONCLUSIONS AND RECOMMENDATIONS

PerfStat has proven to be a valuable tool for collecting and analyzing system performance data. Extensive use of the tool with the VPCS has shown that it can be used to identify areas of performance problems, as well as performing routine monitoring and resource forecasting. Additional investigation is needed to determine how this tool can be most effectively used on the CFS.

Several areas are recommended for future modification on the VPCS. When the operating system is upgraded to UNICOS 7.0 in late August 1994, PerfStat can be used to analyze the effects of performance tuning as outlined by UNICOS guidelines [4]. In addition, the NQS performance should be monitored as the workload fluctuates. Changes should be considered for night and "lunch time" NQS structures to compensate for the predictable varying of the workload. Last, the goals of the system should be considered (batch versus interactive, etc.), and appropriate modifications be made to the scheduling parameters.

REFERENCES

1. *Engineering Analysis and Data System II, Request for Proposal*, RFP No. 8-1-9-AI-00120, George C. Marshall Space Flight Center, NASA, June 19, 1991.
2. *PerfStat Version 2.0 User Guide*, Instrumental, Minneapolis, MN, 1993.
3. *UNICOS Tuning Guide*, SN-2099 6.1, Cray Research, Inc., 1991.
4. *UNICOS Tuning Guide*, SR-2099 7.0, Cray Research, Inc., 1993.

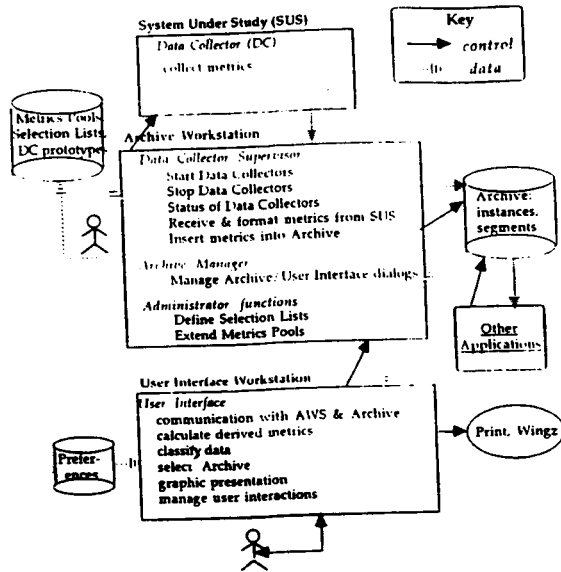


Figure 1. Software Architecture of PerfStat 2.0. [2]

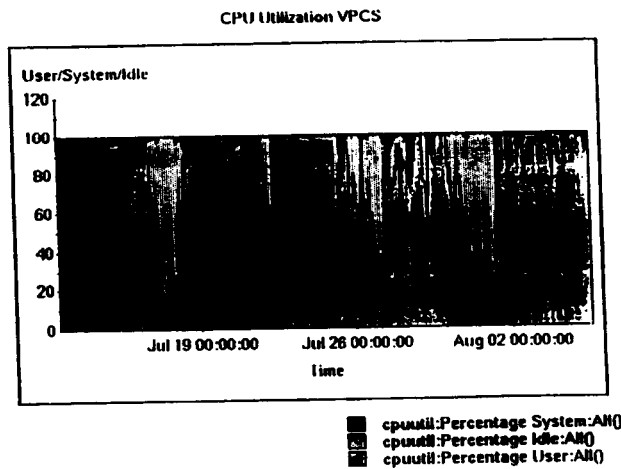


Figure 2. VPCS System Utilization.

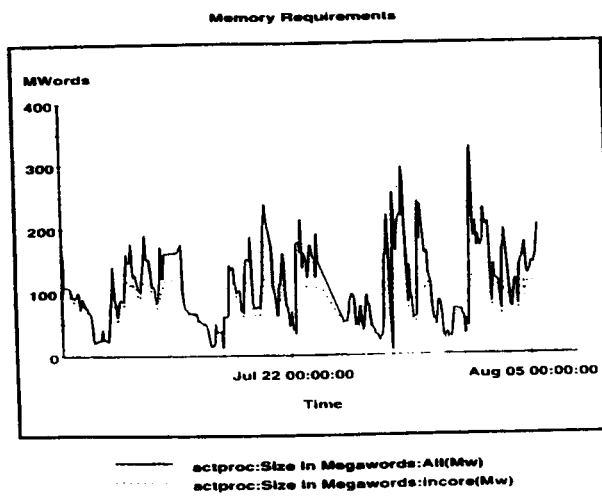


Figure 3. VPCS Memory Requirements.

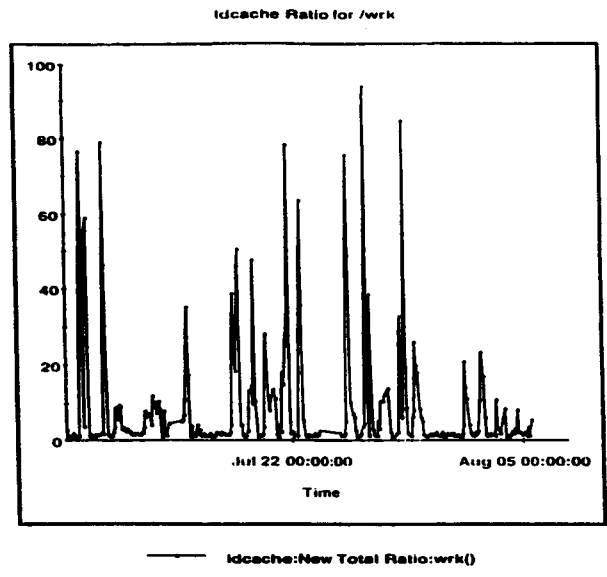


Figure 4. Re-use ratio for ldcache (/wrk).

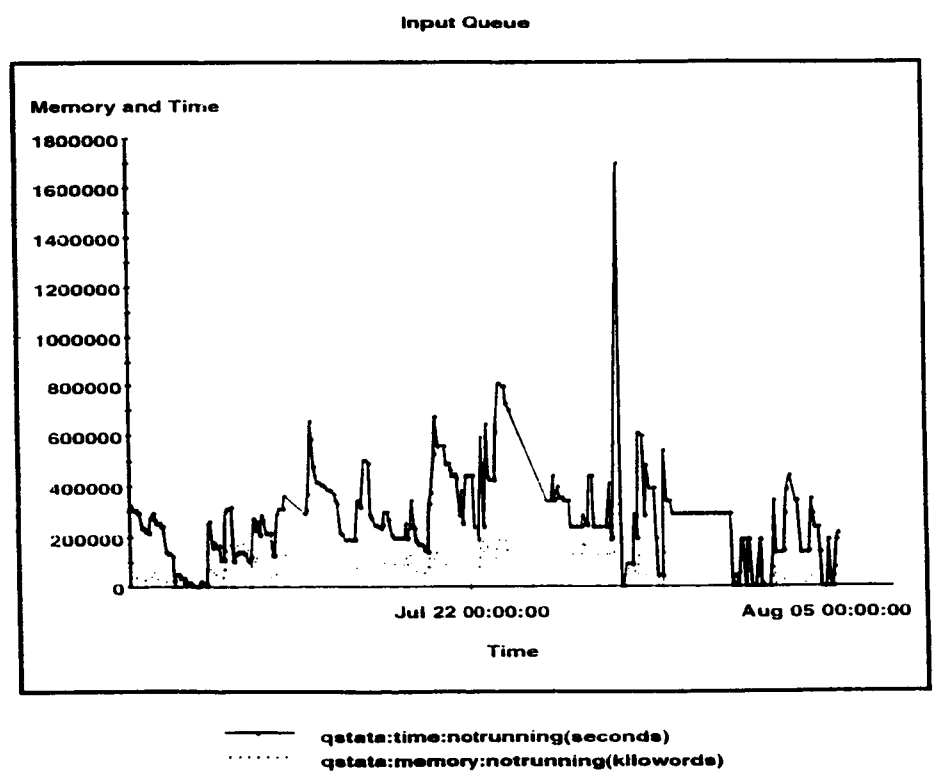


Figure 5. NQS Backlog

112564

5/2-20

26907.

N95-18979

1994

352811

NASA/ASEE SUMMER FACULTY FELLOWSHIP PROGRAM

P.7

**MARSHALL SPACE FLIGHT CENTER
THE UNIVERSITY OF ALABAMA**

OPTICAL MEASUREMENTS IN ROCKET ENGINE LIQUID SPRAYS

Prepared By: Douglas A. Feikema, Ph.D.
Academic Rank: Assistant Professor
Institution and Department: The University of Alabama in Huntsville
Department of Mechanical and Aerospace
Engineering
Propulsion Research Center

NASA/MSFC:

Laboratory: Propulsion
Division: Motor Systems
Branch: Combustion Physics

MSFC Colleagues: Richard Eskridge
Chris Dobson

INTRODUCTION

The performance of liquid propellant rocket engines is dependent upon many elements of the entire system. One of the most fundamental and most critical is the performance of the injector elements. Their characterization is an important part of the development of combustion devices. Optical measurements within these environments have proven to be invaluable tools in quantifying the physical environment of two phase flows. The effort reported herein involves the measurement of drop velocity, drop size, and most importantly mass flux using Phase-Doppler Particle Anemometry within a spray generated by a single swirl injector element operating in atmospheric pressure conditions. The mass flux has been determined and validated by mechanical patternation methods and by profile integration of the mass flux.

EXPERIMENTAL METHODS

The single element injector test facility utilized during the course of the laboratory investigations has been previously developed and described³. A photograph of the test hardware is shown in reference 3. The major features of the system include six pressurized accumulators which are first filled with water and then pressurized with compressed air. These accumulators can deliver approximately six gallons of water at constant delivery pressures up to 500 psia.

A transparent, acrylic, swirl injector element has been characterized in the present investigation which has been previously designed to examine the internal flow environment in the central posts of tangential-entry, swirl coaxial injector elements typical of those used in liquid propellant rockets². Several such injectors have been tested and analyzed² for their internal geometry and measurements were made of the axial pressure distribution, the shape of the air core formed in the post, the velocity profile in the liquid film, and the near exit spatial mass flow distribution of the spray cone. The H-3, I-9 injector from this group was selected for the effort. The injector element was calibrated and later operated at plenum stagnation pressures of 75 to 85 psig (90 to 100 psia) where the water mass flow rate was 1.1 to 1.2 lbm/s (499 to 544 gm/s). Under these conditions the injector could be operated for approximately 50 seconds.

A one-dimensional 23 tube mechanical patternator was used as a mass collection device in order to compare with the Phase-Doppler Particle Anemometry mass flux profile results. The patternator consists of 23 thin-walled, square, cross-sectioned tubes. These tubes have a nominal outer size of 0.125 inches by 0.125 inches and square inner cross-section of 0.101 inches by 0.101 inches. During testing the tube bank was positioned in the spray at the desired measurement position, normal to the spray. The mass of water collected from each tube was suctioned by a vacuum pump into a column of glass collection tubes. The mass collected by each tube in the spray is hereby recorded over a period of time which enables a mean mass distribution profile to be determined across a section of the spray. The mass flux, \dot{m}'' , for each tube was determined from the water column heights using Eqn. 1:

$$\dot{m}'' = \frac{m_{H_2O}}{A_t \cdot T_d} \quad (1)$$

where m_{H_2O} is the mass of water collected by each individual tube, A_c is the capture cross-sectional area of each tube (0.1 in^2), and T_d is the test duration time.

A Phase-Doppler Particle Anemometry (PDPA) Optical System was used to measure the droplet velocities, droplet size, and mass flux. A thorough explanation of the theory, applicability, and assessment of the PDPA can be found in references 4, 5 and 6. A schematic of the present setup is shown in Figure 1. The system is a commercial one-dimensional system fabricated by Aerometrics, Inc. The 514.5 nm line of an Argon-Ion 100 mW laser was aligned into the transmitting optics where the laser beam is split, collimated with a 160 mm lens, and the two beams are focused by a 1000 mm transmitting lens. The laser beams intersect to form fringes which are aligned horizontally, normal to the spray. The collection optics were positioned at 30° off the transmission optics axis where the light scattered by the fringes is dominated by refraction through the drop as opposed to reflection or diffraction. The collection optics consisted of a 500 mm collimating lens and a 238 mm aperture lens. This configuration enabled a droplet size range of $47.7 \mu\text{m}$ to $1671 \mu\text{m}$ to be measured. The objective in using the PDPA was to assess the effectiveness and accuracy of the PDPA system to make accurate mass flux measurements in the dense spray. Hence, it was important in the present effort to capture the largest drops since they contain most of the mass. The probe cross-sectional area is corrected for drop size and it is noted, that the largest probe cross-sectional area computed and used by the software to calculate the volume flux, was $5.0 \times 10^{-3} \text{ cm}^2$.

Figure 2 shows a schematic of the orientation and overview of the flow field. The injector was mounted to a traversing mechanism which allowed the injector to be traversed horizontally, vertically, and rotated in order to align the PDPA measurement volume (horizontal fringes) and the mechanical patternator normal to the most dense portion of the liquid sheet breakup region within the spray cone. The injector was rotated at an angle of 25° which was the experimentally determined spray cone angle. Traverses were made at two axial locations of approximately 17 and 30 injector exit diameters (8.7 mm) from the exit of the injector.

RESULTS AND DISCUSSION

A 1 ms strobe photograph of the swirl spray with an injection pressure of 80 psig is shown in Figure 3. At the exit of the injector a rotating, annular, cross-sectional, liquid sheet exits at a measured mean thickness of $635 \mu\text{m}$ and axial velocity of approximately 35 m/s (Ref. 2). As the liquid sheet leaves the injector body the radial momentum of the fluid induced by the tangential entry ports at the entrance of the post causes the liquid sheet to move radially outward and enhance the breakup of the sheet into ligaments and eventually drops. The photograph attempts to show the evolution of the breakup process.

As indicated above, measurements of mass flux were made using the patternator and the PDPA at axial stations of approximately 17 and 30. The objective was to verify if accurate measurements of mass flux could be made. In addition the mass flux profiles were integrated in order to verify if the total mass could be captured. If tangential symmetry is assumed, the integral of the mass flux profile can be performed using Eqn. 2:

$$\dot{m} = 2\pi \int_{s=0}^{s_{max}} \dot{m}''(s) \cdot s \cdot ds \quad (2)$$

where s is the axis of traversal which for the present measurements is not a true radial coordinate as indicated in Figure 2. In order to evaluate Eqn. 2, discretization was required yielding Eqn. 3:

$$\dot{m}_{Total} = \pi \cdot \sin(90 - \gamma) \cdot \sum_i \dot{m}''(s_{i+1}, s_i) \cdot (s_{i+1}^2 - s_i^2) \quad (3)$$

where \dot{m}_{Total} is the calibrated total mass flow rate, $\dot{m}''(s_{i+1}, s_i)$ is the mean value of the measured mass flux between positions s_{i+1} and s_i , and γ is the spray cone angle of 25° .

The raw PDPA data includes individual drop velocity and particle size. The software calculates the statistical properties of velocity and size as well as the volume flux. Information such as this was collected at several locations within the spray along the two traverse axes. The maximum velocities occur in the most dense portion of the spray where most of the mass is concentrated. The RMS velocity fluctuations range from about 30 to 50 % at both axial stations. The maximum velocities measured were as high as 30 m/s which is less than the calculated injector exit velocity of 35 m/s². The largest drops are found in the dense spray region and the maximum individual drop sizes measured were 1670 μm . This is in agreement with the measured mean exit liquid film thickness at the injector exit of 635 μm ². The RMS fluctuations in the measured drop sizes are 35 % which corresponds to the dynamic range of the PDPA detectors. The smallest drops measured in the dense spray region were 48 μm . Smaller drops exist; however, were not measured because of the limited dynamic range of the detector.

As noted earlier, the present effort was focused on obtaining accurate mass flux measurements and therefore it was necessary to capture the largest drops since they contain most of the mass. Figures 4 and 5 show the patternator and PDPA measured mass flux profiles in gm/s/cm² at both axial positions respectively. The patternator and PDPA mass flux profiles are in agreement at L/D of 30; however, at L/D of 17 the PDPA under predicts the mass flux. This can be explained by noting that in the PDPA method non-spherical particles are rejected. The profiles at L/D of 17 show either the PDPA is not capturing all of the mass, because the breakup of the liquid shear layer is incomplete, or the spray is too dense. However, at L/D of 30 the breakup is complete and the region is comprised of discrete drops. As noted above, if the profiles are correct, integration of the mass flux profiles over the discretized surface areas should recover the total mass flow rate. This has been completed and the results are shown in Table 1.

Table 1

Axial Position	Total Mass Flow Rate (gm/s/cm ²)	Result of Patternator Profile Integration (gm/s/cm ²)	Result of PDPA Profile Integration (gm/s/cm ²)
L/D = 17	499	493	144
L/D = 30	544	518	544

CONCLUSIONS

The following conclusions can be drawn from the results presented:

1. The maximum velocity measured by the PDPA (i.e. 30 m/s) is less than the calculated injector exit liquid film velocity (i.e. 35 m/s).
2. The maximum measured individual drop size (i.e. 1670 μm) is consistent with the independently measured mean liquid film injector exit thickness (i.e. 635 μm).
3. The PDPA can accurately measure mean mass flux in the discrete droplet region of a spray as verified by the patternator mass flux measurements and profile integration at L/D of 30.

ACKNOWLEDGEMENT

The author gratefully acknowledges the assistance of and discussions with Richard Eskridge, Chris Dobson, Tony Robertson, Micheal Lee, and John Hutt of the Combustion Physics Branch in connection with the summer faculty program.

REFERENCES

1. Hutt, J.J., Robertson, T., McDaniels, D., Eskridge, R., and Fisher, M., "Rocket Injector Single Element Characterization at the Marshall Space Flight Center", AIAA 93-2337, AIAA/SAE/ASME/ASEE 29th Joint Propulsion Conference, Sacramento, 1993.
2. Hutt, J.J., McDaniels, D.M., Smith, A.W., "Internal Flow Environment of Swirl Injectors", AIAA 94-3262, AIAA/SAE/ASME/ASEE 30th Joint Propulsion Conference, Indianapolis, IN, 1994.
3. Hartfield, R., Eskridge, R., "Experimental Investigation of a Simulated LOX Injector Flow Field" AIAA 93-2373, AIAA/SAE/ASME/ASEE 29th Propulsion Conference and Exhibit, Monterey, 1993.
4. Bachalo, W.D., "Complete Particle Field Characterization With Optical Diagnostics", Journal of Laser Applications, pp. 33 - 43, July, 1989.
5. Bachelo, W.D., Rudoff, R.C., and Sankar, S.V., "Time Resolved Measurements of Spray Drop Size and Velocity", Liquid Particle Size Measurement Techniques: 2nd Volume, ASTM STP 1083, E. Dan Hirleman, W.D. Bachelo, and Philip G. Felton, Eds., American Society for Testing and Materials, Philadelphia. 1990, pp. 209-224.
6. McDonnell, V.G., and Samuelson, G.S., "Application of Two-Component Phase Doppler Interferometry to the Measurement of Particle Size, Mass Flux, and Velocities in Two-Phase Flows", Twenty-Second Symposium (International) on Combustion/The Combustion Institute, 1988, pp. 1961-1971.

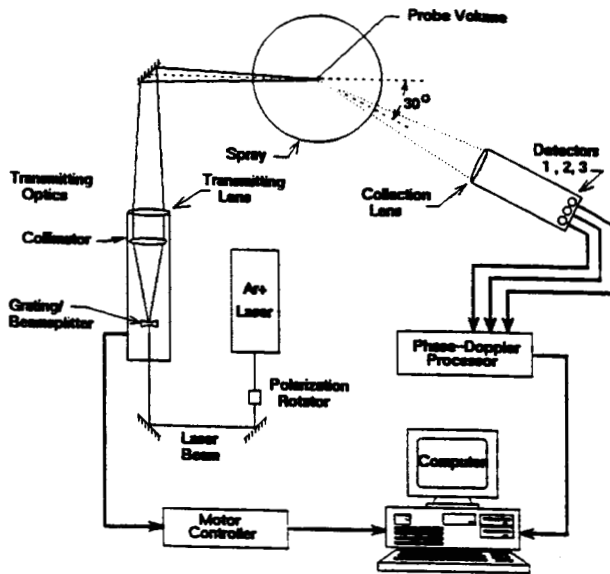


Figure 1 Schematic of the Optical Setup for the Phase-Doppler Particle Anemometry System.

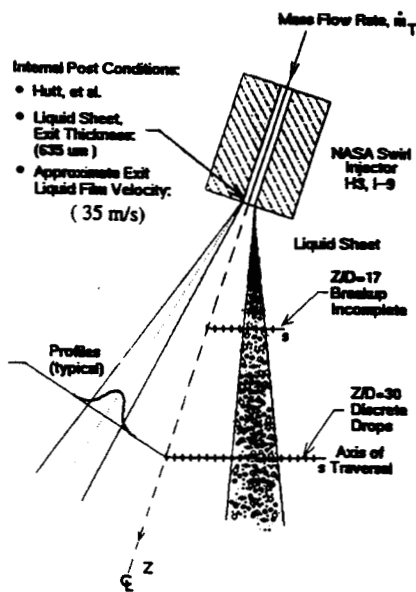


Figure 2 Overview of the Injector Orientation and Axes of Traverse.

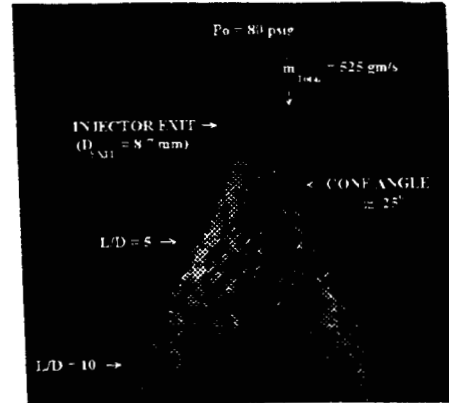


Figure 3 Photograph of the Swirl Spray at a Plenum Injection Pressure of 80 psig and Mass Flow Rate of 525 gm/s.

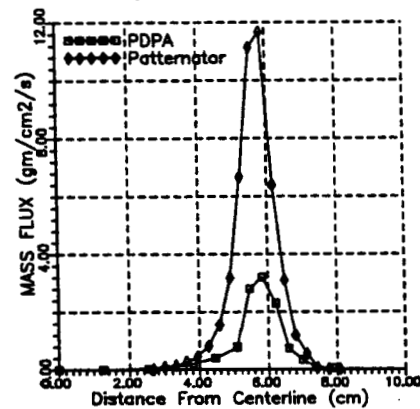


Figure 4 Comparison of Mean Mass Flux Profiles at $L/D = 17$ for the Patternator and PDPA.

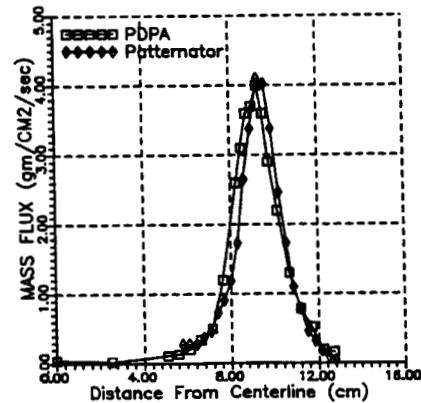


Figure 5 Comparison of Mean Mass Flux Profiles at $L/D = 30$ for the Patternator and PDPA.

112565

N95-18980

1994

NASA/ASEE SUMMER FACULTY FELLOWSHIP PROGRAM

**MARSHALL SPACE FLIGHT CENTER
THE UNIVERSITY OF ALABAMA**

352815

P. 7

DATA DRIVEN PROPULSION SYSTEM WEIGHT PREDICTION MODEL

Prepared By: Richard J. Gerth, Ph.D.
Academic Rank: Assistant Professor
Institution and Department: The Ohio University
Department of Industrial and Systems Engineering

NASA/MSFC:

Laboratory: Propulsion
Division: Motor Systems
Branch: Performance Analysis

MSFC Colleague: Dave Seymour
John Cramer
Richard Ryan
Tom Byrd

INTRODUCTION

The objective of the research was to develop a method to predict the weight of paper engines, i.e., engines that are in the early stages of development. The impetus for the project was the Single Stage To Orbit (SSTO) project, where engineers need to evaluate alternative engine designs. Since the SSTO is a performance driven project the performance models for alternative designs were well understood. The next tradeoff is weight. Since it is known that engine weight varies with thrust levels, a model is required that would allow discrimination between engines that produce the same thrust. Above all, the model had to be rooted in data with assumptions that could be justified based on the data.

The general approach was to collect data on as many existing engines as possible and build a statistical model of the engines weight as a function of various component performance parameters. This was considered a reasonable level to begin the project because the data would be readily available, and it would be at the level of most paper engines, prior to detailed component design.

The modeling database consisted of 18 engines, 14 U.S. and 4 Russian. European and Japanese engines were not included because the data was not readily available. The engines ranged from 15,000 lb thrust to 1.5 million lb thrust. They included GG, expander, and staged combustion cycles. There were both booster and space engines that were fueled by kerosene, or storable propellants, or LOX/H₂. They were all bi-propellant engines without annular nozzles, and made from metals, and not ceramics or composites.

The work is incomplete, and no final models were developed. However, a number of problems were encountered and approaches were attempted which will be described. A model was considered adequate and acceptable if:

- a) it made sense, i.e., the variables in the model are conceptually related to the weight of the component, and the coefficients are of the correct sign;
- b) the R² statistic is 0.85 or better;
- c) the residuals are within 20% of the true weight; and
- d) the model is able to predict other engines, such as paper engines, or engines not in the data base to within 20% of their observed weight.

All statistical analyses were performed in StatGraphics Version 7 by Manugistics. Best subset regression and step-wise regression were the primary modeling methods. Ridge regression and principle components regression were also explored to compensate for collinearity among the independent variables, but not further pursued because they were not appropriate given the lack of understanding of the component relationships.

TOTAL ENGINE MODEL

Since engine weight is strongly correlated with thrust, the following simple thrust model was developed. The model provides a minimum baseline for modeling accuracy, and points out some of the difficulties encountered in modeling. The regression results are presented in Table 1.

The correlation seems high and there is no time effect. However, examination of the residuals revealed two problems. First, the residuals are quite large: the average of their absolute values is 1,000 lb and the maximum is 3,987 lb for the RD170. Second, the residuals are not normally distributed: their pattern indicates a log-log transform into a power model may be more appropriate (see Table 2)

Table 1. Total Engine Thrust Model

Dependent variable: Total Engine Weight

Variable	coefficient	Std. Error	t-value	p
constant	-115.7	480.8	-0.2406	.8129
Thrust	0.0128	.00075	17.0476	0.0000
R ² =.945		Standard Error of Estimate = 1631		Durbin Watson = 1.36

Table 2. Total Engine Thrust Power Model

Dependent variable: LOG(Total Engine Weight)

Variable	coefficient	Std. Error	t-value	p
constant	-3.10	.591	-5.24	.0001
LOG(Thrust)	.897	.0484	18.62	0.0000
R ² =.953		Standard Error of Estimate = 0.255		Durbin Watson = 1.535

The power model has a better fit (higher R² value), and the residuals are normal, albeit still large. But, does it make sense? The LOG(thrust) coefficient is close to 1, which would be a linear model. It would seem that the residual structure and the particular form of this model is a function of the specific engines in the data base. This kind of problem, where the statistically better models did not necessarily make sense from an engineering view point, occurred frequently.

Since the total engine weight models were considered too imprecise, it was decided to model each component's weight separately as a function of component performance characteristics. The total engine weight was broken down into 8 major groups: thrust chamber, including the injectors, main combustion chamber, and nozzle; the individual turbopumps; the gas generator or preburner; the lines, valves, and ducts; the engine mount; the igniter; other itemized weights; and unaccounted for weight. This latter category was the difference between the listed total engine weight and the sum of the other 7 categories. For most engines the unaccounted for weight was 0 or very small (<10%). The thrust chamber, turbopump, and ducts models will be presented.

THRUST CHAMBER MODEL

The thrust chamber was the first component to be modeled, and is probably the most promising, i.e., the component model most able to meet the 4 evaluation criteria. A major problem with this and the turbopump model is that many of the independent variables, such as chamber diameter, exit area, expansion ratio, cycle, L*, etc. are not really independent, but rather collinear. Geometric variables, such as throat area and L* tend to co-vary with thrust levels. Thrust was such a pronounced factor, that if thrust was used as an independent variable, nothing else was significant. Thus, the chamber weight per unit thrust (nweight) became the dependent variable.

The next difficulty was determining which variables were significant, and what the appropriate functional form was for the model. Dimensional analysis was pursued, but did not result in a satisfactory model. A engineering analysis based on wall thickness and chamber volume indicated that the chamber weight per unit thrust was proportional to L*. The expansion ratio and nozzle cooling method are important nozzle variables. Additional variables that were examined were propellant types and engine cycles. The results of a forward step-wise regression are presented in Table 3.

Table 3. Forward Stepwise Normalized Thrust Chamber Model

Dependent variable: COMBUST. nweight

Variable	coefficient	Std. Error	t-value	p
constant	9.759E-6	0.0000594	0.0164	0.9871
ER	.000053	5.09E-6	10.3155	0.0000
1/Pc	2.370	0.31368	7.557	0.0000
ablative/thrust	108.775	50.4	2.16	0.0502
R ² =0.8753 Standard Error of Estimate = 0.000745 Durbin Watson = 2.694				

The residuals and other statistical elements looked fine, except the J-2 and A-7 were very large outliers, but not high leverage points. The R² value is acceptable, but L* proved non-significant. Also there are very few ablative nozzles (3), and thus, their significance must be approached with caution.

The backwards step-wise regression resulted in a model that also included L* and a kerosene propellant effect. However, the residuals in the model were not as well behaved, and the large coefficient values and large errors on the coefficients indicate possible collinearity problems. However, these problems could be overcome with ridge regression, for example, if it was warranted. What is really needed is a subject matter expert who can see how the variables are entering and leaving a particular model, and make value judgments as to the sign and magnitude of coefficients. This is the second type of problem that plagued the modeling process. Numerous models can be constructed, but only a component designer has the expertise to make judgments between them and guide the model building process.

TURBOPUMP MODEL

Total turbomachinery weight is strongly correlated with thrust. But, the thrust model for the turbopumps is complicated by the variety of pump configurations: single turbines driving a single pump or multiple pumps, gear driven or single shaft pumps, boost pumps, etc. Thus, a linear model on thrust, multiple, boost, and gear was attempted. Although, they were significant, the residuals were quite large, often larger than the weight of the pumps. Alternative models were investigated revealing interactions between thrust and the other variables, leading to models of turbopump weight per unit thrust. Constructing these models was difficult because of the many collinear variables, and the many models with high R² values (.85 to .95). The initial models attempted only to model the multiple pump weights per unit thrust. That was not a problem, until one attempted to model the single pumps. The various configurations, and in particular the boost pumps, could not rationally be divided by the thrust. Thus, given the complexity of the configurations, alternative paths were pursued.

A subcomponent model correlating the weight of impellers, housing, and volutes to their sizes was attempted. The housings would be correlated with the impeller sizes, so they did not need to be modeled separately. The volutes would be a function of the volumetric flowrates, if the volutes were external. If they were internal, they could be ignored. This left the impeller size, which is a function of the number of impellers, the diameter of the impeller, and its thickness. I had not found a way to account for the distance between the turbine and the pumps, which on some pumps was large. Using dimensional analysis for compressible flow it can be shown that the impeller diameter, D, is a function of the pump pressure, P, mass flowrate, m-dot, and pump speed, N. However, attempts to validate the relationship from known diameters were inconsistent and it was concluded the relationship was either non-linear, or the approach was not appropriate.

Principle components was attempted to eliminate the collinearity structure. However, the interpretation of the components was beyond the analyst's capability, and thus the principle components regression model is not presented. It is a statistically demanding procedure, and requires extensive component related subject expertise.

Returning to multiple regression approaches, it was recommended to model weight based on configuration parameters: boost, multiple, gear, cycle, and propellant types, as well as on headrise, total volumetric flowrate, and turbine horsepower. I believe this approach is the most sensible. Please note that the turbine horsepower is, in effect, an interaction (product) between the volumetric flow rates and the headrise. Thus, it is likely to be collinear with either of the two (especially flowrate), and it may not be appropriate to model the weight with both horsepower and flowrate. The data thus far indicates that flowrate and headrise correlate with weight better than horsepower. Thus, the models reported here have flowrate and not horsepower as independent variables.

Several models were constructed leading to the conclusion that the flowrates and whether the pumps were single or multiple were the two most important variables. Further investigation showed the interaction to be more significant than the main effects. Although, it is reasonable to expect both pump types to be dependent on flow with different slopes, it is unacceptable that the model be driven by the interaction effect alone because this would exclude all single pumps. This led to attempting to build two models, one for multiple pumps, and one for single pumps.

The multiple pump model is presented in Table 4. The residuals are not that well behaved, but are reasonably small with an error of 30% of the observed value or less for 11 of the 16 observations. Two of the five high percentage outliers are small pumps. The remaining three had errors of 43% to 71%.

Table 4. Multiple Pump Flowrate Model

Dependent variable: Turbopump Weight select (multiple = 1)

Variable	coefficient	Std. Error	t-value	p
constant	41.605	94.00	0.438	0.6681
Ttl_volflow	43.219	2.77	15.61	0.0000
$R^2 = 0.942$		Standard Error of Estimate = 310.0962		Durbin Watson = 2.381

The single pumps are very difficult to model because they include boost pumps and main pumps across different cycles. The single pumps are the 8 pumps of the J-2, SSME, and D170 boost pumps. It is particularly here that the headrise may play a significant role for the staged combustion cycles since low Pc pumps are typically flowrate driven, whereas we would expect to see high Pc engines to have a pressure component. This would be need to be evaluated in future models.

The most recent hypotheses that could not be verified or included in the model due to lack of time are that the headrise will not show a significant effect for low Pc engines, but will play a significant role in high Pc engines, i.e., staged combustion engines. Thus, Pc or an interaction between headrise and staged combustion may improve the model. Another possibility would be to normalize on volumetric flowrate similar to the way the combustion chamber was normalized on thrust: divide the turbopump weight by the volumetric flowrate.

LINES MODEL

Lines and ducts are hypothesized on volumetric flowrate (diameter), pressure (wall thickness), and basic engine size (thrust). In other words, for small engines there is a minimum

weight in ducts that must exist. It is likely that their wall thickness is not pressure driven but structural so that it can withstand handling and assembly. The individual flowrates were summed to obtain a total flowrate and to eliminate collinearity between fuel and oxidizer flowrates.

Examination of the correlation structure among the variables indicates that thrust and the flowrates are correlated as is the chamber pressure and the staged combustion cycle. This makes sense since flowrates scale well with thrust, and the staged combustion cycles typically have much higher Pc's. Thus, neither thrust and flowrate nor staged combustion and Pc should be simultaneously in the same model. There are 4 high leverage engines (heavy duct weights): SSME, F-1, RD0120, and the RD170. Thus, these four engines are likely to drive the coefficient values. The power model results are presented in Table 6.

Table 6. Lines and Ducts Flowrate Power Model

Dependent variable: log(ducts)

Variable	coefficient	Std. Error	t-value	p
constant	3.53	0.1725	20.443	0.0000
log(loxvolflow + fvolflow)	0.586	0.081	7.20	0.0000
MCC Pc	0.000446	0.000132	3.389	0.0044
Russian	0.6126	0.260	2.359	0.0334
R ² = 0.931 Standard Error of Estimate = 0.335 Durbin Watson = 2.083				

This model is believed to be correct. The R² is much better and the intercept is believable. The residual structure is excellent, with no outliers. The variables that were selected were the same as was expected from the initial hypothesis. And, the coefficient on the total flow is very close to 0.5 indicating that the duct weight is proportional to the square root of the total flow, which in turn would be proportional to the diameter. The only variable of concern is Russian, since it is based on so few data points. Of all the models, this is the one in which I have the most faith.

CONCLUSION

A factor that was not considered originally was the effect of "generations" of the same engine, such as the RL10-3-3, RL10-3-3A, and the RL10A-4. In initial models, they were all included in the database to increase the number of data points. This is however false, for two reasons. First it artificially weights characteristics particular to those engines which have multiple generations in the data base versus those that do not, thereby inflating the statistical significance of those characteristics. Secondly, it increases the variation within that engine family. Thus, the earlier generations were eliminated since the most recent generation is more representative of what can be accomplished today.

In retrospect, this logic may be faulty, since this would compare 3rd and 4th generation engines with other 1st generation engines. Thus, it would probably be better to compare first generation engines only. If this were done, a time effect may become evident that would need to be considered. Should sufficient data exist, a separate study involving generations of engines and their evolution may be possible.

From the analysis to date, it appears that there is too much variation between engines to obtain an accurate model at the level that would meet the objective, i.e., within ±10%. If an accurate weight prediction model is to be created from past data, much more detailed weight and engine design information will be needed.

112566

352818

N95-18981

1994

NASA/ASEE SUMMER FACULTY FELLOWSHIP PROGRAM

P.7

**MARSHALL SPACE FLIGHT CENTER
THE UNIVERSITY OF ALABAMA**

REAL-TIME THICKNESS MEASUREMENT OF MCC ABLATOR MATERIAL

Prepared By: R. Bryan Greenway, Jr. Ph.D.
Academic Rank: Assistant Professor
Institution and Department: University of Kansas
Department of Mechanical Engineering

NASAMSFC:

Laboratory: Materials and Processes Laboratory
Division: Fabrication Services
Branch: Process Modeling and Automation

MSFC Colleagues: Maninderpal S. Gill

INTRODUCTION

One of the most favorable characteristics of the Space Shuttle Program is the reusability of two of its primary components: the orbiter itself and the Solid Rocket Boosters (SRB). The SRB's provide the primary source of propulsion for the Space Shuttle during take-off after which they are recovered for refurbishment and reuse. During refurbishment, the SRB's are stripped of all remaining ablative (heat resistant) coating. A new layer is applied to the appropriate sections (nose cone, frustum, forward skirt, and aft skirt). It is the process of applying the ablative coating which provided the impetus for this project. The thickness of this protective layer is considered to be of primary importance to the level of thermal protection provided.

OBJECTIVES

The objectives of this effort are to investigate possible techniques for measuring the thickness of MCC, and if possible to test the specific capabilities of those considered good candidates for implementation. The system should be able to take measurements in real-time as close to the spray gun as possible. This will allow the information to be used in the control of the process without an inordinate time delay between a measurement and its appropriate response. The thickness of the deposited material is to be measured with less than 0.100 inches of uncertainty. This is the defined tolerance window for the ablator thickness. Finally, it must operate within the confines of the chamber which encloses the turntable, robot, and spray system, and therefore is required to be insensitive to, or at least maintainable in, that environment.

PROBLEM DESCRIPTION

Once the SRB's are recovered after a Space Shuttle launch, the individual sections are separated, cleaned and stripped with water blast guns, and inspected for damage. If no critical damage is found, the sections are prepared for reuse. One of the final steps in this process is that of applying the ablative coating to certain sections; the thickness of which depends upon the particular section being sprayed as is indicated in Figure 1.

If the ablator thickness is too small, then there will be insufficient thermal protection. If on the other hand, it is too thick, the additional weight reduces the Space Shuttle's payload capacity. It is desirable to monitor the thickness to not only improve process control, but to help alleviate

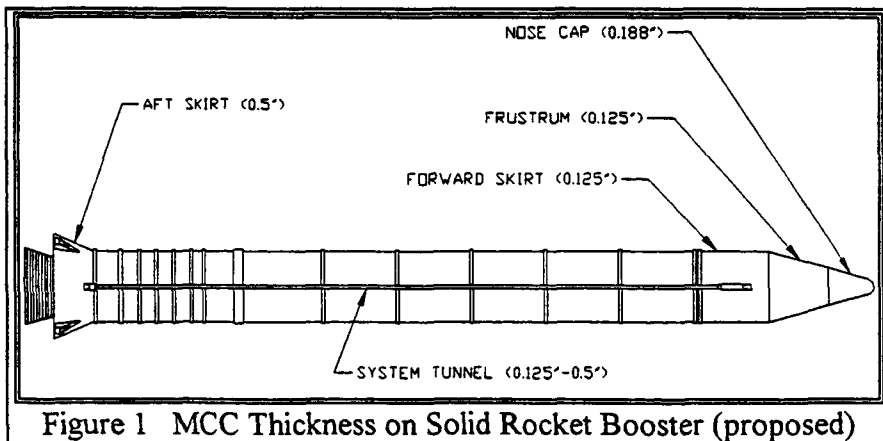
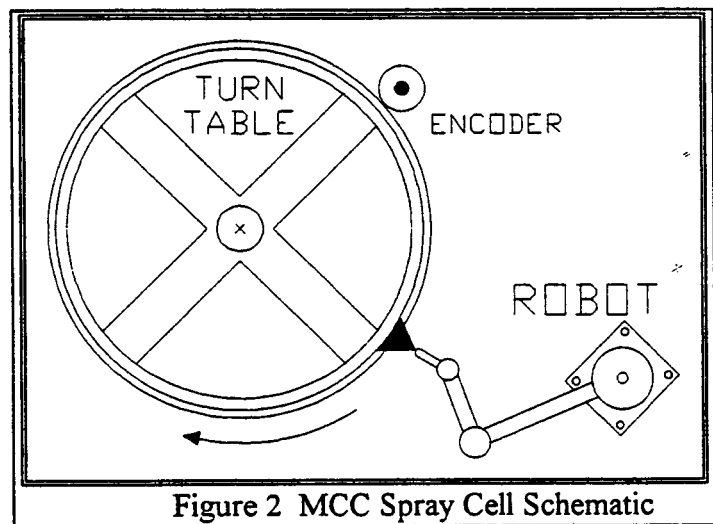


Figure 1 MCC Thickness on Solid Rocket Booster (proposed)

rework. In order to verify the process, thickness measurements are now made after the material is cured. At this point, thicknesses falling outside the permissible tolerances can be very costly.

The material used during this investigation is known as Marshall Convergent Coating (MCC). It is referred to as "convergent" because the components of the material converge and are mixed at the spray gun. MCC is composed primarily of cork and glass and is thus not electrically conductive. It has a fairly high level of surface roughness and moderate porosity. Currently, it is not the material that is "flying", but considered to be the next generation ablator. There are several advantages that MCC has over the previous ablators. There are fewer constituents in MCC, only four versus over ten for some others, which simplifies the management of the process. Previously developed ablators were mixed beforehand in a mixing tank that was used to feed the process. Once the material is mixed, it must be applied within a certain period of time. This added a time constraint to an already complex situation. This also complicated clean-up since the tanks must be cleaned and pumps, valves, and hoses purged. Finally, the absence of environmentally hazardous materials in MCC will comply with governmental regulations to be enforced in the near future.

The application process involves placing a clean skirt, frustum, or nose cone onto a large turn table as shown in Figure 2. The MCC spray gun is mounted to a robot which controls the standoff distance from the material and the angle between the spray gun axis and the surface normal. As the turn table rotates, the robot pans upward. The turn table spins at a rate of 0.5 to 6 rpm depending on the particular section being sprayed. The target substrate speed is approximately 40 feet per minute or 8 inches per second. In other words, the surface of the section being sprayed passes beneath the nozzle at a rate of approximately 8 ips. The rate of robot movement is set such that it moves about one inch vertically per full revolution of the turn table. The resulting pattern of material is that of an overlapping, helical strip with a lead (the amount of vertical travel per revolution) of one inch. Since the substrate and the spray gun are moving relative to one another, it is necessary to perform any thickness measurements on a non-contact basis. The ideal place to mount such a sensing system would be on the end-effector of the robot.



The spray gun emits MCC which fills a conic volume with a cone angle of approximately 31 degrees. The standoff distance (i.e. distance from spray gun tip to the substrate) is approximately 8 inches. This results in a near circular spray pattern with a diameter of 4.5 inches. This can be seen in the Figure 3. It can now be determined from the size of the spray pattern and the amount of lead, that each point on the surface of the substrate will pass through the spray pattern at least four times.

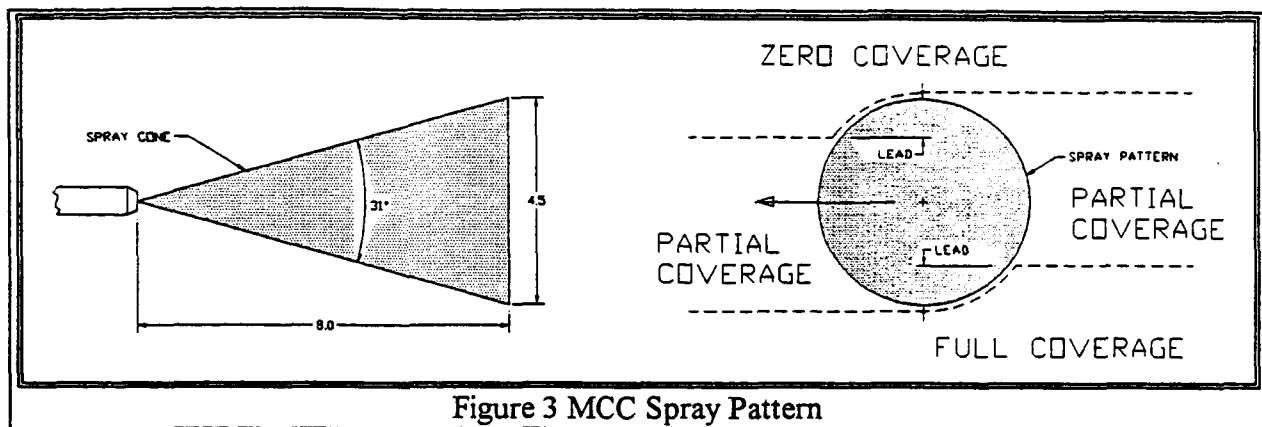


Figure 3 MCC Spray Pattern

APPROACH

With this process understood, different techniques for taking thickness measurements can now be considered. The ideal time to take the measurement is as soon after the application as possible. This will allow for appropriate responses to be undertaken before large areas are created with out of tolerance thicknesses.

One obvious method would be to take a measurement at a point before any ablator (pre-spray) is applied and then again after it is applied (post-spray). Subtracting the two measurements will thus give the thickness of the deposited layer. The pre-spray measurement(s) could be taken completely before the process is started. This would in a sense create a topological map of the bare surface of the substrate. Following this, the ablator is applied during which time post-spray measurements are taken at positions that are coincident with those taken pre-spray. Thereby, thickness measurements are made. This technique would require only one sensor, but the process of taking the pre-spray measurements could significantly lengthen the process.

Another approach would be to mount two sensors to the robot and take all measurements while spraying. If this method is used, however, sensor placement is critical. The pre-spray measurement should find the distance from the sensor to the substrate (i.e. no ablator yet applied). The post-spray measurement should find the distance from the sensor to the outer surface of the MCC after it has been completely applied. From Figure 3 above, it can be seen which areas that the sensors should be aimed to take correct measurements. The pre-spray measurement should fall into the area defined by zero coverage, while the post-spray should fall into the area of full coverage. A pre-spray value will have to be "remembered" for several revolutions before a coincident post-spray value is taken and a thickness calculation made.

In order to accomplish either one of the previously described techniques, a sensor must be obtained which will measure the distance from its mounted position on the robot end-effector to the nearest surface crossing its line of sight. There are many types of transducers that will perform this function of which ultrasonic and laser were considered. This was done not so much as to prove the transducer performance, but to investigate the approach to finding the thickness.

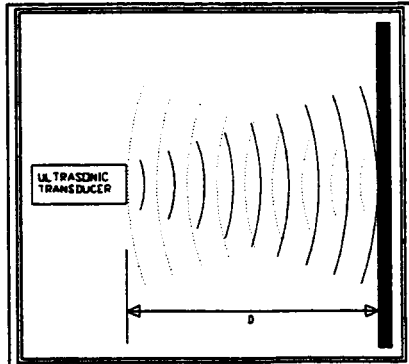


Figure 4 Ultrasonic Ranging

These two transducing methods are shown schematically in Figures 4 and 5. With ultrasonic ranging, sound wave fanout acts as both a help and a hindrance. It helps by averaging out the surface roughness. The disadvantage is that it may miss smaller flaws and undulations of the

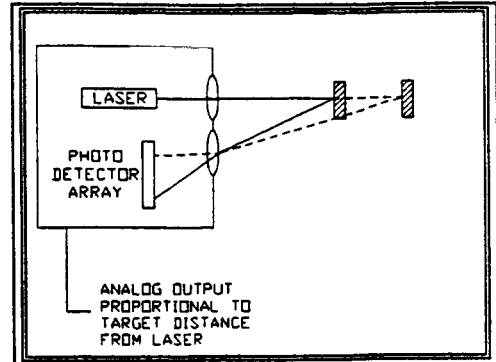


Figure 5 Laser Ranging

surface. On the other hand, the laser ranging method takes a measurement at a point. This gives the advantage of finding small flaws, but requires that several readings be taken and averaged to get a good measurement (because of the surface roughness of MCC). Another problem with the laser approach is that of keeping the laser optics clean. This could probably be taken care of by using some type of air purge system.

Both of the previously described approaches seem feasible if using some sort of pre- and post-spray measurement, but ideally the best method would be to use a single system that could take a direct thickness measurement. In order to do this, the location of the substrate surface must be found by somehow "seeing through" the MCC. The outer surface of the MCC can easily be found by using either ultrasonic or laser ranging. One way to locate the substrate through the MCC would be to use an eddy current (EC) sensor. An EC sensor will find the surface of the nearest electrically conductive material.

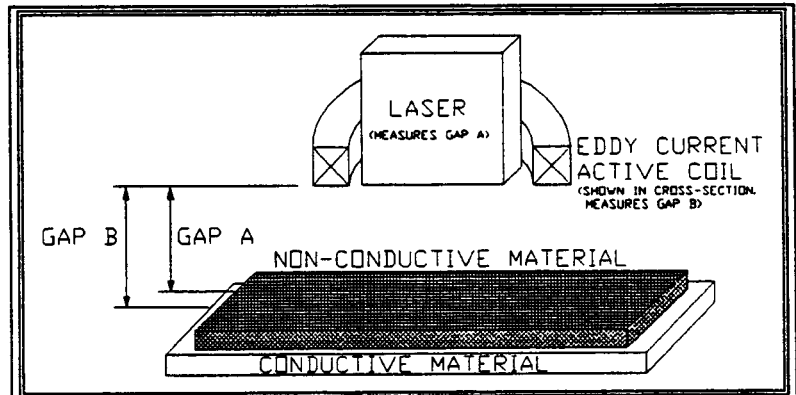
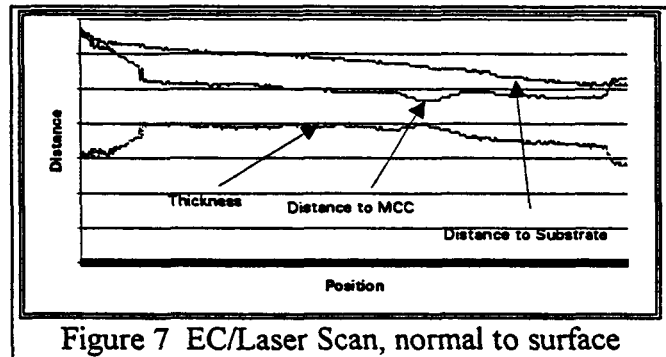


Figure 6 Combined EC/Laser Thickness Sensing

Used in combination with a laser sensor, a system such as that shown in Figure 6 could be used. The EC sensor would measure Gap B (distance to substrate surface) and the laser would measure Gap A (distance to MCC surface). The difference between the two measurements would give the MCC thickness. The down side to this approach is that caused by the maximum standoff distance of the EC sensor. They typically have ranges of 0.1 inch for small diameter sensors to 1.5 inches for those with larger diameters. This could be a problem since the MCC spray gun operates with a stand off distance of 8 inches.

EXPERIMENTAL RESULTS

Both the pre/post spray and the combined EC/Laser techniques were tested by acquiring temporary equipment loans from sensor manufacturers. Two Senix Ultra-S ultrasonic transducers were used for the pre/post spray technique, and a Kaman CTS 8500 EC/Laser system was also tested. Both systems were tested for accuracy and sensitivity to possible alignment errors (i.e. not being perfectly normal to the surface being measured). Figure 7 shows a the output resulting from a linear scan of an MCC test panel. It can be noted from this diagram that even though the distance from the substrate changes (i.e. the robot is not maintaining the standoff distance) that a correct measurement is still obtained.



CONCLUSIONS

The pre/post measurement technique is feasible, but requires time-shifting the data by keeping track of pre-spray measurements for approximately revolutions. These types of measurements were successfully made by both ultrasonic and laser systems with the required accuracy. However, the required mounting for this type of measurement makes the system sensitive to variations from the surface normal.

The EC/Laser system allowed direct measurement of MCC thickness with exceptional accuracy; however, the maximum standoff distance was approximately 1 inch. EC calibration was also somewhat difficult, but should only be required once at installation. The laser optics may need to be protected from airborne particles through the use of an air purge. The approach is must less sensitive to variations from the surface normal.

RECOMMENDATIONS

1. Pursue testing of the EC/Laser system in actual use.
2. Investigate ways to eliminate the problem caused by standoff distance allowed by the EC sensor. This may be done by increasing the EC's active coil diameter, mounting the EC on a retracting mechanism, or by using a different "MCC penetrating" sensing technique (possibly microwave ranging).
3. Investigate the possibility of using only a post spray measurement. Since the hardware being sprayed is of a specified geometry, the robot should be able to hold a fixed distance from the surface while it is spraying. Hence, a pre-spray measurement can be assumed. It should be noted that axial and radial runout can cause errors using this approach.

112567

N95-18982

1994
NASA/ASEE SUMMER FACULTY FELLOWSHIP PROGRAM

MARSHALL SPACE FLIGHT CENTER
THE UNIVERSITY OF ALABAMA

152870

P-7

STEADY AND UNSTEADY BLADE STRESSES WITHIN THE SSME
ATD/HPOTP INDUCER

Prepared By: R. Steven Gross

Academic Rank: Assistant Professor

Institution and Department: Auburn University
Department of Aerospace Engineering

NASA/MSFC:

Laboratory: Structures and Dynamics
Division: Structural Analysis
Branch: Thermostructural Analysis

MSFC Colleague: David Herda

INTRODUCTION

NASA has been developing a new liquid oxygen turbopump for the space shuttle main engine (SSME) for many years. This program is officially designated as the alternate turbopump development (ATD) high pressure oxygen turbopump (HPOTP). This report will explore some of the experimental aspects in the development of the ATD HPOTP inducer which is a critical component of the turbopump.

As the liquid oxygen (LOX) enters the turbopump, the first rotating "pumping" component that it encounters is the inducer. Approximately 30% of the total pressure rise within the pump is accomplished by the inducer while the impeller is responsible for the remaining pressure rise (70%). Physically, the inducer resembles a four-bladed marine propeller. From the structural design standpoint, one of the main concerns is the high-cycle fatigue life of the inducer. High rotational velocities (25,500 rpm) coupled with unsteady fluid flow, including cavitation, produce a high-cycle fatigue environment.

The inducer design criteria requires an infinite design fatigue life. Based on experience with early rocket engines, NASA [1] adopted a design specification for the magnitude of these unsteady dynamic fluid pressures. After calculating the steady-state fluid pressures acting on the inducer blades, the magnitude of the unsteady fluid pressures are assumed to be 20% of the steady-state pressures. This assumed 20% variation from steady-state pressures was later changed to 30% by industrial NASA contractors to produce a more conservative design criteria. To experimentally verify this 30% unsteady pressure excursion value, NASA/Marshall began developing an Inducer Test Loop facility (ITL) in 1990.

The ITL facility is a closed loop water flow system consisting of a test loop and auxiliary loop. The auxiliary loop removes dissolved air from the process water and maintains the process water temperature within a narrow band through use of a heat exchanger. Water filtration and treatment is also performed within the auxiliary loop. The ITL facility does not attempt to completely replicate the inducer working environment, i.e. water is the working fluid in the test loop compared to the LOX employed in the actual SSME turbopump. In addition, a full-scale, clear, acrylic model of the turbopump housing is utilized in the ITL to facilitate inducer flow visualization studies.

The use of the "low strength" acrylic housing model precludes operating the inducer at the rotational speeds common in engine operation (25,500 rpm). The maximum speed possible with the acrylic model is 6,000 rpm. Consequently, scaling of the

experimental results is necessary with regard to both the working fluid density and the rotational speed to match true operating conditions.

EXPERIMENTAL PROGRAM

There were two main goals of the ATD HPOPT inducer test. First, determine the steady and unsteady inducer blade surface strains produced by hydrodynamic sources as a function of flow capacity (Q/N), suction specific speed (N_{ss}), and Reynolds number (Re). Second, to identify the hydrodynamic source(s) of the unsteady blade strains. The reason the aforementioned goals are expressed in terms of blade strains as opposed to blade hydrodynamic pressures is because of the interest regarding the high cycle fatigue life of the inducer blades.

The assumed 30% variation is blade pressure, about the steady-state mean pressure, due to unsteady hydrodynamic sources converts directly into a 30% variation in the blade strains and stresses about their mean levels. This pressure-strain-stress conversion is done using the assumption that the inducer material (Inconel) behaves in a linear manner. The validity of inducer high cycle fatigue life prediction is completely dependent on the accuracy of the steady and unsteady (alternating) blade stress values.

This report will focus on the first goal of the test program which involves the determination of the steady and unsteady strain (stress) values at various points within the inducer blades. Strain gages were selected as the strain measuring devices. The strain gages were electrically connected to the instrumentation via an actively-cooled, slip ring on the rotating inducer shaft.

Concurrent with the experimental program, an analytical study was undertaken to produce a complete NASTRAN finite-element model of the inducer. Computational fluid dynamics analyses were utilized to provide the estimated steady-state blade surface pressure loading needed as load input to the NASTRAN inducer model. The results of the NASTRAN analysis indicated that for the ITL test conditions, the steady-state blade strains would be very small ($< 40\mu\epsilon$). These low estimates for the strain levels coupled with the hydrodynamic test environment created some stringent conditions on the strain gage installation.

A. INSTRUMENTATION

The combination of the centrifugal and pressure loading results in both bending and extension (radial and circumferential) of the inducer blades. Bending is the dominant loading, but the extensional loading is significant. The two main issues which had to be addressed during the instrumentation selection phase were the low anticipated strain levels and the need to develop a "robust" gage installation capable of surviving the hydrodynamic environment.

To compensate for the low strain levels, semiconductor gages were selected for the majority of the gage locations. It was felt that the high strain sensitivity of these gages would allow for the most accurate measurement of the small unsteady (alternating) blade strains while foil gages were selected to measure the steady-state strain levels. The use of semiconductor gages to measure the steady state strains was considered to be less desirable than the use of foil gages due to the significant thermal shift of the semiconductor gages compared to the foils. The gage thermal shift behavior becomes more critical as the measurement time span increases, such as the case for determination of the steady-state strain levels. Once it was decided to employ both the foil and semiconductor types of gages, the next set of decisions concerned the type of bridge to be employed (quarter, half or full) and the gage pattern at each of the strain locations.

A full bridge arrangement was selected based on three factors. First, a full bridge provides the highest bridge output compared to either the quarter or half bridge arrangements. Second, the full bridge provides better temperature compensation. Finally, the slip ring is not in the measurement circuit for the full bridge as opposed to the quarter and half bridge circuits.

Once a full bridge arrangement had been determined, the next decision concerned the selection of the gage pattern at each strain location. Two major factors constrained the selection of the gage pattern to a rather limited set of options. The first constraint was the decision to utilize a full bridge arrangement as discussed in the above section which required four active gages at each strain location for effective temperature compensation and bridge completion. The second major constraint arose from the need to recess the gages into the inducer blade to protect the gages from the fluid flow and limit the distortion of the flow pattern over the blade surface during operation. The minimum required depth of the recesses was 0.035 inches. This depth allowed for protection of the gages while still providing sufficient room to fill the recess with an epoxy potting

compound that could be smoothed to match the blade surface for flow continuity. This minimum recess depth was significant relative to the total blade thickness which varied from a minimum of 0.090 inches to a maximum of 0.170 inches. As a consequence, it was not considered structurally advisable to recess both the pressure side (PS) and the suction side (SS) of the blade at the same location.

Given the two constraints, the gage pattern that was selected consisted of two gages mounted radially relative to the rotational axis of the inducer and two gages mounted circumferential. This bridge circuit results in the following bridge output equation

$$V_o = \frac{V_i GF (1 - \epsilon_c / \epsilon_r)}{[2/\epsilon_r + GF (1 + \epsilon_c / \epsilon_r)]} \quad (1)$$

where V_o = bridge output voltage,
 V_i = input voltage to bridge,
 GF = gage factor,
 ϵ_c = circumferential strain, and
 ϵ_r = radial strain.

The derivation of equation (1) is a rather straightforward procedure starting with the general equation for an unbalanced Wheatstone bridge circuit.

B. DATA REDUCTION

The quantities V_i and GF in equation (1) are known prior to the test and the value of V_o is measured during the test. The two strains ϵ_r , ϵ_c and the strain ratio, ϵ_c / ϵ_r are unknown quantities in equation (1). Calculation of the absolute strain values required the development of a complimentary equation involving the strains to create a system of two equations with two unknown strains. During the search for this complimentary equation, the author examined the NASTRAN inducer model to determine the characteristics of the strain ratio ϵ_c / ϵ_r .

Two characteristics of the strain ratio were clearly discernable from the NASTRAN analysis. First, the strain ratio was a significant value relative to 1.0 and it would be a serious error to eliminate the strain ratio from the term within the denominator in equation (1). Second, the strain ratio value was substantially different at different locations on the blade surface and the ratio values did not correlate

well with the Poisson's ratio of the blade material. The author concluded that the most accurate values available for the strain ratio would be those calculated from the NASTRAN analysis results for each of the gaged locations on the blade. The "analytical" strain ratio values were then employed in equation (1) to calculate the experimental strain ϵ_r . This procedure of employing an analytical value to facilitate the calculation of experimental strains is certainly not an ideal procedure, but the author was unable to develop a more appropriate method.

A simple cantilevered beam specimen was produced to examine the validity of this experimental-analytical method for determining the blade strains. Instrumentation of the beam involved the use of a pattern of four foil gages identical to the foil gages employed on the actual inducer. Machining of the specimen, bonding of the gages, and wiring of the bridge was all accomplished by the same organization responsible for the inducer instrumentation. Loading of the beam involved hanging a set of dead weights at the free end. A finite element model of the beam was constructed from CQUAD4 plate elements using MSC/PAL2 to provide the value of the strain ratio ϵ_c/ϵ_r needed for the calculation of the experimental strains using equation (1).

This finite element model was employed to allow for the modelling of the strain gage recess machined into the beam. The finite element analysis results clearly showed that the presence of the recess strongly influences the strain state. Based on the results of this simple cantilevered beam test case, the finite element model of the ATD inducer was modified to incorporate the strain gage recesses. To calculate the radial and circumferential strains from equation (1), the values of the strain ratio (ϵ_c/ϵ_r) had to be supplied to the data reduction algorithm via the finite element results.

The final section of the data analysis program involved the conversion of the strain results (ϵ_r and ϵ_c) determined from equation (1) by using the experimental bridge output and the strain ratios from the finite element results. These values, ϵ_r and ϵ_c , represent the strains at the bottom of the gage recess. The strains that are needed to predict the high cycle fatigue life of the inducer are those at the blade surface of an unmodified inducer, i.e., one with no machined recesses. The conversion from the measured recess strains to the blade surface strains was accomplished through comparison of the modified (with recesses) and unmodified inducer finite element models.

112568

352822

N95-18983

1994

NASA/ASEE SUMMER FACULTY FELLOWSHIP PROGRAM

**MARSHALL SPACE FLIGHT CENTER
THE UNIVERSITY OF ALABAMA**

P. 7

**SPECIAL RELATIVITY EFFECTS FOR SPACE-BASED COHERENT LIDAR
EXPERIMENTS**

Prepared by: V. S. Rao Gudimetla, Ph. D.
Academic Rank: Assistant Professor
Institution and Department: Oregon Graduate Institute
Department of Electrical Engg. and Applied Physics

NASA/MSFC:

Laboratory: Astrionics
Division: Optics and RF
Branch: Electro-optics

MSFC Colleague: Michael J. Kavaya, Ph. D.

INTRODUCTION

There is a great need to develop a system that can measure accurately atmospheric wind profiles because an accurate data of wind profiles in the atmosphere constitutes single most input for reliable simulations of global climate numerical methods. Also such data helps us understand atmospheric circulation and climate dynamics better. Because of this need for accurate wind measurements, a space-based Laser Atmospheric Winds Sounder (LAWS) is being designed at MSFC¹ to measure wind profiles in the lower atmosphere of the earth with an accuracy of 1 meter/sec at lower altitudes to 5 meters/sec at higher altitudes. This system uses an orbiting spacecraft with a pulsed laser source and measures the Doppler shift between the transmitted and received frequencies to estimate the atmospheric wind velocities. If a significant return from the ground (sea) is possible, the spacecraft speed and height are estimated from it and these results and the Doppler shift are then used to estimate the wind velocities in the atmosphere. It is expected that at the proposed wavelengths, there will be enough backscatter from the aerosols² but there may not be significant return from the ground. So a coherent (heterodyne) detection system is being proposed for signal processing because it can provide high signal to noise ratio and sensitivity and thus can make best use of low ground returns. However for a heterodyne detection scheme to provide best results, it is important that the receiving aperture must be aligned properly and for the proposed wind sounder, this amounts to only a few microradians tolerance in alignment. It is suspected that the satellite motion relative to the ground may introduce errors in the order of a few microradians because of special relativity. Hence the problem of laser scattering off a moving fixed target when the source and receiver are moving, which was not treated in the past in the literature, was analyzed in the following, using relativistic electrodynamics³ and applied to the case of the space-based coherent lidar, assuming flat ground. We are interested in developing analytical expressions for the location of the receiving point for the return with respect to the satellite, receiving angle and Doppler shift in frequency and amount of tip, all as measured in the satellite moving coordinate system and the diffuse scattering angle at the ground which does not require any compensation. All the three cases of retro-reflection, specular reflection and diffuse scattering by the ground should be treated though retro-reflection and diffuse scattering are more important.

METHOD OF ANALYSIS AND PATH GEOMETRY

Figure 1. shows a Laser Atmospheric Wind Sounder System, called AEOLUS. Initially we assume earth is assumed to be flat and a satellite is moving with a horizontal velocity V (along the x axis, parallel to the ground) at a height H above the ground. Our goal is to find out the path of a light ray from a moving source (satellite) to the stationary ground, as observed from the ground (whose coordinate system is not moving) and the paths taken by the reflected and backscattered rays from the ground towards the satellite as observed by a receiver adjacent to the transmitter in the moving coordinate system.

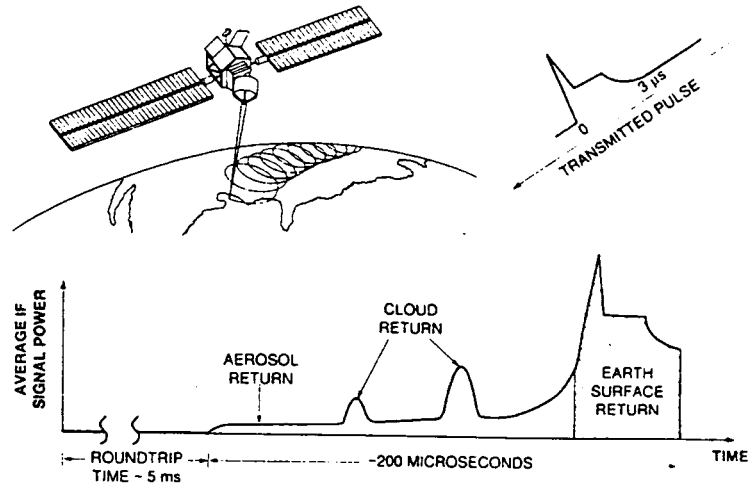


Fig.1. AEOLUS-Laser Atmospheric Wind Sounder

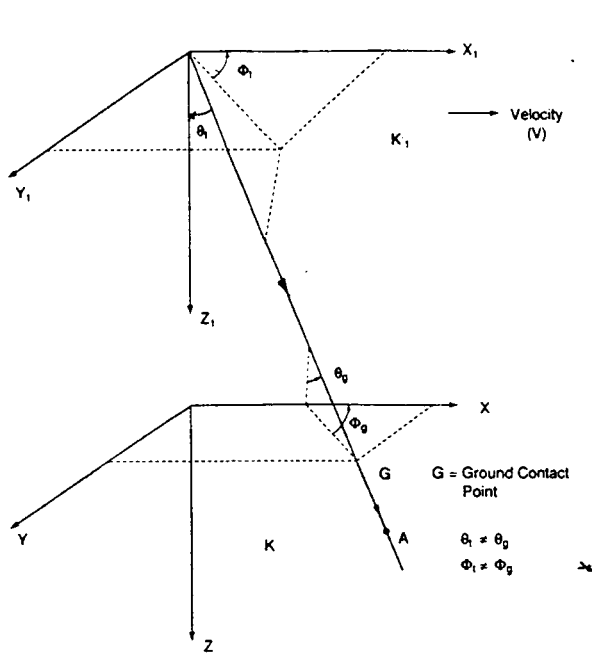


Fig.2. Coordinates Systems for the Analysis

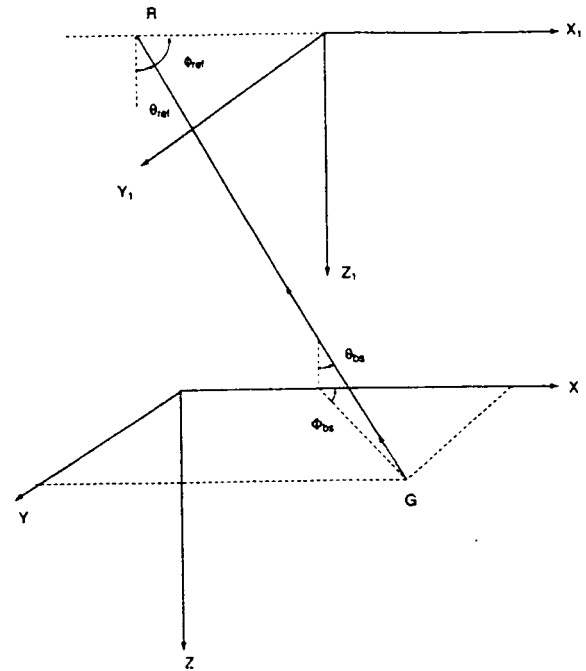


Fig.3. Retro-reflection Path Geometry

Figure 2. shows two coordinate systems. K system is a fixed coordinate system (coordinates are x, y, z and t). K₁ system describes the satellite motion and is moving with respect to K at a velocity V along the x axis (coordinates in K₁ are x₁ , y₁ , z₁ and t₁). A laser transmitter is located at the origin of the K₁ system. Assume at t = t₁ =0, the point (x₁=0 , y₁=0 , z₁=H) of K₁ coordinate system will go past the point (x=0, y=0, z=0) of coordinate system K to set up proper Lorentz transformations.

We used ray formulation first. For this consider a light signal transmitted from the origin of the K₁ system with spherical coordinate angles θ_t and φ_t towards the fixed system on the ground (Figure 2). Assume that light is pulse of very short duration so that during the transmission, the displacement of the origin of the coordinate system can be ignored. For the transmitted ray, the coordinates in the moving frame and fixed frame are calculated. After the ray is incident on the ground, the returning ray angles are determined, depending whether the return is due to retro-reflection, specular reflection and diffuse reflection. The returning ray coordinates are then determined again in both coordinate frames. Since the motion is parallel to x-axis, z coordinate separation (H) remains constant and this is used to calculate the time of transmission from source to the ground and from ground to receiver. Since ray formulation can not give Doppler shift and changes in the electromagnetic fields and reflectance, we used a wave formulation, which provided with the above results as well as verification for some of the results, achieved through the ray formulation. All the details are being published in a NASA Technical Memorandum⁴.

GENERAL RESULTS

When a retro-reflector is located at the point where the above ray is incident on the ground, The incident is scattered back along the receiving angle in the fixed coordinate system (Figure 3). In this case, at the point of return in terms of the satellite coordinate system:

Coordinates of the point of return:

$$x_{1ret} = -2 H \alpha \frac{1+\alpha \sin(\theta_t) \cos(\phi_t)}{(1-\alpha^2) \cos(\theta_t)} \quad y_{1ret} = 0 \quad z_{1ret} = z+H = 0 \quad (1)$$

The spherical coordinate angles and the received frequency ω_{rec}:

$$\cos(\theta_{rec}) = \frac{(1-\alpha^2) \cos(\theta_t)}{1+\alpha^2+2\alpha\sin(\theta_t) \cos(\phi_t)} \quad \tan(\phi_{rec}) = \frac{(1-\alpha^2) \sin(\theta_t) \sin(\phi_t)}{2\alpha+(1+\alpha^2) \sin(\theta_t) \cos(\phi_t)} \quad (2)$$

$$\omega_{rec} = \omega_t \frac{1+\alpha^2+2 \alpha \sin\theta_t \cos\phi_t}{1-\alpha^2} \quad (3)$$

For specular reflection, we assume that the light is reflected back according to Snell law in the fixed system (K). A further analysis gives us:

Coordinates for the point of return:

$$x_{1ret} = 2 H \tan(\theta_t) \cos(\phi_t) \quad y_{1ret} = 2 H \tan(\theta_t) \sin(\phi_t) \quad z_{1ret} = 0 \quad (4)$$

For the receiving angles and frequency:

$$\cos(\theta_{rec}) = -\cos(\theta_t) \quad \tan(\phi_{rec}) = \tan(\phi_t) \quad \omega_{rec} = \omega_t \quad (5)$$

However $\theta_{rec} = -\theta_t$ and $\phi_{rec} = -\phi_t$. Also note that there is no Doppler shift.

For the case of diffuse scattering, the rays of interest lean towards backscattering direction, as opposed to forward reflection. For an arbitrary direction, results are given in the memorandum⁴. It can be shown that most of the rays will miss the receiver except a few near the backscattering direction and in particular, it is possible to find a direction (θ_b and ϕ_b) at the ground for which no compensation is needed and these angles are given as:

$$\cos(\theta_b) = \frac{\cos(\theta_t) \sqrt{1-\alpha^2}}{1-\alpha \sin(\theta_t) \cos(\phi_t)} \quad \tan(\phi_b) = \frac{\sin(\theta_t) \sin(\phi_t) \sqrt{1-\alpha^2}}{\sin(\theta_t) \cos(\phi_t) - \alpha} \quad (6)$$

For this case with no need for adjustments at the receiver, as expected, the coordinates of the point of return are:

$$x_{1ret} = 0 \quad y_{1ret} = 0 \quad z_{1ret} = 0 \quad (7)$$

For the received frequency:

$$\omega_{rec} = \omega_t \frac{1 + \alpha \sin\theta_t \cos\phi_t}{1 + \alpha \sin\theta_t \cos\phi_t} \quad (8)$$

RESULTS AND SUMMARY FOR THE PROPOSED WIND SOUNDER

AEOLUS has a proposed altitude of 350 Kilometers, a velocity of 7704.3 meters/sec, nadir angle of 30^0 , azimuth angle of 45^0 and wavelength of $2 \mu\text{m}$. For this data, in the case of retro-reflection, the returned beam will miss the satellite by about 20.7 meters. If the beam foot print is large on the ground, still a part of the return may be received. Received Angles are 30.0018 degrees for nadir and 44.9958 degrees for azimuth. These correspond to a tilt of 31.43μ radians for nadir and 73.33μ radians for azimuth. For higher velocities ($v/c \geq 0.1$), the receiver may miss the backscatter completely. Angles, through which the receiver has to be tipped, will be much higher. For LAWS, backscatter may be reasonably acceptable. In case of specular reflection off the ground, if the transmission angle is zero, no corrections are required. In this case, for non-zero transmission angles, reflected signal will not see the receiver. In case of diffuse scattering off the ground, for any transmission angle, there exists a return direction, for which no compensation is required at the receiver. For AEOLUS data, this direction differs from the incidence angles at the ground by about 15.7 microradians for elevation angle (theta) and by 36.63 microradians for azimuth (phi) and hence provides a good backscatter and so the system should be successful. Analytical results for the Doppler shift in the frequency show that in case of specular reflection, there is no Doppler shift due to the satellite motion and the relativity. In

case of backscattering and diffuse scattering, there are Doppler shifts due to the satellite motion and relativity. It is found that the Doppler shift due to the relativity is in the order .025 % to .1% for a wind of 1 meters/sec and it should be corrected for.

RECOMMENDATIONS

First, the analysis has to be redone, taking into consideration horizontal movement of the satellite and vertical movement of the target with flat earth. Then relax the assumption that the earth is flat to arrive the more accurate design criteria. Emphasis should be on backscattering and diffuse targets. The light incident on the ground has a finite area. For flat earth, correction for the fact that the light at the receiver is contributed by all the points from the ground, may not be serious. But when we use spherical coordinates, we must take this into account as the local normal is different from point to point. Compare the signal contribution due to relativistic effects with that from satellite motion and wind for a more general analysis that involves spherical earth. Error estimates in wind have to be calculated for the more general case. No Results have appeared in the literature how the Fourier spectrum of a pulse changes for the return geometry under consideration. Develop an analysis for this problem and compare the relativistic contribution.

SUMMARY

In summary, we derived several analytical results based on the special theory of relativity, useful for space-based lidar experiments. We applied our results to the proposed AEOLUS system and found that the current design recommendations are within acceptable tolerances. Some important next steps that will improve the analysis and provide better design rules have been identified.

REFERENCES

1. R. G. Beranek, J.W. Bilbro, D. E. Fitzjarrald, W. D. Jones, V. W. Keller, B. S. Perrine: Laser Atmospheric Wind Sounder (LAWS), S. P. I. E. Vol. 1062 Laser Applications in Meteorology and Earth Atmospheric Remote Sensing, 234-248 (1989)
2. M. J. Kavaya, R. T. Menzies: Lidar aerosol backscatter measurements: systematic, modeling, and calibration error considerations, Appl. Opt., Vol. 24, 3444-34453 (1985)
3. J. Van Bladel: Relativity and Engineering (Springer-Verlag, New York 1984). Chapter 5 in this book has several references related to this work and not cited here due to page limitations.
4. V. S. Rao Gudimetla: Effects of special relativity LAWS system: Presentation at the Meeting of the Working Group on Space-Based Lidar Winds, Huntsville, AL, July 12-14 (1994), to be published as a NASA Technical Memorandum.

112569

N95-18984

1994

NASA/ASEE SUMMER FACULTY FELLOWSHIP PROGRAM

350823

MARSHALL SPACE FLIGHT CENTER
THE UNIVERSITY OF ALABAMA

SURFACE ROUGHNESS MEASUREMENTS

2-3

Prepared By:	Thomas G. Howard
Academic Rank:	Instructor
Institution and Department	Northwest-Shoals Community College Department of Electro-Optics
NASA/MSFC:	
Laboratory:	Astrionics
Division:	Optics and Radio Frequency
Branch:	Optical Fabrication
MSFC Colleague:	Alan Shapiro, Ph.D.

Introduction

The Optics Division is currently in the research phase of producing grazing-incidence mirrors to be used in x-ray detector applications. The traditional method of construction involves labor-intensive glass grinding. This also culminates in a relatively heavy mirror. For lower resolution applications, the mirrors may be of a replicated design which involves milling a mandrel as a negative of the final shape and electroplating the cylindrical mirror onto it. The mirror is then separated from the mandrel by cooling. The mandrel will shrink more than the "shell" (mirror) allowing it to be pulled from the mandrel. Ulmer² describes this technique and its variations in more detail. To date, several mirrors have been tested at MSFC by the Optical Fabrication Branch by focusing x-ray energy onto a detector with limited success. Little is known about the surface roughness of the actual mirror. Hence, the attempt to gather data on these surfaces. The test involves profiling the surface of a sample, replicating the surface as described above, and then profiling the replicated surface.

Results

The sample chosen for this test is a silicon carbide disk 1.5" in diameter. We measured the surface with a TopoMetrix scanning force microscope (SFM) and a WYCO TOPO 3-D. The TopoMetrix has a stylus which contacts the surface while the WYCO is a non-contact interferometric-type profiler. Both are described quite well by Bennett¹. The technology used in the WYCO is well-known while the SFM is a relative new-comer to the industry. The initial measurements made with the SFM were of known "standards" and were within 5% of the published values. However, the height distances on these standards were on the order of 1 k angstroms and the sample was reported by Jean Bennett of Michelson Laboratory and Darrell Englehaupt of The University of Alabama at Huntsville to have an RMS roughness¹ of approximately 1 angstrom. It was quickly realized that the SFM will require critical noise isolation in order to make measurements in the sub-nanometer range. The WYCO with a 20 X objective lens yields a measurement area of approximately 0.5 mm on a side. An "absolute" measuring technique was employed which involves taking a measurement and removing tilt from the sample (with software), translating a distance laterally, and repeating the measurement then obtaining the difference. The 0.940 angstroms measured is comparable to the value mentioned earlier.

At the time of this writing, the replication process is not completed. Measurements on the replicated surface compared to the previous measurements will yield valuable information which will aid in refining the replication process.

Reccomendations

Due to the noise problems encountered with the scanning force microscope, the instrument must be relocated to an area more conducive to its operation. Specifically, acoustic noise seems to be its greatest nemesis.

References

1. Bennett, J., and Mattsson, L., Introduction to Surface Roughness and Scattering, Optical Society of America, Washington, D.C., 1989.
2. Ulmer, M., et al, "Electroformed grazing incidence x-ray mirrors for a mirror array telescope," Applied Optics, Vol. 26, pp.3852-3857, 1987.

112570

30908

N95-18985

1994

NASA/ASEE SUMMER FACULTY FELLOWSHIP PROGRAM

P. 6

MARSHALL SPACE FLIGHT CENTER
THE UNIVERSITY OF ALABAMA

PROBING THE CHEMISTRY OF NICKEL / METAL HYDRIDE BATTERY CELLS
USING ELECTROCHEMICAL IMPEDANCE SPECTROSCOPY

S/S-33

30908

P. 6

Prepared By: Bryan J. Isaac, Ph.D.
Academic Rank: Assistant Professor
Institution and Department: Catawba College
Department of Chemistry

NASA/MSFC:

Laboratory: Astrionics
Division: Electrical Design
Branch: Failure Analysis

MSFC Colleague: David H. Burns

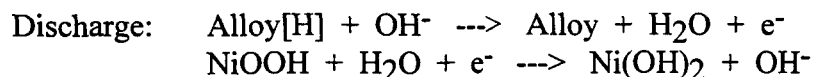
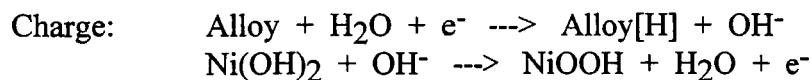
Electrochemical Impedance Spectroscopy (EIS) is a valuable tool for investigating the chemical and physical processes occurring at electrode surfaces. It offers information about electron transfer at interfaces, kinetics of reactions, and diffusion characteristics of the bulk phase between the electrodes. For battery cells, this technique offers another advantage in that it can be done without taking the battery apart. This non-destructive analysis technique can thus be used to gain a better understanding of the processes occurring within a battery cell. This also raises the possibility of improvements in battery design and identification or prediction of battery characteristics useful in industry and aerospace applications.

Impedance spectroscopy is an alternating current (ac) method, while battery cells are useful chiefly as a supply of direct current (dc). The ac signal is applied while the battery is held at a desired potential, and the signal perturbs the battery system slightly. The frequency of the ac signal is scanned to yield an ac frequency spectrum, normally ranging in this work from 10 kHz to 10 mHz, and often scanned to frequencies as low as 0.2 mHz. The highest frequencies generally give information about the fastest processes, such as electron transfer, charge transfer, and some chemical reactions. The lower frequencies result in data relating to the slower phenomena, such as diffusion parameters of the cell.

EIS as a technique is powerful and capable of yielding significant information about the cell, but it also requires that the many parameters under investigation can be resolved. This implies an understanding of the processes occurring in a battery cell. Many battery types were surveyed in this work, but the main emphasis was on nickel / metal hydride batteries.

Nickel / metal hydride battery cells are in the class of rechargeable cells along with nickel cadmium (NiCd) and nickel hydrogen (NiH₂) batteries. One electrode is NiOOH (which becomes Ni(OH)₂ in the discharged state), while the other is a metal alloy which is formed on a nickel substrate (at the charged state this forms a hydride, and at discharge the hydride is taken off). The first electrode is also used in other nickel cells, including the NiCd battery.

The chemical reactions of the cell during charging and discharging processes are:



One advantage of the Ni/MH cell over NiCd is an increase in the charge density, which results in more capacity for battery cells of the same mass. Various nickel-metal alloys are under consideration, each with somewhat different properties.¹

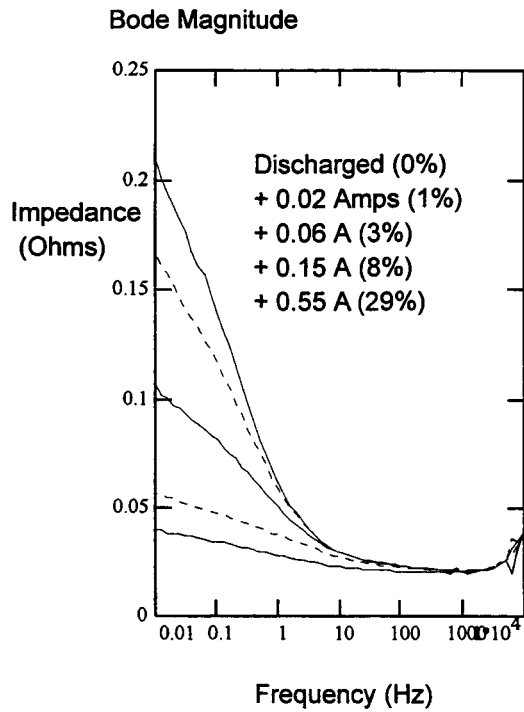
EIS is a method which probes all of the battery cell, not just a single area of interest, so one must have some general understanding of the processes occurring within the cell to be able to comprehend the results. Many of these processes are listed below:

- resistance at the metal-metal junctions within the leads and the electrodes;
- any effects related to a possible passivation layer on the NiOOH electrode;
- processes occurring at the interface of the electrode and the bulk phase (between the electrodes),
 - resistance due to electron transfer (e.g., electrons are given up by the hydride to the alloy in order to form the positive hydrogen ions),
 - resistance due to the chemical reaction (e.g., hydrogen ions reacting with hydroxide ions),
 - resistance associated with decreased availability of reactant (in the case of a limiting reactant),
 - capacitance associated with the double layer (a phenomenon occurring a few atom diameters away from the electrode surface caused by a response of the bulk phase to the charging of the electrode); and
- processes in the phase between the electrodes (referred to as the "bulk"),
 - resistance of the bulk (analogous to solution resistance in a typical electrochemical cell), and
 - impedance due to diffusion (this is known as the Warburg impedance).

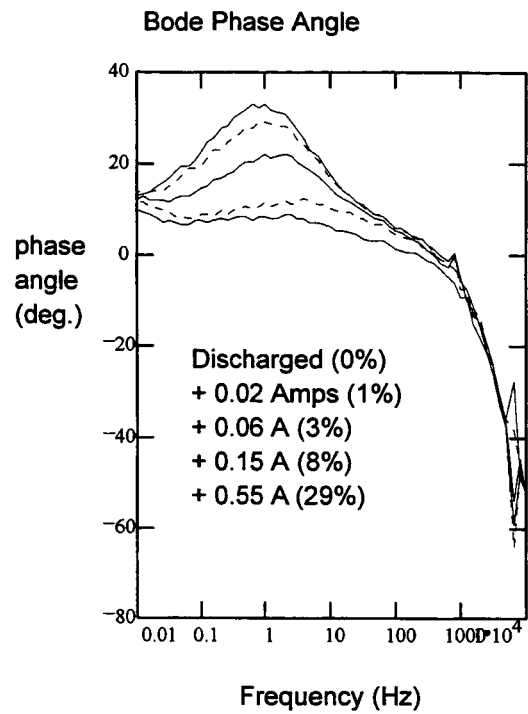
The large number of phenomena can result in a problem of resolving each interaction from the other, or may imply that many parameters are held constant and one or two of interest are investigated. To reach the goal of characterizing a battery cell with a model to show the contributions of each process, one would need to be able to either resolve each parameter (which is not possible) or have some control over a large number of these factors. This is a requirement which is beyond our capabilities at this time. We can, however, study the cell in a region in which we can resolve some of the chemical and physical phenomena, and gain some understanding of those processes.

The method employed in these experiments was to charge or discharge the battery cell to a desired level, allow the cell to equilibrate, and scan the impedance spectrum. It was noted that the impedance measurements varied considerably for the Ni/MH cell near the region of complete discharge. This region is presented in Figure 1. [An explanation of the graphical presentation of impedance spectra may be in order here. The plots included represent various forms of the information: one gives the magnitude of the impedance as a function of ac frequency; the second is a measure of the shift in the phase of the response when compared to the excitation frequency (known as the phase angle) as a function of ac frequency; and the third is a complex plane plot, presented with the real impedance -- the impedance in phase with the excitation -- on the x-axis, and the imaginary impedance -- the component out of phase with the excitation -- on the y-axis. The third plot (the complex plane plot) could also be presented as a three-dimensional figure, because the real and imaginary impedances are each a function of frequency. The result is that the highest frequencies yield points near the lower left of the graph and the lower frequencies appear at the upper right.]

A.



B.



C.

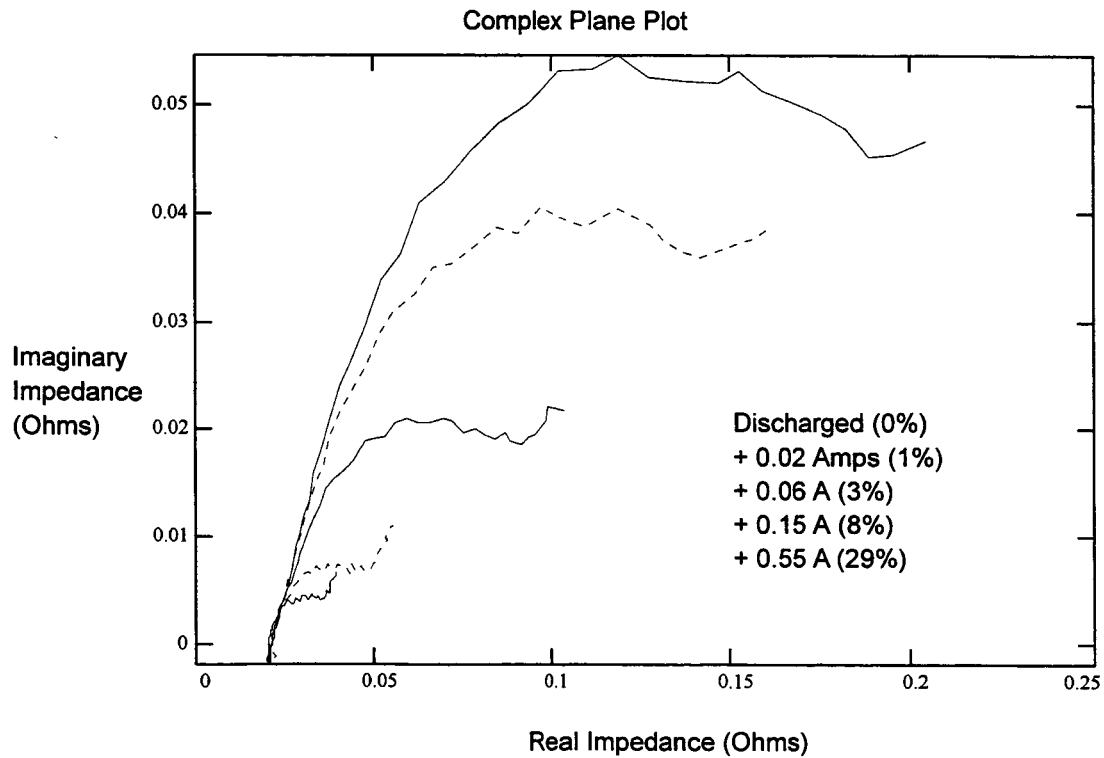


Figure 1. Ni/MH cells near full discharge. A) Bode Magnitude plot of total impedance. B) Bode Angle plot. C) Complex Plane plot; imaginary impedance versus real impedance.

The figures show a significant change in the impedance spectra as the cell approaches complete discharge. The capacity of the cell studied was 1.88 Amp-hours, and the percent charge is given in parentheses with each figure (legends correlate top-to-bottom with the various curves).

From the data shown, one can obtain information about the various resistance and capacitance processes for the cell. An equivalent circuit model is required, and one must choose a model which is appropriate. These vary considerably, ranging from simple models which do not even separate the contributions at separate electrodes, to those which model each conceivable contribution. Because of our efforts to look at only one type of change at a time, we chose the most simple model, deducing the responsible chemical or physical parameter from there. This model is given below in Figure 2. R_u is the uncompensated bulk resistance (including any ohmic resistance contribution from the electrode connections), C_{dl} is the capacitance of the double layer, R_{ct} is the charge transfer resistance (includes any resistance at the interface of electrode and bulk), and Z_W is the Warburg impedance (diffusion-related).

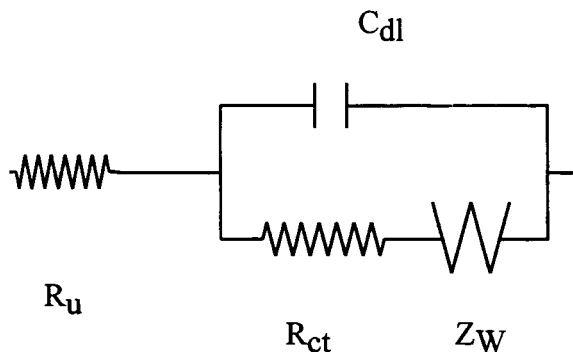


Figure 2. Circuit model used to determine chemical and physical parameters.

Analysis of the data show that the only significant trend is in the charge transfer resistance, R_{ct} . These data are given in Table 1, and the resistance values are graphed in Figure 2. The phenomena included in R_{ct} are electron transfer from the hydride to the electrode, charge transfer from the electrode to the hydroxide, and chemical reaction of hydrogen ion and hydroxide ion. Of these phenomena, the only one that actually is different near the discharge end must be the chemical reaction, analogous to a limiting reactant in chemistry. If the surface hydride is being depleted as the cell discharges, this would present a resistance to the cell, shown in the charge-transfer resistance. This effect is clear in the data presented by a previous author, but it is not discussed nor is any indication of its cause given.²

A second phenomenon observed was the change in impedance spectrum as the cell was cycled. A new battery cell yields different impedance spectra than a cell which has undergone charge and discharge cycles. The appearance of the spectra is similar, but they are offset by a factor. The resulting values of R_u , R_{ct} , and C_{dl} show the same trend in the charge-transfer resistance, but also show that the ohmic resistance, R_u , is changed. This value decreases as the

cell is moved through these "wake-up" cycles. The average value of R_{U} for new cells (not previously cycled) is approximately 0.13 ohms, while the resistance drops to 0.02 ohms for a cell which has been cycled. This could be due to several phenomena, including a change in the porosity of the electrode surface, a decrease in some passivation layer, or other processes unknown to us.

CHANGES NEAR COMPLETE DISCHARGE

Charge (Amp-hrs)	Cell Potential (Volts)	Capacitance (Farads)	Warburg Impedance (slope)	Resistance -- ohmic (Ohms)	Resistance -- chrg trnsfr (Ohms)
0.000	1.206	6.27	0.73	0.0215	0.1750
0.020	1.225	5.22	1.26	0.0218	0.1330
0.060	1.254	5.54	1.03	0.0215	0.0768
0.147	1.290	4.36	0.67	0.0207	0.0290
0.551	1.349	7.29	0.70	0.0202	0.0136
1.172	1.389	9.31	0.81	0.0202	0.0107
1.773	1.420	10.10	1.06	0.0204	0.0125

Table 1

This work shows that some chemical and physical parameters can be determined by the use of EIS. It is also clear, however, that more control of the chemical and physical processes is needed and that components of various composition are needed to separately determine the influence of changes in these processes and components. Others who have attempted to model such cells through the use of components with varying composition, have had some success, but have limited themselves to studies of single electrodes which are not part of working cells.³

This EIS technique is powerful in resolving the chemical and physical processes at work in an electrochemical system, but is likely to be limited to systems with a relatively small number of such processes.

¹Gates Aerospace Industries, "Nickel Metal Hydride Battery Product Information", 1992.

²M. A. Reid, *Electrochimica Acta*, **38**(14), 2037-2041.

³N. Kuriyama, T. Sakai, H. Miyamura, I. Uehara, H. Ishikawa, and T. Iwasaki, *J. Electrochem. Soc.*, **139** (7), L72-L73.

112571

352829

N95-18986

1994

NASA/ASEE SUMMER FACULTY FELLOWSHIP PROGRAM

**MARSHALL SPACE FLIGHT CENTER
THE UNIVERSITY OF ALABAMA**

519-82
30909
p.6

**A HYPERTEXT-BASED INTERNET-ASSESSABLE DATABASE
FOR THE MSFC TECHNOLOGY TRANSFER OFFICE**

Prepared By: Jeff Jackson, Ph.D.
Academic Rank: Assistant Professor
Institution and Department: The University of Alabama
Department of Electrical Engineering

NASA/MSFC:

Laboratory: Technology Transfer Office

MSFC Colleagues: Harry Craft
Gabe Wallace, Ph.D.

INTRODUCTION

There exists a continuing need to disseminate technical information and facilities capabilities from NASA field centers in an effort to promote the successful transfer of technologies developed with public funds to the private sector. As technology transfer is a stated NASA mission, there exists a critical need for NASA centers to document technology capabilities and disseminate this information on as wide a basis as possible. Certainly local and regional dissemination is critical, but global dissemination of scientific and engineering facilities and capabilities gives NASA centers the ability to contribute to technology transfer on a much broader scale. Additionally, information should be disseminated in a complete and rapidly available form.

To accomplish this information dissemination, the unique capabilities of the Internet are being exploited. The internet allows wide scale information distribution in a rapid fashion to aid in the accomplishment of technology transfer goals established by the NASA/MSFC Technology Transfer Office. Rapid information retrieval, coupled with appropriate electronic feedback, allows the scientific and technical capabilities of Marshall Space Flight Center, often unique in the world, to be explored by a large number of potential benefactors of NASA (or NASA-derived) technologies. Electronic feedback, coupled with personal contact with the MSFC Technology Transfer Office personnel, allows rapid responses to technical requests from industry and academic personnel as well as private citizens.

The remainder of this report gives a brief overview of the Mosaic software and a discussion of technology transfer office and laboratory facilities data that has been made available on the Internet to promote technology transfer.

Introduction To Mosaic

MOSAIC is a distributed hypermedia system, available on most all modern computing platforms, which has been designed to allow information access over the Internet. This information may currently take the form of text data, images, animations, database queries, etc. In this sense, the system may be viewed as a Internet-based multimedia system. MOSAIC provides a unified interface to various network protocols, data formats, and information archives available on the Internet. The unified interface allows even novice computer users to effectively browse the internet, through hypertext sensitive documents, to discover, use, and share information.

Data sent from Internet servers to clients (in most cases a PC, Macintosh, or workstation running MOSAIC) are termed documents. Documents may contain plain text, inlined graphics, sound, other multimedia data, or hyperlinks to other documents. These documents may be located anywhere on the Internet. In MOSAIC, a hyperlink typically takes the form of an underlined phrase or a highlighted graphic. These hyperlinks, when clicked on with a mouse, causes the client to connect to a specified document, located anywhere on the Internet, and to retrieve and display the referenced document.

Initial implementations of MOSAIC include functionality for display of plain text, formatted text and hypertext, inlined graphics, audio clips, and animation sequences. A graphical user interface includes numerous point-and-click style operations for document manipulation, editing, and network traversal. In addition to the native HTTP protocol support, MOSAIC provides protocol interfaces for common TCP/IP communication including FTP, NNTP, Gopher, Archie, X.500, and WAIS data sources. This functionality establishes MOSAIC as a powerful Internet browsing tool. An attractive feature of MOSAIC is that it is free and publicly available and distributable. MOSAIC is available via anonymous ftp from <ftp.ncsa.uiuc.edu>.

Technology Transfer Data

The data included in the database from the Technology Transfer Office includes an overview of the office, a description of the mission of the office, and ways to work with the office. Specifically, the database describes memoranda of understanding with numerous regional states, industrial visits by MSFC technology transfer personnel, and site visits of Marshall Space Flight Center. Also included is data describing the patent licensing process and example technology transfer "success stories" from MSFC. A snapshot of a portion of the technology transfer "home page" is shown in Figure 1.

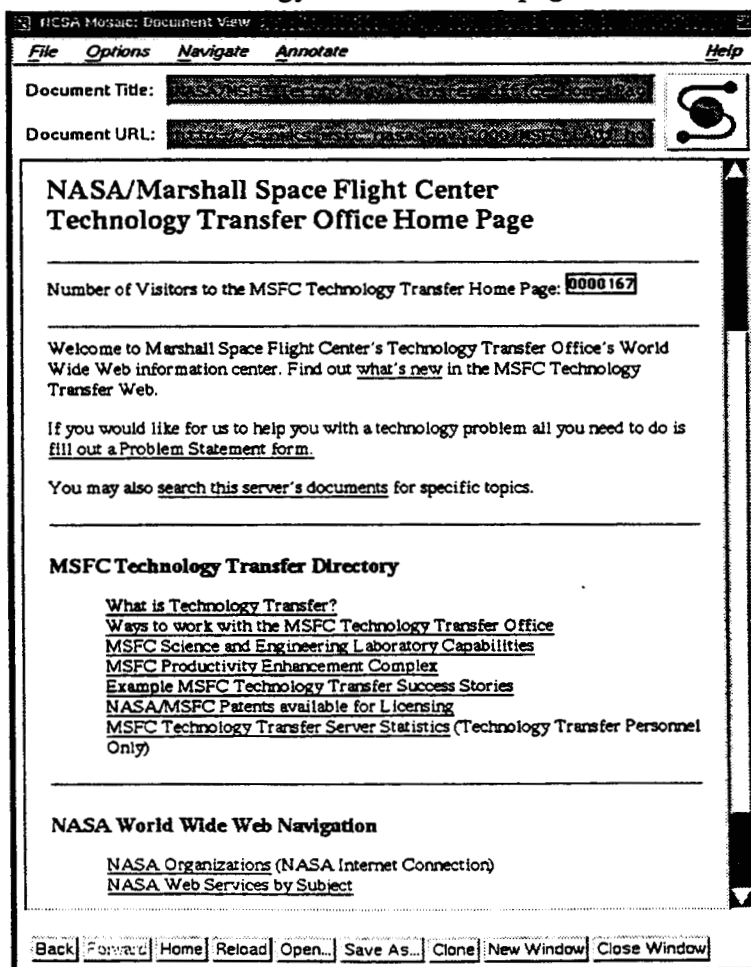


Figure 1. NASA/MSFC Technology Transfer Office Mosaic Home Page.

MSFC Science and Engineering Laboratory Capabilities

An overview of major science and engineering and laboratory capabilities available at MSFC is also included in the database. These laboratories include: Astrionics, Propulsion, Space science, Structures & Dynamics, Materials & Processes, Mission Operations, and Systems Analysis & Integration. The database describes primary missions for each lab, areas of current research, and example technology capabilities. Included in the database are images representative of ongoing developments in the laboratories. A snapshot of the MOSAIC screen for the Solid Propulsion Test Assembly, as a part of the Propulsion Lab, is shown in Figure 2.

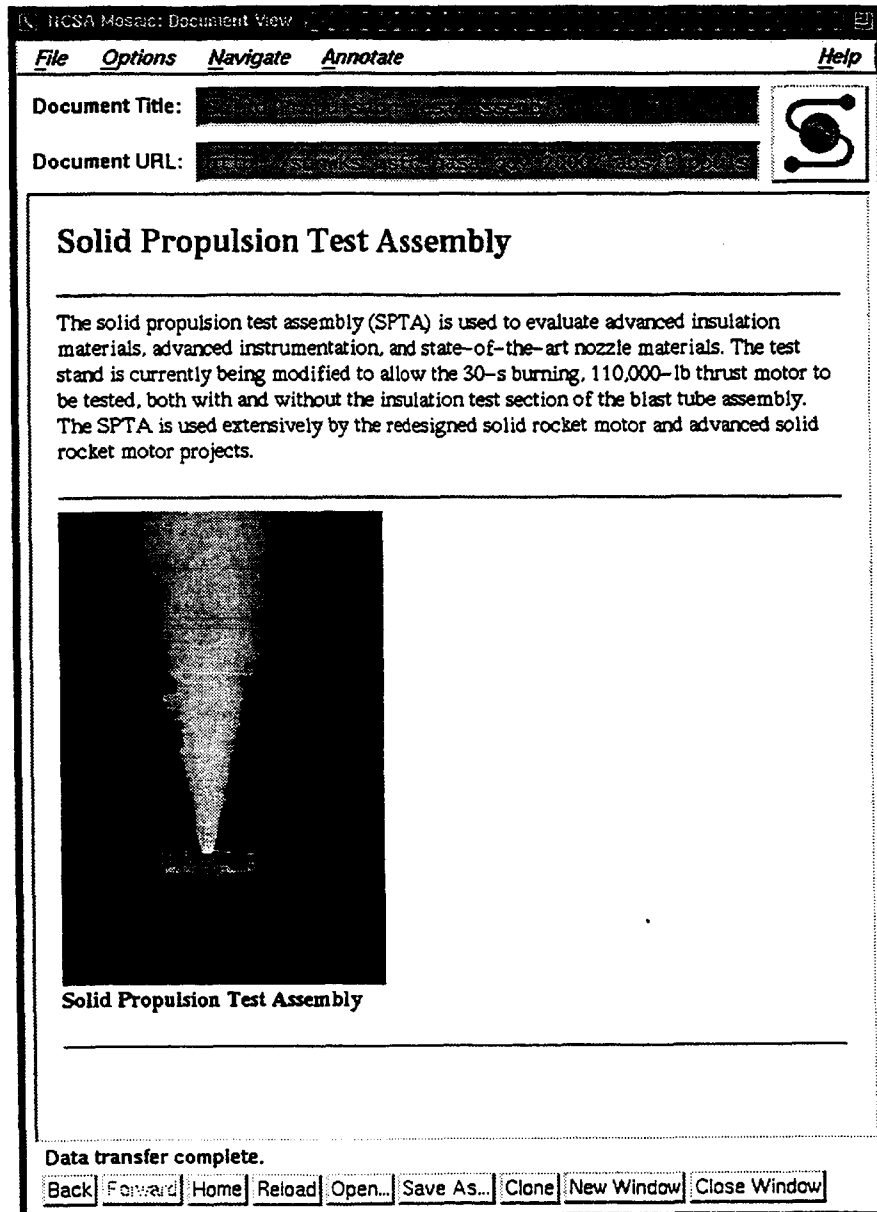


Figure 2. MOSAIC Screen Snapshot of the Solid Propulsion Test Assembly.

The Productivity Enhancement Complex

The unique capabilities of the Productivity Enhancement Complex are also described in the developed database. These capabilities include research, facilities, and MSFC personnel with technical capabilities in the fields of Coatings, Composites, Metals Processing, Robotics, Testing & Evaluation procedures, Insulations, and Engineering Support. One example technology described in the Metals Processing field is the Variable Polarity Plasma Arc Welding process. The database "page" for this technology is shown in Figure 3.

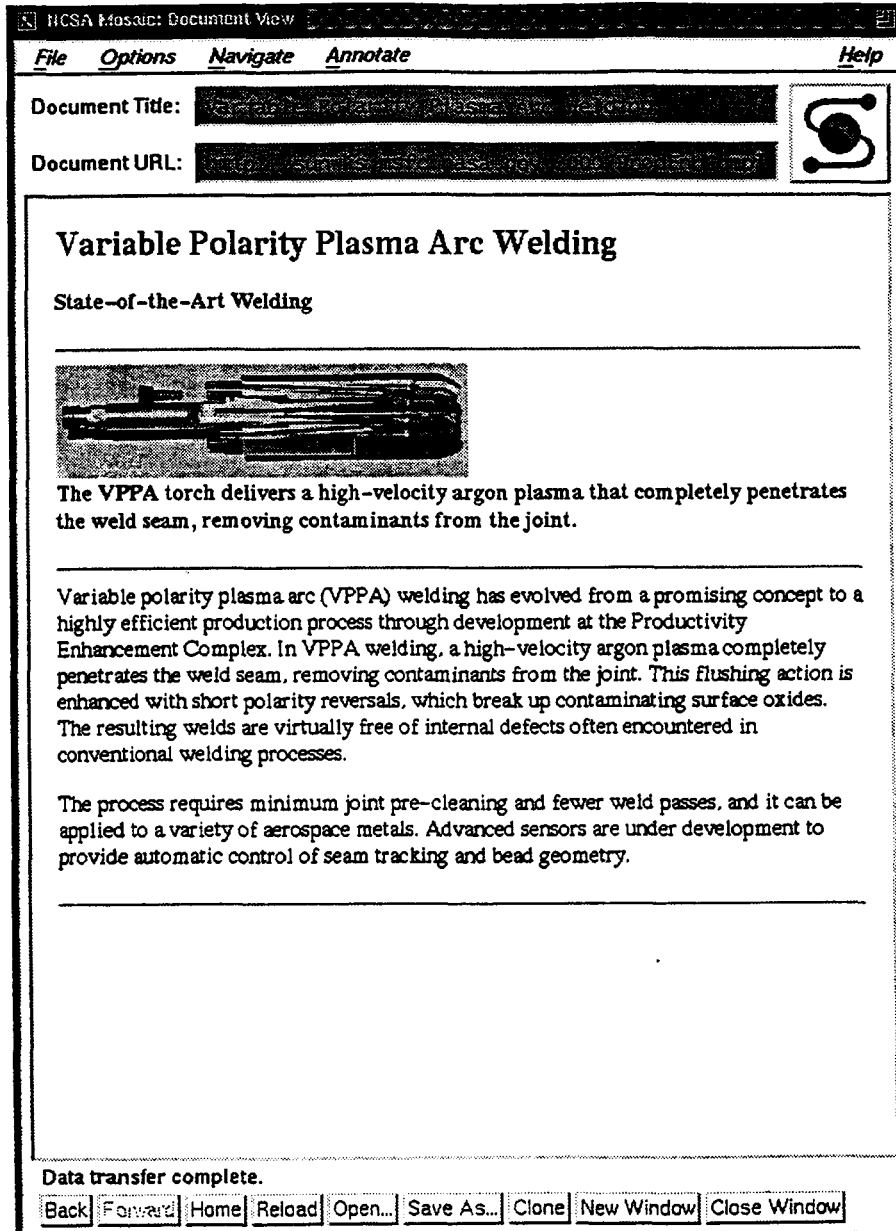


Figure 3. MOSAIC Screen Snapshot of the VPPA Welding Process.

The portion of the database describing the Productivity Enhancement Complex (PEC) contains a description of the 30 research cells including images of research equipment, facility operation, and a description of typical research investigations conducted by PEC personnel.

Additional Database Capabilities

An addition to previously mentioned data content and database capabilities, the database also provides interactive feedback between the user, a potential benefactor of MSFC technology, in the form of an electronic problem statement form. This form, when filled in by the user through the MOSAIC software, may be electronically submitted the MSFC Technology Transfer personnel. The data is transparently converted to the form of an email submission.

The database also supports a search query of all "pages" within the database based on a user specified search term. The database returns a list of documents, in a hyperlink format, that match the keyword specified. This feature allows the potential user to quickly locate information about specific technologies of interest.

Finally, the database supports the generation of access statistics reports to allow MSFC Technology Transfer Office personnel to establish metrics concerning use of the database thereby measuring its potential as a technology transfer tool.

Conclusions and Future Research

The Internet, and particularly the MOSAIC browser, offers a new source for information dissemination, a vital component of the technology transfer process. Rapid availability and wide, spread access are significant advantages to describing the technology transfer process, facilities, and capabilities in this database form. Continuing developments include enhancement and expansion of the existing database, inclusion of additional scripts for generating metrics data, and an expansion of this form of information dissemination to a full scale multimedia demonstration of MSFC technologies and capabilities. This format would be particularly effective for field demonstrations of MSFC technologies by Technology Transfer personnel.

Bibliography

1. *MSFC Laboratory Capabilities*, George C Marshall Space Flight Center, NASA.
2. *Technology in Action*, MSFC Technology Utilization Office, 1992 Annual Report.
3. *Focus on the Future*, NASA/MSFC, Materials and Processes Laboratory, Technology Utilization Office.
4. Andreessen, M., "Getting Started with NCSA Mosaic," NCSA Technical Report, May 8, 1993.
5. Andreessen, M., "NCSA Mosaic Technical Summary," NCSA Technical Report, May 8, 1993.

112572

352834
N95-18987

1994

30910
P. 6

NASA/ASEE SUMMER FACULTY FELLOWSHIP PROGRAM

**MARSHALL SPACE FLIGHT CENTER
THE UNIVERSITY OF ALABAMA**

**A PRELIMINARY ANALYSIS OF LOW FREQUENCY
PRESSURE OSCILLATIONS IN HYBRID ROCKET MOTORS**

Prepared By: Rhonald M. Jenkins, Ph.D.
Academic Rank: Associate Professor
Institution and Department: Auburn University
Department of Aerospace Engineering

NASA/MSFC

Laboratory: Propulsion
Division: Motor Systems
Branch: Solid Motor Design

MSFC Colleague: Jerry R. Cook

INTRODUCTION

Past research with hybrid rockets has suggested that certain motor operating conditions are conducive to the formation of pressure oscillations, or flow instabilities, within the motor combustion chamber. These combustion-related vibrations or pressure oscillations may be encountered in virtually any type of rocket motor and typically fall into three frequency ranges: low frequency oscillations (0-400 Hz); intermediate frequency oscillations (400-1000 Hz); and high frequency oscillations (> 1000 Hz)¹. In general, combustion instability is characterized by organized pressure oscillations occurring at well-defined intervals with pressure peaks that may maintain themselves, grow, or die out. Usually, such peaks exceed $\pm 5\%$ of the mean chamber pressure.

For hybrid motors, these oscillations have been observed to grow to a limiting amplitude which may be dependent on factors such as fuel characteristics, oxidizer injector characteristics, average chamber pressure, oxidizer mass flux, combustion chamber characteristic length L^* , and grain geometry¹. Mechanisms which have been postulated as causes of instability in hybrid motors include

Instabilities associated with the time lag of vaporization and combustion of liquid droplets^{2,3}. Inadequate droplet atomization and vaporization, as well as inadequate vaporization chamber residence time, are regarded as primary contributing factors. These are, in turn, influenced by factors such as droplet size and initial injection velocity i.e., injector design, and vaporization chamber geometry (e.g., volume, the use of splashblocks, etc.). This type of instability is characterized by low frequency pressure oscillations (5-10 Hz) and it operates generally in the low oxidizer mass flow - low chamber pressure regime⁴.

Instabilities associated with periodic accumulation and break-off of melted layers or char layers from the burning propellant surface². Propellant formulation and thermal response time are believed to be primary contributing factors. This type of instability is characterized by low frequency pressure oscillations (1-100 Hz) and occurs with low regression rate motor operation⁴.

Instabilities associated with some boundary layer mechanism which couples the combustion response (regression rate) to externally imposed pressure oscillations². These instabilities occur in low total mass flux regimes (where radiation is the dominant heat transfer mechanism) and in high total mass flux and/or low chamber pressure regimes (where finite-rate reaction kinetics becomes important)⁵.

Instabilities associated with low impedance LOX feed system design, wherein chamber pressure fluctuations result in LOX flow fluctuations. Generally, it is believed that fluctuations in LOX flow rate may enhance chamber pressure oscillations, but do not initiate them³.

Instabilities associated with shear layer/acoustic interactions in either the vaporization chamber or the aft-end mixing chamber of the motor⁶.

Instabilities associated with the (possibly) time-dependent nature of the boundary layer leading edge position (flameholder effects)⁷.

PRELIMINARY INSTABILITY ANALYSIS

Low frequency, or so-called "non-acoustic" instabilities have been observed in a number of hybrid motor tests^{2,3,6,8,9,10}. As the name implies, hybrid motors share common characteristics with both liquid propellant and solid propellant rocket motors. On the other hand, hybrids possess certain unique characteristics. For instance, the ability to throttle hybrids over a wide range

of operating conditions, coupled with time-varying internal geometry (fuel grain configuration), increases the probability of encountering conditions favorable to the onset of instability⁷. In solid propellant motors the combustion process is assumed to be localized in a zone close to the propellant surface. The combustion is then treated as a boundary condition for the fluid dynamics problem, greatly simplifying a stability analysis by isolating chemical reactions from the cavity analysis. The combustion dynamics problem is then defined as the response of a thin combustion zone at the cavity wall to an imposed flow environment. In liquid propellant motors, on the other hand, the flow and combustion problems are coupled throughout the entire volume of the combustor.

Hybrid motor combustion typically occurs in a thin flame sheet located within a boundary layer located near the surface of the fuel grain. Fuel is partly decomposed and gasified at the solid surface by heat transfer and diffuses outward towards the flame zone. At the same time, oxidizer diffuses inward towards the flame zone through the boundary layer. At a point where the oxidizer-to-fuel concentration (O/F ratio) is slightly on the fuel-rich side of stoichiometric, combustion occurs in a zone whose thickness is about 10% of the boundary layer thickness. Some hybrid motors also inject oxidizer into a cavity located downstream of the solid fuel grain, so that a secondary combustion process occurs in this region. Hybrid motors can then be expected to exhibit the combustion characteristics of both solid and liquid rocket motors.

Hybrid Motor L* Instability Analysis

The approach taken in the present analysis is to develop a modified L* instability theory which accounts for the relationship between pressure and O/F ratio in the motor. The analysis proceeds along the lines of that first suggested by Beckstead and Price¹¹ for solid propellant motors, with the following simplifying assumptions:

- The combustion process is assumed to be localized in a zone close to the propellant surface.
- The analysis is for one-dimensional flow of a calorically perfect gas. Temperature, molecular weight, and pressure are spacially uniform throughout the combustion volume. Molecular weight is either not oscillating or has a large oscillation period relative to the flow residence time (quasisteady).
- The nozzle discharge is quasisteady, with inlet stagnation conditions approximated by static conditions.
- All flow variables (except the oxidizer mass flow rate) can be expressed as the sum of a mean (constant) term and a time-dependent term
- The oxidizer mass flow is constant.

The continuity equation applied to the thrust chamber takes the form

$$\frac{\tau_c}{n} \frac{d(\bar{p})}{dt} + \frac{\bar{p}}{P} = \frac{1}{1+\bar{\alpha}} + \frac{\bar{\alpha}}{1+\bar{\alpha}} \frac{\alpha}{\bar{\alpha}} \quad (1)$$

where p is pressure, t is time, $(-)$ denotes a mean value, τ_c is the so-called motor fill (or flush) time, defined as

$$\tau_c = \frac{L^* c^*}{RT} \quad (2)$$

and

$$\alpha = \frac{\dot{m}_f}{\dot{m}_o} \quad (3)$$

is the inverse of the O/F ratio, and $n = 1$ or γ depending on whether the core flow is considered to be isothermal or isentropic. In the limit $\bar{\alpha} \rightarrow \infty$, Eq.(1) degenerates to the solid rocket motor relations of Reference 11. Now let

$$\frac{p}{\bar{p}} = 1 + \frac{p_o}{\bar{p}} e^{\beta t} \cos(\beta t) \quad (4)$$

$$\frac{\alpha}{\bar{\alpha}} = 1 + \frac{\alpha_o}{\bar{\alpha}} e^{\beta t} \cos(\omega t + \tau) \quad (5)$$

where β is a growth rate constant for oscillations and τ is the lead time of the fuel-oxidizer ratio relative to the pressure. One can define a response function Ψ as

$$\Psi = \frac{\frac{\alpha_o}{\bar{\alpha}}}{\frac{p_o}{\bar{p}}} \quad (6)$$

where α_o and p_o are oscillation amplitudes of the fuel-oxidizer ratio and pressure at some (arbitrary) time t , respectively. Combining Eqs.(1)-(5) and solving yields two conditions (expressed in terms of O/F ratio):

$$\Psi \frac{1}{1+O/F} \cos(\omega\tau) = 1 + \beta \frac{\tau_c}{n} \quad (7)$$

$$\Psi \frac{1}{1+O/F} \sin(\omega\tau) = \omega \frac{\tau}{n} \left(\frac{\tau_c}{\tau} \right) \quad (8)$$

Equations (7) and (8) represent a set of 1-D stability oscillator equations for hybrid rocket motors. As such, they describe the dynamic behavior of a hybrid motor in terms of the oscillation variables (ω, β) as functions of the combustion dynamics (\bar{Y}, τ) , the mean O/F ratio (O/F) , and the motor fill time (τ_c) . The motor fill time is, in turn, dependent on L^* .

Stability Trends

If one considers the interval $-\pi < \omega\tau < \pi$ for the combustion (i.e., fuel-oxidizer ratio) phase angle, one can quickly show that

$$\tau > 0$$

(9)

i.e., combustion oscillations lead pressure oscillations for all values of $\overline{O/F}$, for either isothermal or isentropic core flow. Considering that the stability limit is defined by the condition $\beta = 0$, one can show that the oscillator equations impose a minimum value constraint on the response function Ψ , and that this value is a function of the (mean) motor O/F ratio. This constraint is simply stated as

$$\Psi_o \geq 1 + \overline{O/F} \quad (10)$$

where the subscript "o" denotes conditions at the motor stability limit. Thus, a hybrid propellant motor can be treated (from the standpoint of 1-D L stability) as a solid propellant motor with the response function modified to account for O/F ratio. Finally, the expected pressure oscillation frequency can be estimated as

$$f = \frac{n}{2\pi\tau_c} \arccos\left(\frac{1}{\Psi_o}\right) = f(\tau_c, \overline{O/F}) \quad (11)$$

so that the expected oscillation frequency depends directly on the system fill time τ_c (or L^*) and the average O/F ratio.

Sample Results

Guthrie and Wolf³ reported non-acoustic instabilities in a series of motors, ranging in size from 10,000 lbs thrust to 75,000 lbs thrust, which had been developed and tested by the American Rocket Company (AMROC). They then applied solid rocket motor instability theory and compared its predictions with their experimental data. In their work, they attempted to correlate data from "several solid fuels", and concluded that $\Psi = 1.3$. According to Eq.(10) of the hybrid motor theory developed here, the correct value is $\Psi_o = 3.09$ (i.e., $\overline{O/F} \sim 2.09$). A comparison of predicted vs. observed oscillation frequencies is shown in Figure 1. Predicted frequencies are obtained using values of combustor fill time reported in Reference 3. It can be seen that the hybrid motor theory provides excellent agreement with the observed values of oscillation frequency.

SUMMARY AND CONCLUSIONS

The hybrid stability theory presented here is a 1-D model derived along the same lines as for solid rocket motors, with account taken for a separate oxidizer mass flow. It represents a first step towards the understanding of non-acoustic oscillations in hybrid rocket motors. Since it is fundamental in nature, it necessarily employs a number of simplifying assumptions which restrict the applicability and adaptability of the model in more complex situations, and limit the type of information which the model can provide. Based upon the limited data presented here, the model can predict, to a reasonable degree, the frequency of non-acoustic oscillations in simple hybrid motor systems. It must be noted that the present theory cannot predict whether or not a given system will oscillate, nor can it suggest what measures should be undertaken to reduce or eliminate oscillations.

Calculated vs. Observed³ Instability Behavior
American Rocket Company Motors

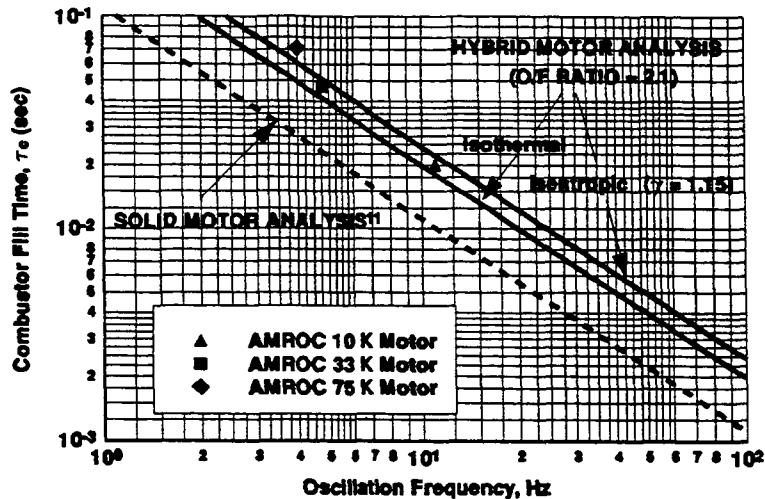


Fig. 1: Predicted vs. Observed Oscillation Frequency, AMROC Motors

REFERENCES

- ¹G.P. Sutton, Rocket Propulsion Elements, 6th ed., Wiley and Sons, Inc., 1992.
- ²C.E. Wooldridge and G.A. Markman, "Combustion Instability and the Role of Chemical Kinetics in Hybrid Combustion," AIAA Paper No. 68-498, June 1968.
- ³D.M. Guthrie and R.S. Wolf, "Non-Acoustic Combustion Instability in Hybrid Rocket Motors," Report by American Rocket Company, Camarillo, CA, 1990.
- ⁴A.M. Helmy, "Chronicle Review of the Hybrid Rocket Combustion," AIAA Paper No. 94-2881, June 1994.
- ⁵R.J. Muzzy, "Applied Hybrid Combustion Theory," AIAA Paper No. 72-1143, Nov. 1972.
- ⁶B. Greiner and R.A. Frederick, Jr., "Experimental Investigation of Labscale Hybrid Instability," AIAA Paper No. 94-2878, June 1994.
- ⁷Personal Communication, Dr. Ronn Carpenter, Thiokol Corporation, June 1994.
- ⁸L.D. Strand, M.D. Jones, and R.L. Ray, "Characterization of Hybrid Rocket Internal Heat Flux and HTPB Fuel Pyrolysis," AIAA Paper No. 94-2876, 1994.
- ⁹B. Goldberg and J. Cook, "Preliminary Results of NASA/Industry Hybrid Propulsion Program," AIAA Paper No. 92-3299, 1992.
- ¹⁰M.H. Lee, C.F. Schafer, G.A. Robertson, D. Straub, R.H. Eskridge, and C.C. Dobson, "Pressure Oscillations in a Laboratory Scale Hybrid Motor," Conference on Advanced Earth-to-Orbit Propulsion Technology, NASA Marshall Space Flight Center, Huntsville, AL, 1994.
- ¹¹M.W. Beckstead and E.W. Price, "Nonacoustic Combustor Instability," AIAA Journal, Vol. 5, No. 11, Nov. 1967.

110573

300887

N95-18988

1994

NASA/ASEE SUMMER FACULTY FELLOWSHIP PROGRAM

**MARSHALL SPACE FLIGHT CENTER
THE UNIVERSITY OF ALABAMA**

521-20
30911
p. 6

**DEVELOPMENT OF CFD MODEL FOR AUGMENTED CORE
TRIPROPELLANT ROCKET ENGINE**

Prepared By: Kenneth M, Jones, Ph.D.
Academic Rank: Assistant Professor
Institution and Department: North Carolina A&T State University
Department of Mechanical Engineering

NASA/MSFC:

Laboratory: Structures and Dynamics
Division: Fluid Dynamics
Branch: Computational Fluid Dynamics

MSFC Colleagues: Paul K. McConnaughey, Ph.D.
Joseph H. Ruf

INTRODUCTION

Many experts feel that the future of mankind depends on the economic accessibility to and effective use of space. Regardless of the approach taken, all human explorations will require delivery of substantial mass (personnel and equipment) to a low earth orbit. Therefore, it will be imperative that a dependable, affordable propulsion system be developed that will allow the economical exploitation of space to proceed in a rapid and orderly manner. The new propulsion systems will require the use of our best technologies, avoid immature or marginal designs, and a streamlined program that will bring rocket propulsion to the maturity of jet propulsion [1,2].

Early rocket pioneers recognized that the ultimate earth to orbit launch vehicle would consist of only a single stage, which discarded only propellants. Ideally, the launch vehicle would be all propellant; the airframe, tankage and subsystems would weigh almost nothing. As early as 1971, the mixed mode principle was suggested as a means of achieving single stage-to-orbit (SSTO) [1]. This principle involves the use of a dense propellant combination at liftoff, followed by a less dense, but higher performing combination at altitude. The benefit of the mixed mode system is that about 50 percent of the propellant would be spent in achieving 15 percent of the orbital velocity. When a high density propellant combination is used in the initial phase of flight, the resultant vehicle size and dry mass is less for a fixed payload mass. However, at this point in time the technology base for propellants or engines had not advanced to the point of achieving SSTO.

The Space Shuttle era has made major advances in technology and vehicle design to the point that the concept of a single-stage-to-orbit (SSTO) vehicle appears more feasible. In fact the recent NASA study "Access to Space" supports the concept that SSTO rockets could be demonstrated in the near term [3]. NASA presently is conducting studies into the feasibility of certain advanced concept rocket engines that could be utilized in a SSTO vehicle. One such concept is a tripropellant system which burns kerosene and hydrogen initially and at altitude switches to hydrogen. This system will attain a larger mass fraction because LOX- kerosene engines have a greater average propellant density and greater thrust-to-weight ratio.

This report describes the investigation to model the tripropellant augmented core engine. The following sections will discuss the physical aspects of the engine, the CFD code employed and results of the numerical model for a single modular thruster.

PHYSICAL AND NUMERICAL MODEL

The tripropellant engine is composed of a main H_2/O_2 engine with smaller RP_1/O_2 thrusters arranged around the base of the main engine. An extended nozzle encloses the thrusters and main engine to form an bell/annular engine as seen in Figure 1.

The physical arrangement of the engine dictates the modeling process. Since the engine components are symmetric about the centerline of the main H_2/O_2 engine, the numerical model can treat the physical problem as axisymmetric. This means only one thruster will have to be modeled. Therefore, the engine can be modeled as three different problems: (1) thruster, (2) main engine and (3) combined exhaust nozzle. The solutions for the thruster and the main engine will

be totally independent; however, the numerical model for the combined exhaust nozzle will require the converged solutions of the other two regions to start its solution process.

The numerical model has to be more than just a flow solver. The model will require that a chemistry model be incorporated to simulate the combustion process. A turbulence model will also be required to simulate the boundary layer at the walls as well as the shear layer that will be formed in the combined exhaust nozzle. In addition, a computational mesh must be generated such that the grid points are clustered in regions that will capture flow disturbances and form a well defined boundary layer.

NUMERICAL METHOD

The computational fluid dynamics (CFD) code GASP version 2.3 was used to model the Tripropellant Augmented Core Engine. The code solves the integral form of the time-dependent, three-dimensional Reynolds-Averaged Navier-Stokes (RANS) equations and its subsets subject to boundary and initial conditions. The code is a cell-centered, finite volume formulation with upwind based spatial discretization. GASP employs both explicit and implicit time integration methods to obtain solutions. GASP is a fully conservative shock capturing CFD code. In addition, the code gives the user the option of selecting from several turbulence, thermodynamic and chemistry models. For the high Reynolds number option, the two-equation k-epsilon turbulence model uses wall functions instead of artificial damping terms.

The GASP software does not include a complete grid generation package. Therefore, the user is responsible for importing a grid suitable for use by GASP. For this investigation, the computational mesh was generated by the computer code GENIE ++, which is a grid generation system developed by Mississippi State University.

RESULTS

The initial phase of this study was concerned with learning GASP. This was accomplished by developing solutions for each section of the engine using a perfect gas model for air on an unrefined grid. This solution process was accomplished on a Convex computer. This procedure allowed the user to develop a feel for the sensitivity of the code to CFL, boundary conditions and other user specified parameters.

The modular thruster was modeled with the computational grid shown in Figure 2. The thruster could not be treated axisymmetrically, therefore the entire thruster had to be modeled. The total computational grid was 81 axial by 31 radial points. Hyperbolic tangent stretching was used to cluster grid point axially at the inlet plane, throat region and the exit plane. Hyperbolic tangent stretching was also employed to cluster points radially at the nozzle wall. A nine species chemistry model, "NASP3", was used to model the RP₁/O₂ combustion [5].

The solution was initialized by running the coarse grid (41 axial by 16 radial) for approximately 1000 iterations. Then the solution was converted to the fine grid. It was discovered that if one tried to switch a well converged solution to the fine grid, the code's grid sequencing option just "bogged down" and the code would stop.

The thruster solution was started using frozen flow with a laminar boundary layer. The residual for this solution was dropped three orders of magnitude. The laminar solution was then used to restart a new solution using a Baldwin-Lomax algebraic turbulence model. The residual for this case was again allowed to drop three orders of magnitude. The Baldwin-Lomax solution was then used to restart a new solution using the low Reynolds number, Lam-Bremhorst k-epsilon turbulence model. This solution converged for two orders of magnitude and then began to diverge very rapidly. The solution was stopped. The Baldwin-Lomax solution was then used to restart a new solution using the high Reynolds number k-epsilon model with wall functions. As with the low Reynolds case, the residual initially dropped. As the subsonic section cleared, the residual began to oscillate every other iteration by three order of magnitude while continuing to drop.

The k-epsilon turbulence model is known to be difficult to initialize. But this does not appear to be the reason for the solution to go unsteady. An investigation of the grid points near the wall showed that the Y^+ was in the appropriate range for both cases. One possible explanation could be the thruster's geometry. The thruster's throat is skewed and the flow has to make an abrupt turn into the diverging section of the nozzle. Snapshots of the flow at different iterations indicate that this region could be causing disturbances as the flow tries to expand. Thus, causing the solution with the k-epsilon model to become unsteady.

Finally, the Baldwin-Lomax solution was used to restart the finite rate chemistry solution. This residual for this solution was dropped seven orders of magnitude. A Mach contour for this case is given in Figure 3. This solution process was carried out on a CRAY YMP computer.

CONCLUSIONS / FUTURE WORK

A CFD model for the modular thruster has been developed using GASP. The model incorporates the thermodynamics, turbulence and chemistry required to simulate the RP_1/O_2 combustion process. Initial results indicate that model can be used to analyze thruster contours and operating conditions. This model can now be extended to the main engine and combined exhaust nozzle.

Future tasks should include: 1) Modify thruster grid and determine if the grid spacing near the wall is the cause of the turbulence model going unsteady. 2) Using results of thruster grid investigation, modify main nozzle grid and develop solution. 3) Develop solution for the combined exhaust nozzle. 4) Investigate the slipstream formed in the combined exhaust nozzle and determine if it affects the engine's performance like that reported in Reference 6. 5) Finally, investigate the "engine out problem" when the modular thruster are shutdown at altitude.

REFERENCES

1. Beichel, R., O'Brien, C.J. and Taylor, J.P., *The Next Generation Rocket Engines*, IAF-88-229, October, 1988.

2. Beichel, R., O'Brien, C.J. and Taylor, J.P., *Is There a Future in Liquid Rocket Propulsion*, AIAA Paper No. 91-2049, June, 1991.
3. Bekey, I., *SSTO Rocket: A Practical Possibility*, Aerospace America, July, 1994.
4. McGrory, W.D., Slack, D.C., Applebaum, M.P. and Walters, R.W., *GASP Version 2.2 User's Manual*, AeroSoft, Inc., 1993.
5. Langley Committee, *Hypersonic Combustion Kinetics*, NASP TM 1107, May, 1990.
6. Sutor, A.T., *Rocket Engine Nozzle Compendium*, Rocketdyne Report No. RI/RD85-222, August, 1985.

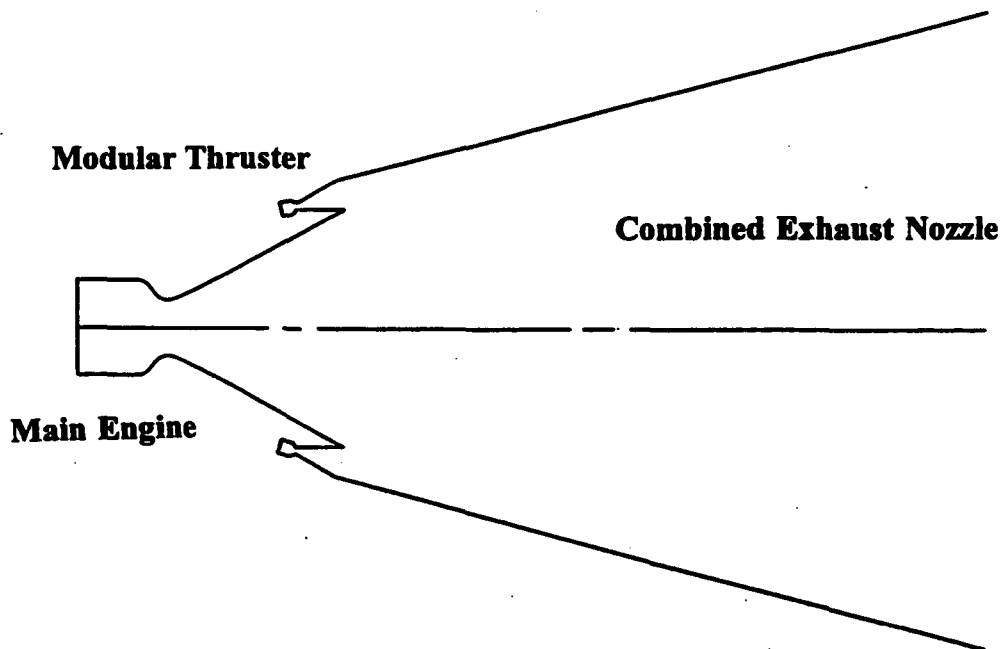


Figure 1: Layout of Augmented Core Engine

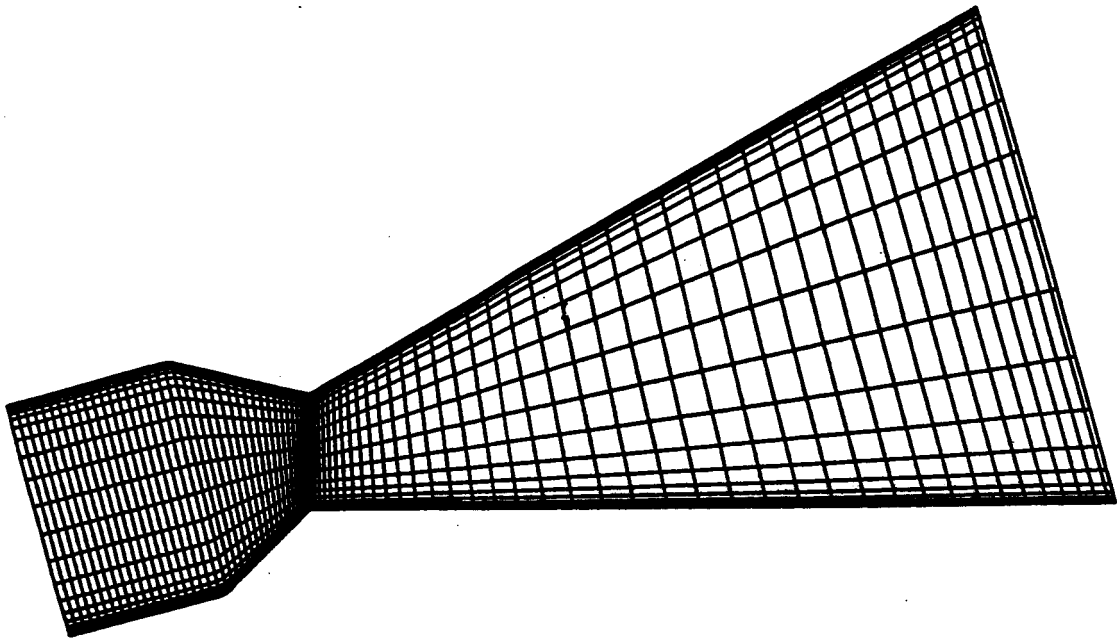


Figure 2: Computational Grid for Modular Thruster

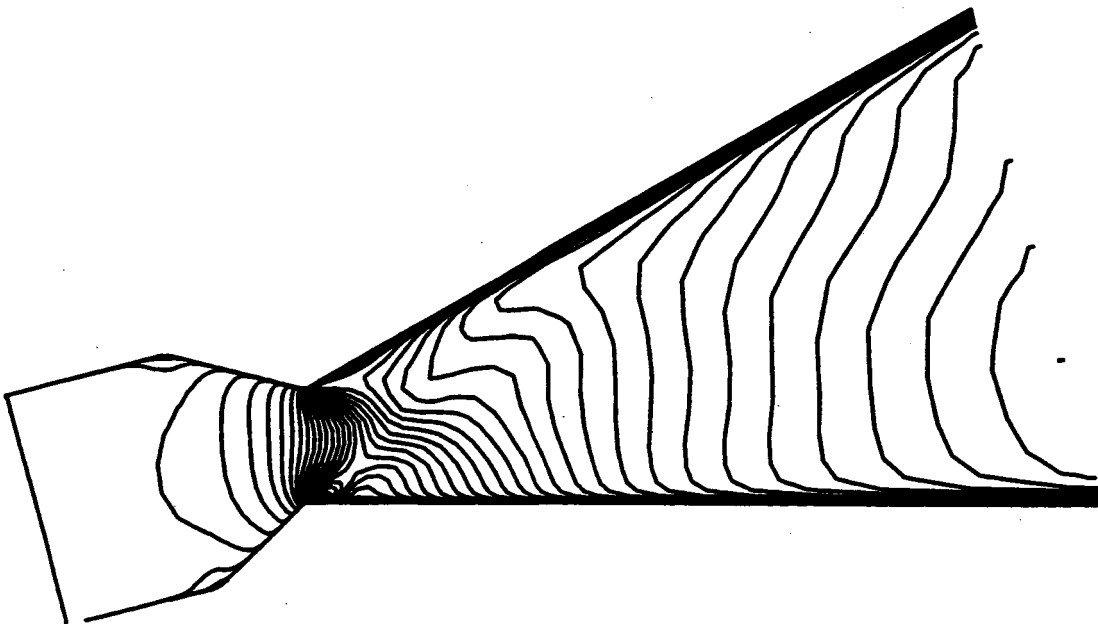


Figure 3: Mach Contours for Thruster with Turbulence and Finite-rate Chemistry

112574

352838

N95-18989

1994

NASA/ASEE SUMMER FACULTY FELLOWSHIP PROGRAM

**MARSHALL SPACE FLIGHT CENTER
THE UNIVERSITY OF ALABAMA**

COMPUTATIONAL SIMULATION OF LIQUID FUEL ROCKET INJECTORS

Prepared By:

D. Brian Landrum, Ph.D.

S22.20

Academic Rank:

Assistant Professor

30912

p. 6

Institution and
Department:

The University of Alabama in Huntsville
Department of Mechanical and Aerospace Engineering

NASA/MSFC:

Laboratory:
Division:
Branch:

Structures and Dynamics
Fluid Dynamics
Computational Fluid Dynamics

MSFC Colleague:

Ten-See Wang, Ph.D.

COMPUTATIONAL SIMULATION OF LIQUID FUEL ROCKET INJECTORS

D. Brian Landrum, Ph.D.
Assistant Professor

Dept. of Mechanical and Aerospace Engineering
The University of Alabama in Huntsville

INTRODUCTION

Affordable, efficient access to space is a priority for NASA. As the primary NASA center for rocket system research, Marshall Space Flight Center (MSFC) maintains ongoing programs to improve the performance of existing systems, such as the Space Shuttle Main Engine (SSME), and to develop new systems, such as tripropellant engines currently proposed for Single-Stage-To-Orbit (SSTO) vehicles. To aid this mission, development of models to predict overall system performance and run-time anomalies are required. Due to the complexity of the fluid dynamic flow fields associated with liquid rockets, NASA has increasingly used Computational Fluid Dynamics (CFD) techniques and modeling tools.

A major component of any liquid propellant rocket is the propellant injection system. In the SSME preburner and main combustion chambers, liquid or gaseous hydrogen (LH_2/GH_2) fuel is coaxially injected with liquid oxygen (LOX). Issues of interest include the degree of liquid vaporization and its impact on the combustion process, the pressure and temperature fields in the combustion chamber, and the cooling of the injector face and chamber walls.

The Finite Difference Navier-Stokes (FDNS) code (1) is a primary computational tool used in the MSFC Computational Fluid Dynamics Branch. The branch has dedicated a significant amount of resources to development of this code for prediction of both liquid and solid fuel rocket performance. The FDNS code is currently being upgraded to include the capability to model liquid/gas multi-phase flows for fuel injection simulation. An important aspect of this effort is benchmarking the code capabilities to predict existing experimental injection data.

The objective of this MSFC/ASEE Summer Faculty Fellowship term was to evaluate the capabilities of the modified FDNS code to predict flow fields with liquid injection. Comparisons were made between code predictions and existing experimental data. Therefore, a significant portion of the effort included a search for appropriate validation data. Also, code simulation deficiencies were identified.

COMPUTATIONAL CODE

The FDNS code was developed for NASA by Engineering Sciences, Inc. A detailed description of the code is given in Reference 1. The code can model incompressible or compressible, 2-D planar, 2-D axisymmetric, or 3-D problems including real gas effects and chemical reactions. The FDNS code uses a pressure-based predictor/multi-corrector solution procedure which is suitable for all speeds. Several higher order upwind and central difference schemes can be employed for spatial discretization. A time-centered Crank-Nicholson time-marching scheme is used for the temporal discretization of time-accurate problems. Several turbulence models and finite rate chemistry models are also available.

FDNS was developed with the capability to model solid rocket combustion and the associated solid particulates (e.g., AL_2O_3) which are produced. The present method solves the particle

equations of motion and the particle energy equation in a Lagrangian framework. Particle groups are injected and then tracked through the flow field. Each group represents a number of "real" particles. The code is currently being upgraded to predict the transient injection of liquid particles. These modifications are described in the following injection modeling section.

LIQUID INJECTION MODELING

Liquid propellant rocket injection is a complex combination of physical processes including jet atomization, droplet breakup, evaporation and chemical reactions. The multi-phase nature of the constituents significantly increases the complexity. In order to make the injection problem numerically tractable, these physical processes are described by reasonably simple submodels (2).

A review of atomization modeling capabilities was presented by Liang, et al. (3). The modified FDNS code uses the Blob Atomization Model in which the liquid jet is represented by injected drops which are approximately the size of the injection port. Primary droplet breakup is modeled by Reitz's approximation of surface wave dispersion on a cylindrical surface. Breakup is a function of droplet aerodynamics and liquid surface tension and viscosity.

Another critical aspect of injection modeling is an accurate representation of the liquid/vapor interface. The FDNS code uses the Volume of Fluid (VOF) technique in which the fractional volumes of liquid, droplets and gas are tracked in each computational cell. This approach is iterative and computationally intensive. Also, the actual interface shape is generally not maintained. Therefore, the VOF formulation has been coupled to the new Continuum Surface Force (CSF) model (4). The CSF model incorporates surface tension and interface effects into a volume force which becomes a source term in the momentum equation. This approach eliminates the VOF iteration requirements, significantly increasing computational speed. An overview of the VOF and CSF models is presented by Tucker (5).

Droplet evaporation is modeled by assuming a vapor-liquid film on the droplet surface as discussed by Liang and Ungewitter (6). An important aspect of this model is the theoretical capability to model "supercritical" evaporation. This capability may be important for problems such as LOX injection in the SSME preburner.

EXPERIMENTAL DATABASE

A relatively large data base has been compiled for plain and coaxial injection using a variety of test liquids and gases. An excellent summary of this data base is provided by Rahman and Santoro (7). A data base for LOX/GH₂ coaxial injection with combustion is currently being developed at the Pennsylvania State University Propulsion Engineering Research Center (8). The coaxial injection problem with combustion is a significant challenge for any numerical prediction technique. Therefore, a relatively simple plain injection problem was chosen in order to perform a preliminary evaluation of the upgraded FDNS code. This evaluation was based on the diesel injection study of Hiroyasu and Kadota (9).

In the Hiroyasu and Kadota study, diesel fuel was injected through a single hole plain orifice injector into ambient nitrogen gas. The orifice diameter was 0.3 mm. The diesel fuel ($\rho = 840$ kg/m³) was injected from a reservoir pressure of 9.9 MPa. The ambient chamber, or back, pressure was varied between 0.1 and 5.0 MPa. The injection velocity was determined based on the pressure differential, liquid density, and an orifice discharge coefficient of 0.8. Using photographs, the characteristics of the spray, such as penetration length and particle diameters, were determined as a function of back pressure, etc. This data set is believed to be of reasonable

quality for numerical validation. One major deficiency is the lack of information on experimental data uncertainty. Therefore, the comparisons between computation and experiment must be interpreted with this in mind.

FDNS INJECTION SIMULATION RESULTS

The Hiroyasu and Kadota experiment was simulated using the FDNS code. The upper half of the experimental chamber (120 mm long by 20 mm radius) was modeled by an axisymmetric grid of 45 axial by 25 radial points. The grid was exponentially stretched in both the axial and radial directions. The upstream and top boundaries were modeled as no slip walls. The lower boundary was a symmetry plane. The downstream boundary was modeled as a constant pressure boundary based on the experimental back pressure. Back pressures of 1.1 and 5.0 MPa were simulated. The FDNS code was run in the time-accurate transient mode with a total of 500 particles injected. The penetration length was calculated along with particle location, velocity, diameter and temperature as a function of time. Results of the comparison are shown in Figures 1 and 2.

In Figure 1, the penetration length in millimeters is plotted versus time in milliseconds for the two back pressures. The experimental data is shown as solid and dashed lines while the code predictions are shown as symbols. As expected, increasing back pressure reduces penetration length primarily due to the decrease in injection velocity. Results show that the initial diameter of the injected particles has a significant effect on the resultant predictions. Based on the blob injection model, the injected particles should have the same diameter as the injection port of 0.3 mm or 300 microns. For both chamber pressures, injecting 300 micron particles produced a significant overprediction of the penetration length. A second simulation was run in which the experimental data was used to approximate the initial particle diameter. For 1.1 MPa this diameter was 100 microns. The 1.1 MPa penetration length was still overpredicted but not as significantly. The experimentally determined injection diameter was 170 microns for the 5.0 MPa back pressure. The predictions based on this diameter initially show an overprediction of the penetration length at earlier times but then an underprediction of the length at latter times. Overall, the predictions based on the experimentally derived injection diameters compare reasonably well with data, especially when considering that the experimental uncertainty could be significant.

Figure 2 is a plot of Sauter mean diameter (SMD) versus back pressure. The Sauter mean diameter is a measure of the ratio of droplet volume to surface area. This is an important parameter in problems involving combustion and evaporation. The SMD values shown in Figure 2 were calculated for the total spray. Two prediction values are shown at the two simulated back pressures. The circles represents predictions based on particle injection diameters of 300 microns. The predicted SMD based on this value significantly overpredicts the experimental values. The second set of predictions is based on the experimentally based injection diameters of 100 (1.1 MPa) and 170 (5.0 MPa) microns. These results display a better comparison to the data but underpredict the experimental values by a factor of approximately 1.8. The predictions also do not display the expected increase of SMD with increasing back pressure. Other detailed results not presented in this report indicate that the injected particles break up much faster than the experiment. This is a deficiency in the breakup model which should be addressed.

CONCLUSIONS/RECOMMENDATIONS

A preliminary evaluation of the capabilities of the upgraded FDNS code to predict liquid injection has been performed. Comparisons of code predictions have been made with data (penetration length, Sauter mean diameter) from a diesel injection experiment. The computational predictions show that droplet breakup does occur. Best results were obtained when the particle injection diameters were derived from the experiment as opposed to the injection port diameter.

Obviously, it is desirable that the code be able to simulate flows for which data does not exist. Code and experimental comparisons also indicated that the droplet breakup occurs too quickly.

These questions about the code performance should be addressed. Evaluation of the breakup model should be continued based on comparisons of code predictions with data from other cold flow injection experiments. The impact of particle injection diameter and droplet breakup rate should be investigated. Based on the results of this study, simulations of coaxial injection with reactions can be performed.

ACKNOWLEDGMENTS

The author would like to acknowledge the assistance of his NASA Colleague, Ten-See Wang, during this project. Mr. Paul Liaw of ESI was especially helpful in understanding the modified FDNS code. The contributions of these individuals are greatly appreciated.

REFERENCES

1. Chen, Y. S., "FDNS - A General Purpose CFD Code: User's Guide, Version 3.0," *ESI-TR-93-01*, Engineering Sciences, Inc., May 1, 1993.
2. Landrum, D. B., "CFD Simulation of Coaxial Injectors," 1993 NASA/ASEE Summer Faculty Fellowship Program, Report XXIV, NASA CR 193862, November, 1993.
3. Liang, P. Y., Przekwas, A. J., and Santoro, R. J., "Propellant Injection and Atomization," Presented at the Combustion-Driven Flow Technology Team Meeting, NASA MSFC, July 1993.
4. Brackbill, J. U., Kothe, D. B., and Zemach, C., "A Continuum Method for Modeling Surface Tension," *Journal of Computational Physics*, Vol. 100, No. 2, 1992, pp. 335-354.
5. Tucker, P. K., "Efficient Interfacial Transport Treatment for Spray Combustion Simulation," Presentation to MAE 750 class, The University of Alabama in Huntsville, August 16, 1994.
6. Liang, P. Y., and Ungewitter, R., "Multi-Phase Simulations of Coaxial Injector Combustion," *AIAA 92-0345*, 1992.
7. Rahman, S. A., and Santoro, R. J., "A Review of Gas/Liquid Spray Experiments and Correlations," *AIAA Paper 94-2772*, 1994.
8. Pal, S. Moser, M. D., Ryan, H. M., Foust, M. J., and Santoro, R. J., "Flow field Characteristics in a Liquid Propellant Rocket," *AIAA Paper 93-1882*, 1993.
9. Hiroyasu, H., and Kadota, T., "Fuel Droplet Size Distribution in Diesel Combustion Chamber," *SAE Paper 740715*, 1974.

Data : Hiroyasu and Kadota, 1974

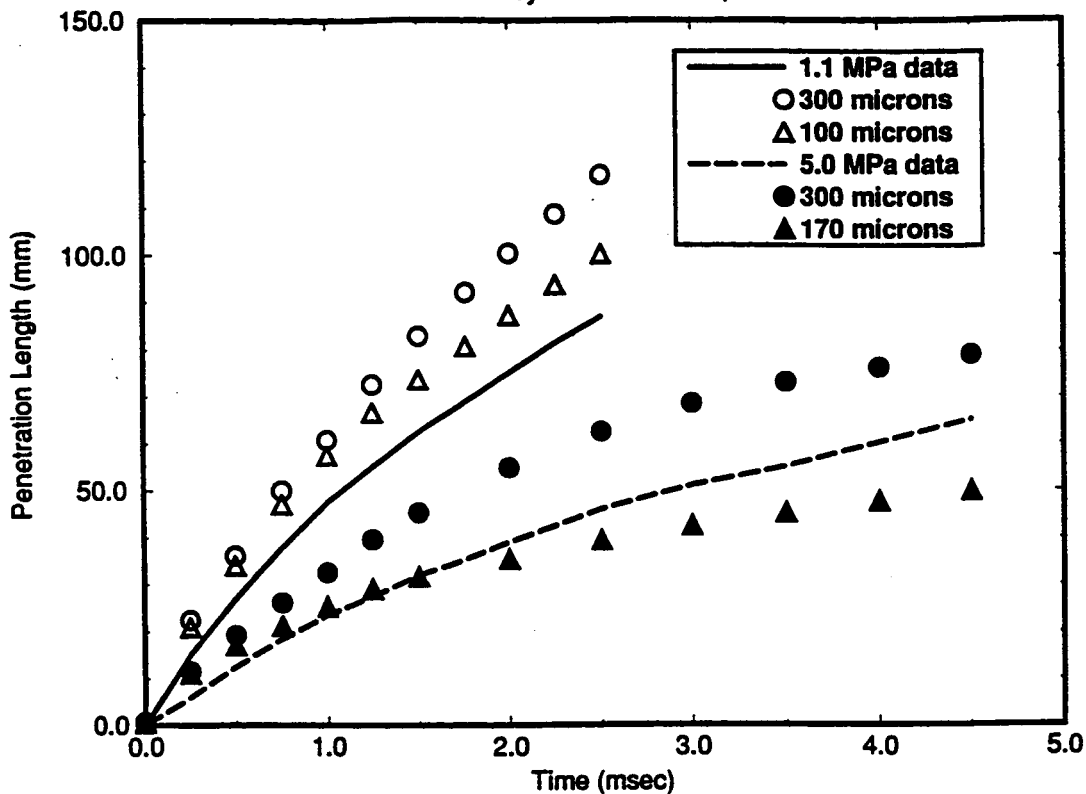


Fig. 1 FDNS prediction of spray tip penetration versus time.

Data : Hiroyasu and Kadota, 1974

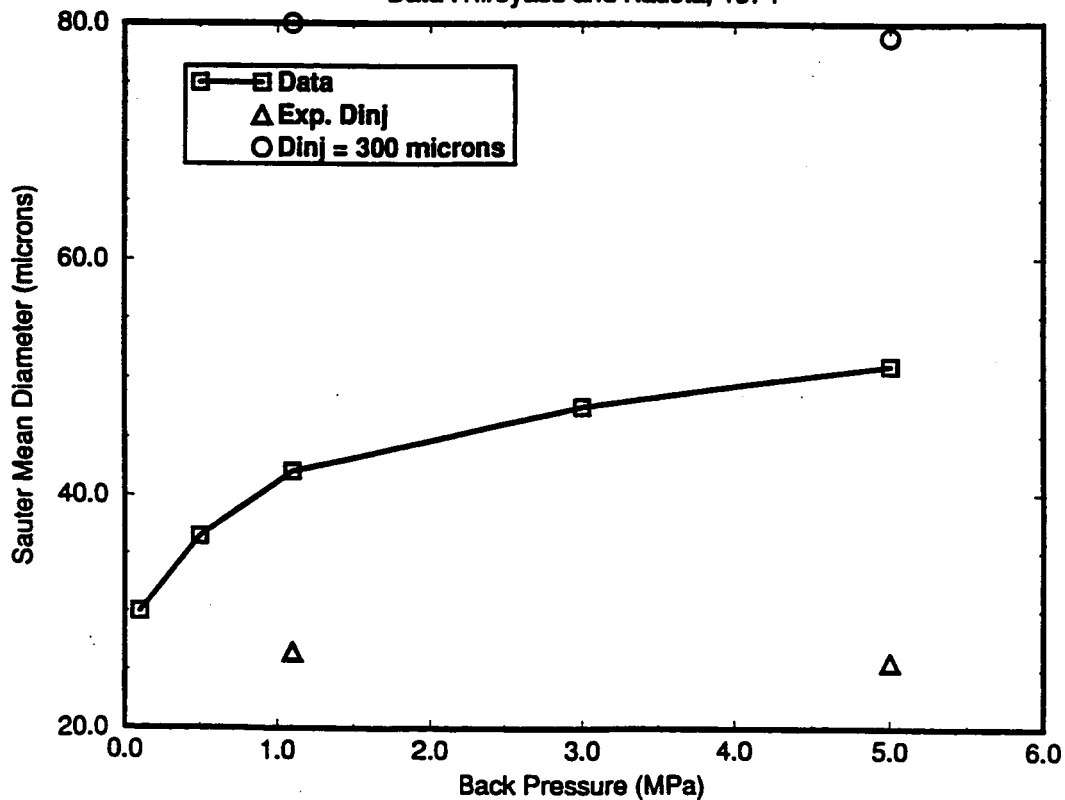


Fig. 2 FDNS prediction of spray Sauter mean diameter versus back pressure.

112575

302837

N95-18990

**1994
NASA/ASEE SUMMER FACULTY FELLOWSHIP PROGRAM**

523-54
30913
p.6

**MARSHALL SPACE FLIGHT CENTER
THE UNIVERSITY OF ALABAMA**

**DEVELOPMENT OF MICROGRAVITY, FULL BODY FUNCTIONAL REACH
ENVELOPE USING 3-D COMPUTER GRAPHIC MODELS AND
VIRTUAL REALITY TECHNOLOGY**

Prepared By:	Patricia F. Lindsey
Academic Rank:	Lecturer
Institution and Department:	East Carolina University School of Human Environmental Sciences
NASA/MSFC:	
Laboratory:	Mission Operations Laboratory
Division:	Operations Engineering Division
Branch:	Crew Systems Engineering
MSFC Colleague:	Joseph P. Hale

INTRODUCTION

In microgravity conditions mobility is greatly enhanced and body stability is difficult to achieve (Fauquet & Okushi, 1991). Because of these difficulties, optimum placement and accessibility of objects and controls can be critical to required tasks on board shuttle flights or on the proposed space station. Anthropometric measurement of the maximum reach of occupants of a microgravity environment provide knowledge about maximum functional placement for tasking situations.

Calculations for a full body, functional reach envelope for microgravity environments are imperative. To this end, three dimensional computer modeled human figures, providing a method of anthropometric measurement, were used to locate the data points that define the full body, functional reach envelope. Virtual reality technology was utilized to enable a occupant of the microgravity environment to experience movement within the reach envelope while immersed in a simulated microgravity environment.

THE HUMAN BODY IN A MICROGRAVITY ENVIRONMENT

In micro-gravity the human body experiences significant changes in perception, posture, and efficiency of movement (Fauquet & Okushi). Due to liberation from supporting the body's weight, space between each vertebra expands, and the spinal length escalates, therefore increasing the height of the person by approximately three per cent (NASA, 1978). There is, however, a decrease in effective body height resulting from the crouched neutral body posture brought on by life in microgravity (Fauquet & Okushi). The frame, nevertheless, is extended when stretching to reach for an object or control if anchored in body or foot restraints. This study is undertaken to determine the maximum reach, along a variety of planes, under these conditions.

NEED FOR A MICROGRAVITY, FULL BODY FUNCTIONAL REACH ENVELOPE

Distinct problems in the placement and adjacency of controls and equipment are encountered in a micro-gravity environment. It is necessary to the health, comfort, and productivity of participants in such an environment that maximum reach envelope calculations be established and tested to assist in the placement of equipment in relation to body restraint apparatus and adjacency of equipment that must be used simultaneously or in sequence. "In order to choreograph human/machine interface within physically and emotionally supportive body envelopes the characteristics of the interface morphology of human mobility in microgravity must be understood", (Fauquet & Okushi, p. 1).

Review of the literature reveals only partial reach envelope

data for this environmental situation (NASA, 1978 and NASA, 1989). Fully developed reach envelope calculations are needed and should be presented in a way that may be used for training or interactive experience--not for information alone.

Calculation of maximum extension points within a full body reach envelope cannot be achieved by usual means in Earth's gravity. Body positions that can be achieved under micro-gravity conditions must, in Earth's gravity, be simulated in contrived situations such as in a neutral buoyancy diving tank or during a flight that is designed to provide a few seconds of micro-gravity experience. Such flights are conducted by NASA's K-135 (Fauquet & Okushi).

These methods are costly and have limitations due to required life support equipment and/or necessary brevity of the experiment. Limitations of this type restrict researchers' ability to calculate a variety of reach envelope maximum data points.

SETTING REACH ENVELOPE DATA POINTS USING THREE DIMENSIONAL COMPUTER GENERATED HUMAN MODELS

Mannequin uses a library of ergonomic data that allows human to figures be integrated into simulations to make a designed environment or object more functional (Gamble-Risley, 1992). The human model chosen for this study was defined by Mannequin Pro as a large, American, male, adult of average build, corresponding to the a 95th percentile male in stature (Biomechanic Corporation of America 1992 & NASA, 1989).

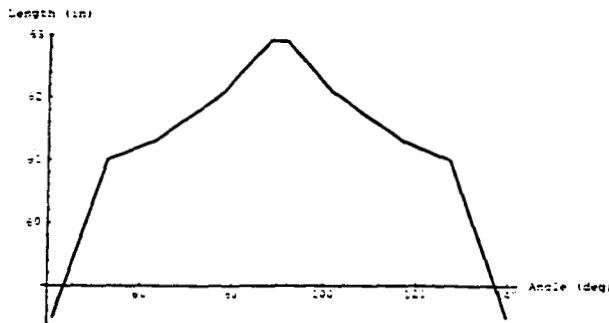
Human models provided in Mannequin Pro software were used to find data points along a curve that defined the reach envelope (Figure 1 and Figure 2). Data points were dimensioned and coordinates were recorded for additional points including the fingertip, top of head, and suprasternum. The suprasternum data point was chosen as the point from which to calculate the curve along which the figure moves to form each plane of the reach envelope (Figure 3 and Figure 4).

The figure was manipulated to move from zenith to the left side (Figure 1) and forward and backward (Figure 2). Since the figure existed in simulated microgravity, it was not necessary to keep the center of gravity above the feet. Range of motion for the figure was from zero degrees to 180 degrees. The curve was calculated and graphics produced by Mathematica software (Figure 3 and Figure 4).

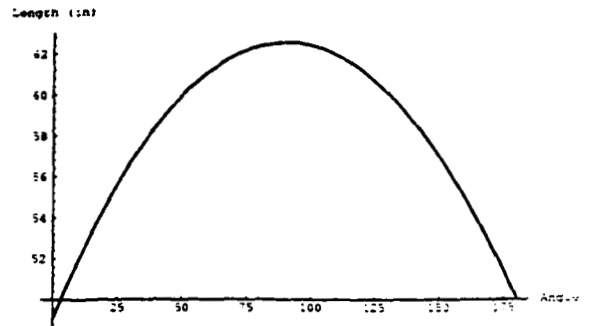
USING IMMERSIVE VIRTUAL REALITY TECHNOLOGY TO ILLUSTRATE THE REACH ENVELOPE

Swivel 3-D by VPL Research Incorporated is the modeling software

Angle From Horizontal vs. Foot Restraint - Supersternum Distance
in Side-to-Side Plane - Manniquin Data



Angle From Horizontal vs. Foot Restraint - Supersternum Distance
in Side-to-Side Plane - Curve Fitted to Manniquin Data

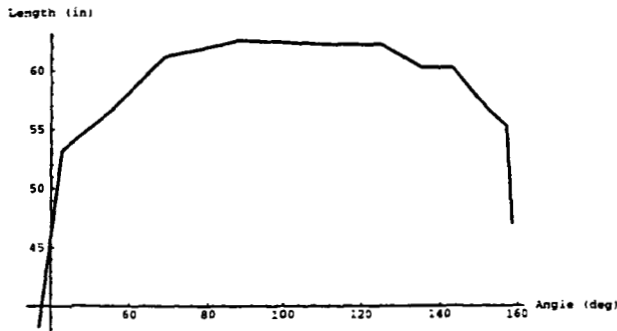


These are the raw datapoints obtained from Manniquin for subject motion in the side-to-side plane. The angle is measured from the horizontal on the subject's left-hand side to the foot restraint-supersternum line.

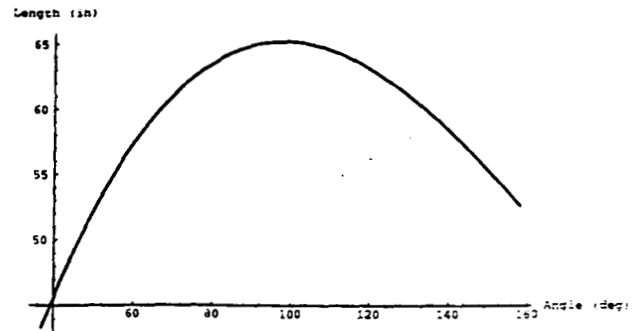
```
SSdatapoints = {{41.2,58.5},{52.8,61.0},{62.9,61.3},{78.3,62.1},{88.2,62.9},{91.8,63.0},
{101.7,62.1},{117.1,61.3},
{127.2,61.0},{139.8,58.5}};
ListPlot[SSdatapoints,PlotJoined->True,AxesLabel->{"Angle (deg)","Length (in)"}]
```

Figure 3.

Angle From Horizontal vs. Foot Restraint - Supersternum Distance
in Forward-Backward Plane- Manniquin Data



Angle From Horizontal vs. Foot Restraint - Supersternum Distance
in Forward-Backward Plane- Curve Fitted to Manniquin Data



These are the raw data points obtained from the Manniquin software. The first number of each pair is the angle from the floor directly in front of the subject to the foot restraint-supersternum line. The second point is the length of the foot restraint-supersternum line.

```
FBdatapoints={{37.1,38.2},{42.8,53.2},{55.7,56.7},{68.8,61.2},{87.9,62.6},
{111.9,62.3},{124.8,62.3},{135.1,60.3},{143.0,60.3},{152.2,56.7},
{157.1,55.3},{158.6,47.0}};
```

Figure 4.

used for this study. Body Electric Visual Programming Language connects input by the operator to drive the simulator. As the user makes head or body movements, Body Electric registers the changes to the virtual environment. Information sent by Body Electric to drive the simulator is translated by Isaac software.

Data points found using Mannequin figures were placed in a virtual reality simulation of the IML-2. The user is immersed in the simulated reach envelope within the IML-2 and may pivot from side to side or front to back within the confines of the reach envelope by using a joy stick for manipulation. The user may also move along the curve of the reach envelope moving from one set point to another as assigned in Body Electric.

RECOMMENDATIONS FOR FURTHER STUDY

It is recommended that reach enveloped data be collected along additional planes, expanding the data base for a full body, functional reach envelope.

It is recommended that real human subjects be used to collect data in a simulated microgravity situation such as a neutral buoyancy tank or K-135 flight or under actual microgravity conditions.

It is recommended that data be compared to the data set by Mannequin and placed in the virtual reality environment and refinements made where variances exist.

REFERENCES

- Biomechanic Corporation of America. (1992). Mannequin Designer Users' Guide. HumanCad. Melville, NY.
- Fauquet, R. S. & Okushi, J. (1991). Architectural ideas relating to the question of human body motion in microgravity.
- Gamble-Risley, M. (1992, July). One size doesn't fit all. California Computer News.
- NASA. (1989). Man-systems integration standards: NASA-STD-3000, volume I, revision A. National Aeronautics and Space Administration.
- NASA (1978). Anthropometric source book, Volume II: A handbook of anthropometric data. National Aeronautics and Space Administration Scientific and Technical Office. (Eds.) Staff of Anthropology Research Project. Yellow Springs, OH.
- Pspotka, J. (1991). Immersive tutoring systems: Virtual reality and education and training. Paper in progress. U. S. Army Institute. Alexandria, VA.

112576

352840
N95-18991

1994

NASA/ASEE SUMMER FACULTY FELLOWSHIP PROGRAM

**MARSHALL SPACE FLIGHT CENTER
THE UNIVERSITY OF ALABAMA**

**A GIS APPROACH TO URBAN HEAT ISLAND RESEARCH: THE CASE OF
HUNTSVILLE, AL.**

524-45
30914
p-6

Prepared By: Chor P. Lo, Ph.D.

Academic Rank: Professor

Institution and Department: The University of Georgia
Department of Geography

NASA/MSFC:

Laboratory: Space Science
Division: Earth Science and Applications
Branch: Earth System Processes and
Modeling Branch

MSFC Colleagues: Dale A. Quattrochi
Jeffrey C. Luvall

INTRODUCTION

GIS (Geographic Information System) is a system of hardware, software, and procedures designed to support the capture, management, manipulation, analysis, modeling and display of spatially-referenced data for solving complex planning and management problems.¹ In essence, GIS performs three major functions: (1) to process and display maps, (2) to create a database, and (3) to carry out spatial analysis.² With the advent of personal computer technology in recent years, the capability of GIS has been greatly enhanced particularly in the area of mapping and spatial data manipulation. A typical application of GIS involves overlaying different layers of spatial data together to produce a new map of some desired characteristics, normally involving the concept of union and intersection in Boolean algebra. GIS has been used extensively in ecology and environmental research,³ but not much in the atmospheric science. This paper advocates its use in an urban heat island study.

The urban heat island represents a case of inadvertent human modification of climate in an urban environment. Changnon⁴ suggested that the magnitude and extremes of the changes in urban precipitation and temperature were similar to those predicted to develop over the next 100 years by the global climate models. Urbanization changes the nature of the surface and atmospheric properties of a region. As a result, radiation balance in the urban areas is altered and sensible heat is added to the point that urban areas are warmer than surrounding rural areas. Oke⁵ observed that at the boundary between the rural area and the urban area, a sharp rise in temperature occurs, culminating to a peak temperature at the Central Business District (CBD) of the city, hence the name "urban heat island". The extent and intensity of the urban heat island are a function of population size, land use, and topography.^{6,7} Because the urban heat island exhibits spatial variations of temperatures, the use of GIS is appropriate.

The research on the urban heat island focuses on the acquisition of 15 bands of visible and thermal infrared data (ranging from 0.45 to 12.2 μm) from an aerial platform using NASA's ATLAS (Airborne Thermal/Visible Land Application Sensor) sensor over Huntsville, Alabama. These data will be acquired in early September. The research reported in this paper is an analysis of the impact of population, land use, and topography on the shape of the urban heat island that could be developed in Huntsville using the GIS approach. The outcome of this analysis can then be verified using the acquired remotely sensed data.

THEORETICAL CONSIDERATIONS

All surfaces on earth receive short-wave radiation during the day and exchange long-wave radiation continuously with the atmosphere. The net amount of radiation received by a surface depends on the temperature, emissivity and reflectivity of the surface exposed to radiative exchange. The general form of the equation describing the radiation budget is:

$$R_n = (1-\rho)S_t + L_d - L_u \quad (1)$$

where R_n is net radiation, ρ is reflection coefficient, S_t is the total flux (short-wave atmospheric radiation, being made up of a direct flux on the horizontal surface (S_b) and a diffuse flux (S_d)), L_d is the downward flux (long-wave atmospheric radiation received at the surface) and L_u is the upward flux (long-wave emission from the surface).⁸ The amount of total flux depends on the cosine of the zenith angle ψ , or the amount of sky visible to the surface. In the urban area, man-made land surfaces have changed the reflectivity and hence the amount of reflected solar radiation. Because of the heterogeneous nature of the land use pattern in the urban area, reflection coefficients vary across the urban area. According to the Stefan-Boltzmann law, the flux of radiation emitted by the surface, i.e., L_u in Equation (1), depends on the surface temperature as:

$$L_u = \sigma T^4 \quad (2)$$

where σ is the Stefan-Boltzmann constant ($= 5.67 \times 10^{-8} \text{ W m}^{-2} \text{ K}^{-4}$), and T is the surface temperature in absolute (K) units. However, reflectivity of the surface refers to short-wave radiation ($0.15\text{-}3 \mu\text{m}$), while the overall emissivity (ϵ) of the surface refers primarily to the long-wave radiation ($3\text{-}100 \mu\text{m}$) as in this case. Equation (2) has to be modified to become:

$$L_u = \epsilon \sigma T^4 \quad (3)$$

By the principle of conservation of energy that absorptance + reflectance + transmittance = 1, and by assuming that the surfaces are opaque to thermal radiation (as in most remote sensing applications), we can establish the relationship that absorptance + reflectance = 1. According to Kirchhoff radiation law that spectral emissivity of a surface equals its spectral absorptance, we can establish the relationship that the higher the surface's reflectance, the lower its emissivity and absorptance, and vice versa.⁹

In applying all the above considerations to urban heat island research, one should note a two-layer classification of urban modification put forth by Oke (1976). There is a distinction between the Urban Boundary Layer (UBL) and the Urban Canopy Layer (UCL) because the processes responsible for its creation may be different. UBL refers to the layer above the roofs of buildings in the urban area, which is an advective phenomenon involving internal radiative effects and the entrainment of warm air from the inter-building spaces beneath and the inversion of the mixed layer above. UCL is near the street level where the magnitude and dynamics of the heat island are largely a response to microscale site factors such as building geometry and surface materials. The amount of sky visible at the street level will affect the amount of atmospheric radiation received. The analysis presented in this paper focuses on the UCL rather than the UBL.

METHODOLOGY

The analysis requires a number of data input: (1) reflectance of the land use surfaces in the city of Huntsville, (2) population distribution, and (3) topography of the site.

To obtain the reflectance data for the land use surfaces, color infrared aerial photography acquired on October 9, 1992 at the nominal scale of 1:48,000 was used. First, fifteen aerial photographs were manually interpreted with the aid of a mirror stereoscope supplemented by ground checking. Eleven classes of land use/cover were delineated: (1) forest, (2) commerce and services, (3) high-tech offices and factories, (4) residential, (5) agricultural, (6) military, (7) quarry, (8) educational, (9) golf courses and parks, (10) wetland, and (11) water bodies. The result is a land use/cover map at the scale of 1:48,000. Next, two aerial photographs (frame numbers 13 and 20) which covered the major part of the city and its adjacent rural area were scanned using a flat-top color scanner with a resolution of 600 bpi. This produced a digital image of the photograph in three bands (blue, green, and red) with digital values of the pixels ranging from 0 to 255 (i.e., 8-bit data). The green band was found to be the best to use to obtain the reflectance data of each land use/cover type. By calibrating the data using a lake (such as the lake at the University of Alabama at Huntsville) which should have a reflectance of 0 per cent and the quarry which exhibited the brightest reflectance (assumed to be 100 per cent), the digital number for each class of land use/cover was converted into reflectance data. All these were accomplished with the aid of a raster GIS software package known as IDRISI developed by Clark University. The land use/cover map was reduced to a scale of 1:75,000. It was then digitized and transformed into a raster-based map with a cell size of 571.5 m x 571.5 m. Because the land use/cover map was directly traced from the aerial photographs, distortions caused by tilts and relief displacements were present. The rasterized image of the map was rectified and transformed into the Universal Transverse Mercator (UTM) coordinates based on four GPS ground control points provided by the Planning Department of the City of Huntsville, with the aid of the IDRISI program. By assigning the reflectance value to the appropriate land use/cover class, a reflectance map in correct UTM coordinates was produced.

Population data for Madison County in 1990 by census tracts were obtained from the Planning Department of the City of Huntsville. The census tract boundary map for Huntsville was digitized and converted into raster format with the same resolution as that of the land use/cover map and rectified to the same UTM coordinate system. Population density was then assigned to each appropriate census tract using the IDRISI program, thus producing a map of population densities by census tracts.

Topography was represented in terms of terrain heights acquired by GPS for 363 points covering the city of Huntsville. A program called SURFER was used to carry out a spatial interpolation of the heights points by the method of kriging. The result was a rasterized

contour map, which was then imported to IDRISI where it was made to register with the land use/cover map.

Because these three layers of data were registered to the same UTM coordinate system, they could be overlaid by the IDRISI program to create a new map and to investigate the spatial relationships among these layers. This is the typical GIS approach. In this analysis, our objective is to determine the interaction between reflectance and population density, in particular, the locations where both high reflectance and high population density occur together. These would be areas of high temperatures in the city. Their locations were then related to the topography.

RESULTS OF ANALYSIS

High reflectance was found to occur in the commerce/services uses which are found along the major highways and in the Central Business District (CBD). High population densities were found in the Mastin Lake Road area, Oakwood Avenue area, and Bob Wallace-Drake Street area --- located respectively to the northwest, east and southwest of the Memorial Parkway. A big contrast in population density between the city and the rural area was seen. The high reflectance and high population density produced a distinct urban heat island following the North-South aligned Memorial Parkway and the East-West running I-565 offshoot. This North-South alignment has been dictated by the North-South trending mountain ridge (Green Mountain) to its east. The land use/cover type on the mountain ridge is predominantly forest (low reflectance and hence high emissivity and high absorptance), thus presenting a contrast to the generally high reflectance land use surfaces of the city. The Tennessee River runs across the southern edge of the city. The Redstone Arsenal to the southwest of the city has low population density but some high reflectance. The combined effect of the two has not produced significantly high temperature in the region, and presented a contrast to the city area to its northeast. All these results suggest that the site of Huntsville is most favorable to the development of urban heat island.

IMPLICATIONS TO THE THERMAL INFRARED IMAGING AND CLIMATE CHANGE

The analysis above presented some interesting observations to the use of thermal infrared imaging for urban heat island detection in Huntsville. The North-South running Memorial Parkway is an important corridor along which the reflectivity of the land use surfaces will have a significant impact on urban heat island development at the Urban Canopy Layer (UCL). By integrating the visible channels of the ATLAS sensor (channels 1 to 6: 0.45-0.90 μm), reflection coefficients of the different land use surfaces can be obtained. Emissivity of the land use surfaces can be obtained from the thermal infrared channels of 3.35 μm to 12.2 μm (channels 9 to 15). Based on the Stefan-Boltzmann Law, the radiant temperature (T_{rad}) of

the land use surfaces can be calculated. With a knowledge of emissivity of each surface, the kinetic temperature (T_{kin}) of the surface can be computed using the following relationship:

$$T_{rad} = \epsilon^{1/4} T_{kin} \quad (4)$$

Finally, it has been observed by examining past records of temperature and precipitation data for Huntsville from 1959 to 1991 that Huntsville appeared to be in the cycle of temperature and precipitation increase in recent years, as revealed by the three-yearly moving averages. One can only speculate whether such increases in temperature and precipitation have been impacted by the possible intensification of urban heat island effect in recent years.

REFERENCES

1. Rhind, D., "Why GIS?" *Arc News*, Vol. 11, No. 3, 1989.
2. Maquire, D. J., "An Overview and Definition of GIS," in D.J. Maguire, M. F. Goodchild and D. W. Rhinds (eds), *Geographical Information Systems: Principles and Applications*, Vol. 1 (New York: Wiley, 1991), pp.9-20.
3. Remillard, M. M. and Welch, R. A., "GIS Technologies for Aquatic Macrophyte Studies," *Landscape Ecology*, Vol. 7, pp.151-162, 1992; Vol. 8, pp.163-175, 1993.
4. Changnon, S. A., "Inadvertent Weather Modification in Urban Areas: Lessons for Global Climate Change," *Bulletin American Meteorological Society*, Vol. 73, pp.619-627, 1992.
5. Oke, T. R., *Boundary Layer Climates* (London: Methuen, 1987), pp.272-303.
6. Oke, T. R., "City Size and the Urban Heat Island," *Atmospheric Environment*, vol. 7, pp.769-779, 1973.
7. Landsberg, H. E., *The Urban Climate* (New York: Academic Press).
8. Monteith, J. L. and Unsworth, M. H., *Principles of Environmental Physics* (London: Edward Arnold, 1990), p.54.
9. Aryan, S. P., *Introduction to Micrometeorology* (San Diego: Academic Press, 1988), pp.23-24.

112577

352 841

N95- 18992

1994

NASA/ASEE SUMMER FACULTY FELLOWSHIP PROGRAM

**MARSHALL SPACE FLIGHT CENTER
THE UNIVERSITY OF ALABAMA**

525-63
30915
P. 6

**NEURAL NETWORKS APPLICATIONS TO CONTROL AND
COMPUTATIONS**

Prepared By: Dr. Leon A. Luxemburg

Academic Rank: Assistant Professor

Institution and Department: Texas A&M University

NASA/MSFC:

Laboratory: Structures and Dynamics
Division: Control Systems
Branch: Flight Dynamics

MSFC Colleagues: Richard Dabney
Henry Waites, Ph.D.

APPLICATIONS of NEURAL NETWORKS to FAST COMPUTATIONS

Our first problem is to use neural networks to develop a general high precision computational algorithm for feedforward neural networks and to show its efficiency by applying it to a solution of the inverse perspective transformation problem in the Automated Rendezvous and Capture Space program.

The inverse perspective problem for the Automated Rendezvous and Capture program is defined as the determination of the 6 degrees of freedom of the chase vehicle relative to the target vehicle. The solution involves the Newton-Raphson method which is rather cumbersome computationally. Therefore, a neural network approach was suggested by Richard Dabney [1]. He suggested that instead of solving a system of equations for each point, parameters of these equations can be considered as inputs to some neural network and the solution of these equations as an output. However, the major problem was the accuracy of the solution. While an RMS value was quite low, the worst case precision for a case of pitch angle remained unacceptably high- around 19.1%

We have used this problem to demonstrate a new approach to a fast, high precision neural computing which reduces the errors to a more acceptable level. This problem was successfully solved by introducing and training a different type of neural network. We have achieved a reduction of the worst case error to about 8.4% instead of 19.1% and the RMS error was also reduced by about 30%. In our approach we used a network with two layers with nodal sigmoid functions being hyperbolic tangent and in the output layer we used identity function $f(x)=x$ as a nodal function. This choice of architecture can realize any function of n variables as soon as we choose sufficiently many neurons in the two inner layers. This follows from the Kolmogorov's theorem on representation of function of several variables by using a superposition of functions of one variables and arithmetic operations.

One of the essential features of our approach is to use an adaptive learning rate to speed up learning and to minimize the worst case error instead of sum-squared error as is usually done. We used a standard backpropagation approach to learning with momentum and adjustable biases. This helped to overcome a number of convergence and precision problems encountered in the initial approach.

APPLICATIONS TO CONTROL PROBLEMS

Consider a linear plant

$$\begin{aligned} \dot{x} &= Ax + Bu \\ y &= Cx \end{aligned} \tag{1}$$

We assume that this system is controllable and observable and that n , p and q are the dimensions of vectors x, u, y respectively. Our problem is to demonstrate a capability of artificial neural networks to stabilize linear plants.

Here we would like to construct a controller and a feedback

$$\begin{aligned} \dot{z} &= Fz + Gy + Hu \\ u &= K_1 z + K_2 y + r \end{aligned} \tag{2}$$

such that the overall system 1-2 is stable, where z is an $n-q$ dimensional vector and r is an external input. First, we want to formulate this control problem in terms of an interpolation problem for a neural network with linear nodal functions and with six layers. The overall system (1-2) can be presented in the form:

$$\dot{w} = Tw + Ru$$

where

$$T = \begin{vmatrix} A + BK_2C & BK_1 \\ GC + HK_2C & F + HK_1 \end{vmatrix} \quad \text{and} \quad R = \begin{vmatrix} B \\ H \end{vmatrix}$$

Furthermore, T can be represented as a product of three matrices

$$A^1 A^2 A^3 \quad \text{where} \quad A^1 = \begin{vmatrix} A & \text{zeros}(n,n) B \\ \text{zeros}(n-q,n) & F \quad G \quad H \end{vmatrix}$$

is a $(2n-q) \times (2n+p)$ matrix, $A^2 = \begin{vmatrix} I_{2n} & \\ \text{zeros}(p,n) & K_1 & K_2 \end{vmatrix}$ is a

$(2n+p) \times (2n)$ matrix, and $A^3 = \begin{vmatrix} I_{2n-q} & \\ C & \text{zeros}(q,n-q) \end{vmatrix}$ is a

$(2n) \times (2n-q)$ matrix. Now we recall a Lyapunov's Theorem [2] which says that a matrix T which has a full rank is stable if and only if for any positive definite matrix N there exists a positive definite matrix M such that $T' M + M T = -N$, where T' is a transpose of T . In this theorem N can be taken to be a unit matrix rather than an arbitrary matrix. Note also, that for any positive definite matrix M there exists a matrix g such that $M = gg'$. Therefore, in order to stabilize system (1) with a controller of system (2) there should exist such matrices F, G, H, K_1, K_2, g such that

$$T gg' + gg' T + I_{2n-q} = 0 \quad (3)$$

Now, expression $gg' T$ is a product of six matrices g, g', A^1, A^2, A^3 and a unit matrix (in this order). Therefore, this expression can be viewed as a realizing function of a six layer neural network with weights of synaptic interconnections given by matrices g, g', A^1, A^2, A^3 , with input vectors being columns of the unit matrix and with linear nodal functions. Analogously, expression $T gg'$ is a realizing function of another neural networks with synaptic weight matrices transposed and in reverse order. Taking a discrete sum N of these two neural networks we see that equation (3) is equivalent to an interpolation problem for a neural network. This reduces our stabilization problem for a plant (1) to an interpolation problem (3) for a neural network N . Interpolation problems for a given neural network are typically solved by a backpropagation method. Notice that in our case some of the weights of the neural network are fixed and the only variables weights are the ones that correspond to the unknown matrices F, G, H, K_1, K_2, g . Let matrix E be given by the following formula:

$$E = T gg' + gg' T + I$$

and let SSE be the sum of squared elements of E . Then the following formulas are true:

$$\frac{\partial SSE}{\partial g} = 4(TE + ET)g, \quad \frac{\partial SSE}{\partial A^1} = 4gg' E(A^3)'(A^2)', \quad (4)$$

$$\frac{\partial SSE}{\partial A^2} = 4(A^1)' gg' E(A^3)', \quad (5)$$

In order to solve equation (3), we need to drive SSE to 0, therefore a training of the neural net can proceed via a gradient descent method using equations (4) and (5) with the obvious modification due to the fact that the only elements in matrices A^1, A^2, A^3 that change are the elements of matrices F, G, H, K_1, K_2 . This gradient descent method has to be slightly modified, so that we proceed by training each layer separately rather than all layers at once in order to avoid getting stuck in local minima. We used momentum and adaptive learning rate in our gradient descent method to speed up learning. The method described above has been successfully used to stabilize a specific numerical example with a nonminimal phase plant.

A NEW METHOD OF LEARNING FOR FEEDFORWARD NEURAL NETWORKS

We have successfully implemented a new method of training neural nets which is a combination of gradient descent and a Newton-Raphson method. This method significantly decreases the learning time. The details are presented below. Let us consider a neural network N with k variable weights. We can represent each set of weights as a vector w in a k -dimensional Euclidean space R^k . Let $P = \{p_i\}$ be a finite set of input vectors to a neural network N and let $T = \{t_i\}$ be the set of corresponding target output vectors. For every set of weights w from R^k there is a set of output vectors $O = \{o_i\}$ of N corresponding to the set of inputs. Then the sum-squared error function $f(w)$ is defined as $f(w) = \sum_i \|o_i - t_i\|^2$. Our goal is to drive the error function to 0, i.e. to find a set of weights w such that $f(w) = 0$. We try to find this w by an iteration process starting from some w_0 . Let w_i be defined then we assume that there exists a vector Δ from the weight space R^k such that $f(w_i + \Delta) = 0$ and let $f(w_i + \Delta) - f(w_i) = \nabla f(w_i) \Delta$ be a first order approximation. Then in order to find Δ we need to solve the equation

$$f(w_i) + \nabla f(w_i)\Delta = 0 \quad (7)$$

This is an underdetermined linear equation with respect to Δ . Let us add to (7) another system of k equations:

$$\alpha\Delta = 0 \quad (8)$$

where α is some nonzero constant. The solution of (7)-(8) does not exist if $\nabla f(w_i)$ is nonzero, however we can find the least squares solution Δ . Then we define $w_{i+1} = w_i + \Delta$. Continuing to update w_i in this fashion we hope to find w_i arbitrary close to a solution of $f(w_i) = 0$. In this algorithm we vary α in order to minimize the error. Notice that α serves as a magnitude control factor so that the magnitude of solution of (7)-(8) decreases as α increases. In this method we start with weight vector w_0 obtained after some initial gradient descent training and then proceed with the method just described. The obtained results are very encouraging. We applied this method to the control problem described above to compare it with the gradient descent method and found that the speed of conversion increases 8-10 times.

CONCLUSION

We have described several interrelated problems in the area of neural network computations. First we considered an interpolation problem, then we have shown how to reduce a control problem to a problem of interpolation by a neural network via Lyapunov function approach, and finally we introduced a new, faster method of learning as compared with the gradient descent method.

REFERENCES

1. Richard W. Dabney, Application of Neural Networks to Autonomous Rendezvous and Docking of Space vehicles. AIAA Space Programs and Technologies Conference, March 23-27, 1992, Huntsville, AL.
2. C.T. Chen, Linear System Theory and Design, Holt, Rhinehart and Winston, New York, 1984.

112578

352042

N95-18993

1994

NASA/ASEE SUMMER FACULTY FELLOWSHIP PROGRAM

**MARSHALL SPACE FLIGHT CENTER
THE UNIVERSITY OF ALABAMA**

526-15
30916
p. 6

**A CMC DATABASE FOR USE IN THE
NEXT GENERATION LAUNCH VEHICLES (ROCKETS)**

Prepared By:	Kamala Mahanta, Ph.D.
Academic Rank:	Assistant Professor
Institution and Department:	The State University of New York College at Oneonta Department of Physics and Astronomy

NASA/MSFC:

Laboratory:	Materials and Processes
Division:	Non-Metallics
Branch:	Ceramics and Coatings

MSFC Colleague: **Dr. R.G. Clinton**

INTRODUCTION

Ceramics Matrix Composites are being envisioned as the state-of the-art material capable of handling the tough structural and thermal demands of advanced high temperature structures for programs such as the SSTO (Single Stage to Orbit), HSCT (High Speed Civil Transport) etc. as well as for evolution of the industrial heating systems.

Particulate, whisker and continuous fiber ceramic matrix (CFCC) composites have been designed to provide fracture toughness to the advanced ceramic materials which have a high degree of wear resistance, hardness, stiffness and heat and corrosion resistance but are notorious for their brittleness and sensitivity to microscopic flaws such as cracks, voids and impurity.

THE BEHAVIOR OF CFCC

CFCCs have been singled out as the most efficient one for the more demanding projects because the fibers can control crack propagation by dissipating the crack tip energy. Fracture toughness¹ measured in terms of K_{IC} (or K_Q) values for CMCs have caught up with the lower limit (30 MPa m^{1/2}) of that for tough metals (30-200 MPa m^{1/2}). WOF (Work of Fracture) for unidirectional long fiber CMCs tends to vary from a few KJ/m² to about 100 KJ/m² whereas for monolithic structural ceramics it is just a few Joules/m².

Also the scatter in strength, measured in terms of the Weibull Modulus has shown considerable improvement in the case of CFCCs (30 for SiC/Borosilicate glass and 6-8 for monolithics). This is a more desirable situation for the designer because a higher proportion of the Ultimate Strength becomes available for component design.

C/SiC AND SiC/SiC CMCS

In elevated temperature applications, C/SiC and SiC/SiC CMCs are the materials with the highest expectations because of their greater oxidation resistance compared to

Carbon/Carbon composite which oxidizes easily even at moderate temperatures. A host of studies are going on currently all over the world on C/SiC, SiC/SiC and SiC/Glass types of composites.

Matrix microcracking² and hence the microcracking threshold stress σ_{mc} (about 120 MPa with 0.1% strain at room temperature for SiC_f/CAS) plays a critical role in the performance of the CMC in fatigue and in oxidizing environments. C/SiC composites are weak in this aspect because it tends to have a non-existent σ_{mc} (the stress-strain behavior is a non-linear one right from the beginning of loading). This is caused by the fact that the carbon fibers have a CTE (coefficient of thermal expansion) mismatch ($\alpha_m > \alpha_f$) with the SiC matrix forcing the material to have microcracks in the matrix during the cooling from a high temperature in the fabrication process.

SOME RECENT TESTS ON C/SiC CMC

A. An attempt at taking a C/SiC composite³ to a temperature range of 1770°C-1810°C with the hope of finding a better material for the TPS system TOPHAT led to the conclusion that the C/SiC material (with fiber and matrix volumes of 40% and 60% respectively) failed mainly due to full oxidation of a thin SiC coating at the fabric holes as well as processing flaws. Oxidation occurs internally and progresses to expose carbon fibers directly to the oxidizing material.

Suggestions such as (1) a continuous and thicker coating in the holes of the fabric; (2) reduction of misalignment of fabric plies; (3) use of a fabric with smaller tows and a denser weave so as to reduce the size of the voids as well as distribute them more homogeneously through the thickness and also have a more uniform surface with holes easier to fill by a polymer assisted CVD/CVI SiC processing technique have been made.

B. Higher fiber volume and higher densities have been shown by Headinger et al⁴ to correspond to higher tensile

strength and/or shear strength in an investigation, sponsored by the Air Force, on the dependence of the mechanical properties of C/SiC turbine rotors. While density had greater influence on tensile strength, higher fiber volume seemed to improve toughness with no clear effect of density observed.

C. The development of a C/SiC turbine rotor⁵ published in the NASA-CP 3235 reports a good correlation between coupon testing and spindisk testing. The material, when designed to have higher oxidation resistance will enable the design of a rotor which will not require cooling resulting in an improved thrust and reduced fuel consumption.

A CMC DATABASE: THE SUMMER PROJECT

The database has specifically aimed at data on C/SiC and SiC/SiC CMCs due to the fact that these materials tend to maintain their mechanical properties even at high temperatures and exhibit greater resistance to oxidation in comparison with other structural materials. However, considerable work seems to be in progress on glass ceramics also.

The following companies and institutions have been contacted for CMC data:
DuPont, B. F. Goodrich, Amercom, Pratt & Whitney, McDonnell Douglas, SEP, Dow-Corning, LTV, NASA Lewis, Boeing, Williams International, Oakridge Laboratory, University of Michigan, Southern Research Institute, Wright Patterson AFB, NIST, General Electric, Grumman, FMI/EMTL, United Technologies Research Center. So far data have been provided by : DuPont, Williams International, Southern Research Institute (reports), B. F. Goodrich, NASA Lewis, University of Michigan, Amercom, WPAFB + McDonnell Douglas (yet to arrive), Dow - Corning (promised) and Boeing (promised).

The rest have either referred to the above or are in the process of generating data.

VISITS : A trip was taken to Southern Research Institute to visit their labs and also to look into the possibility of

acquiring current data on CMCs. The test organization was impressive. They are in the process of testing several CMCs for various clients; but do not have the proprietary rights to make those available to NASA/MSFC yet.

THE DATABASE SYSTEM : The MAPTIS and the M/VISION systems have been analysed for advantages and disadvantages.

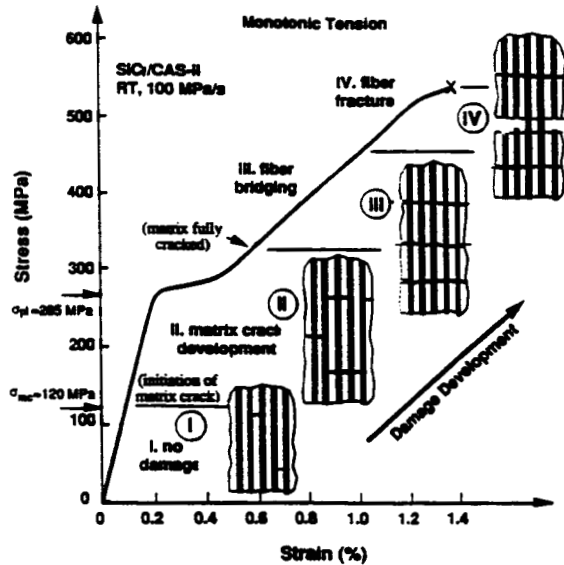
EXAMPLES OF THE DATA COLLECTED : DuPont (Nicalon/SiC, Enhanced SiC/SiC with a matrix enhancement and T-300/SiC); B. F. Goodrich (Nicalon/SiC, T-300/SiC); Williams International (data from various sources on SiC/SiC, C/SiC, SiC_{p&t}/Al₂O₃, NiC/SiC); the University of Michigan (Fatigue, High Temp. Creep, Environmental behavior of CMCs).

FUTURE WORK : The data will have to be evaluated for quality prior to putting them in the database. The criteria for evaluation are to be established based on a thorough study of the factors affecting the pedigree of the data, information supplied by the manufacturers as well as using theoretical models and softwares based on the micromechanical behavior of CMCs.

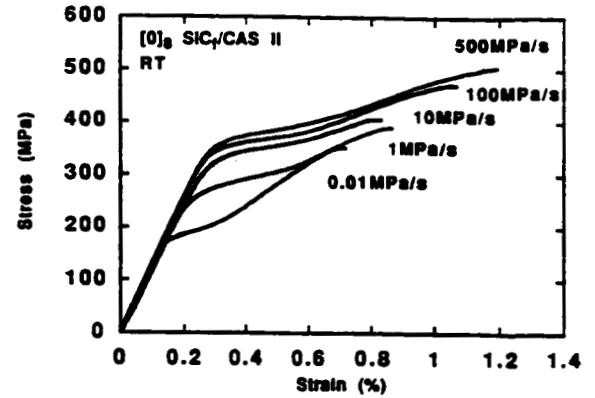
REFERENCES

1. D. C. Phillips, "Ceramic Matrix Composites", edited by R. Warren, p 167-198, Chapman and Hall, 1992.
2. J. W. Holmes and B. F. Sorensen, "Fatigue Behavior of Continuous Fiber-Reinforced Ceramic Matrix Composites", to appear in November, 1994 in Elevated Temperature Mechanical Behavior of Ceramic Matrix Composites, edited by S. V. Nair and K. Jakus (Butterworth - hienneman).
3. J. J. Schlautmann and S. R. Riccitiello, "High Temperature Oxidation Failure of C/SiC Continuous Fiber Ceramic Matrix Composites", NASA - CP 3235, May, 1994, p743-758.
4. M. H. Headinger, R. W. Klacka, S. L. Bors and W. R. Moschelle, "The Effects of Density and Fiber Volume on the Mechanical Properties of SiC Matrix Composites Reinforced with T-300 fibers", NASA - CP 3235, May, 1994, P 567-582.
5. R. W. Klacka, M. H. Headinger, W. R. Moschelle and J. D. Farr, "C/SiC Turbine Rotor Development", NASA - CP 3235, May, 1994, p 855-862.

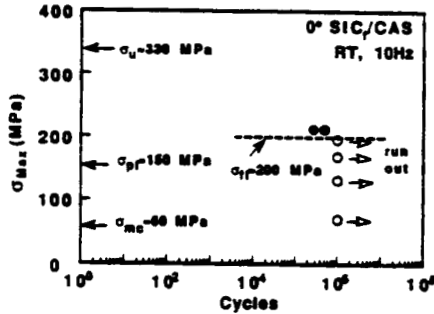
Characteristics of Monotonic and cyclic loading2 :



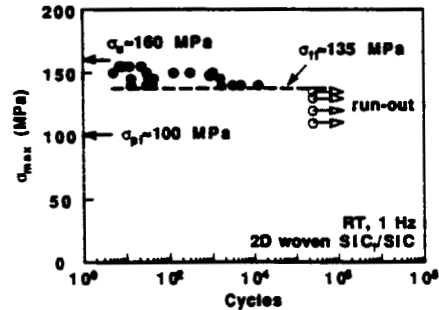
Monotonic stress-strain behavior of unidirectional SiC_f/CAS.



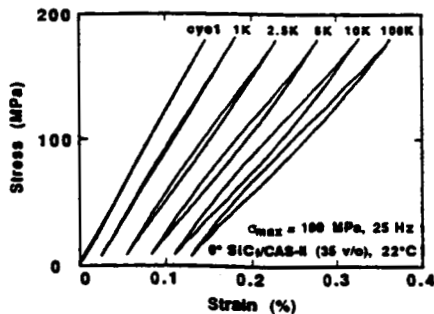
Influence of loading rate on the monotonic stress-strain behavior of SiC_f/CAS-II in air at 20°C.



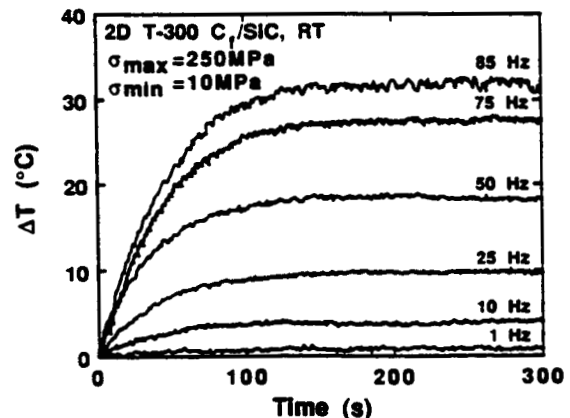
Fatigue life diagram



SN curve at room temperature



Changes in hysteresis behavior during fatigue



Influence of loading frequency on the surface temp rise during tension-tension fatigue

352813
N95-18994

112579

20711
p.6

1994

NASA/ASEE SUMMER FACULTY FELLOWSHIP PROGRAM

**MARSHALL SPACE FLIGHT CENTER
THE UNIVERSITY OF ALABAMA**

LEAN SPACECRAFT AVIONICS TRADE STUDY

Prepared By: John A. Main, Ph.D.
Academic Rank: Research Assistant Professor
Institution and Department: Vanderbilt University
Department of Mechanical Engineering

NASA/MSFC:

Laboratory: Preliminary Design
Division: Systems Engineering
Branch: Systems Analysis

MSFC Colleague: Melody Herrmann

BACKGROUND

Spacecraft design is generally an exercise in design trade-offs: fuel vs. weight, power vs. solar cell area, radiation exposure vs. shield weight, etc. Proper analysis of these trades is critical in the development of lightweight, efficient, "lean" satellites. The modification of the launch plans for the Magnetosphere Imager (MI) to a Taurus launcher from the much more powerful Delta has forced a reduction in spacecraft weight availability into the mission orbit from 1300 kg to less than 500 kg. With weight now a driving factor it is imperative that the satellite design be extremely efficient and lean. The accuracy of engineering trades now takes on an added importance.

In some cases the balance between design utility and design "cost" are clear. For example, given the choice for a satellite stabilization system between an active gas jet system or a passive mass-spring-damper system, the passive system is clearly the choice in terms of cost and reliability if it can provide the necessary performance. Less clear are the trades involved in the avionics requirements for a given satellite, particularly when the avionics in question interface with the payload instruments. Optimal requirements for instrument avionics are difficult to define because they generally involve interactions between electrical systems (computers, instruments, power supplies, guidance and control electronics, etc.), mechanical systems (instruments, guidance and control hardware, mass balance systems, etc.), and information (software, telemetry data, instrument data, instrument controller commands).

An understanding of spacecraft subsystem interactions is critical in the development of a good spacecraft design, yet it is a challenge to define these interactions while the design is immature. This is currently an issue in the development of the preliminary design of the Magnetosphere Imager (MI). The interaction and interfaces between this spacecraft and the instruments it carries are currently unclear since the mission instruments are still under development. It is imperative, however, to define these interfaces so that avionics requirements ideally suited to the mission's needs can be determined.

PROJECTED INSTRUMENT PAYLOAD

The proposed MI payload consists of three instruments: (1) the Far Ultraviolet Imager (FUV), (2) the Plasmasphere Imager, and (3) the Hot Plasma Imager. Exact instrument interfaces are impossible to define at this point of the design process, but some general ideas of payload requirements can be gleaned from examining the heritage of the payload instruments.

Wilson (1993) compiled an extensive report on the development history of the MI instruments. This report was used in addition to conversations with members of the Magnetosphere Imager Science Definition Team (SDT) to gain a better understanding of the functional requirements of the payload instruments. The results of this effort are embodied in the bullets in the following sections.

Far Ultraviolet Imager

- Essentially a monochromatic telescope (photon counter)
- Requires a filter wheel and associated motor to move the wheel to look at different wavelengths
- Image may be swept across a CCD as the spacecraft rotates, or the instrument may use a periscope to stare at one point in the sky

- May be a problem if the instrument sweeps across a bright object before a darker object of interest (blooming)
- Goal is to produce 1 image per minute
- Commands that may be uploaded include changes in image integration time, compression schemes, ON/OFF cycling, instrument status checks, uploading code to instruments, performing passive telemetry on instrument, filter wheel movement, periscope rate of movement, etc.
- SDT specified FOV 40°x360°
- SDT dimensions .70x.80x.30 m
- SDT masses 30 kg
- SDT power 25 W
- SDT data rates 15 kbs
- SDT pointing accuracy 0.025 deg

Plasmasphere Imager

- Essentially a photon counter
- SDT specified a 135°x180° FOV but it is likely that the scientists will want data from the full spin (135°x360°)
- The plasmasphere imager cuts a 135° degree swath through the sky as the craft rotates. A CCD element will be used to capture the images, either a 1-D array that will sweep across a very small field of view, or a wider 2-D array which will allow more image integration time as the image sweeps across it.
- Goal is to produce 1 image per minute
- Should be able to achieve high data compression ratios with the image files
- No moving parts
- Commands that may be uploaded include changes in image integration time, compression schemes, ON/OFF cycling, instrument status checks, uploading code to instruments, performing passive telemetry on instrument.
- SDT specified FOV 135°x180°
- SDT dimensions imager .48x.16x.20 m
 electronics .23x.18x.20 m
- SDT masses imager 7.2
 electronics 11.8kg
- SDT power imager 4.5
 electronics 16.5 W

- SDT data rates 7 kbs
- SDT pointing accuracy 0.5 deg

Hot Plasma Imager - High and Low Energy

- Essentially an event counter, used to look at various q/m ratio particles
- Instrument will require specification of spin rate from the spacecraft (or ground operator)
- Unusual in that it requires a controllable high voltage power supply
- Goal is to produce 1 image per minute
- No moving parts
- Commands that may be uploaded include changes in image integration time, compression schemes, ON/OFF cycling, instrument status checks, uploading code to instruments, performing passive telemetry on instrument, change in high voltage level, temperature data, etc.
- SDT specified FOV - 4π str
- SDT dimensions High Energy .51x.35x.51 m
 Low Energy .30x.30x.25 m
 electronics .30x.30x.30 m
- SDT masses High Energy 14 kg
 Low Energy 7 kg
 electronics 8 kg
- SDT power High Energy 4 W
 Low Energy 7 W
 electronics 12 W
- SDT data rates High Energy 12 kbs
 Low Energy 6 kbs
- SDT pointing accuracy 5 deg

THE MI INSTRUMENT-AVIONICS INTERFACE

The challenge in defining the instrument interface to the MI avionics system is centered around the fact that the satellite instruments are still undefined at this point. There are ways to address this problem, however. What we can do is define two interfaces, basically a worst-case and a best-case. These two options are chosen with knowledge of only the most basic facts about the instruments such as weight, power, field of view, and instrument heritage. With such limited knowledge it is difficult to explicitly design the interface, or controller, so the goal is to define with these two designs the spectrum of possibilities in which the final instrument control system will fall. We can do this with confidence because the requirements and specifications in the previous section do not

specify any instrument characteristics that are unusual enough to drastically impact the controller design.

Option 1-Distributed Instrument Control. The two instrument control schemes conceived for MI are illustrated in Figure 1. The first scheme to be discussed is the distributed control scheme. This design is basically the "high performance" option. The operation of each science instrument is independent in this design, with each having its own computer/controller that acts as the interface between it and the main onboard computer. The advantages of this control strategy are numerous. Distributing control to each science instrument maximizes the probability of getting at least some data from the spacecraft. It also simplifies and compartmentalizes software, saving programming time. In this same vein it allows the science instrument developers, who may be geographically distributed, development independence.

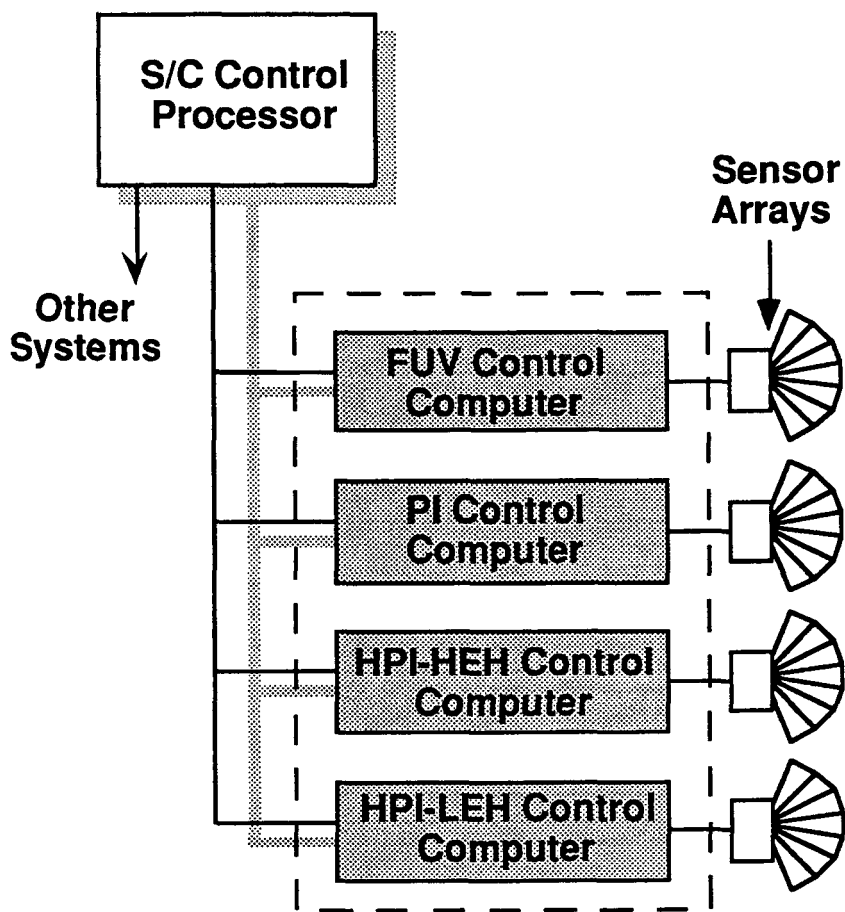


Figure 1. Sketch of the MI instrument controller options.

On the other side of the coin, distributed control has design costs that may preclude its use. Since each instrument has a dedicated and independent computer that is not available for any other tasks, the spacecraft computer may need a backup in case it fails. This means that there may be five or six computers that must be qualified for the mission. Each computer adds mass, but the overriding consideration may be the cost to space qualify all this electronic hardware. Significant savings might be achieved by combining the controllers of two or more of the instruments.

Option 2-Centralized Instrument Controller. The logical extension of combining two instrument controllers into one is to combine all the instrument controllers into one. This master controller is represented in Figure 1 by the dotted box that surrounds the four distributed control computers. This strategy results in a number of advantages, including a lower mass system, a lower power system, and the need to qualify fewer components. If the system is properly designed the master control computer and the spacecraft computer could be used as backups for each other, eliminating the need for a backup spacecraft computer. This was the control strategy used in the recent low-cost Clementine project at the Naval Research Laboratory.

Obviously there are disadvantages to this method as well. The two most important appear to be an increased complexity in the software and the necessity for significant coordination among the science instrument designers/builders.

CONCLUSIONS

A range of control possibilities are defined by the two control options presented herein. It is likely that both will prove to be impractical in some respect: option 1 may prove to be too expensive and option 2 may not provide the necessary performance. Currently in the overall MI design option 1 is baselined, but there is a risk involved here. Option 1 certainly represents a "worst case" option in terms of cost, weight, and power. For planning purposes this is a good, conservative, model. The risk comes when talks begin with the science instrument builders. If they perceive that the distributed control scheme is the baseline scheme, they will be very reluctant to give up any of their control computers to save cost and weight. If possible, the baseline control system that is presented to the instrumenters should be as close as possible to option 2. This will start the process at the low cost option and the design process can then proceed in a rational fashion. The instrumenters and spacecraft design team can add controllers when performance makes it necessary, instead of giving all instruments a control computer, potentially adding unneeded weight, capacity, and cost.

REFERENCES

Wilson, G.R., "Inner Magnetosphere Imager (IMI) Instrument Heritage", NASA Contractor Report 4498.

112580

352794
N95-18995

1994

30918
P. 6

NASA/ASEE SUMMER FACULTY FELLOWSHIP PROGRAM

MARSHALL SPACE FLIGHT CENTER
THE UNIVERSITY OF ALABAMA

MANN -- A PROGRAM TO TRANSFER DESIGNS FOR
DIFFRACTIVE OPTICAL ELEMENTS
TO A MANN
PHOTOLITHOGRAPHIC MASK GENERATOR

Prepared by:	Donald R. Matthys, Ph.D.
Academic Rank:	Professor
Institution and Department	Marquette University (Milwaukee, WI) Department of Physics

NASA/MSFC:

Laboratory:	Astrionics
Division:	Optics and RF
Branch:	Optical Analysis

MSFC Colleague	H. J. Cole
----------------	------------

c-3

N

INTRODUCTION

Optics is a discipline which deals with the control and manipulation of light. Although there are three basic mechanisms known for achieving this control, *i.e.*, refraction with lenses, reflection with mirrors, and diffraction with gratings, almost all optical systems utilize only the first two. The principal reason for this avoidance of diffraction is that whereas when the first two mechanisms bend, shape, focus, and redirect light they generally leave a single ray or beam as a single ray or beam, the third mechanism tends to divide any incoming rays into a multiplicity of rays. This splitting of light into different rays is sometimes useful, as in spectrometry, but it is generally not desired because the optical energy is divided up among the various beams. So most optical devices use only lenses and mirrors, with gratings generally being found only in spectrometers and monochromators, instruments used when the principal interest is spectral content or purity of optical waves, rather than their image content.

However, this last-mentioned application brings out the strength of diffractive elements: they bend light much more strongly than lenses and they are very wavelength sensitive, a characteristic that could be very desirable for some applications. In addition, the characteristic property of gratings, multiplicity of output, can be exploited in optical fanout, where it is desired to split an optical beam into a set of equivalent beams. Even if only a single output beam is desired, gratings can be designed so as to concentrate optical energy into a single refracted beam. In traditional optics, this is done by *blazing* a grating, and in the emerging field of diffractive optics, techniques for producing single beam output have also been developed. In sum, if the negatives of diffraction as applied to common optical applications can be exploited or eliminated, then the positive characteristics of diffractive elements such as light weight, small size, and minimal material, can be used to produce effective and efficient optical devices.

DESIGN OF DIFFRACTIVE OPTICAL ELEMENTS

There are two basic areas of interest for diffractive optics. In the first, the property of wavefront division is exploited for achieving optical fanout, analogous to the more familiar electrical fanout of electronic circuitry. The basic problem here is that when using a simple uniform diffraction grating the energy input is divided unevenly among the output beams. For example, when using a traditional grating the output energy is basically described using a sinc function with most of the energy either undiffracted or in the first few diffraction orders. However, H. Dammann¹ showed that by designing a non-uniformly spaced grating, using the requirement that the coefficients of the Fourier transform of the grating's transmission function should be equal, the energy could be uniformly divided among the various orders. Thus by exploiting local variations in grating line spacing and depth, uniform optical fanout can be obtained. Since the basic design is a simple problem in Fourier analysis, calculation of the grating design is straightforward, although a computer must be used to obtain numerical solutions.

The other area of interest is the use of diffractive elements to replace or supplement standard refractive elements such as lenses. Again, local grating variations can be used to control

the amount of bending imparted to optical rays, and the efficiency of the diffractive element will depend on how closely the element can be matched to the design requirements. In general, production restrictions limit how closely the element approaches the design, and for the common case of photolithographic production described below, a series of binary masks is required to achieve high efficiency. G. Swanson² showed that, even with only four masks, efficiencies of over 95% can be achieved. The actual design process is much more involved than in the case of elements for optical fanout, as the desired phase of the optical wavefront over some reference plane must be specified and the phase alteration to be introduced at each point by the diffraction element must be known. This generally requires the utilization of a standard optical design program. Two approaches are possible. In the first approach, the diffractive element is treated as a special type of lens and the ordinary optical design equations are used. W. Sweatt³ showed that the diffractive element could be treated as an extremely thin lens of very high index of refraction, and it is possible to design elements using this approximation. However, optical design programs tend to follow a second approach, namely, using the equations of optical interference derived from holographic theory and then allowing the introduction of phase front corrections in the form of polynomial equations. The output from these programs usually consists of a plot of the desired phase change as a function of radial distance from the optical axis, and a polynomial equation for the phase versus radius function. The required phase changes can be reduced modulo 2π and then the transition locations where the phase changes by submultiples of 2π can be used to determine the local spacing of the diffractive grating.

By using either of these two methods, diffractive elements can be used not only to compensate for distortions such as chromatic or spherical aberration, but also to perform the work of a variety of other optical elements such as null correctors, beam shapers, *etc.*

FABRICATION OF DIFFRACTIVE OPTICAL ELEMENTS

Of course, having uses for diffractive optical elements and even being able to design them is of little importance unless they can actually be manufactured. Depending on the scale of the grating required, it might be possible to produce the grating by actually cutting it into a substrate with a diamond cutting tool. However, the small size of many gratings generally leads to efforts to produce them using well-established techniques developed in the microelectronics industry. This also has the advantage of integrating the fields of optics and electronics, an alliance which is being zealously pursued in today's environment of fiber optics and laser diodes. It is possible to produce continuous phase variations across a substrate by using e-beams to produce varying depth etch patterns, but the simpler technique of applying semiconductor photolithography methods to resist-coated substrates can be used if a discontinuous approximation to the desired phase map is acceptable. This approach is generally called *binary optics* because each step is a binary operation of etching or not etching at a particular location on the substrate, and the desired phase distribution is approximated by a series of mask patterns and etchings as described in the report by G. Swanson².

The production of a binary optic is a complex and expensive process, requiring that a

series of binary masks be prepared, and then that these masks be used to expose a resist-coated substrate which is etched and then must be re-coated, re-exposed, and re-etched for each mask. This substrate can then be used as a master to make copies, just as in the electronics industry. However, mass production is required to achieve a reasonable cost per optic.

FROM DESIGN TO FABRICATION -- MANN

One problem has not yet been discussed and that problem is the main focus of the project described in this report -- how is the design information from the lens design program incorporated into the photolithographic process? Optical design tends to be built around circular design elements (most designs are radially symmetric), while the electronic industry with its photolithography is built around straight lines. Optical programs output phase plots and give phase changes as a function of radial distance, while photolithographic machines use rectangular apertures to control areas of exposure on a substrate. The optical design program's output will look something like

$$\phi(r) = A + Br^2 + Cr^4 + Dr^6 + Er^8 \quad (1)$$

where $\phi(r)$ is the phase as a function of radial distance and {A,B,C,D,E} are the set of constants approximating the equation to the desired phase distribution. Some programs may even give a list of those values of r where the phase change is a multiple of 2π . However, the mask generator machine generally wants a list of apertures showing where the resist-covered substrate will be exposed. For example, for the MANN USG3000 mask generator used during this project the required input is an ASCII text file consisting of a long list of lines having the form

$$X15000Y-1200W310H150A721 \quad (2)$$

where X and Y are the location of the center of the aperture, W and H are its width and height, and A is the inclination of the aperture with respect to the horizontal x-axis, expressed in tenths of a degree. All length dimensions are in microns.

Going from (1) to (2) is a non-trivial task. Basically, to prepare the data from the first equation for producing a binary optic mask, an annular ring representing the area between two transition radii must be filled with rectangular boxes. This cannot be done without error, and as an additional constraint it is generally desired to reduce the number of exposures or boxes required to make the mask. To calculate the error introduced by using straight lines to approximate curves, the geometry of Figure 1 was used to determine the proper limits that stay within the maximum error. It is easy to show that the error, or sag, is approximately given by $t = r^2/(2R)$. Figure 2 shows the geometry used to fill an annular ring. Most of the geometry is self explanatory. For the project being described, the allowed error t was one micron. By calculating the width of the box using the sag calculated from the inner radius and then spacing the rectangles around the annulus using the outer corners of the rectangle, the annulus is filled with a minimal number of exposures subject to the limiting error distance t . The overlap between adjacent boxes is not harmful to the design and only represents the loss due to double-exposing the resist in the region of overlap.

A more difficult case occurs when the two rings defining the annular region intersect the boundaries of the binary optic cell being designed. An example of this is shown in Figure 3 which shows an annular ring clipped by the upper right corner boundaries of the mask cell. The central region of the segment may be filled using the method described above but the triangle-shaped areas at the ends need a different approach. In order to maintain the least number of exposures while still staying within the error limitation of 1 micron, a binary divide technique is implemented. Starting at the inner radius, the height of the box is chosen to extend halfway to the outer wall, and then the length is

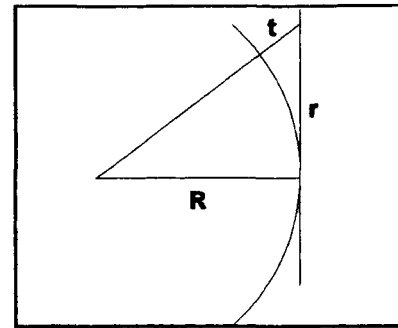


Figure 1. Geometry for calculating error between line and curve: $t = f(r)$.

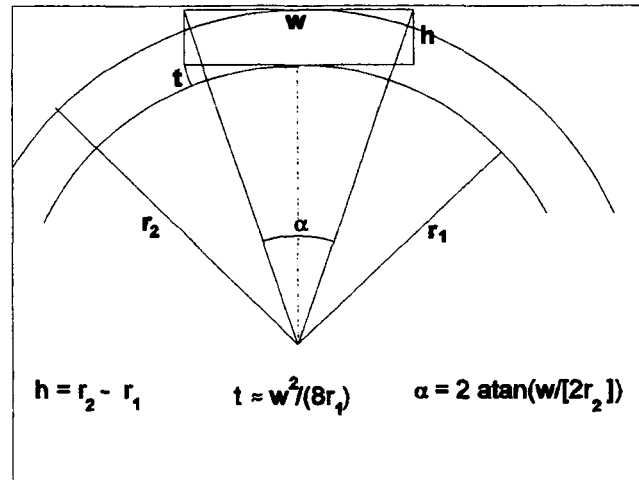


Figure 2. Filling an annular ring with rectangular boxes.

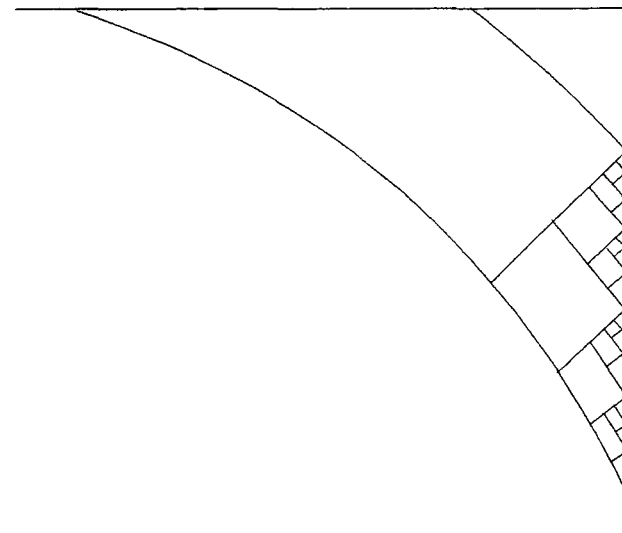


Figure 3. Filling triangular end of partial annulus in upper right corner of mask cell.

extended until it encounters the bounding wall. A second box is then placed adjacent to each side of the first box, with each of their heights extending half way to the boundary. This process is continued until the distances fall below a minimum feature size characteristic of the particular mask generator, in this case 10 microns. With these filling algorithms incorporated into the program, as well as a couple of other algorithms for special cases, procedures for generating box lists can be completed. It then remains to incorporate these routines into a complete program named *MANN*. As completed, *MANN* allows the generation of one- or two-dimensional Dammann gratings, using either data taken from published articles⁴ or allowing the user to enter transition points for symmetric gratings of unit period. The program also allows the generation of masks to produce simple lenses or lens arrays, using simple built-in formulae for focal length and mask number.⁵ In addition, for more complex designs, the program contains a text filter allowing radially symmetric designs from Code V (Optical Research, Inc.) to be incorporated. Finally, *MANN* contains a viewing routine which allows the mask box lists to be visually presented at varying magnifications on the computer monitor, allowing the user to see what the mask will look like. This mask image can be saved as a TIFF file to allow incorporation into documents and reports. The interface was designed to be friendly, with suggested values given for user inputs, and robust, with validation of all user responses. *MANN* thus fills the need for a link between lens design programs and mask generation controllers.

Further work on the program will incorporate additional text filters, to allow incorporation of designs from programs such as Mathematica (Wolfram Research), or other optical design programs.

REFERENCES

1. H. Dammann and K. Görtler, "High-Efficiency In-Line Multiple Imaging by Means of Multiple Phase Holograms," *Optics Communications* **3**, 312-315 (1971).
2. G. Swanson, "Binary Optics Technology: The theory and Design of Multi-level Diffractive Optical Elements," Technical Report 854, Massachusetts Institute of Technology Lincoln Laboratory, August 14, 1989.
3. W. C. Sweatt, "Describing holographic optical elements as lenses," *Journal of the Optical Society of America* **67**, 803-808 (1977).
4. U. Krackhardt and N. Streibl, "Design of Dammann Gratings for Array Generation," *Optics Communications* **74** (1,2), 31-36 (1989).
5. Georgia Institute of Technology, *Manual for Diffractive Optics Workshop*, Sept 1993, Atlanta, GA, p. 2-12.

112581

302845
N95-18996

1994

30919
p. 6

NASA/ASEE SUMMER FACULTY FELLOWSHIP PROGRAM

**MARSHALL SPACE FLIGHT CENTER
THE UNIVERSITY OF ALABAMA**

DESIGN OF HIGH PRESSURE WATERJET NOZZLES

Prepared By:	Andre P. Mazzoleni
Academic Rank:	Assistant Professor
Institution and Department:	Texas Christian University Department of Engineering
NASA/MSFC:	
Laboratory:	Materials and Processes
Division:	Fabrication Services Division
Branch:	Process Automation and Modeling
MSFC Colleague:	Eutiquio Martinez

Introduction

The Hydroblast Research Cell at Marshall Space Flight Center is used to investigate the use of high pressure waterjets to strip paint, grease, adhesive and thermal spray coatings from various substrates. Current methods of cleaning often use ozone depleting chemicals (ODC) such as chlorinated solvents. High pressure waterjet cleaning has proven to be a viable alternative to the use of solvents [4,5]. A popular method of waterjet cleaning involves the use of a rotating, multijet, high pressure water nozzle which is robotically controlled. This method enables rapid cleaning of a large area, but problems such as incomplete coverage (e.g. the formation of "islands" of material not cleaned) and damage to the substrate from the waterjet have been observed.

This report summarizes research conducted by the author as a Summer Faculty Fellow at MSFC in 1994. The project consisted of identifying and investigating the basic properties of rotating, multijet, high pressure water nozzles, and how particular designs and modes of operation affect such things as stripping rate, standoff distance and completeness of coverage. The study involved computer simulations, an extensive literature review, and experimental studies of different nozzle designs.

Definitions

Since there is no widespread convention regarding terminology of waterjet production, we define here the terms used in this paper: **target**: object upon which waterjet impinges, **substrate**: material to be cleaned, usually coated with paint, grease or other material which needs to be removed via waterjet, **coating**: generic name for material to be removed from substrate, **nozzle**: device for delivering high pressure waterjets to target - is usually attached to a robotic arm, **orifice**: final exit device for waterjet - there are several orifices on a single multijet nozzle, **orifice configuration**: placement of orifices on surface of nozzle, **orifice geometry**: the internal structure of an individual orifice, **sweep rate**: rate at which nozzle is moved parallel to the target, or target is moved past nozzle (as is the case when the target is on a rotating turntable), **nozzle angular velocity**: rate at which nozzle rotates, **standoff distance**: distance from nozzle to target, **islands**: regions of the target where the coating has not been removed from the substrate after waterjet cleaning, **dwelt time**: the amount of time a waterjet is in continuous contact with a particular region of the target, **stripping width**: width of the cleaning path as the nozzle is moved over the target.

Factors Affecting Waterjet Cleaning Requirements

Of paramount concern in waterjet cleaning is maintaining the integrity of the substrate. Thus, for a particular material, we need to know the effect of standoff distance, water pressure and dwell time on the substrate to be cleaned and the coating to be removed. This information is not the focus of this paper and hence will be assumed to be known, either through theory, or more likely, through experiment. Given this information, standoff distance, water pressure and dwell time can be adjusted so that the coating is removed and the substrate is not damaged. The impact of the water on the target increases with increases in pressure and dwell time and decreases with increased standoff distance. It may

be necessary to make several passes over the target in order to remove the coating without damaging the substrate. This can also be accomplished via overlap from multiple jets.

Another important constraint is the time required to clean the target. This will be a function of the stripping width, the sweep rate and the number of passes necessary for cleaning.

Standoff distance will be constrained by the geometry of the target. For a perfectly flat plate, there is no constraint on possible standoff distance. If there are protrusions, however, such as bolts or ridges, then this will limit the possible standoff distances, unless the robot to which the nozzle is attached is equipped with the means to adjust to variations in the target geometry.

Factors Affecting Waterjet Cleaning Performance

To maximize waterjet cleaning performance, it is desirable to have complete coverage, i.e. to eliminate the production of coating "islands", and have the largest possible standoff distance. The coverage aspect of waterjet cleaning will be a function of the orifice configuration. The standoff distance will be a function of the compactness of the jet issuing from each orifice. Jet compactness is determined by the way in which the water is delivered to the individual orifices, and the internal geometry of each orifice.

Coverage

The main factors affecting coverage are the number of orifices and the placement of these orifices on the nozzle.

The angular velocity of the nozzle necessary for full coverage goes down as the number of orifices increases. However, since there is a maximum flow rate associated with each pump, there is a limit to the number of orifices that can be added. (In theory, an unlimited number of orifices can be added by simply decreasing the exit diameter of each orifice, but manufacturing considerations place a lower limit on the diameter of the orifice.) Below, we derive a formula for the maximum number of orifices that can be placed on a nozzle for a given flow rate, pressure and orifice exit diameter. Let F = flow rate, A = cross sectional area of orifice exit, v = exit velocity of waterjet, d = exit diameter of orifice, p = pump pressure, p_a = atmospheric pressure, ρ = density of water and n = number of orifices. Then $F = nvA$. But $A = \pi d^2/4$ and from a modification of Bernoulli's law we have $v = c_v \sqrt{\frac{2(p-p_a)}{\rho}}$, where c_v is an experimentally determined constant called the velocity coefficient which is usually between 0.9 and 0.95 [4]. So, $n \leq \frac{4F}{\pi d^2} \sqrt{\frac{\rho}{2(p-p_a)}}$. For a conservative assessment of n , we set $c_v = 1$. Thus if $F = 13 \text{ gpm} = 50 \text{ in}^3/\text{sec}$, $p = 36,000 \text{ psi}$, and $d = .019 \text{ in}$, we have $n \leq 6.36$ (i.e. $n \leq 6$). Once the number of orifices for the nozzle is chosen, the effect of different placements can be studied.

In studying the effect of orifice placement, we consider the path traced by each orifice as the nozzle rotates and translates. We label the orifices $i = 1, \dots, n$ and denote their positions by radial distance from the center, r_i , and angular position on the nozzle, φ_i , as shown in Fig. 1a. Then the path traced out by each orifice is given by the set of parametric equations $\{x = v_0 t + r_i \cos(\omega t + \varphi_i + \varphi_0), y = r_i \sin(\omega t + \varphi_i + \varphi_0)\}$ where v_0 is the sweep rate, ω is

the angular velocity of the nozzle and φ_0 is the angular displacement of the line from the center of the nozzle to orifice number 1 from the x axis at $t = 0$. Fig.1b shows the path traced out by a single orifice over one complete rotation of the nozzle. It can be seen from this figure that the trace assumes a roughly circular shape. It then seems reasonable to try and design a system such that the "circle" traced by each orifice lies exactly one trace width to the right of the "circle" traced by the preceding orifice. (The trace width will be determined by the jet shape and standoff distance.)

One way to accomplish this is to arrange the orifices at an equal distance from the center of the nozzle with equal angular spacing. Then, if the minimum trace width of all the orifices is denoted by w_t , sweep rate and angular velocity must satisfy the relation $\omega \geq \frac{2\pi v_0}{n w_t}$ if we are to have complete coverage [4]. For example, if $n = 6$, $w_t = 0.5$ mm and $v_0 = 30$ mm, then we require $\omega \geq 20\pi$ for complete coverage. Fig.2a shows the trace of a single orifice (for $\omega = 20\pi$) and Fig.2b shows the trace of the complete nozzle and demonstrates that complete coverage is achieved. Note that each point on the target is actually hit at least twice, once by the "right" half of a "circle", and once by the "left" half of a "circle". Points at the top and bottom of the path will be hit several times, with the exact number dependent upon the shape and dimensions of the trace. Increasing ω , or decreasing v_0 , will increase the amount of overlap and hence the number of times each point on the target will be hit by a waterjet.

Many existing rotary nozzles have orifices placed at various radial distances from the center of the nozzle. If we take, for example, $r_1 = 7, r_2 = 14, r_3 = 21, r_4 = 28, r_5 = 35, r_6 = 42$ (millimeters), we can see that each nozzle will trace out a band of height $h_1 = 14, h_2 = 28, \dots, h_6 = 84$ (millimeters). Combining these in Fig.3 for the same v_0 and ω as for the nozzle whose trace is depicted in Fig.2b, we see that the nozzle will trace out a pattern which leaves many coating "islands" where water does not hit the target. This has been observed in hydroblast operations at MSFC. Thus a nozzle with orifices all at an equal distance from the center of the nozzle with equal angular spacing gives superior coverage compared to a nozzle whose orifices are arranged at unequal distances from the center. The latter nozzle design would be more appropriate for applications such as rock drilling, where it is desirable to have more energy delivered to the center of the target than at the edges.

The preceding analysis assumes that all of the orifices emit jets that travel parallel to the centerline of the nozzle and that the centerline is aligned perpendicular to the target which is assumed flat. If the nozzles are slanted with respect to the nozzle and the nozzle is slanted with respect to the target (as shown in Fig.4), then the trace width will vary over each complete revolution of the nozzle. A precise characterization of the jet shape is thus necessary to determine what the trace will be. The jet shape is a primarily a function of the orifice geometry and the water pressure, as is discussed below. We note here that the influence of gravity on the jet must also be accounted for, although this effect will be negligible for short jets.

Water Delivery System

In order to have a jet stream which can travel a long distance before breaking up, it is necessary to have a non-turbulent flow delivered to the orifices. Therefore, the channel which delivers the water to the orifices should be designed so that bends (especially right angles) are minimized.

Orifice Geometry and Jet Compactness

A liquid jet issuing into the air has a structure [4] which consists of a core surrounded by a layer of droplets (Fig.5). Increasing the core length increases the standoff distance we can use in cleaning operations. We call the region of the jet which contains a core the "compact" region of the jet. Many papers have studied the effect of various orifice designs on jet compactness [1-3, 6]. Once a basic shape for the internal profile of the orifice is chosen, one can attempt to maximize the core length of the jet produced by varying the internal parameters of the orifice. For this study, two basic orifice geometries (see Figs.6a and 6b) were selected after a thorough literature search for orifice designs which yield highly compact jets. To start the process of optimizing these designs, it was decided that the effect of various L/D ratios on jet compactness would be studied experimentally. The method chosen for evaluating the nozzles was high speed video imaging. At the time of completion of this report, manufacture of the nozzles was not complete, so test results will have to be presented in a future report.

Summary

Basic properties of rotating, multijet, high pressure water nozzles have been outlined. An orifice configuration which enables complete coverage during cleaning has been identified. Orifice geometries likely to produce highly compact jets have been presented. Various orifice configurations will be tested and the results presented in a future report.

References

- [1] R. Kobayashi, T. Arai and Y. Masuki, "Water Jet Nozzle Geometry and Its effect On Erosion Process of Metallic Material", *5th American Water Jet Conference*, August 29-31, 1989, Toronto Canada, pp.59-68.
- [2] S. J. Leach and G. L. Walker, "The Application of High Speed Liquid Jets to Cutting", *Phil. Trans. Roy. Soc. (London)*, Vol. 260, Series A, pp. 295-308.
- [3] M. J. McCarthy and N. A. Molloy, "Review of the Stability of Liquid Jets and the Influence of Nozzle Design", *The Chemical Engineering Journal*, Vol. 7, 1974, pp.1-20.
- [4] P. J. Singh, J. Munoz and W. L. Chen, "Ultra-High Pressure Waterjet Removal of Thermal Spray Coatings", *Jet Cutting Technology*, Kluwer, 1992, pp.461-480.
- [5] J. M. Sohr and M. L. Thorpe, "Stripping of Thermal Spray Coatings with Ultra High Pressure Water Jet", *28th Annual Aerospace/Airline Plating & Metal Finishing Forum and Exposition*, San Diego, CA, 1992, paper 920939.
- [6] P. F. Thorne and C. R. Theobald, "The Effect of Nozzle Geometry on the Turbulent Structure of Water Jets - A Photographic Study", *Fourth International Symposium on Jet Cutting Technology*, Canterbury, England, 1978, paper A4.

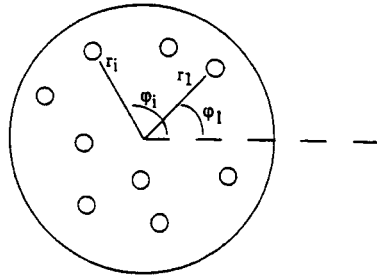


Fig. 1a

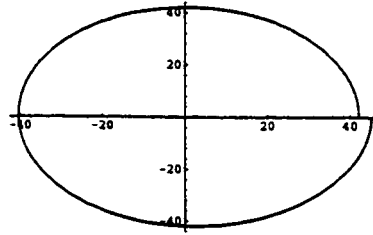


Fig. 1b

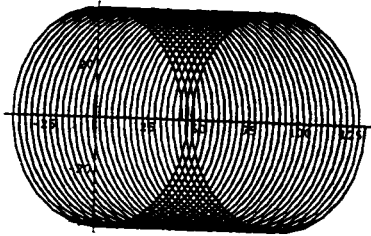


Fig. 2a



Fig. 2b

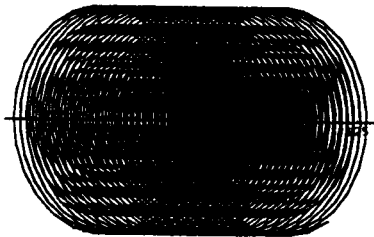


Fig. 3

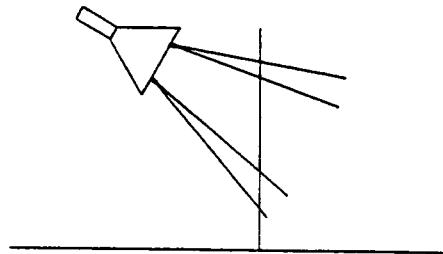


Fig. 4

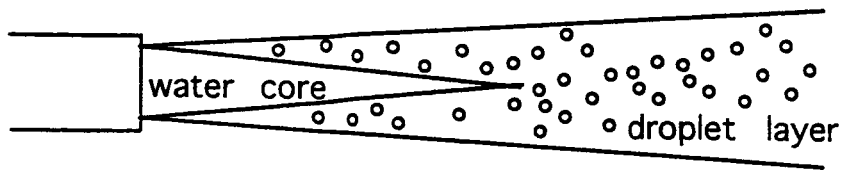


Fig. 5

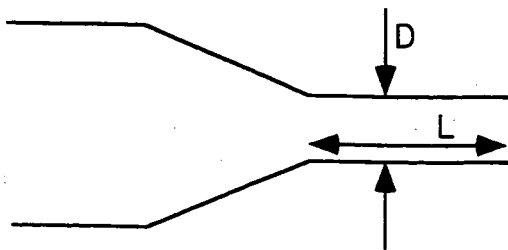


Fig. 6a

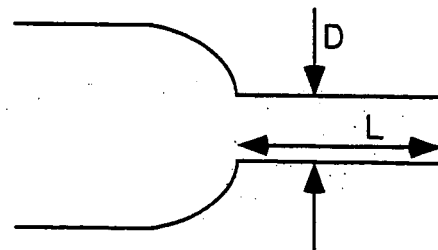


Fig. 6b

112582

352846.
N95-18997

1994

30920

P. 6

NASA/ASEE SUMMER FACULTY FELLOWSHIP PROGRAM

**MARSHALL SPACE FLIGHT CENTER
THE UNIVERSITY OF ALABAMA**

CONCENTRATION AND TEMPERATURE EFFECTS ON OVOSTATIN ACTIVITY

Prepared by: Debra M. Moriarity
Academic Rank: Associate Professor
Institution and Department: The University of Alabama in Huntsville
Department of Biological Sciences

NASA/MSFC:

Laboratory: Space Science Laboratory
Division: Microgravity Science and Applications
Branch: Biophysics

MSFC Colleague: Marc L. Pusey

XXX

Introduction

Ovostatin is a 780,000 MW protein, originally isolated from chicken egg white (1). Structural studies indicate that the protein is a tetramer of identical subunits of 165,000 MW which can be separated upon reduction with β -mercaptoethanol. Chicken ovostatin exhibits protease inhibitor activity against metalloproteases such as collagenase and thermolysin (1), and of acid proteases such as pepsin and rennin (2). Ovostatin isolated from duck eggs (3) and crocodile eggs (4) appears to be similar to chicken egg ovostatin, but with significant differences in structure and function. Duck ovostatin contains a reactive thiol ester which is not found in the chicken protein, and duck and crocodile ovostatin inhibit serine proteases such as trypsin and chymotrypsin, while the chicken protein does not. Electron microscopy (4,5) of ovostatin indicates that two subunits associate near the middle of each polypeptide to form a dimer with four arms. Two of these dimers then associate to produce a tetramer with eight arms, with the protease binding site near the center of the molecule. Upon binding of the protease, the enzyme cleaves a susceptible bond in the "bait" region of the ovostatin. Cleavage of this bond causes a conformational change in which all eight arms of the ovostatin molecule curl up towards the center, effectively trapping the protease and sterically hindering access of large substrates to its active site. The structural organization and mechanism of action proposed for ovostatin are nearly identical to that proposed for α_2 -macroglobulin, a serum protease inhibitor (6) which may play an important role in regulation of proteases in animal tissues.

Although the general arrangement of subunits appears to be the same for all ovostatins studied so far, some differences have been observed, with chicken ovostatin more closely resembling reptilian ovostatin than the duck protein. This is a surprising result, given the evolutionary relatedness of chickens and ducks. It is possible that the difference in structures may be due to deformed subunit arrangements which occur during the processing and fixing necessary for electron microscopy (4). Examination of the native structures of these proteins using X-ray crystallography would help clarify these discrepancies. Crystals of chicken ovostatin have recently been prepared at MSFC which will allow such studies to be performed.

Body

Previous experiments using the chicken ovostatin purified at MSFC indicated that it did not display the same degree of inhibitory activity against thermolysin as had been reported by Nagase *et al.* (1). Using azocasein as a substrate for thermolysin, Nagase found that an ovostatin/thermolysin molar ratio (O/T) of 0.5 produced 50% inhibition, and a ratio of 1.0 produced 90% inhibition. Based on these results they concluded that the stoichiometry of interaction between ovostatin and thermolysin was 1:1. Assay of the MSFC ovostatin indicated that a much higher ratio of ovostatin to thermolysin was needed to produce a similar level of inhibition. For example, an O/T of 2.0 produced only about 50% inhibition at 23°C, and an O/T greater than 8.0 was required to produce nearly 90% inhibition. Experiments were therefore undertaken to try to understand properties of the ovostatin or factors in the assay which could produce these results. The ovostatin purification scheme was examined by assaying the various column fractions at different steps in the procedure. It was found that the thermolysin inhibitory activity coincided with the protein that was being purified and that the

ovostatin did not appear to be losing activity through the purification process. The purified ovostatin preparations have been used to successfully prepare crystals of the protein.

Light scattering experiments performed by Dr. William Wilson at Mississippi State University using the MSFC ovostatin preparations indicated that at low ovostatin concentrations, below 0.2 mg/ml, the protein was dissociating from a tetramer into dimers. Since the proposed mechanism of action involved the tetrameric form of the protein, we hypothesized that perhaps under the conditions of our assays at various O/T ratios the ovostatin was becoming dissociated into an inactive dimer. To examine this possibility we assayed the ovostatin activity as a function of ovostatin concentration and of temperature of the assay. Figures 1-4 below show the results of these assays at 23°C, 30°C, 37°C and 42°C respectively.

Fig. 1: Effect of [OVSTN] at 23°C

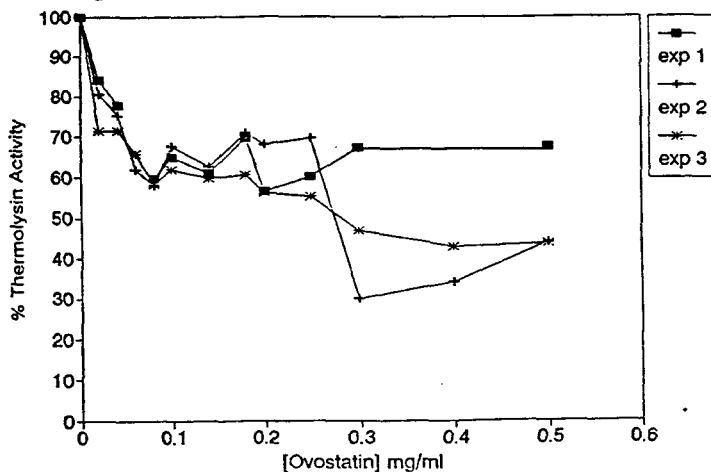


Fig. 2: Effect of [OVSTN] at 30°C

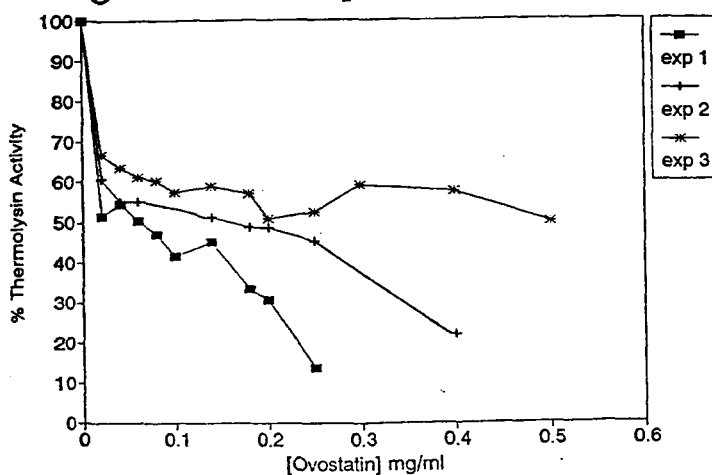


Fig. 3: Effect of [OVSTN] at 37°C

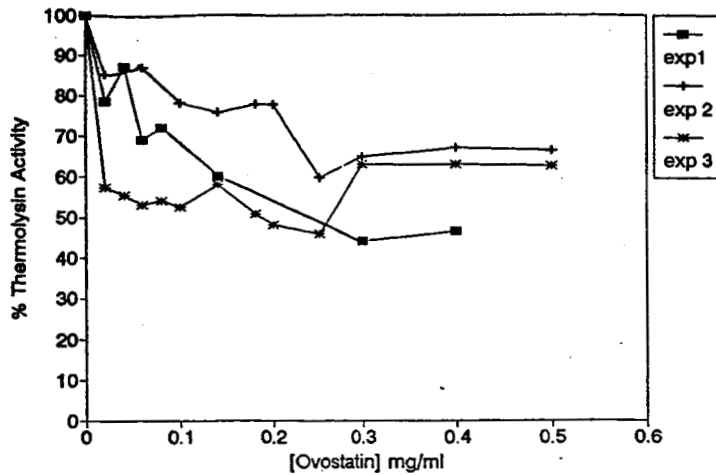
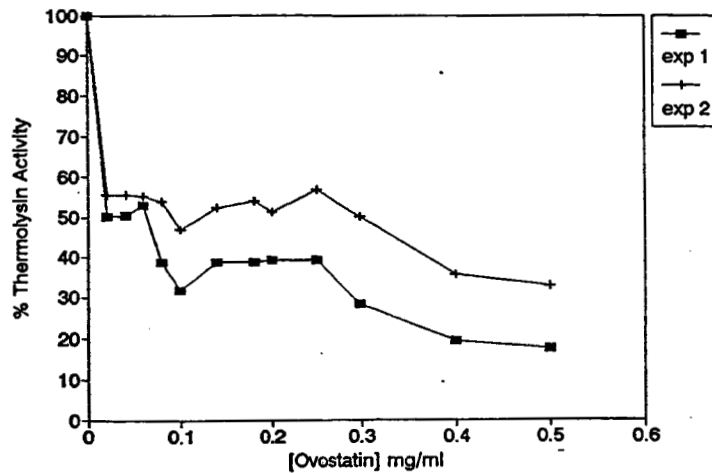


Fig. 4: Effect of [OVSTN] at 42°C

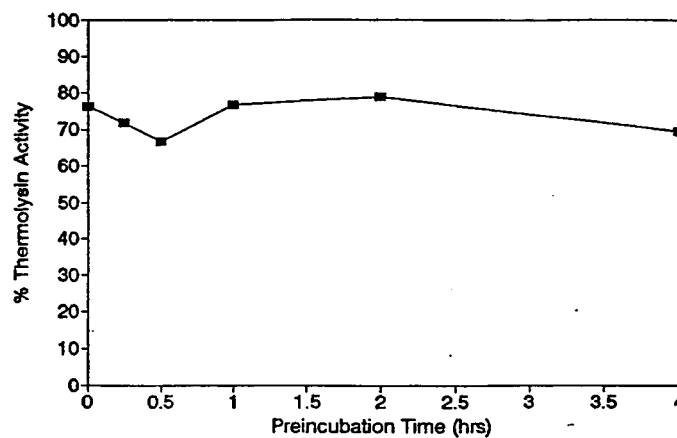


The data at 23°C clearly indicate an increase in activity of the ovostatin going from 0.2 to 0.8 mg/ml. The data at the other temperatures is less clear, but does show a trend towards less activity of ovostatin at lower concentrations, below 0.06 mg/ml. However, at concentrations where the light scattering data indicate that the ovostatin exists primarily in the dimer, and supposedly less active, form, we still observe between 20 and 50% inhibition at the different temperatures. Thus, it is possible that the dimer form of the ovostatin may also be able to interact with the thermolysin in such a way as to inhibit it. The data also appears to indicate that there is not a significant affect of temperature on the ovostatin, although there may be an observable difference between the 23°C data and the 42°C data, with slightly higher ovostatin activity at the higher temperature. These results are consistent with recent light scattering data which also showed no significant affect of temperature on the tetramer-dimer dissociation.

In considering the light scattering data showing the dissociation of the ovostatin, we questioned whether there is a time dependence of the dissociation, reflected in lower activity of the dimer with increased time at the lower concentrations. We therefore, diluted the ovostatin to 0.06 mg/ml, a concentration at which the ovostatin should exist primarily as the dimer, and incubated it at 37°C for various times from 15 minutes to 4 hours, before adding the thermolysin. Figure 5 shows that there was no significant difference in the ovostatin activity over this time interval.

Fig.5: Effect of Time on OVSTN Activity

37°C, O/T = 2.0, 0.06 mg/ml Ovostatin



During the course of these studies it was noted that Nagase *et al.* (1) had not reported the source of the thermolysin used in their assays. A search of the commercially available thermolysin preparations revealed that two different specific activity preparations are available: a lower specific activity thermolysin from Sigma Chemical Co., which is the one we have been using, and a higher specific activity product from Calbiochem. Since part of the proposed mechanism of action for ovostatin inhibition of thermolysin involves cleavage of a peptide bond in the ovostatin by the thermolysin, the activity of the enzyme itself could conceivably affect the observed inhibitory activity of the ovostatin. We attempted to obtain this higher specific activity thermolysin, but were told that it was backordered until late August, 1994. Thus, it will not be possible to test the hypothesis that the thermolysin itself is causing the discrepancy between our results and those of Nagase *et al.* (1) until after this program has been terminated.

Conclusions

The data are highly suggestive that there is a decrease in ovostatin activity as the concentration of the protein falls below 0.06 mg/ml. This may not be of any physiological importance, however, since the concentration of ovostatin in the egg is about 0.5 mg/ml. Curiously, the dissociation of the tetramer into dimers does not show a significant temperature dependence as would be expected for an equilibrium reaction. Whether this is in fact the case, or whether the differences are so small as to not be discerned from the current data remains to be seen. Another aspect to consider, is that in the egg the primary role of the ovostatin may or may not be as a protease inhibitor. Although the inhibition of collagenase by ovostatin may be an important aspect of embryogenesis, it is also possible that it functions as a binding protein for some substance. In this regard, all ovostatin preparations from MSFC have shown an approximately 88,000 MW protein associated with the ovostatin. The identity of this protein is not currently known and may be the subject of future studies.

References

1. Nagase, H. and Harris, E.D., Jr. (1983) *J. Biol. Chem.* 258, 7481-7489.
2. Kato, A., Kinemitsu, T. and Kobayashi, K. (1991) *J. Agric. Food Chem.* 261, 41-43.
3. Nagase, H., Harris, E.D., Jr. and Brew, K. (1986) *J. Biol. Chem.* 261, 1421-1426.
4. Ikai, A., Kikuchi, M. and Nishigai, M. (1990) *J. Biol. Chem.* 265, 8280-8284.
5. Ruben, G.C., Harris, E.D., Jr. and Nagase, H. (1988) *J. Biol. Chem.* 264, 2861-2869.
6. Sjorberg, B. and Sarolta, P. (1989) *J. Biol. Chem.* 264, 14686-14690.

112583

352847

N95-18998

1994
NASA/ASEE SUMMER FACULTY FELLOWSHIP PROGRAM
MARSHALL SPACE FLIGHT CENTER

THE UNIVERSITY OF ALABAMA
ERROR CODING SIMULATIONS IN C

221-17
30921
P-5

Prepared by:	Viveca K. Noble
Academic Rank :	Instructor
Institution and Department	Tuskegee University Department of Electrical Engineering
MSFC Colleagues:	Bernd K. Seiler Helen L. Thomas
NASA/MSFC:	
Office:	Astrionics Laboratory
Division:	Computers and Data Management
Branch:	Flight Data Systems

Introduction

When data is transmitted through a noisy channel, errors are produced within the data rendering it indecipherable. Through the use of error control coding techniques, the bit error rate can be reduced to any desired level without sacrificing the transmission data rate.[2]

The Astrionics Laboratory at Marshall Space Flight Center has decided to use a modular, end-to-end telemetry data simulator to simulate the transmission of data from flight to ground and various methods of error control. The simulator includes modules for random data generation, data compression, Consultative Committee for Space Data Systems (CCSDS) transfer frame formation, , error correction/detection, error generation and error statistics . The simulator utilizes a concatenated coding scheme which includes CCSDS standard (255,223) Reed-Solomon (RS) code over $GF(2^8)$ with interleave depth of 5 as the outermost code, (7, 1/2) convolutional code as an inner code and CCSDS recommended (n, n-16) cyclic redundancy check (CRC) code as the innermost code, where n is the number of information bits plus 16 parity bits. The received signal-to-noise for a desired bit error rate is greatly reduced through the use of forward error correction techniques. Even greater coding gain is provided through the use of a concatenated coding scheme.[4] Interleaving/deinterleaving is necessary to randomize burst errors which may appear at the input of the RS decoder.[5] The burst correction capability length is increased in proportion to the interleave depth.[2] The modular nature of the simulator allows for inclusion or exclusion of modules as needed. This is a cost-effective means of determining optimal error control schemes for a given error distribution.

System Description, Initial Development and Results

A block diagram illustrating the operation of the simulator is shown in Figure 1.

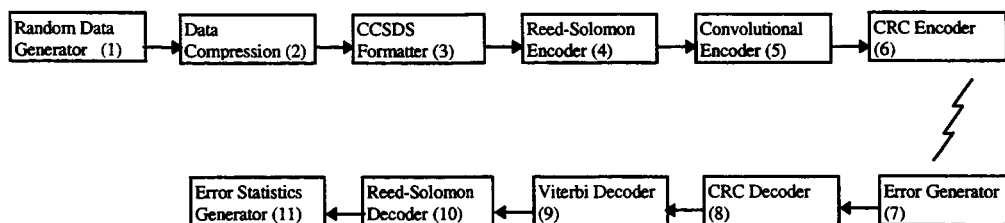


Figure 1

In the initial development phase of the simulator, modules (1), (3), (6), (7), (8) and (11) were developed in FORTRAN and the code simulating the CRC encoder and decoder shown in Figures 3 and 4, respectively, were verified for up to 3 random errors. The CCSDS formatter inserts a 32-bit sync marker (1ACFFC1D_{hex}) and stores the 48 bits immediately following the sync marker as header information as shown in Figure 2. The following recommendations and/or tasks resulted from this work: [4]

- Convert simulation programs from FORTRAN to C
- Determine appropriate error distributions
- Develop Reed-Solomon and convolutional code simulator programs
- Add data compression modules
- Develop more refined and flexible error generator program

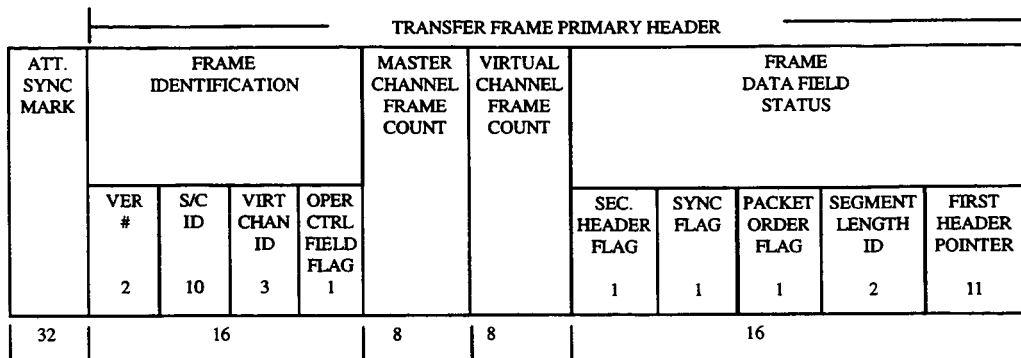


Figure 2

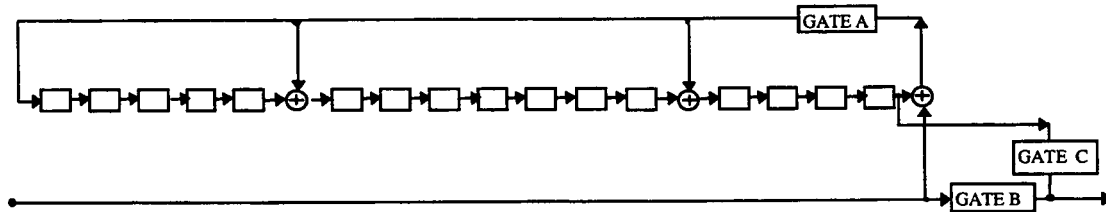


Figure 3

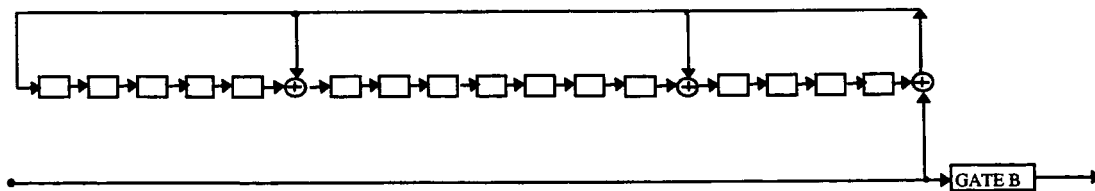


Figure 4

Intermediate Development and Results

Code which was written during the initial development phase has been converted to C due to the flexibility of the language. It was determined that random errors are represented by an additive white Gaussian distribution and bursts are represented by a Markov Chain model.[1]

The error generator that was developed initially was random in nature; in order to be “more refined and flexible”, the error generator should possess the ability to generate random, burst and a combination of random and burst errors. Code written in C that simulates a RS encoder/decoder [Rockliff, Simon- University of Adelaide] was obtained from an Internet users’ group. The testing of the code in various bit error rate environments is a continuous process due to the very purpose of the simulator which is to determine optimal error control schemes for a given error distribution.

Encoding for the RS code mentioned above is in systematic form and the Berlekamp iterative algorithm is used for decoding. The code may be modified to suit particular needs, that is, one may specify m (any positive integer), n (the length of the codeword), k (the length of the information string) and t (the number of errors that can be corrected). Also, the irreducible polynomial must be specified to generate the Galois field, $GF(2^m)$. These polynomials may be found in [2]. In its present form, the code does not handle erasures but may be modified to do so by using the Berlekamp-Massey algorithm. In addition, it does not attempt to decode beyond the BCH bound.[Rockliff, Simon - University of Adelaide]

Research regarding various error control coding and increases in coding gain revealed that that increases in coding gain resulted in increases in decoding complexity. The degree of decoding complexity far exceeded the degree to which the coding gain increased. Thus, hardware implementation of such a decoder was not justified.[3]

Exploration of Software Tools

In addition to developing its own telemetry data simulator, the Astrionics Laboratory is investigating the possibility of using Comdisco SPWTM in its efforts to determine optimal error control schemes. SPWTM (Signal Processing WorksystemsTM - a trademark of Comdisco) has built-in libraries for data generation, noise generation, RS encoding and convolutional encoding. One may create various coding schemes by arranging and rearranging these software modules. During construction of the error control coding scheme, only block diagrams representing its components may be seen. However, one may “step down” by levels and view the circuit diagram of the encoders as well as the C code which was written to simulate each component. Since there are library functions for the components, encoders may also be “constructed” from circuit diagrams by simply drawing the circuit in the SPWTM environment. This software tool is phenomenal.

Conclusion and Future Tasks

The C code for the Reed-Solomon has been verified. Research regarding algorithms for burst error generation, data compression and convolutional encoding will continue. Once obtained, code for these modules will be written and verified. Once all modules are complete, they will be compared to their hardware equivalents, if application, to verify the correct operation of the software. Investigation into the possibility of using SPWTM to verify the software will continue.

References

- [1] Berman, Ted and Dr. Jeffrey Freeman, *Non-interleaved Reed-Solomon Coding Over A Bursty Channel*, Communications - Fusing Command, Control and Intelligence Conference, Vol. 2, 1992, p. 580
- [2] Lin, Shu, Daniel J. Costello, Jr., *Error Control Coding: Fundamentals and Applications*, Prentice Hall, Inc., Englewood Cliffs, N.J., 1983, pp. 1, 28, 272
- [3] Lin, Shu, Daniel J. Costello, Jr., Warner H. Miller, James C. Morakis, William B. Poland, Jr., *Bandwidth Efficient Coding for Satellite Communications*, NAG 5-931 and NAG 5-557
- [4] Noble, Viveca K., *Error Coding Simulations*, Final Report, Contract NASA, CR-193862, August 1993, p.1
- [5] Siveski, Z., Bozovic, R., Schilling, D. L., *Concatenated Trellis/High-Rate Reed-Solomon and Projection Codes*, IEEE International Conference on Communications, Vol.1, 1989, p. 563

112584

352848

N95-18999

1994

30922
p. 6

NASA/ASEE SUMMER FACULTY FELLOWSHIP PROGRAM

**MARSHALL SPACE FLIGHT CENTER
THE UNIVERSITY OF ALABAMA**

A NEW PISTON CONTROL STRATEGY FOR SEGMENTED MIRRORS

Prepared by: Philip D. Olivier
Academic Rank: Associate Professor
Institution and Department: Mercer University
Electrical and Computer Engineering

NASA/MSFC:

Laboratory: Astrionics
Division: Optics and Radio Frequency
Branch: Optical Fabrication

MSFC Colleagues: Steven Fawcett
Henry Waites

INTRODUCTION

One approach to the adaptive control of large segmented mirrors¹ involves sending tilt commands to each segment and allowing each segment to minimize the distance between its edges and those of (all or some of) its neighbors. This approach has been adopted in the Phased Array Mirror, Extendible Large Aperture, PAMELA™, testbed now located at NASA's Marshall Space Flight Center, Huntsville, AL. This approach minimizes 1) the communication between the sensors and the segment actuators and 2) computations required by the central controlling computer. When fully implemented, the PAMELA™, concept envisions that each mirror segment will be equipped with integrated computational ability on the same silicon substrate that provides the mirrored surface. This integration is consistent with either analog, digital, or hybrid computational components. In the current PAMELA™ testbed the edge matching computations occur in digital electronics that are not integrated into the mirror segments and the edge matching actuators are voice coil actuators with enhanced damping.

To reduce the cost of sensors, and hence segments, no absolute piston sensors are implemented. This means that the edge sensors that provide the relative position of a segment with respect to three of its six neighbors are the only data used by a segment to adjust its piston. In fact, each segment adjusts its piston according to the following algorithm:

$$1) \quad p_{\text{new}} = p_{\text{old}} + (e_1 + e_2 + e_3)/3$$

This algorithm is called the 3-edge inner algorithm. Currently, a segment does not know its p_{old} , nor does it know e_1 , e_2 , or e_3 separately. The inner algorithm was chosen by trading off between performance (i.e. edge matching ability or the ability to achieve a smooth surface), implementational complexity, speed, and communication requirements¹ within an analog implementation environment.

This report discusses issues that large segmented mirrors built around the PAMELA™ concept (such as SELENE) will face when they migrate to integrated, and presumably to digital, on-segment computational ability and high bandwidth response. This paper relies on the background in adaptive optics found in Tyson's book³ and on the specifics of the PAMELA concept found in Rather's summary¹. An interesting account of a global approach to piston control can be found in the paper by Enguehard and Hatfield².

PROBLEMS WITH DIGITAL IMPLEMENTATION

A simulation of a 36 segment PAMELA™ concept mirror under digital piston control with perfect (both speed of response and length of movement) actuators indicates 2 potentially serious problems that result from the attempt to limit global communication. The first problem is delay induced chatter, and the second problem is periphery-to-periphery delay. Solutions to these

problems are suggested that rely only on simple modifications of the existing local communication based on the segment edge sensors. The delay induced chatter problem will appear in any size mirror under true digital control, whereas the periphery-to-periphery delay problem will become worse as the mirror size increases.

Delay induced chatter. Consider the mirror shown in Figure 1 where the sensors are indicated by dots. Suppose that the mirror has adjusted itself correctly according to the inner algorithm and let the horizontally shaded segment be rotated about the x-axis. How long will it take for the moved segment to sense its own motion? Initially it will not be able to sense its own motion because its 3 o'clock sensor will not move relative to its neighbor, whereas its 7 o'clock sensor will move up and its 11 o'clock sensor will move down identical amounts hence the inner algorithm calculates its new piston to be identical to the old piston. Even though the moved segment will not sense its movement, two of its neighbors will sense movement. These segments are numbered 1 in the figure. At the first control cycle after the initial movement, these segments will move to balance their errors. At the second control cycle after the initial movement, neighbors of these segments, segments numbered 2, will sense movement and adjust to balance their errors. At the third control cycle, the initial movement will be sensed by the segment that initially moved. This phenomenon gives rise to a chatter in the output that has a period of 3 iterations. As can be seen in Figure 2, the magnitude of this chatter can be significant i.e. about 5%.

Periphery-to-periphery delay. Consider the mirror shown in Figure 3 with sensors indicated by dots. Suppose that the mirror has adjusted itself correctly according to the inner algorithm and let the shaded segment be moved in either piston or tilt. How long will it take for the segment furthest away to sense its motion? The segment-to-segment communication takes about 9 iterations for initial partial information to arrive. The information is partial because each segment adjusts to the average of its edge errors, so the full impact of the initial motion is not instantaneous on its neighbors. As can be seen in Figure 2 the settling time is about 20 iterations.

These problems are less significant in analog implementations for two reasons. First, the delay induced chatter will be reduced by any damping in the analog actuators and second, some communication is virtually instantaneous (i.e. about as fast as the speed of sound in the material). But in a digital implementation the delay induced chatter will be significant for any size mirror regardless of the iteration cycle time and the periphery-to-periphery delay will be important once the mirror exceeds some size that is dependent on the iteration cycle time. For example, a 200,000 segment mirror has about 400 rings of segments. It will take 800 iterations for preliminary information to traverse the structure. If the piston loop must have a bandwidth of 1 kHz (settling time significantly less than 10^{-3} seconds) and if it takes 4 periphery-to-periphery exchanges for the surface to settle down,

the each segment must perform its calculations (3 additions and 1 division) significantly faster than $(1/1.6)*10^{-6}$ seconds. The periphery-to-periphry delay has been recongnized and it has been suggested that for mirrors with very many segments, that an enhanced algorithm¹ be implemented that includes absolute piston sensing and command for some segments that are distributed throughout the mirror.

SOLUTIONS

This report suggests solutions to these two problems and evaluates the solutions via simulation. The solution to the delay induced chatter is called **algorithmic damping**, and the solution to periphery-to-periphery delay involves the introduction of **spines**.

Algorithmic Damping. The solution to the delay induced chatter problem is to introduce damping into the piston control problem. For each segment adjust the piston according to

$$2) \quad p_{new} = p_{old} + \epsilon(e_1 + e_2 + e_3)/3 \quad 0 < \epsilon < 1$$

When $\epsilon = .99$ simulations indicate that oscillations remain but damp out. For $\epsilon = .9$ simulations indicate that oscillations virtually disappear, see Figure 3.

Spines. Consider some segments that do not look at three of their neighbors. These segments take their commands directly from only one of their neighbors. The motivation for this is to speed communication through the structure. For this study 3 spines that radiate from the center were investigated, see Figure 4. Figure 5 shows the simulation results.

Switching. Simulations were conducted that investigated the initial use of spines followed by switching to the current inner algorithm. The switches occurred after 10 and 20 iterations. This investigation, while preliminary, indicates that it is a potentially useful approach.

Comparisons. The results are summarized in the following table.

	smoothness	max(p) - min(p)	iterations
theoretical best	.0213	.0850	NA
current	.0229	.1097	20
spines	.0228	.1052	13
switch-10	.0229	.1098	14
switch-20	.0229	.1098	21
	$*10^{-3}$	$*10^{-3}$	eyeballed 95% settling time

The settling time when spines are used is significantly better than the inner algorithm. When the switch was made at the 10 iteration, the settling time went to 13, which is still better than

the current algorithm. The surface smoothness is virtually identical regardless of the algorithm used.

CONCLUSIONS

Three conclusions can be drawn from this preliminary study: first, that a digital implementation will require 'algorithmic damping' to reduce delay induced chatter; second, the use of spines will allow larger mirrors to be controlled quicker without the introduction of absolute piston commands to reference segments; and third, that switching from the use of spines to independent segments appears to be useful strategy for large mirrors. Such switching should also be useful when using reference segments. That is, a segment might initially be a reference segment and receive an absolute piston command to speed up control communications, and then after a few iterations it might become an independent edge matching segment to enhance surface smoothness.

QUESTIONS

This study suggests several questions. Among them:

Should spines branch out for larger mirrors?

What percentage of the segments can/should be on a spine?

How many segments can be controlled with spines?

What is the optimal switching strategy?

REFERENCES

1. J. D. G. Rather, Power Transmission Optics Issues: SELENE Optics, NASA report, May 1991.
2. S. Enguehard and B. Hatfield, An exact analytic solution to segmented-mirror adaptive-optics control, J. Opt. Soc. Am. A/Vol. 11, No. 2/ Feb. 1994, pp. 874 - 879.
3. R. K. Tyson, Principles of Adaptive Optics, 1991, Academic Press, Inc, Boston.

FIGURES

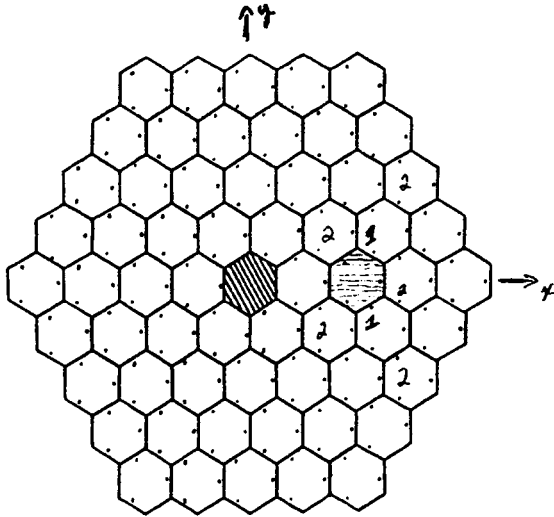


Figure 1. Delay induced chatter explanation

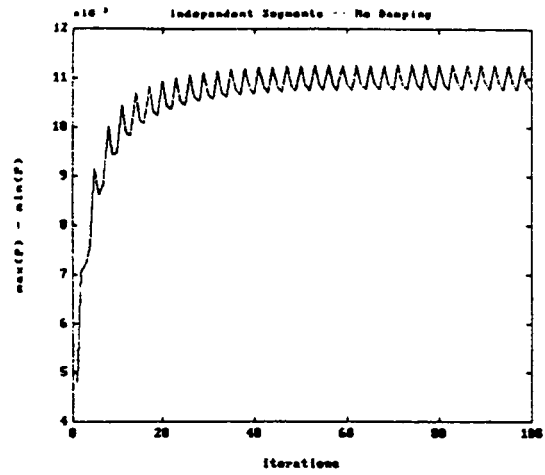


Figure 2. Delay induced chatter simulation

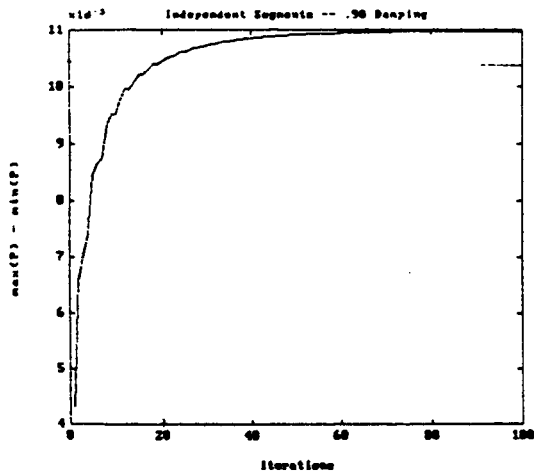


Figure 3. $\epsilon = .9$ algorithmic damping

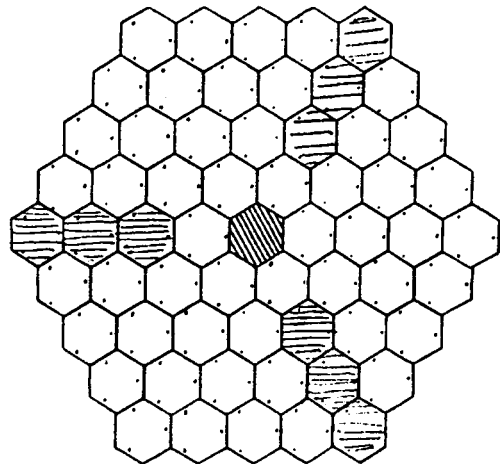


Figure 4. 3 Radial Spines

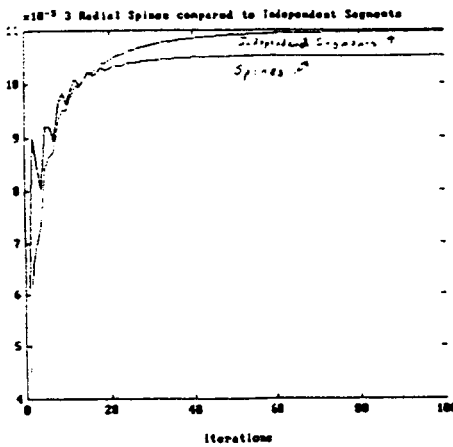


Figure 5. 3 Radial Spine simulation results

352849
N95-19000

7

112585

30923
1.7

1994

NASA/ASEE SUMMER FACULTY FELLOWSHIP PROGRAM

**MARSHALL SPACE FLIGHT CENTER
THE UNIVERSITY OF ALABAMA**

**GROWTH OF THIN FILMS OF DICYANOVINYLANISOLE
ON QUARTZ AND TEFLON-COATED QUARTZ
BY PHYSICAL VAPOR TRANSPORT**

Prepared By: Earl F. Pearson, Ph.D.
Academic Rank: Professor
Institution and Department: Western Kentucky University
Department of Chemistry

NASA/MSFC:

Laboratory: Space Sciences
Division: Microgravity Science and Application
Branch: Thin Films

MSFC Colleagues: Benjamin Penn
Donald Frazier

INTRODUCTION

For a number of years now, nonlinear optics has been a field receiving intense research effort. This activity has been spurred by the tantalizing potential for developing optical equivalents of wires (wave guides), switches and gates (threshold sensitive devices). In theory, at least, these may be formulated and interconnected to produce all-optical computers, holographic pattern recognition devices and electro-optical modulators and multiplexers. Such optical devices can carry much more information and operate at the speed of light.

Early work in nonlinear optical devices centered around inorganic crystalline materials such as quartz, potassium dihydrogen phosphate and lithium niobate and more recently of materials such as KTiOPO_3 , BaB_2O_4 , and LiB_3O_5 . Organic materials are now receiving attention due to the discovery of organic crystals with nonlinearities which are orders of magnitude greater than that of the best inorganic crystals.

Organic compounds offer the possibility of molecular engineering in order to optimize the nonlinearity and minimize damage due to the high-power laser used in such devices. Recently dicyanovinylanisole (DIVA), {[2-methoxyphenyl]methylenepropanedinitrile} has been shown to have a second order nonlinearity 40 times that of α -quartz(1).

Organic crystalline materials have disadvantages for fabrication into optical devices because they often lack the mechanical stability required for grinding and polishing into high-quality optical surfaces. Thin crystalline films may offer the advantages of organic crystals without the need for further mechanical fabrication.

Orientalional order of the organic molecules is important to the production of nonlinear optical signals from bulk samples(2). Many techniques have been used to bring organic molecules into bulk orientational order. These include: Langmuir-Blodgett films(3,4,5), stretched polymeric films(6), electric field (corona discharge) poling(7,8,9,10), growth on oriented Teflon(11) and vapor deposition(12,13,14,15).

Debe *et.al.* (16,17,18) have shown that a high degree of orientational order exists for thin films of phthalocyanine grown by physical vapor transport in microgravity. The microgravity environment eliminates convective flow and was critical to the formation of highly ordered dense continuous films in these samples.

This work seeks to discover the parameters necessary for the production of thin continuous films of high optical quality in Earth gravity. These parameters must be known before the experiment can be planned for growing DIVA in a microgravity environment. The microgravity grown films are expected to be denser and of better optical quality than the unit gravity films as was observed in the phthalocyanine films.

EXPERIMENTAL

DIVA was prepared by reaction of o-methoxybenzaldehyde with malononitrile in a single-step reaction. The resulting compound was separated from unreacted starting material and purified by fractional crystallization from acetone solution(19). The molecular structure is shown in Figure 1 below.

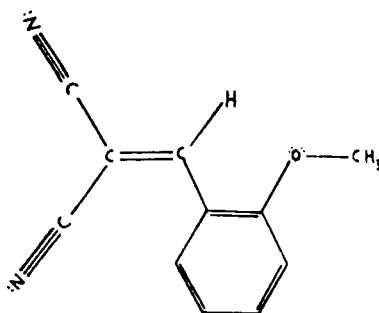


Figure 1 Molecular Structure of DIVA

Two features of the molecular structure of DIVA are important to its high nonlinear optical properties. These are extensive π -electron delocalization and a planar configuration which preserves the overlap of orbitals necessary for the delocalization. The planar configuration is the result of hydrogen bonding between the vinyl hydrogen and the oxygen atom on the ortho position of the aromatic ring. DIVA crystallizes in the $P2_1$ noncentrosymmetric space group of the monoclinic crystallographic system(1).

The physical vapor transport apparatus is shown in Figure 2.

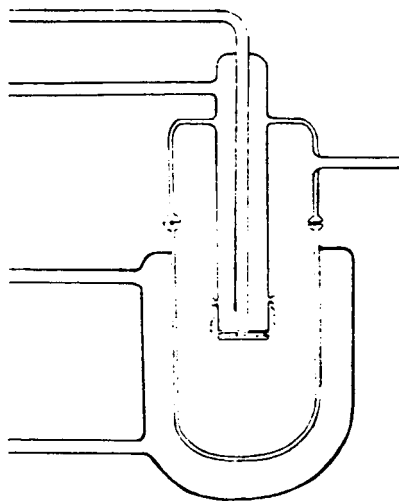


Figure 2 Physical Vapor Transport Apparatus

The optimum conditions for growth of good quality films were: a substrate temperature between 0 and 5°C, a sample temperature between 20 and 45°C, a cell pressure between 5 and 30 millitorr and a deposition time between 1 and 3 minutes.

The quality of the films was examined under polarized light using a Zeiss Ultraphot II optical microscope. The magnification was approximately 100X. Films were viewed in both reflectance and transmittance. Transmittance was used to observe the extinction of single-crystalline areas as the polarization of the analyzer was changed. This allows an estimate of the size of single crystalline areas within the film. All photographs (used in later figures) were taken in reflectance mode because more surface details were visible making it easier to judge the quality of the resulting film.

Film Stability

When initially deposited, the films appear amorphous, being composed of randomly oriented small specks with no indication of the linear edges and fixed angles characteristic of crystalline materials. (See Figure 3--Left Side.) However, within a matter of minutes the smaller particles begin to disappear and small crystals begin to form. Typically, within 24 hours, most of the evidence of the amorphous film will have vanished and well-defined crystal plates will have formed. (See Figure 3--Right Side.)

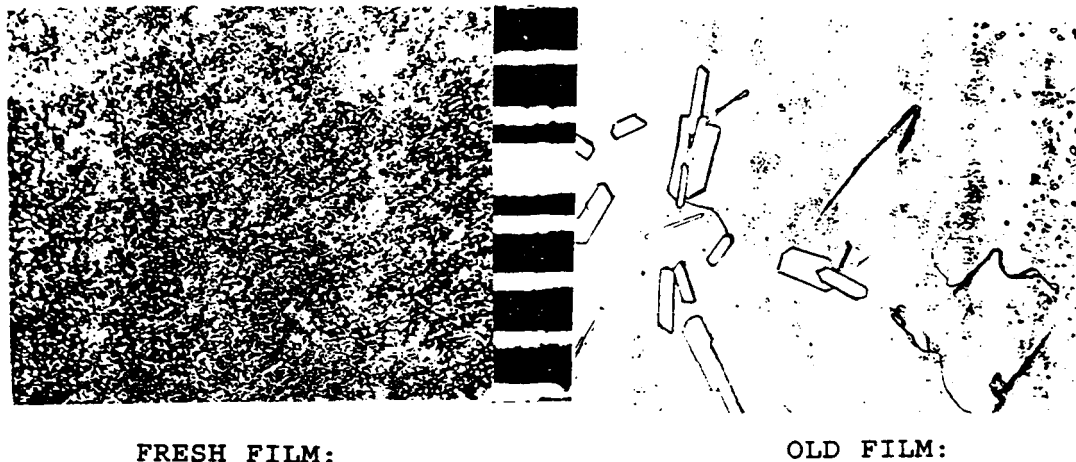


Figure 3 Film Stability
The spacing between the small white lines in the center of the figure is 0.1 mm.

This behavior is observed for both Teflon coated and uncoated fused quartz substrates. At substrate temperatures greater than 10°C, and pressures greater than 150 millitorr, crystalline material is formed initially and the amorphous film is not observed.

At temperatures below 5°C, the initial film is composed of randomly positioned super-cooled liquid droplets which crystallize within a matter of minutes. During the time that crystals are forming and growing, the smallest drops disappear and larger ones in the vicinity grow even larger. This is similar to the process known as Ostwald ripening by which vapor is transported from small droplets to larger ones. The driving force for migration is the surface free energy of molecules on droplets. The surface free energy decreases as the radius of curvature increases.

Film Uniformity

While most of the film appears uniform, a small region around the edge is quite different. The edges tend to be more thickly coated than the center while the amorphous film is present. After the film has reached equilibrium, the center appears coated with small micro crystals with their long axis lying in the plane of the film but randomly placed on the surface of the substrate. (See Figure 4--Left Side.) The edge is covered with crystalline material with no linear sides and no definite angles. Under polarized light, the edge is found to be composed of large irregularly shaped plates with the same orientation of crystallographic axes. (See Figure 4--Right Side.)



Figure 4 Film Uniformity

The spacing between the small white lines in the center of the figure is 0.1 mm.

Teflon Coated Substrates

Pooley and Tabor(20) showed that thermoplastic polymers form oriented films when frictionally transferred to flat substrates. Since this early work, others have used atomic force microscopy to show that a Teflon film surface is composed of separated aligned molecules in which the individual fluorine atoms are resolved(20,21). It has also been demonstrated that these films are also effective in orienting other molecules which are deposited on them(11).

The crystalline films shown in Figure 4 were deposited on Teflon coated quartz substrates. It is obvious that voids between the micro crystals follow the drag direction on the Teflon film (vertical). It is also noted that the long axis of the micro crystals are somewhat ordered relative to this direction also. The most dominant angle is about 45° . It is intriguing that the fluorine atoms follow a helical twist angle of about 42° relative to the molecular axis.

DISCUSSION

The observations of this work can be qualitatively explained by assuming that the topography of the surface of the substrate gives rise to regions of varying attractive potential energy for DIVA molecules. The regions of lowest potential energy are probably randomly (not isotropically) ordered. Most sites are probably much farther apart than the distance between

DIVA molecules in single crystals. The DIVA molecules migrate along the surface finding the minimum energy for the entire assembly. The surrounding temperature provides the thermal energy necessary (activation energy) for moving molecules from site to site along the surface until a suitable seed crystal fragment is formed. (The migration of molecules might also occur through a supercooled liquid layer on the surface.)

The "edge effect" might arise from a temperature difference between the center and the edge of the substrate, a radial temperature gradient along the gas layer in contact with the substrate, or convective flow around the edges of the substrate.

It is found that a crystalline film similar to that observed on the edges is formed at low temperatures (0°C). This would seem to indicate that the isotropic film has a low activation energy for migration. At low temperature, the amorphous film forms "droplets" of supercooled liquid. The slower migration at lower temperature produces fewer seed crystals, resulting in larger, more irregularly shaped crystal fragments which merge into each other.

RECOMMENDATIONS

All the results should be reproduced as similar studies are carried out involving other organic compounds. If these effects are common to other materials, the temperature and pressure should be referenced to the critical temperature and pressure to see if a pattern exists. The kinetics of transition between the amorphous and the crystalline forms should be studied.

Since the interest in these films is for their nonlinear optical properties, techniques for protecting the film should be investigated. Perhaps they could be coated with a polymer film or other material.

The orientation of DIVA molecules in the films would be measured using polarized infrared spectroscopy as has been done for other films (16,23,24,25). It would also be interesting to study the films formed on cleaved crystalline substrates such as quartz, KBr and NaCl.

LITERATURE CITED

1. T. Wada, C. H. Grossman, S. Yamada, A. Yamada, A. F. Garito and H. Sasabe, Mat. Res. Soc. Symp. Proc., 1990, 173, 519-524.
2. J. D. LeGrange, M. G. Kuzyk, and K. D. Singer, Mol. Cryst. Liq. Cryst., 1987, 150, 567-605.
3. K. Ogawa, I. Yonehara, T. Shoji, S. Kinoshita, and E. Maekawa, Thin Solid Films, 1989, 178, 439-443.
4. Y. Tomioka, S. Imazeki, and N. Tanaka, Chem. Phys. Lett., 1990, 174, 433-437.

5. W. Yan, Y. Zhou, X. Wang, W. Chen, and S. Xi, Chem. Comm., 1992, 873-875.
6. M. Wan, M. Li, J. Li, and Z. Liu, J. Appl. Poly. Sci., 1994, 53, 131-139.
7. M. A. Mortazavi, A. Knoesen, and S. T. Kowel, J. Opt. Soc. Am. B, 1989, 6, 733-741.
8. M. G. Kuzyk, K. D. Singer, H. E. Zohn, and L. A. King, J. Opt. Soc. Am. B, 1989, 6, 742-752.
9. K. D. Singer, J. E. Sohn, and S. J. Lalama, Appl. Phys. Lett., 1986, 49, 248-250.
10. M. G. Kuzyk, R. C. Moore, and L. A. King, J. Opt. Soc. Am. B, 1990, 7, 64-71.
11. J. Whittman and P. Smith, Nature, 1991, 352, 414-417.
12. T. Kanetake, *et. al.* Appl. Phys. Lett., 1989, 54, 2287-2289.
13. C. J. Liu, M. K. Debe, P. C. Leung, and C. V. Francis, Appl. Phys. Comm., 1992, 11, 151-164.
14. P. V. Shibaev and M. B. Guseva, J. Cryst. Growth, 1992, 119, 399-402.
15. M. S. Paley, D. O Frazier, H. Abeledeyem, S. P. McManus and S. E. Zutaut, J. Am. Chem. Soc. 1992, 114, 3247-3251.
16. M. K. Debe, *et.al.*, Thin Solid Films, 1990, 186, 257-288.
17. M. K. Debe and K. K. Kam, Thin Solid Films, 1990, 186, 289-325.
18. M. K. Debe and R. J. Poirier, Thin Solid Films, 1990, 186, 327-347.
19. Ronald Clark, Chemistry Department, New Mexico Highland University., Private Communication, 1994.
20. C. M. Pooley and D. Tabor, Proc. R. Soc. Lond. A, 1972, 329, 251-274.
21. H. Hansma, *et. al.*, Polymer, 1992, 33, 647-649.
22. P. Dietz, *et. al.*, J. Mat. Sci., 1993, 28, 1372-1376.
23. R. G. Greenler, J. Chem. Phys., 1966, 44, 310-315.
24. M. K. Debe, J. Appl. Phys., 1984, 55, 3354-3366.
25. M. K. Debe and T. N. Tommett, J. Appl. Phys., 1987, 62, 1546.

112586

352850
N95-19001

17

1994

30924

p. 6

NASA / ASEE SUMMER FACULTY FELLOWSHIP PROGRAM

MARSHALL SPACE FLIGHT CENTER
THE UNIVERSITY OF ALABAMA

**TWO SPACE SCATTERER FORMALISM CALCULATION
OF BULK PARAMETERS OF THUNDERCLOUDS**

Prepared by:
Academic Rank:

Dieudonné D. Phanord, Ph.D.
Associate Professor

Institution and
Department:

University of Wisconsin at Whitewater
Department of Mathematics
and Computer Science

NASA / MSFC:
Laboratory:
Division:
Branch:

Space Science
Earth Sciences / Applications
Remote Sensing

MSFC Colleagues:

William Koshak
Richard Blakeslee
Hugh Christian

I. INTRODUCTION

In (1), the single space scatterer formalism based on (2) is used to evaluate the bulk parameters of a cloud illuminated from outside. The single space scatterer formalism allows an obstacle excited by an incident wave traveling in free space to radiate in free space. The calculations of (1) took only into account contributions due to dry air and water. The approximations for the attenuation agree closely with those obtained using number density and the scattering cross section of water drops. The results are obtained directly and they represent a solid starting point for subsequent developments.

In (3), we used a modified two-space scatterer formalism of Twersky (4) and (5) to establish for a cloud modeled as a statistically homogeneous distribution of spherical water droplets, the dispersion relations that determine its bulk propagation numbers K_j and bulk indexes of refraction η_j ($j=1,2$) in terms of the vector equivalent scattering amplitude \vec{G} and the dyadic scattering amplitude \vec{g} of the single water droplet in isolation. The results of (3) were specialized to the forward direction of scattering while demanding that the scatterers preserve in the sense of (5), the incident polarization. This requirement did allow us in (3) to drop the subscript j and to look for K and η .

Here, we apply (3) to obtain specific numerical values for the macroscopic parameters of the cloud. We work as in (6), with a cloud of density $\rho=100\text{ cm}^{-3}$, a wavelength $\lambda=0.7774\text{ }\mu\text{m}$, and with spherical water droplets of common radius $a=10\text{ }\mu\text{m}$. In addition, the scattering medium is divided into three parts, the medium outside the cloud with propagation parameter $k_o = \frac{2\pi}{\lambda} = 8.0823\text{ }\mu\text{m}^{-1}$, moist air (the medium inside the cloud but outside the droplets) corresponding to $\kappa_1 = k_o\eta_1$, and the medium inside the spherical water droplets specified by $\kappa_2 = \kappa_1\eta_2$. The physical constants η_1 , and $\eta_2 = 1.33+i7.33 \times 10^{-8}$ (from (7)) are the relative indexes of refraction of moist air and water respectively. The numerical values of K and η are important to the innovative work of (8) for lightning due to point sources inside the cloud.

In this modified two-space scatterer formalism, a single spherical water droplet is allowed to be excited by a wave traveling in K -space (the space of the equivalent medium) but to radiate in κ_1 -space instead of the usual free or k_o -space. This is possible since we have a sparse distribution of scatterers (i.e., the particles in the distribution are located at a significant distance away from each other as compared to their radius) and the boundary correction terms due to back and forth reflections from κ_1 -space to k_o -space or vice versa are negligible.

The results of this report are applicable to a cloud of any geometry since the boundary does not interfere with the calculations. Also, it is important to notice the plane wave nature of the incidence wave $\vec{\phi}_1$ in the moist atmosphere. Should the cloud be of a geometry such that its direct response to an initial outside excitation $\vec{\phi}_o$ be of spherical type, one would have to make the plane wave approximation in order to apply the work of Twersky. The theory of Twersky is mostly suitable for a slab distribution of scatterers. However, it can be extended to cover the present problem without a loss of generality since the contributions of the boundary layer surfaces are small and most lightning activities usually occur inside the cloud.

In order to avoid repetition, we cite key equations of (3-5, 10). In general, we work in spherical coordinates. We use bold face or an arrow to denote a vector or a vector operator. A circumflex indicates a vector of unit magnitude. A tilde on the top of a letter denotes a dyadic (second rank tensor). For brevity, we use [5:4] for equation 4 of Re. (5) etc.

II. MATHEMATICAL ANALYSIS

For an incident plane harmonic electromagnetic wave $\vec{\phi}_1 = \hat{\mathbf{a}}_1 e^{i(\vec{\kappa}_1 \cdot \mathbf{r} - i\omega t)}$ in the moist air due to an initial outside excitation $\vec{\phi}_0$ of the cloud, the self-consistent integral equation governing the multiple configurational scattering amplitude as in (5) is

$$\mathbf{G}_i(\hat{\mathbf{r}}) = \tilde{\mathbf{g}}_i(\hat{\mathbf{r}}, \hat{\kappa}_1) \cdot \hat{\mathbf{a}}_1 e^{i\vec{\kappa}_1 \cdot \mathbf{r}_i} + \sum'_c \int \tilde{\mathbf{g}}_i(\hat{\mathbf{r}}, \hat{\mathbf{r}}_c) \cdot \mathbf{G}_m(\hat{\mathbf{r}}_c) e^{i\vec{\kappa}_{1c} \cdot \mathbf{R}_{tm}}, \quad [1]$$

where $\mathbf{R}_{tm} = \mathbf{r}_t - \mathbf{r}_m$, $\int = \frac{1}{2\pi} \int d\Omega_c$. The single dyadic scattering amplitude $\tilde{\mathbf{g}}(\hat{\mathbf{r}}, \hat{\kappa}_1) \cdot \hat{\mathbf{a}}_1 = \mathbf{g}(\hat{\mathbf{r}}, \hat{\kappa}_1 : \hat{\mathbf{a}}_1)$ is defined in (3:4). The magnitude of the separation distance $|\mathbf{R}_{tm}| < D$ (the diameter of the cloud).

After taking the ensemble average of [1], using the quasi-crystalline approximation of Lax (9), the equivalent medium approach, and Green's theorems, the dispersion relations determining the bulk parameters (for more details see (5)) are

$$\vec{\mathcal{G}}(\vec{\kappa}_1 | \vec{K}_j) = -\frac{\rho}{c_0(K_j^2 - \kappa_1^2)} \left\{ \left[e^{-i\vec{K}_j \cdot \mathbf{R}}, \vec{U}_j \right] \right\} + \rho \int_{V_D - v} [f(\mathbf{R}) - 1] e^{-i\vec{K}_j \cdot \mathbf{R}} \vec{U}_j d\mathbf{R}, \quad [2]$$

where $d\mathbf{R}$ denotes volume integration over $(V_D - v)$. Here, $\vec{\mathcal{G}}$ is the equivalent scattering amplitude and \vec{U}_j is a radiative function defined by $\vec{U}_j = \int_c \tilde{\mathbf{g}}(\hat{\mathbf{r}}, \hat{\mathbf{r}}_c) \cdot \vec{\mathcal{G}}(\vec{\kappa}_{1c} | \vec{K}_j) e^{i\vec{\kappa}_{1c} \cdot \mathbf{R}}$, and $c_0 = \kappa_1/4\pi i$. The bulk propagation parameter is $K_j = \kappa_1 \eta_j$ with η_j being the bulk index of refraction, and $\{[f, g]\} = \int_S [f \partial_n g - g \partial_n f] dS$ is the Green surface operator. The ensemble is specified as in (5) by the average number ρ of scatterers in unit volume and by $\rho f(\mathbf{R})$ with $f(\mathbf{R})$ as the distribution function for separation of \mathbf{R} pairs.

Similar to (3), the model is required to neglect all phase transition effects (10) and to take only into account pair interaction due to central forces. Neglecting the inter-droplet potential, the distribution function $f(\mathbf{R})$ can be chosen to be always equal to unity. Hence, [2] is simplified to

$$\left[(K^2 - \kappa_1^2) \tilde{\mathbf{L}}_* + \left(\frac{\rho}{c_0} \right) \tilde{\mathbf{g}}(\hat{\mathbf{r}}, \hat{\mathbf{K}}) \right] \cdot \vec{\mathcal{G}}(\vec{\kappa}_1 | \vec{K}) = 0. \quad [3]$$

In [3], we let $\hat{\mathbf{r}} = \hat{\mathbf{K}}$ and use the fact that the scatterers preserve the incident polarization to transform [3] into

$$(K^2 - \kappa_1^2) = -\left(\frac{\rho 4\pi i}{\kappa_1} \right) g(\hat{\mathbf{K}}, \hat{\mathbf{K}}), \quad \eta^2 - 1 = -\left(\frac{\rho 4\pi i}{\kappa_1^3} \right) g(\hat{\mathbf{K}}, \hat{\mathbf{K}}) \quad [4]$$

where the subscript j is no longer necessary. In [4], the two-space scatterer formalism scattering amplitude corresponding to the spherical droplet, a large tenuous scatterer, must be evaluated in the forward direction of scattering (i.e., $\mathbf{g} = \mathbf{g}(\hat{\mathbf{r}}, \hat{\mathbf{r}}) = \hat{\mathbf{a}}_1 \cdot \mathbf{g}(\hat{\mathbf{K}}, \hat{\mathbf{K}})$). The unit vector $\hat{\mathbf{K}}$, the direction of the bulk propagation vector $\vec{\mathbf{K}}$, is such that $\hat{\mathbf{K}} \cdot \hat{\mathbf{a}}_1 = 0$.

III. NUMERICAL CALCULATIONS

To start the numerical calculations, we use the WKB approximation corresponding to a bulk excitation associated with an incident electric field $\vec{\varphi} = \hat{\mathbf{x}} e^{i\mathbf{K}\hat{\mathbf{z}}\cdot\mathbf{r}}$ for the two-space scatterer formalism scattering amplitude $\mathbf{g} = \mathbf{g}(\hat{\mathbf{r}}, \hat{\mathbf{r}}) = \hat{\mathbf{x}} \cdot \mathbf{g}(\hat{\mathbf{K}}, \hat{\mathbf{K}})$ in the forward direction. The WKB approximation (12) consists of replacing the field inside the scatterer by a field traveling in the direction of the incident excitation which propagates inside the scatterer with propagation constant of the medium of the scatterer. For the two space scatterer formalism, the propagation parameter of the incident wave is different from that of the radiated wave. Therefore, the conventional WKB method is not applicable here. Using a modified version given in (4) and the two space scatterer formalism volume integral representation of the scattered wave, it can be shown that

$$\begin{aligned} \mathbf{g}(\hat{\mathbf{K}}, \hat{\mathbf{K}}) \cdot \hat{\mathbf{x}} &= \frac{i\kappa_1}{4\pi} \mathcal{T} \left[\left(1 - \frac{1}{\mu_2}\right) \kappa_1 \kappa_2 - \left(\kappa_1^2 - \frac{\kappa_2^2}{\mu_2}\right) \right] I_1 \\ &\quad - \frac{i\kappa_1}{4\pi} \mathcal{T} \left[\left(1 - \frac{1}{\mu}\right) \kappa_1 K - \left(\kappa_1^2 - \frac{K^2}{\mu}\right) \right] I_2. \end{aligned} \quad [5]$$

Here, as in (4) and (12),

$$\begin{aligned} \mathcal{T} &= \frac{2}{1 + \frac{\kappa_2 \mu}{K \mu_2}}, \quad I_1 = \frac{2\pi}{i(\kappa_2 - \kappa_1)} \left[e^{iqa} \left(\frac{a}{iq} + \frac{1}{q^2} \right) - \frac{1}{q^2} \right]_{q_1}^{q_2}, \\ q_2 &= 2\kappa_2 - K - \kappa_1, \quad q_1 = \kappa_1 - K, \\ I_2 &= \frac{4\pi}{a(K - \kappa_1)} \left[\frac{\sin[a(K - \kappa_1)]}{a^2(K - \kappa_1)^2} - \frac{\cos[a(K - \kappa_1)]}{a(K - \kappa_1)} \right]. \end{aligned} \quad [6]$$

Inserting [5] into [4] yields the desired results for the bulk propagation number K

$$\begin{aligned} (K^2 - \kappa_1^2) &= \rho \mathcal{T} \left[\left(1 - \frac{1}{\mu_2}\right) \kappa_1 \kappa_2 - \left(\kappa_1^2 - \frac{\kappa_2^2}{\mu_2}\right) \right] I_1 \\ &\quad - \rho \mathcal{T} \left[\left(1 - \frac{1}{\mu}\right) \kappa_1 K - \left(\kappa_1^2 - \frac{K^2}{\mu}\right) \right] I_2 \end{aligned} \quad [7]$$

and the bulk index of refraction η

$$\begin{aligned} (\eta^2 - 1) &= \rho \mathcal{T} \left[\left(1 - \frac{1}{\mu_2}\right) \kappa_2 / \kappa_1 - \left(1 - \frac{\kappa_2^2}{\mu_2 \kappa_1^2}\right) \right] I_1 \\ &\quad - \rho \mathcal{T} \left[\left(1 - \frac{1}{\mu}\right) \eta - \left(1 - \frac{\eta^2}{\mu}\right) \right] I_2 \end{aligned} \quad [8]$$

where the physical constants μ_2 , and μ are the magnetic permeability of the medium inside the water droplet and the bulk magnetic permeability respectively. The formulae for the calculation of μ , and ϵ in the forward direction of scattering are obtained from (11:28)

$$\begin{aligned}\mu^{-1} &= 1 - 2\pi\rho(\mathcal{F} - \mathcal{F}')/\eta\kappa_1^2, \quad \epsilon = 1 + 2\pi\rho(\mathcal{F} + \mathcal{F}')/\kappa_1^2, \\ \mathcal{F} &= \frac{g}{i\kappa_1}, \quad \mathcal{F}' = \mathcal{F}(-\kappa_1).\end{aligned}\quad [9]$$

To work with [7-9], we need to calculate the value of $\kappa_1 = k_0\eta_1 = k_0(\eta_{1r} + i\eta_{1i})$, and $\kappa_2 = \kappa_1\eta_2 = \kappa_1(1.33 + i7.33 \times 10^{-8})$. The real part η_{1r} of η_1 is obtained from the formula given by (13)

$$\begin{aligned}(\eta_{1r} - 1)10^6 &= \left[0.378,125 + \frac{0.002,141,4}{\lambda^2} + \frac{0.000,017,93}{\lambda^4}\right] \\ \times \frac{p\{1 + (1.049 - 0.015t)p \times 10^{-6}\}}{1 + 0.003661t} &- \left[0.0624 - \frac{0.000,680}{\lambda^2}\right] \frac{f}{1 + 0.003661t}\end{aligned}\quad [10]$$

where from (14), f (the vapor pressure at $t=10^\circ C$) = 9,209 mmHg, and the pressure $p = 720$ mmHg is the lowest permissible for [10]. With $\lambda = 0.7774 \mu m$ in [10], we have $\eta_{1r} = 1.00026476$, and $\kappa_{1r} = 8.08443$.

To obtain the imaginary part κ_{1i} of κ_1 , we use the result of (15) for the attenuation of intensity in the air $Ie^{-\alpha d} = 0.8I$, where I is the intensity, $\alpha = 2\kappa_{ai}$ (the subscript a is used to indicate air), and the path is taken to be 11 km. From the above, we have $\kappa_{ai} = 1.014 \times 10^{-11}$. Using Archimedes principle, the value of κ_{ai} , and the sphericity of the water droplets in the cloud, we can write $\kappa_1 = 8.08443 + i1.0446 \times 10^{-11}$, $\kappa_2 = 10.75229 + i5.9260 \times 10^{-6}$.

To proceed with these calculations, we must verify the validity of the approximation that gives [5]. The WKB approximation is valid according to (12) if the host medium is such that $\Re(\kappa_1)2a(\epsilon_{1r} - 1) \gg 1$ and $(\epsilon_{1r} - 1) < 1$ where $\epsilon_1 = \epsilon_{1r} + i\epsilon_{1i}$, $\epsilon_{1r} = \eta_{1r}^2 - \eta_{1i}^2$, $\epsilon_{1i} = 2\eta_{1r}\eta_{1i}$ since the magnetic permeability μ_1 is assumed to be one. In this case, the above conditions are satisfied. From the imaginary part of κ_1 , we deduce the value of $\eta_{1i} = (\kappa_{1i}/k_0) = 1.2924 \times 10^{-12}$.

Equations [7], [8], and [9] form a coupled nonlinear system for the bulk parameters K , η , ϵ , and μ . To solve the system numerically, we approximate the exponential factor of I_1 by its leading term and use the values given in (1) as initial data. Hence, we have

$$\begin{aligned}K &= 8.08442974208285 + i3.14117832893745 \times 10^{-8}, \\ \epsilon &= 1.00000000014550 + i3.87231835597287 \times 10^{-9}, \\ \mu &= 1.00000000014570 + i3.89603100094467 \times 10^{-9}, \\ \eta &= .999999968400000 + i3.88417455500000 \times 10^{-9}, \\ \mathcal{F} &= 15.1452985315156 + i404.033753935163, \\ \mathcal{F}' &= -1.01021251084684 \times 10^{-2} + i1.23330047641423.\end{aligned}\quad [11]$$

The results of [11] are close as expected, to those given in (1). Should the incident wave were magnetic in nature, ϵ and μ would have been interchanged. To improve [11], one

can upgrade the model and construct $f(\mathbf{R})$ numerically. The values given in [11] can be directly applied to the problem of lightning due to point sources located inside the cloud.

ACKNOWLEDGMENT

The author expresses his appreciation to William Koshak, Richard Blakeslee, Hugh Christian, and Richard Solakiewicz for their time, help, and ideas during his appointment as a NASA/ASEE Summer Faculty Fellow. The financial support of the NASA/ASEE Summer Faculty Fellowship Program and the assistance of Michael Freeman, Gerald F. Karr, Director and Frank Six, Administrator, are gratefully acknowledged

References

1. Solakiewicz. R., "Calculations of bulk parameters.", IPA-NASA/Chicago State University, (unpublished) (1993).
2. Twersky, V., "On the scattering of waves by random distributions. I. Free-space scatterer formalism.", *J. Math. Phys.*, 3, 4 (1962) 700-715.
3. Phanord. D. D., "Lrat: Lightning radiative transfer.", NASA-MSFC, Summer (1993), XXXVII.
4. Twersky, V., "On a General Class of Scattering Problems.", *J. Math. Phys.* 3, 4, (1962), 716-723.
5. Twersky, V., "Coherent electromagnetic waves in pair-correlated random distributions of aligned scatterers." *J. Math. Phys.*, 19, 1, (1978), 215-230.
6. Thomason, L. W., and E. P. Krider, "The effects of clouds on the light produced by lightning." *J. Atmos. Sci.*, 39, (1982), 2051-2065.
7. Hale, G. and M. Querry., "Optical constants of water in the 200 μm to 200 nm wavelength region.", *Appl. Opt.* 12, 3 (1973) 555-564.
8. Solakiewicz. R., "Scattering of point source illumination by an arbitrary configuration.", NASA-MSFC, Summer (1994), XXXIX.
9. Lax . M., "Multiple Scattering of Waves." , *Rev. Modern Phys.* 23, (1951), 287-629.
10. H. Eyring, D. Henderson, and W. Jost, *Physical Chemistry, An Advance Treatise*, Volume VIII A (Academic Press, New York, 1971
11. Twersky, V., "On the scattering of waves by random distributions. II. Two-space scatterer formalism.", *J. Math. Phys.*, 3, 4 (1962) 724-734.
12. Ishimaru, A., *Wave Propagation and Scattering in Random Media (Single Scattering and Transport Theory)*, Vol. 1, Academic Press, New York (1978) 12-68.
13. Barrell, H. and J. E. Sears., "The refraction and dispersion of air for the visible spectrum." *Phil. Trans. Roy. Soc. London, A*, 238, (1939), 1-64.
14. *CRC Handbook of Chemistry and Physics*, 66th Ed., R. Weast, Ed., Chemical Rubber Co., Boca Raton, Florida (1985) D190.
15. Kuo. N. L., *An Introduction to Atmospheric Radiation*, Academic Press, New-York, (1980), 28-49.

112587

352851
N95-19002

30725
p. 6

1994

NASA/ASEE SUMMER FACULTY FELLOWSHIP PROGRAM

**MARSHALL SPACE FLIGHT CENTER
THE UNIVERSITY OF ALABAMA**

EVALUATION OF SSME TEST DATA REDUCTION METHODS

Prepared By:

L. Michael Santi, Ph.D.

Academic Rank:

Associate Professor

Institution and Department:

**Christian Brothers University
Mechanical Engineering Department**

NASA/MSFC:

**Laboratory:
Division:
Branch:**

**Propulsion
Motor Systems
Performance Analysis**

MSFC Colleague:

John P. Butas

INTRODUCTION

Accurate prediction of hardware and flow characteristics within the Space Shuttle Main Engine (SSME) during transient and main-stage operation requires a significant integration of ground test data, flight experience, and computational models. The process of integrating SSME test measurements with physical model predictions is commonly referred to as data reduction. Uncertainties within both test measurements and simplified models of the SSME flow environment compound the data integration problem.

SSME performance models require specification of a number of hardware characteristics including turbomachinery maps and other hardware specific parameters. These characteristics are required in order to obtain formal closure of the engine mathematical model. They contain the accumulated historical data base of SSME performance. Each hardware parameter has an uncertainty consistent with the data base dispersion upon which its value is estimated.

Complete specification of SSME performance requires the identification of thermodynamic properties and flow rates throughout the engine system, as well as specification of various hardware characteristics such as valve positions, torques, and speeds. These performance characteristics are obtained by solution of a set of nonlinear relations incorporating the physical requirements of subsystem mass and energy conservation as well as semi-empirical relations for duct/valve pressure losses, turbomachinery performance, and a variety of other hardware specific operating properties. Mathematically the performance prediction problem can be expressed as

$$F(P; H) = 0$$

where

- F - the set of nonlinear physical relations governing SSME performance
- P - the set of solution variables including thermo-fluid properties, etc.
- H - the set of assumed constant hardware characteristics based on past test experience.

Individual engine tests provide indications of specific physical characteristics in set P. If these characteristics are fixed at test values, a like number of hardware characteristics must be allowed to vary in order to satisfy the set of governing equations. The revised data reduction problem can be expressed as

$$F(P_o, H_o ; P^*, H^*) = 0$$

where

- P_o - the remaining set of physical property variables (P-P*)
- H_o - the new set of variable hardware characteristics
- P* - the set of physical conditions fixed by specific test data
- H* - the remaining set of fixed hardware characteristics (H-H_o).

The data reduction process is depicted conceptually in Figure 1. Abscissa values represent hardware characteristics and ordinate values represent physical characteristics. The line $F = 0$ represents combinations of physical and hardware characteristics providing exact solutions to the physical relations. The point (H,P) represents an initial solution prior to new test data input. The point (H*,P*) represents the data reduction solution after incorporation of new test data. Since exact solutions to nonlinear system equations are rare, neither point is on the exact solution curve, however, both must lie within a tolerance limit for convergence.

Uncertainty bands associated with hardware characteristics (UH), physical properties (UP), and model balance relations (UF) are also shown in Figure 1. UH represents uncertainty in the experience base which is associated with the fixed hardware characteristics H. UP represents uncertainty in the physical test measurements and UF represents balance point uncertainty due to model simplification of physical relations.

DATA REDUCTION STRATEGIES

The first objective of this effort was to establish an acceptability criterion for data reduction solutions. Any solution that falls within the uncertainty band intersection depicted in Figure 2 is acceptable. More "exact" reduction techniques which attempt to enforce balance within tight tolerance limits are severely limited by normal dispersions in reduction test data. These dispersions can prevent tight tolerance solution or enforce unrealistic physical balances in an attempt to match data exactly at measurement points.

Within large system projects, the traditional data reduction approach is heuristic. In an effort to match test results precisely, physical relations are relaxed in a simplistic manner. This can lead to questionable results which enforce agreement with the hardware experience base but sacrifice physical consistency [1]. Typical results of a heuristic data reduction techniques are presented in Figure 3. In extreme cases, the desire to match new test data can provide solutions outside the experience base as depicted in Figure 4. Predictions from heuristic reduction strategies often fall outside the common acceptable region described in Figures 2-4. These are at best difficult to defend and at worst provide erroneous predictions costly both in time and resources.

An ongoing effort to improve data reduction capability is currently being supported by NASA/MSFC/EP14. A new approach termed the reconciliation strategy [2] was developed to improve data reduction capability within the existing SSME performance model. The reconciliation method is based on a systematic optimization strategy that incorporates test information, the historical data base, and balance relation uncertainties within a computational procedure that returns the best possible estimate of engine performance characteristics. The reconciliation method requires a physically consistent model of system operation in order to achieve high quality data integration. In another ongoing effort to improve performance prediction capability, NASA supported development of the ROCKET Engine Transient Simulation or ROCETS [3] system. ROCETS is a well documented and structured platform for modeling liquid rocket propulsion systems. It provides a modular high level programming capability for constructing physically consistent engine performance simulations. The ROCETS platform does not, however, explicitly incorporate a data reduction strategy.

SSME ROCETS MODEL DATA REDUCTION PROCEDURE

The second objective of this effort was to investigate the data reduction potential of the ROCETS simulation platform. A simplified ROCETS model of the SSME was obtained from the MSFC Performance Analysis Branch (EP14). This model was examined and tested for physical consistency. Two modules were constructed and added to the ROCETS library to independently check the mass and energy balances of selected engine subsystems including the low pressure fuel turbopump (LPFTP), the high pressure fuel turbopump (HPFTP), the low pressure oxidizer turbopump (LPOTP), the high pressure oxidizer turbopump and preburner pump (HPOTP+PBP), the fuel preburner (FPB), the oxidizer preburner (OPB), the main combustion chamber coolant circuit (MCC clnt), and the nozzle coolant circuit (NOZ clnt).

A sensitivity study was then conducted to determine the individual influences of forty-two hardware characteristics on fourteen high pressure region prediction variables as returned by the SSME ROCETS model. The object of this study was to determine appropriate hardware characteristics to vary in order to match ROCETS predictions with performance variable test data. Table 1 includes a partial listing of normalized sensitivities, defined as the percent change in physical characteristic (left column) divided by the percent change in hardware characteristic (top rows).

A reduction procedure was implemented within the SSME ROCETS model by adding balances that would enforce agreement with specific test measurements. SSME data was obtained from a recent TTB test (TTB-50). Results of the sensitivity study were used to help construct a series of reduction analyses with increasing numbers of measurement anchor points.

SSME ROCETS MODEL DATA REDUCTION RESULTS

The independent balance calculations verified that the SSME ROCETS model obtained mass flow balance in all devices. Energy flows were balanced in all pure component flow systems. However, energy imbalance predictions were relatively large in devices with hot gas flows. Although energy related computations were physically consistent, hot gas enthalpy calculations were performed using a crude ideal gas model. Standard state indexing for combustion calculations was similarly crude. The independent balance module was unable to verify accurate energy calculations in the hot gas region due to the lack of water property data.

Table 2 presents results from the ROCETS SSME data reduction model. Column one contains test data for various SSME internal parameters obtained at 100% rated power level during TTB-50. Column two contains theoretical predictions derived at the corresponding SSME inlet conditions. The next four columns represent adjustments to the theoretical predictions based on matching specific SSME measurements to specific engine hardware characteristics. Of the seventeen parameters evaluated, seven were anchored to test data. The final data reduction results showed that of the ten parameters that were allowed to vary, three moved towards measured test data. These three parameters were characterized within the adjusted engine hardware characteristics. Solutions for the other seven parameters diverged from measured test data. This may be the result of incomplete modeling of the SSME hardware, as well as inherent weakness in the "exact" data reduction strategy. This observation supports the need for a reconciliation strategy which recognizes uncertainty limitations within the physics, test data, and hardware characteristics. Information needed to establish an accurate and fundamentally sound approach to test data reduction has been developed during this effort..

RECOMMENDATIONS

Based on a study of data reduction procedures and experience with the SSME ROCETS model as a data reduction tool, the following recommendations are made:

1. The SSME ROCETS model should be developed as a production level performance prediction platform. Improvement of hot gas property computations is needed to provide confidence in energy computations. SSME system detail should be added to the existing model including POGO flow refinement, repressurization systems, MCC and Nozzle leakage, and pump cavitation computations.
2. A robust reconciliation strategy for system level data reduction should be implemented as an option within the SSME ROCETS model. The reconciliation strategy should be phased in as a replacement for existing heuristic reduction methods.
3. Uncertainty estimates associated with SSME test measurements, hardware characteristics, and model balance relations should be established to provide a logical basis for data reduction.
4. A procedure for systematic updating of SSME hardware performance characteristics within the SSME ROCETS model should be implemented. A method for maintaining model integrity needs to be established.

REFERENCES

1. Santi, L. M., "Validation of the Space Shuttle Main Engine Steady State Performance Model," NASA contract report NGT-01-002-099, 1990.
2. Santi, L. M., "Integrated Model Development for Liquid Fueled Rocket Propulsion Systems," UAH subcontract associated with NASA contract NAG8-212, Task No. 6, June, 1993.
3. "ROCETS System Design Specification," Pratt & Whitney FR-20284, May, 1990.

Figure 1. Data Reduction Process

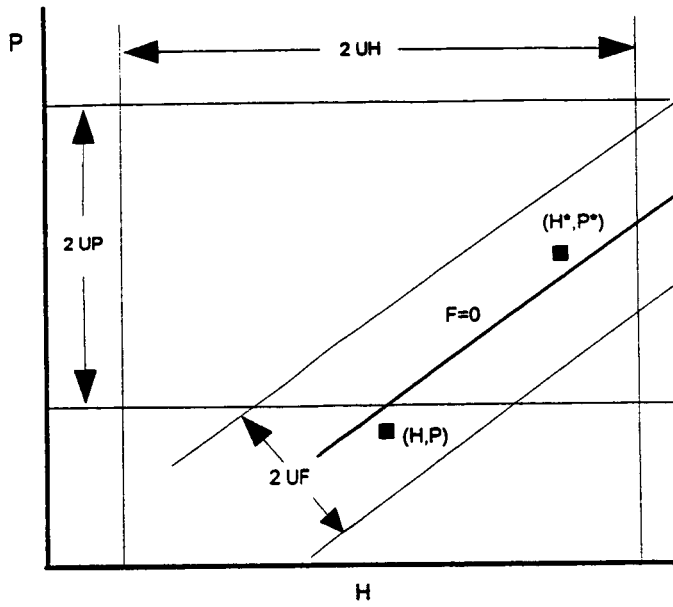


Figure 2. Acceptable Point Region

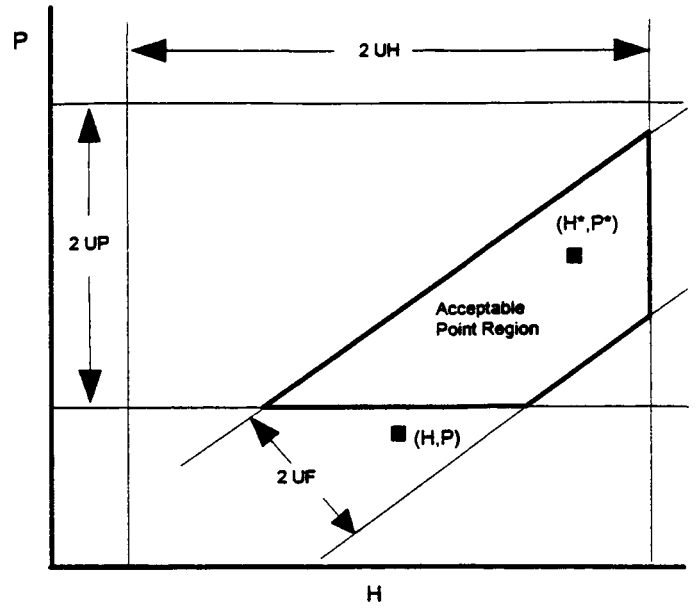


Figure 3. Typical Heuristic Solution

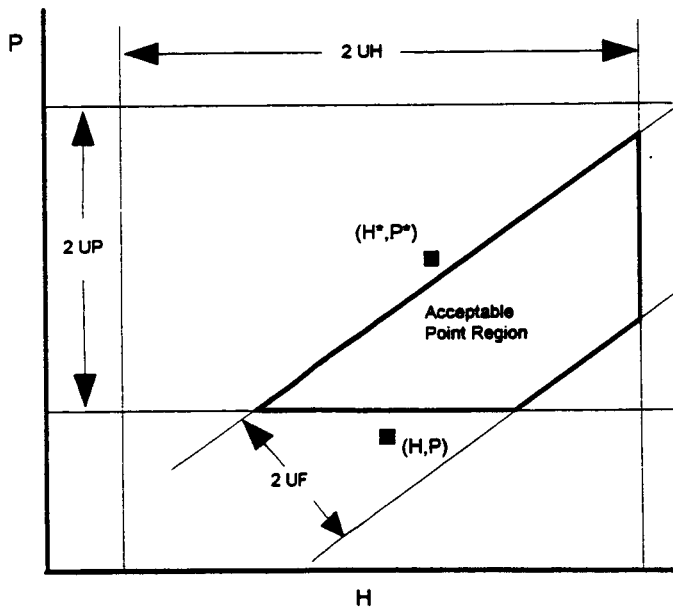


Figure 4. Unacceptable Solution

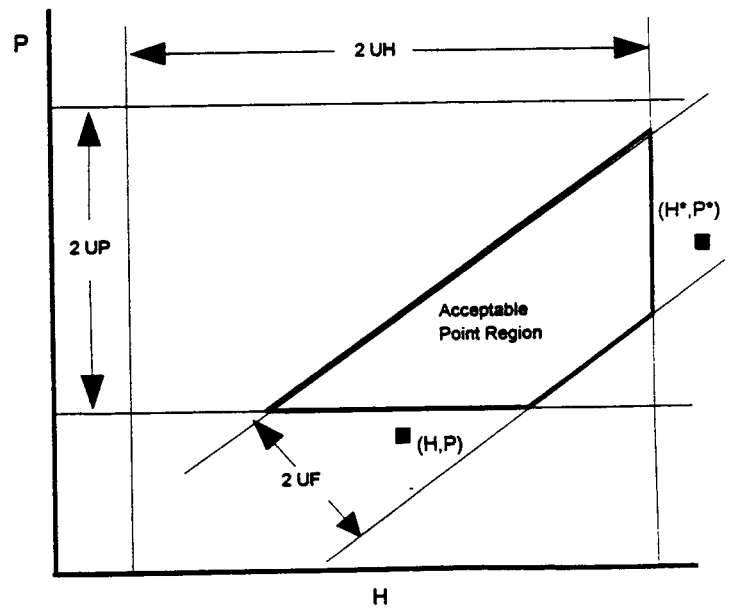


Table 1. Normalized Sensitivities from SSME ROCETS model

HARDWARE	ETA M	ETA M	TORQ M	TORQ M	TORQ M	RES M	AREA M
	HPOT	HPFT	HPOP	HPFP	PBP	MFV	LPFT
PHYSICAL							
HPOT DS T	-1.827	1.094	1.910	-1.629	0.103	0.412	0.102
HPFT DS T	0.390	-1.339	-0.419	1.869	-0.023	-0.096	0.090
OPB Pc	-0.259	-0.055	0.279	0.080	0.015	0.063	-0.003
FPB Pc	-0.040	-0.299	0.043	0.453	0.002	0.009	-0.003
PBP DS PR	0.104	0.248	-0.079	-0.352	-0.044	0.232	-0.015
HPOP DS PR	0.016	0.045	0.010	-0.063	-0.001	0.246	-0.003
HPFP DS PR	-0.079	-0.144	0.085	0.285	0.004	0.019	-0.022
MCC CLNT DS PR	-0.052	-0.100	0.057	0.161	0.003	0.013	-0.222
OPB FUEL FLOW	0.836	-0.810	-0.909	1.266	-0.049	-0.206	-0.074
OPB OXID FLOW	-1.500	0.651	1.672	-1.045	0.088	0.355	0.051
FPB OXID FLOW	0.150	-1.130	-0.163	1.650	-0.011	-0.038	0.035

Table 2. TTB Data Reduction Results

(Power level = 100% RPL, MCC Pc = 2746 PSIA, M/R = 6.090)
 (LPOP in Pr = 137.6 psia, LPOP in Tmp = 167.3 °R, LPOP in W = 901.0 lb/sec)
 (LPFP in Pr = 40.4 psia, LPFP in Tmp = 36.6 °R, LPFP in W = 149.0 lb/sec)

PARAMETERS	TTB-50 TEST DATA	ROCETS PREDICTION	P(1)-HPOT EFF P(1)-HPOT EFF P(1)-HPOT EFF P(1)-HPOT EFF P(2)-HPFT EFF P(2)-HPFT EFF P(2)-HPFT EFF P(2)-HPFT EFF P(3)-HPOP TRQ P(3)-HPOP TRQ P(3)-HPOP TRQ P(3)-HPOP TRQ P(4)-HPFP TRQ P(4)-HPFP TRQ P(4)-HPFP TRQ P(4)-HPFP TRQ P(5)-PBP TRQ P(5)-PBP TRQ P(5)-PBP TRQ P(5)-PBP TRQ P(6)-MFV RES P(6)-MFV RES P(6)-MFV RES P(6)-MFV RES P(7)-LPFT AREA P(7)-LPFT AREA						
P(1) HPOT Td (AVG)	1269	1336	1269	1269	1269	1269	1269	1269	1269
P(2) HPFT Td (AVG)	1492	1502	1492	1492	1492	1492	1492	1492	1492
LPFTP SPEED	15460	14353	14289	15285	15281	15281	15636	15636	15636
HPFTP SPEED	33360	31855	31810	41535	41502	41502	40705	40705	40705
OPOV POSITION	64.3	60.1	58.8	58.4	57.4	57.4	57.8	57.8	57.8
FPOV POSITION	74.2	71.3	70.8	73.4	71.9	71.9	72.7	72.7	72.7
P(3) OPB Pc	4536	4489	4444	4536	4536	4536	4536	4536	4536
P(4) FPB Pc	4555	4401	4375	4555	4555	4555	4555	4555	4555
P(5) PBP DS PR	6688	6598	6619	6540	6688	6688	6688	6688	6688
P(6) HPOP DS PR	3907	3718	3723	3696	3698	3698	3907	3907	3907
HPFP DS PR	5507	5451	5424	5869	5868	5868	5858	5858	5858
P(7) MCC CLNT DS PR	4236	4005	3992	4093	4093	4093	4236	4236	4236
LPFT INL FLOW	26.50	25.28	25.10	24.63	24.64	24.64	23.69	23.69	23.69
OPB FUEL FLOW	33.16	32.10	32.68	35.16	35.16	35.16	35.46	35.46	35.46
OPB OXID FLOW	24.20	20.74	19.81	18.74	18.75	18.75	18.65	18.65	18.65
FPB FUEL FLOW	76.63	71.60	71.24	69.72	69.72	69.72	70.31	70.31	70.31
FPB OXID FLOW	57.54	55.45	54.77	57.65	57.72	57.72	57.65	57.65	57.65

112580

352852
N95-19003

30926
p.6

1994

NASA/ASEE SUMMER FACULTY FELLOWSHIP PROGRAM

**MARSHALL SPACE FLIGHT CENTER
THE UNIVERSITY OF ALABAMA**

**CRACKING CHARACTERISTICS OF A HABITABLE MODULE
PRESSURE WALL FOLLOWING ORBITAL DEBRIS PENETRATION**

Prepared By:	William P. Schonberg, Ph.D.
Academic Rank:	Associate Professor
Institution and Department:	The University of Alabama in Huntsville Department of Civil & Environmental Engineering

NASA/MSFC:

Laboratory:	Structures and Dynamics
Division:	Structural Design
Branch:	Structural Development

MSFC Colleague:	Dr. Joel Williamsen
------------------------	----------------------------

INTRODUCTION

All long-duration spacecraft in low-earth-orbit are subject to high speed impacts by meteoroids and pieces of orbital debris. The threat of damage from such impacts is a significant design consideration in the development of long duration earth-orbiting spacecraft. This report presents the results of a study whose objective was develop an empirical model to predict the magnitudes of the various cracking and through-hole creation phenomena accompanying a habitable module penetration. The significance of the work performed is that the model predictions can be fed directly into a survivability analysis (see, e.g. [1,2]) to determine whether or not module unzipping would occur under a specific set of impact conditions. The likelihood of module unzipping over a structure's lifetime can also be determined in such an analysis. In addition, effective hole size predictions can be used as part of a survivability analysis to determine the time available for module evacuation prior to the onset of incapacitation due to air loss. Some of the phenomena considered include maximum petal length, maximum tip-to-tip crack distance, depth of petal deformation, number of cracks formed, orientation of the maximum tip-to-tip distance with respect to the inner wall grain direction, and the effective inner wall hole diameter.

EXPERIMENTAL SET-UP AND DATA

Figure 1 shows the normal impact (i.e. $\theta=0$) of a dual-wall structure impacted by a spherical projectile. A total of 105 high speed impact tests were conducted at the NASA/MSFC Space Debris Simulation Facility [3]. To simulate the presence of thermal insulation in the spacecraft wall, a blanket of multi-layer insulation (MLI) was inserted between the bumper and inner wall. The witness plates behind the inner wall are used to characterize the lethality of the debris exiting the inner wall in the event of inner wall perforation.

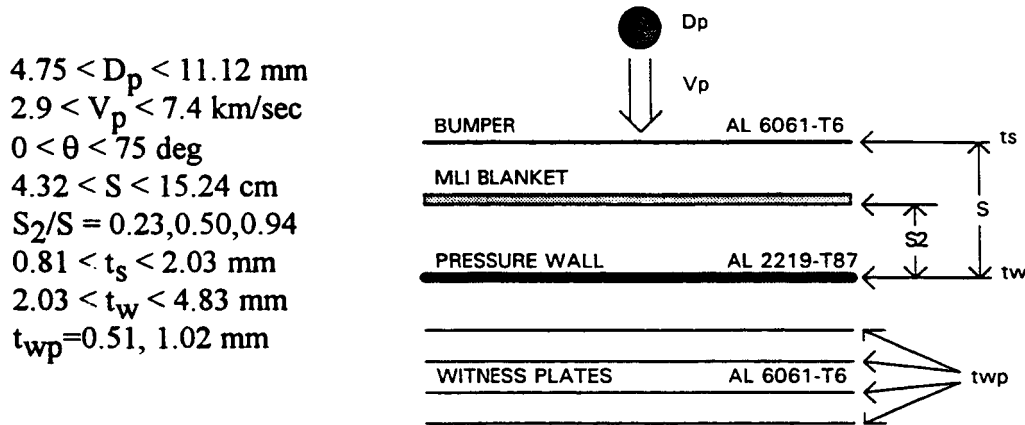


Figure 1. Hypervelocity Impact of a Generic Dual-Wall Structure

EMPIRICAL PREDICTOR EQUATIONS

Equations (1-19) are the result of a multiple linear regression analysis performed on the data; Tables 1-3 provide corresponding average errors (in percent) between actual data and regression equation predictions, standard deviations of the errors (also in percent), and correlation

coefficients. In equations (1-19), $C_w = \sqrt{E_w/\rho_w}$ is the speed of sound in the pressure wall material. In equation (7), the quantity $\theta_{tt} - \theta_{gr}$ denotes the orientation of the max tip-to-tip crack distance with respect to the orientation of the pressure wall grain direction. In equations (8-19), N_{kl} refers to the number of kapton layers in the MLI blanket.

MLI On The Pressure Wall, Normal and Oblique Impact, Unstressed Pressure Walls

Effective Hole Diameter

$$D_h / D_p = 5.8067(V_p / C_w)^{0.6155} (t_b / D_p)^{-0.6274} (S / D_p)^{-0.5953} (t_w / D_p)^{-0.0601} \cos^{2.1245} \theta \quad (1)$$

Maximum Petal Length

$$L_{cm} / D_p = 2.8014(V_p / C_w)^{1.7544} (t_b / D_p)^{-0.2247} (S / D_p)^{-0.4759} (t_w / D_p)^{-2.0642} \cos^{2.9966} \theta \quad (2)$$

Maximum Tip-to-Tip Distance

$$L_{tt} / D_p = 10.879(V_p / C_w)^{1.8626} (t_b / D_p)^{-0.9733} (S / D_p)^{-0.9040} (t_w / D_p)^{-0.9542} \cos^{3.6414} \theta \quad (3)$$

Depth of Petal Deformation

$$d_{pt} / t_w = 0.4815(V_p / C_w)^{1.0036} (t_b / D_p)^{-0.6534} (S / D_p)^{-1.1993} (t_w / D_p)^{-4.8489} \cos^{2.6228} \theta \quad (4)$$

Number of Cracks

$$N_{cr} = 7.7852(V_p / C_w)^{1.5215} (t_b / D_p)^{-0.8364} (S / D_p)^{-0.5892} (t_w / D_p)^{0.5680} \cos^{1.1995} \theta \quad (5)$$

Number of Perforated 0.51 mm (0.020 in.) Witness Plates

$$1 + N_{wp} = 2.6460(V_p / C_w)^{1.0061} (t_b / D_p)^{-0.7948} (S / D_p)^{-0.6114} (t_w / D_p)^{0.1398} \cos^{-0.8025} \theta \quad (6)$$

Orientation of Max Tip-to-Tip Distance

$$1 + \tan(\theta_{tt} - \theta_{gr}) = 0.9923(V_p / C_w)^{-0.4292} (t_b / D_p)^{-0.05545} (S / D_p)^{-0.01039} (t_w / D_p)^{-0.1486} \cos^{-0.1305} \theta \quad (7)$$

Table 1. Statistical Information for Equations 1-7

Equation No.	No. of Tests	Average Error (%)	Standard Deviation (%)	Correlation Coefficient (R ²)
(1)	74	5.93	34.59	0.71
(2)	50	5.48	34.54	0.81
(3)	50	6.68	38.52	0.86
(4)	26	2.47	23.25	0.88
(5)	47	2.57	22.96	0.67
(6)	34	3.69	28.39	0.75
(7)	42	0.19	6.27	0.74

MLI Off The Pressure Wall, Normal Impact, Unstressed Pressure Walls

Effective Hole Diameter

$$D_h / D_p = 3.0325 \times 10^{-15} (V_p / C_w)^{1.7614} (t_b / D_p)^{-6.9854} (S_2 / S)^{1.6062} (N_{kl} / 30)^{0.7160} (t_w / D_p)^{-8.2895} (S / D_p)^{6.1144} \quad (8)$$

Maximum Petal Length

$$L_{cm} / D_p = 13202 \times 10^{-8} (V_p / C_w)^{1.0708} (t_b / D_p)^{-1.4767} (S_2 / S)^{-0.4639} (N_{kl} / 30)^{0.1456} (t_w / D_p)^{-5.3054} (S / D_p)^{4.7029} \quad (9)$$

Maximum Tip-to-Tip Distance

$$L_{tt} / D_p = 4.2440 \times 10^{-8} (V_p / C_w)^{0.9314} (t_b / D_p)^{-1.3902} (S_2 / S)^{-0.7480} (N_{kl} / 30)^{0.2337} (t_w / D_p)^{-5.2516} (S / D_p)^{4.5715} \quad (10)$$

Depth of Petal Deformation

$$d_{pt} / t_w = 4.0125 \times 10^{-8} (V_p / C_w)^{1.6275} (t_b / D_p)^{-1.6092} (S_2 / S)^{-0.3884} (N_{kl} / 30)^{-1.1108} (t_w / D_p)^{-5.7128} (S / D_p)^{3.8105} \quad (11)$$

Number of Cracks

$$N_{cr} = 33609 \times 10^{-3} (V_p / C_w)^{0.5492} (t_b / D_p)^{-0.5330} (S_2 / S)^{-0.1374} (N_{kl} / 30)^{-0.06364} (t_w / D_p)^{-2.1578} (S / D_p)^{1.6227} \quad (12)$$

Number of Perforated Witness Plates

$$1 + t_{wp} N_{wp} = 0.6902 (V_p / C_w)^{0.05889} (t_b / D_p)^{-0.1442} (S_2 / S)^{0.03125} (N_{kl} / 30)^{0.02083} (t_w / D_p)^{-0.07840} (S / D_p)^{0.04118} \quad (13)$$

Table 2. Statistical Information for Equations 8-13

Equation No.	No. of Tests	Average Error (%)	Standard Deviation (%)	Correlation Coefficient (R ²)
(8)	23	4.49	29.98	0.89
(9)	23	3.51	27.08	0.73
(10)	23	4.51	31.31	0.70
(11)	23	5.37	34.06	0.81
(12)	23	1.27	16.99	0.64
(13)	23	0.02	1.80	0.78

MLI Off The Pressure Wall, Oblique Impact, Unstressed Pressure Walls

Effective Hole Diameter

$$D_h / D_p = 3.8204 \times 10^{-4} (V_p / C_w)^{0.3675} (t_b / D_p)^{-1.9899} (S_2 / S)^{-8.7042} (N_{kl} / 30)^{14.77} (t_w / D_p)^{-1.6684} (S / D_p)^{1.4838} \cos^{1.2267} \theta \quad (14)$$

Maximum Petal Length

$$L_{cm} / D_p = 247.6(V_p / C_w)^{1.4212} (t_b / D_p)^{0.8384} (S_2 / S)^{-2.4893} (t_w / D_p)^{0.1953} (S / D_p)^{-2.0912} \cos^{0.8878} \theta \quad (15)$$

Maximum Tip-to-Tip Distance

$$L_{tt} / D_p = 823.36(V_p / C_w)^{4.9848} (t_b / D_p)^{0.8501} (S_2 / S)^{0.6084} (t_w / D_p)^{-1.7837} (S / D_p)^{-1.8892} \cos^{0.9630} \theta \quad (16)$$

Depth of Petal Deformation

$$d_{pt} / t_w = 5.6351 \times 10^4 (V_p / C_w)^{-1.6074} (t_b / D_p)^{3.6979} (S_2 / S)^{-3.2146} (t_w / D_p)^{-1.2269} (S / D_p)^{-2.7819} \cos^{-0.2215} \theta \quad (17)$$

Number of Cracks (6.3 < V < 6.5 km/s, t_b = 1.01 mm, t_w = 2.03 mm, S = 4.32 cm, S₂/S = 0.5 ONLY)

$$N_{cr} = 20.604(V_p / C_w)^{0.5726} (S / D_p)^{-1.3485} \cos^{-0.4642} \theta \quad (18)$$

Number of Perforated Witness Plates

$$1 + t_{wp} N_{wp} = 0.339(V_p / C_w)^{0.9278} (t_b / D_p)^{-0.1005} (S_2 / S)^{-0.2958} (t_w / D_p)^{-0.1803} (S / D_p)^{0.1754} \cos^{0.0774} \theta \quad (19)$$

Table 3. Statistical Information for Equations 14-19

Equation No.	No. of Tests	Average Error (%)	Standard Deviation (%)	Correlation Coefficient (R ²)
(14)	38	5.50	34.96	0.79
(15)	17	4.97	35.86	0.90
(16)	17	6.81	43.45	0.85
(17)	17	1.23	15.42	0.99
(18)	6	0.72	13.54	0.78
(19)	17	0.02	2.11	0.54

COMMENTS AND OBSERVATIONS

Equations (1-19) were applied to the impact of a dual-wall system with a 1.6 mm (0.063 in.) thick bumper and a 3.18 mm (0.125 in.) thick pressure wall 10 cm (4.0 in.) away from the bumper. Results were generated for 6.35, 7.95, and 9.53 mm (0.250, 0.313, and 0.375 in.) spherical projectiles impacting the dual-wall system at velocities between 3 and 7.5 km/sec. Based on the results obtained, the following general observations were made regarding the effect of MLI placement on the cracking response of a Space Station module pressure wall.

For the impact of small projectiles (i.e. 6.35 mm diameter), moving the MLI away from the pressure wall to either midway in between the bumper and pressure wall or to a position just under the bumper significantly reduced the effective pressure wall hole diameter and the extent of pressure wall cracking damage (i.e. smaller petals and crack lengths, smaller effective hole diameters, smaller petal deformation depths, fewer petals, and fewer perforated witness plates). However, for the impact of large projectiles (i.e. 9.53 mm diameter), moving the MLI away from the pressure wall did not always reduce all forms of pressure wall damage. While moving the

MLI off the pressure wall did result in smaller petals, crack lengths, and petal deformation depths, it was found that placing the MLI either midway in between the bumper and the pressure wall or near the bumper resulted in more petals, more perforated witness plates, and larger effective hole diameters (especially when the MLI was near the bumper).

Apparently, moving the MLI off the pressure wall reduces the impulsive loading of the MLI that is delivered to the pressure wall. This reduces the crack lengths and petal deformation depths. However, moving the MLI off the pressure wall also reduces its ability to trap individual debris cloud particles, especially for large projectile impacts. When the projectile is small, the energy of the debris cloud striking the MLI is relatively low. Hence, in this case the MLI is still able to trap individual debris cloud particles and produce an overall reduction in pressure wall damage. However, when the original projectile is large, the debris cloud is highly energetic. When the MLI is near the bumper, the debris cloud is still in a relatively compact state when it encounters the MLI. In such a case, the MLI is unable to trap any of the debris cloud particles and the effective hole diameter can be rather large.

CONCLUSIONS AND RECOMMENDATIONS

Based on the results obtained, it is concluded that, in most cases, moving the MLI off the pressure wall has the effect of decreasing the effective pressure wall hole diameter and the extent of pressure wall cracking damage following a pressure wall perforation. It also appears that the optimum position for the MLI is midway between the pressure wall and the bumper. This conclusion reinforces that conclusions made in two previous studies of the effect of MLI placement on dual-wall system response to high speed particle impact [4,5]. It is recommended that additional work be performed to determine the effect of module curvature on the nature and extent of pressure wall cracking following a perforation. Crack limit curves also need to be developed to define the onset of critical cracking as a function of geometry and impact conditions.

REFERENCES

1. Williamsen, J.E., Vulnerability of Manned Spacecraft to Crew Loss from Orbital Debris Penetration, NASA-TM-108452, Marshall Space Flight Center, Alabama, 1994.
2. Micrometeoroid and Orbital Debris Induced Catastrophic Failure Prediction Methods, Space Station Freedom Program Office, Report No. GSS-40.05-RPT-6-003, Reston, Virginia, 1994.
3. Taylor, R.A., "A Space Debris Simulation Facility for Materials Evaluation", *SAMPE Quarterly*, Vol. 18, 1987, pp. 28-34.
4. Jolly, W.H. and Williamsen, J.E., "Ballistic Limit Curve Regression for Freedom Station Orbital Debris Shielding", AIAA Space Programs and Technologies Conference, Paper No. 92-1463, Huntsville, Alabama, 1992.
5. Schonberg, W.P., "Effect of Multi-Layer Thermal Insulation Thickness and Location on the Hypervelocity Impact Response of Dual-Wall Structures", *Acta Astronautica*, in press, 1994.

112589

N95-19004

1994

352853

24/2/1
p. 6

NASA/ASEE SUMMER FACULTY FELLOWSHIP PROGRAM

**MARSHALL SPACE FLIGHT CENTER
THE UNIVERSITY OF ALABAMA**

**EVALUATION OF THE EFFICIENCY AND RELIABILITY OF
SOFTWARE GENERATED BY CODE GENERATORS**

Prepared By: Barbara Schreur, Ph.D.
Academic Rank: Associate Professor
Institution and Department: Texas A&M University - Kingsville
Department of Electrical Engineering and
Computer Science

NASA/MSFC:

Laboratory: Astrionics
Division: Software
Branch: Systems Engineering

MSFC Colleague: Kenneth S. Williamson

Introduction

Traditional software development follows a cycle wherein the project phases of requirements definition, analysis, design, system construction and system testing are performed sequentially. In software engineering, as in manufacturing, the end product is improved when there is overlap between the phases. This is because feedback from those executing later phases may improve the work of those executing earlier phases. Thus leading to a more coherent finished product. CASE Tools which automate the entire software development cycle encourage the team engineering approach since all that is necessary is that developing files be shared among the various groups.

There are numerous studies, [1, 2] which show that CASE Tools greatly facilitate software development. As a result of these advantages, an increasing amount of software development is done with CASE Tools. As more software engineers become proficient with these tools, their experience and feedback lead to further development with the tools themselves. In fact, new versions of software development programs appear with a similar frequency to those of operating systems and office application software.

What has not been widely studied, however, is the reliability and efficiency of the actual code produced by the CASE Tools. This investigation considers these matters.

Method

Three segments of code generated by MATRIXx ,one of many commercially available CASE Tools, were chosen for analysis . ETOFLIGHT is a portion of the Earth to Orbit Flight software and ECLSS and PFMC are modules for Environmental Control and Life Support System and, Pump Fan Motor Control, respectively. The selection criteria [3] were that:

1. the segments be produced using a code generator,
2. the language available be the C language, and
3. there be no more than 2000 lines of code,.

The original code for ETOFLIGHT was produced in the C language while ECLSS and PFMC were in ADA. MATRIX X was used to regenerate the ECLSS and PFMC code in C from the design diagrams. That this was readily done without code conversion illustrates one of the advantages of CASE Tools. To be honest, the procedure did require a service call to Matrix X as well as considerable transfer of files over the network, but that is simply part of the learning curve.

The software was analyzed with the aid of the McCabe Tool, a commercially available software package. This software preprocesses the code and provides the following:

1. a graphical representation of the relationships between the various modules of the program.

The graphical representation, the Battlemap, shows the relationship between the modules and gives the cyclomatic, $v(g)$, and essential complexities, $ev(g)$. The cyclomatic complexity measures a model's decision structure while the essential complexity is a measure of the unstructured elements of the module, eg. a jump out of a loop.

2. flow charts of each of the coded modules.

The flow charts for each coded module also contain a code by which the corresponding section of code can be identified. Each module contains three flow charts. I primarily used the cyclomatic and essential complexity charts.

3. several metrics for each module.

The metrics [4,5] that I obtained from the tool where

- a) $v(g)$ numerically,
- b) $ev(g)$ numerically,
- c) the number of lines of code,
- d) the number of branches in the code,
- e) the number of lines containing code, comments, or code and comments, and
- f) Halstead metrics consisting of
 - i) program length - the number of occurrence of operators and operands
 - ii) program difficulty - a measure of how hard it is to follow the code
 - iii) error estimate - an estimate of the number of errors in the code
 - iv) program volume - minimum number of bits required
 - v) intelligent content - a complexity based on the algorithm used without language dependence
 - vi) programming time - estimate of the time needed to produce code
 - vii) program level - how difficult it is to understand the code
 - viii) programming effort - an estimate of the effort necessary to produce the code

Observations

Before utilizing the McCabe Tool, the C code was examined manually. Three points became apparent. First, a switch statement with one choice was generated where one would normally expect a simple if statement.

```
2117  
2118 C99      ; switch( ITSK ){
```

```

2119 C100          case 1 : SUBSYSTEM01(); break;
2120 C101          default : break;
2121 C102          }
2122                ;

```

The relative efficiency of switch versus if statements is compiler dependent but the CASE Tools make the decision for you. Thus it does not optimize for efficiency.

Secondly, Matrix X terminated the last case in a nested switch structure without a break, relying on a fall through to the terminating break of the switch structures. Standard practice is to terminate every case with a break unless a fall through is explicitly desired. Modification of the program by adding a new choice to the switch structure could lead to an unexpected fall through. This would not be a problem if the program were regenerated by the CASE Tool but extreme care would have to be taken with manual change to the C code.

```

1929 C8           switch( TASK_STATE[NTSK] ){
1930                case IDLE :

1932 C9           switch( TCB[NTSK].TASK_TYPE ){
1933                case PERIODIC :
1934 C10           if( TCB[NTSK].START == 0 ){
1935 C11           READY_COUNT ++ ;

                ...

1938                }else{
1939 C12           TCB[NTSK].START = TCB[NTSK].START - 1;
1940 C13           }
1941                break;
1943                case ENABLED_PERIODIC :

                ...

1977                case TRIGGERED_SAF :
1978 C31           if( TCB[NTSK].OUTPUT == 0 ){
1979 C32           BUS_OFFSET[NTSK] = 15 - BUS_OFFSET[NTSK];

                ...

1985                }
1986 C35           }
1987 C36 C37       }
1988                break;

1990                case RUNNING :

```

Lastly, in one module, 1 was the condition in five if statements as shown by the example below.

```

3877 H29          if( 1 ){
3878 H30          fprintf( fp, "YTIME   %5ld%5ld%5d%11s\n",
3879                YCOUNT-1+IUCNT, ICOL, IIMG, "(1P3E25.17)" );
3880          }else{
3881 H31          fprintf( fp, "YTIME   %5ld%5ld%5d%10s\n",
3882                YCOUNT-1+IUCNT, ICOL, IIMG, "(1P5E15.7)" );
3883 H32          }

```

For efficiency, these sections of code should be reduced to the statements contained in the true branch, thus reducing the complexity and testing procedures.

An analysis of the flow charts generated by the McCabe Tool showed that three of the subroutines in the one program are identical except for variables used and the order in which some statements are executed. A single subroutine could have been used in their place. This approach, using global parameters, may execute faster than using a single subroutine with passed parameters but the single subroutine makes more efficient use of memory. This is a choice which should be made in the analysis and design phases but the subroutine repetition may well be inadvertent. Future versions of CASE Tools might point out such instances.

Of the two McCabe metrics considered, the cyclomatic complexity gives a good indication of the complexity of a module. The essential complexity is in some cases higher than necessary. In those modules that contain return statements in the middle of a structure, the code cannot be represented as fully structured statements since this represents a jump outside a structure. The essential complexity can be reduced if this jump is performed at a later time. This increases the overall complexity of the program. Statements, such as returns, should be represented by a symbol and not add to the essential complexity of structured programs.

All eight of the calculated Halstead metrics are strongly correlated. Thus, there is no reason to calculate all eight.

Conclusion

The code produced by the code generator was more uniform over the three modules than that that would be produced by hand. The efficiency, though, would benefit from hand optimization.

Future Work

- Comparison of machine generated code and manually generated code.
- Compare to code produced by the next version of the code generator
- Determine if compiler dependence for the most commonly used structure types.

References

1. Weitz, Lori, "Code Generators Gain Versatility", *Software*, vol. 12, no. 11, August 1992, pp. 38-44.
2. Keyes, Jessica, "Team Tools Targeting Development Process", *Software*, vol. 12, no. 15, November 1992, pp. 45-56.
3. Schreur, Barbara, "Evaluation of the Efficiency and Fault Density of Software Generated by Code Generators", NASA CR-193862, November 1993, pp. XL-XL3.
4. McCabe, Thomas, "A Complexity Measure", *IEEE Transactions on Software Engineering*, vol. SE-2, no. 4, December 1976, pp 308-320..
5. Halstead, Maurice, "Elements of Software Science", Elsevier, New York, 1977.
6. Keyes, Jessica, "Gather a Baseline to Assess Case Impact", *Software*, vol. 10, no.10, August 1990, pp. 30-43.

352854

112590

N95-19005

30923

p. 6

1994

NASA/ASEE SUMMER FACULTY FELLOWSHIP PROGRAM

**MARSHALL SPACE FLIGHT CENTER
THE UNIVERSITY OF ALABAMA**

**A REPORT OF WORK ACTIVITIES ON THE
NASA SPACELINK PUBLIC ELECTRONIC LIBRARY**

Prepared By: Willard A. Smith
Academic Rank: Associate Professor
Institution and Department: Tennessee State University
Department of Physics,
Mathematics and Computer Science

NASA/MSFC

Division: Public Affairs Office
Branch: Education

MSFC Colleague: Bill Anderson

INTRODUCTION

NASA Spacelink is a comprehensive electronic data base of NASA and other source Educational and Informational Materials. This service originates at Marshall Space Flight Center (MSFC) in Huntsville, Alabama. This is an educational service of NASA Headquarters, through the MSFC Education Office, that first began in February of 1988. The usage of this public-access network grew from less than three thousand callers per year in 1989, to over three thousand callers per month in 1993.(1) During the concurrence of the twenty-fifth anniversary of the Apollo Moon Mission, the flight of STS-65, and the crash of P-Shoemaker-Levy 9 into Jupiter the old system answered fourteen hundred plus calls per day and denied two to three times more callers.(2)

NASA Spacelink provides a wide variety of information including: NASA News, History, Projects, the Astronauts, the Space Agency and its Centers, Space Vehicles, Educational Materials for teachers of K-12 and beyond, and Aeronautics. The materials on NASA Spacelink include not only text, but, maps, drawings, photos, and other computer produced graphic representations of data and visual materials.

The new NASA Spacelink Public Electronic Library was the result of a study conducted to investigate an upgrade or redesign of the original NASA Spacelink.(3) The need for new user interfaces and access methods resulted in a radical departure from the old system on the Data General hardware, using the customized adaptations of Data General's Operating System and Applications Software that made the original Spacelink operational.

The UNIX Operating System was chosen to be the host operating system for the new NASA Spacelink Public Electronic Library. The UNIX system was selected for this project because of the strengths built into the embedded communication system and for its simple and direct file handling capabilities.

The host hardware of the new system, is a Sun Microsystems SPARCserver 1000 computer system. The configuration has four 50-MHz SuperSPARC processors with 128 megabytes of shared memory;

three SB800 serial ports allowing 24 cable links for phone communications; 4.1 giga bytes of on line dick storage; and ten (10) CD-ROM drives. Communications devices on the system are sufficient to support the expected number of users through the Internet, the local dial services, long distance dial services; the MSFC PABX, and the NPSS (NASA Packet Switching System) and 1-800 access service for the registered teachers.

UNIX AS A UNIQUE APPLICATION

The application of the UNIX Operating System in the manner done on the NASA Spacelink project seemed to be unique. A search of the literature and contact with other users indicated that the use of UNIX as the Data Base manager, with support for such a divers group of user protocols, and across so many different access mediums was a new application of the UNIX Operating System.

The unique features of the NASA Spacelink system are most evident in the software configuration. The foundation of the system is Solaris 2.3 with SunOS 5.3, Open Network Computing (ONC), Open Windows, and the Desk Set.(4) This is Sun Microsystems Version of the Standard UNIX SVR4 with some Sun enhancements. The Operating system through it's built in features and linked with World Wide Web (WWW), Gopher, File Transfer Protocol (FTP), and Bulletin Board Software (BBS) servers are handling all of the communications and the data base management tasks. No other data base management software is running on the system. The UNIX Operating System Software, SunOS Solaris 2.3, is running as it came from the supplier.

The client server software packages, running on NASA Spacelink, were selected from the public domain software whenever possible. The exception was the ZMAX XChange Bulletin Board Software. The selection of public domain software kept down the cost to NASA and to the users. World Wide Web (WWW) through Internet supports the MOSAIC Protocol. MOSAIC is a public domain software package. Developed at The University of Illinois it has many powerful features in its text and graphic handlers. Gopher is a public domain software package developed originally at the University of Minnesota. It, like MOSAIC, is free to the user and accesses NASA Spacelink through the Internet. Gopher supports text and graphics file transfer and viewing. File Transfer Protocol (FTP)

is also a free access software package and a part of UNIX. FTP supports text and graphics with the assist of graphic viewing software on the receiving client computer.

The ZMAX XChange Bulletin Board Software was selected for the diverse features it supports. Many of the teachers using NASA Spacelink do not have access to the Internet. The Bulletin Board Software specifications for the system required this plus broad services for the schools. ZMAX XChange met those requirements. There was no public domain software package that met the specifications of the new system. This BBS allows for dial in access and support of any computer that can emulate a VT100 Terminal.

FILE DESIGN

The file structure for Spacelink, adapted by the NASA development team, uses the standard structure of UNIX files.(5) This required the development of logical names for the files to be placed in the UNIX File Structure. A set of Naming Conventions were developed to implement file names in UNIX that could be commonly shared by all the user interfaces of the system.(6) This allowed for the most direct transfer of many of the files in the "Old Spacelink" data base to the New Spacelink. The only change in many of the transfers was the change of the old file name to the the new file structrue. This allowed for the transfer of some 5000 plus documents in a short period of time with no direct name mapping.

A sample of the file structure and naming conventions are found in Figure 1. This is an abridged section of the NASA Spacelink Public Electronic Library. The figure illustrates the basic structure and the depth of the files under the directories.

The use of the UNIX file structure allows additional files to be added as NASA Spacelink grows. This continual growth requires the addition of several files per day. The use of the directory, to sub directory, to sub directory, and so on, provided for a heirachy of logically organized files. With this simple inverted tree paradigm come effective, efficient access for all to NASA Spacelink.

Figure 1 below is also an illustration of the file structure of the section of Educational Services and Instructional Materials.

```

Instructional.Materials
"  Careers
"    "  Careers.in.Aerospace
"    "    "  Astronaut
"    "  Civil.Service.Requirements
"    "  Specialties.of.Aerospace.Technology
"  Curriculum.Materials
"    "  Art
"    "  Geography
"    "  History
"    "  Language.Arts
"    "  Mathematics
"    "  Sciences
"    "    "  Astronomy
"    "    "    "  Astronomical.Keydates
"    "    "    "  Comet.Shoemaker-Levy9
"    "    "    "    "  Comet.Fact.Sheets
"    "    "    "    "  Images
"    "    "    "  Small.Bodies
"    "    "    "  Space.Astronomy.Update
"    "    "    "  The.Earths.Moon
"    "    "    "  The.Night.Sky
"    "    "    "    "  Sky.Charts
"    "    "  Biology
"    "    "  Chemistry
"    "    "  Environmental.Science
"    "    "  General.Science
"    "    "  Geology
"    "    "  Microgravity
"    "    "  Physical.Science
"    "    "  Physics
"    "  Technology
"  Interdisciplinary.Materials
"  Software

```

Figure 1.
Abridged Section of the NASA Spacelink Public Electronic Library

This key section of the NASA Spacelink format came from intensive interaction with teachers. One of the primary goals of this project was to make the materials on Spacelink as accessible as possible to the classroom teachers. This section of NASA Spacelink was reviewed by several groups of teachers. Figure 2 below illustrates the earliest view of this section and shows the impact the teachers had on the final design of this area of the Spacelink Directory.

"	Instructional.Materials
"	" .readme
"	" Aerospace.Careers
"	" Curriculum
"	" " Historical
"	" " Life.Sciences
"	" " Mathematics
"	" " Physical.Sciences
"	" " Technology
"	" Software
"	" " Apple.II
"	" " IBM.PC
"	" " Macintosh

Figure 2
Original Section on Instructional Materials

There is considerable work yet to be done on the new NASA Spacelink. Several sections will be enhanced over the coming months and years. The work done by the development team on the NASA Spacelink Public Electronic Library should serve NASA well into the future as an effective server on the Information Super Highway.

REFERENCES

1. Spacelink Monthly Report, *Internal Documents*, NASA, MSFC, Alabama, Jan. 1994.
2. Spacelink.Monthly.Report. *InternalDocuments*, NASA, MSFC, Alabama, July 1994.
3. Cunningham, Alan, Engineering Study for "Replacement of Existing NASA Spacelink" Requirement 97748, NASA/MSFC *Internal Documents*, July 1993.
4. Helsop, Brent and Angell, David; Mastering Solaris 2, San Francisco, California, Sybex, 1993
5. Cobb, Jeff; Cunningham, Alan; Wild, Flint; NASA Spacelink Public Electronic Library, *Internal Documents*, NASA, MSFC, Huntsville, Alabama, May, 1994.
6. Smith, Willard A. et.al., *Internal Documents*, NASA, MSFC, Huntsville, Alabama, May, 1994.

112591

352253
N95-19006

1994

NASA/ASEE SUMMER FACULTY FELLOWSHIP PROGRAM

30929
p. 6

MARSHALL SPACE FLIGHT CENTER
THE UNIVERSITY OF ALABAMA

**SCATTERING OF POINT SOURCE ILLUMINATION
BY AN ARBITRARY CONFIGURATION**

Prepared by:
Academic Rank:

Richard Solakiewicz
Associate Professor

Institution and
Department:

Chicago State University
Department of Mathematics
and Computer Science

NASA/MSFC
Laboratory:
Division:
Branch:

Space Science
Earth Sciences/Applications
Remote Sensing

MSFC Colleagues:

William Koshak
Richard Blakeslee
Hugh Christian

Monte Carlo Simulations [1], equivalent medium approaches [2, 3], and methods based on Boltzmann transport theory [4, 5] have been applied to study the scattering of light produced by lightning in a thundercloud. The Monte Carlo approach is the most straightforward but other approaches may yield better insight into the phenomena.

The cloud is assumed to consist of a uniform, homogeneous, random distribution of spherical water drops with an average radius of 10 μm and number density $\rho = 100 \text{ cm}^{-3}$. In particular, light in the near infrared, $\lambda = 0.7774 \mu\text{m}$, is of interest. The equivalent medium approach, based on methods due to Twersky [6, 7], yields the coherently scattered fields. For the ratio of the average separation distance between water drops to the wavelength, the scattering is considered to be almost totally incoherent [8]. During the time interval of a typical lightning event, the movement of the water drops is negligible. For fixed configurations of scatterers, the distinction between coherent and incoherent scattering is not very clear in the literature. The best explanation in the author's estimation is given by Foldy [9], who admits that for a fixed configuration of scatterers, all of the scattering is strictly coherent. A rather artificial distinction is made. The following definition is unambiguous: the square magnitude of an average field $|\langle\psi\rangle|^2$, $\psi = \mathbf{E}$ or \mathbf{H} , is proportional to the coherent intensity; $V = \langle|\psi|^2\rangle - |\langle\psi\rangle|^2$ is proportional to the incoherent intensity. The function V is approximately given in terms of the square magnitude of the radiated field from a scatterer at \mathbf{b} , averaged over all possible configurations of the remaining scatterers,

$$\approx \rho \int d\mathbf{r}_s \langle |U_s|^2 \rangle_s \approx \rho \int d\mathbf{r}_s \langle |U_s| \rangle_s^2, \quad (1)$$

where $d\mathbf{r}_s$ is a volume element in local coordinates $\mathbf{r}_s = \mathbf{r} - \mathbf{b}_s$.

The problem of electromagnetic scattering of an incident plane wave by an arbitrary configuration of obstacles was solved by Twersky [10]. In this report, the results are extended to point source incidence corresponding to a Hertz dipole. Knowledge of the response of a fixed configuration of scatterers excited by a point source may provide insight to improve the accuracy of the values of bulk parameters for clouds which have been found using plane wave excitation.

As in [3], we transform to the frequency domain; time domain solutions are recovered by a Fourier integral. A dyadic formalism is used throughout. We will employ the following notation: ϕ , u , and ψ will denote the incident, scattered, and total fields respectively. Lower case letters will correspond to single scattering (an object in isolation); upper case letters will be used for multiply scattered fields. Functional dependencies in brackets imply plane wave incidence; the use of parentheses is reserved for fields corresponding to a point source. Modification from plane wave to point source excitation is accomplished by operating on the plane wave results with a Sommerfeld-type contour integral representation [11] of a spherical Hankel function.

Generally speaking, if a transverse wave has a direction $\hat{\mathbf{r}}$, its dyadic form will look like $\tilde{\mathbf{I}} - \hat{\mathbf{r}}\hat{\mathbf{r}}$, where $\tilde{\mathbf{I}}$ is the identity dyad. Incident fields will have the form

$$\tilde{\phi}[\mathbf{r}, \hat{\mathbf{k}}] = (\tilde{\mathbf{I}} - \hat{\mathbf{k}}\hat{\mathbf{k}})\phi[\mathbf{r}, \hat{\mathbf{k}}], \quad \phi[\mathbf{r}, \hat{\mathbf{k}}] = e^{i\mathbf{k}\cdot\mathbf{r}}, \quad \tilde{\phi}(\mathbf{r}, \mathbf{r}') = \left(\tilde{\mathbf{I}} + \frac{\nabla\nabla}{k^2} \right) \phi(\mathbf{r}, \mathbf{r}'), \quad \phi(\mathbf{r}, \mathbf{r}') = h_0^{(1)}(k|\mathbf{r} - \mathbf{r}'|), \quad (2)$$

where the first argument refers to the point of observation and the second is the direction of incidence or the source location. The plane wave can be taken as the incident electric or magnetic

field. The function $\tilde{\phi}(\mathbf{r}, \mathbf{r}')$ specifies the fields due a dipole located at \mathbf{r}' . For an electric or magnetic dipole with directions $\hat{\mathbf{p}}, \hat{\mathbf{p}}_m$, we have [3]

$$\begin{aligned} \mathbf{E}^i &= \frac{ik^3}{4\pi\epsilon_0} \tilde{\phi}(\mathbf{r}, \mathbf{r}') \cdot \hat{\mathbf{p}}, \quad \mathbf{H}^i = \frac{k^3}{4\pi\omega\mu_0\epsilon_0} \nabla h_0^{(1)}(|\mathbf{r} - \mathbf{r}'|) \times \hat{\mathbf{p}}, \\ \mathbf{E}_m^i &= -\frac{k^3}{4\pi\omega\epsilon_0} \nabla h_0^{(1)}(|\mathbf{r} - \mathbf{r}'|) \times \hat{\mathbf{p}}_m, \quad \mathbf{H}_m^i = \frac{ik^3}{4\pi} \tilde{\phi}(\mathbf{r}, \mathbf{r}') \cdot \hat{\mathbf{p}}_m, \end{aligned} \quad (3)$$

where ϵ_0 and μ_0 are the permittivity and permeability of the medium external to the scatterers. Here, \mathbf{E}^i and \mathbf{H}^i are the electric and magnetic field vectors due to an electric dipole; the subscripts m denote the corresponding quantities due to a magnetic dipole. We will solve for electric fields when given an electric dipole for the source and work with magnetic fields for a magnetic dipole. The remaining fields may be found using Maxwell's eqs.

A dyadic version of the Helmholtz surface integral representation is given by [10]

$$\tilde{\mathbf{u}} = \frac{k}{4\pi i} \int dS(\mathbf{r}) \left\{ [\hat{\mathbf{n}} \times \tilde{\phi}(\mathbf{r}, \mathbf{r})]^T \cdot [\nabla \times \tilde{\psi}] - [\nabla \times \tilde{\phi}(\mathbf{r}, \mathbf{r})]^T \cdot [\hat{\mathbf{n}} \times \tilde{\psi}] \right\} \equiv \{ \tilde{\phi}(\mathbf{r}, \mathbf{r}), \tilde{\psi} \}, \quad (4)$$

where ∇ operates on the variables associated with the vector \mathbf{r} to a point on the surface of integration, T denotes the transpose, and $\hat{\mathbf{n}}$ is the outward normal. In (4), $\tilde{\psi} = \tilde{\psi}[\mathbf{r}, \hat{\mathbf{k}}]$ or $\tilde{\psi}(\mathbf{r}, \mathbf{r}')$ and $\tilde{\mathbf{u}}$ can be $\tilde{\mathbf{u}}[\mathbf{r}, \hat{\mathbf{k}}]$ or $\tilde{\mathbf{u}}(\mathbf{r}, \mathbf{r}')$ depending on the initial excitation.

As $r \sim \infty$, we can write

$$\tilde{\phi}(\mathbf{r}, \mathbf{r}) \sim (\tilde{\mathbf{I}} - \hat{\mathbf{r}}\hat{\mathbf{r}}) h_0^{(1)}(kr) e^{-ik\hat{\mathbf{r}} \cdot \mathbf{r}} \quad (5)$$

in (4) to obtain

$$\tilde{\mathbf{u}} \sim h_0^{(1)}(kr) \tilde{\mathbf{g}}, \quad \tilde{\mathbf{g}} = \{ (\tilde{\mathbf{I}} - \hat{\mathbf{r}}\hat{\mathbf{r}}) e^{-ik\hat{\mathbf{r}} \cdot \mathbf{r}}, \tilde{\psi} \}. \quad (6)$$

Single scattering amplitudes for both kinds of excitations may be defined in this way. Sommerfeld's integral representation for $h_0^{(1)}$ is given by

$$\left(\tilde{\mathbf{I}} + \frac{\nabla\nabla}{k^2} \right) h_0^{(1)}(k|\mathbf{r} - \mathbf{r}|) = \frac{1}{2\pi} \int d\Omega(\hat{\mathbf{r}}_c) (\tilde{\mathbf{I}} - \hat{\mathbf{r}}_c\hat{\mathbf{r}}_c) e^{ik\hat{\mathbf{r}}_c \cdot (\mathbf{r} - \mathbf{r})}, \quad (7)$$

where $\hat{\mathbf{r}}_c = \hat{\mathbf{r}}_c(\theta_c, \varphi_c)$, $0 \leq \varphi_c \leq 2\pi$, and θ_c starts at zero and goes to $\theta_i - i\infty$, where θ_i is in an interval which guarantees the convergence of the integral. Substituting in (4), reversing the order of integrations, and recognizing $\tilde{\mathbf{g}}$ from (6), yields the spectral representations

$$\tilde{\mathbf{u}}[\mathbf{r}, \hat{\mathbf{k}}] = \frac{1}{2\pi} \int d\Omega(\hat{\mathbf{r}}_c) e^{ik\hat{\mathbf{r}}_c \cdot \mathbf{r}} \tilde{\mathbf{g}}[\hat{\mathbf{r}}_c, \hat{\mathbf{k}}], \quad \tilde{\mathbf{u}}(\mathbf{r}, \mathbf{r}') = \frac{1}{2\pi} \int d\Omega(\hat{\mathbf{r}}_c) e^{ik\hat{\mathbf{r}}_c \cdot \mathbf{r}} \tilde{\mathbf{g}}(\hat{\mathbf{r}}_c, \mathbf{r}'). \quad (8)$$

These representations are valid for r greater than the scatterer's projection on $\hat{\mathbf{r}}$.

Eq. (7) shows that a point source can be written as a superposition of plane waves. If the response of an object for plane wave excitation is known, its response to a point source can be obtained by superposition. Allowing the direction of incidence of a plane wave $\hat{\mathbf{k}}$ to be complex and regarding $\exp[-i\hat{\mathbf{k}} \cdot \mathbf{r}']$ in (7) as a phase factor, we find the relation

$$\tilde{g}(\mathbf{r}, \mathbf{r}') = \frac{1}{2\pi} \int d\Omega(\hat{\mathbf{k}}) e^{-i\mathbf{k}\cdot\mathbf{r}'} \tilde{g}[\hat{\mathbf{r}}, \mathbf{k}] \quad (9)$$

An integral operator like (9) will be used to modify plane wave forms to point source excitation.

For spherical scatterers, explicit forms for the scattering amplitudes may be written in terms of Hansen's functions. The excitations may be written as

$$\begin{aligned} \tilde{\phi}[\mathbf{r}, \hat{\mathbf{k}}] &= \sum i^n \sqrt{n(n+1)} Q_n^m \left[\mathbf{M}_{mn}^1(k, \mathbf{r}) \mathbf{C}_{-mn}(\hat{\mathbf{k}}) - i \mathbf{N}_{mn}^1(k, \mathbf{r}) \mathbf{B}_{-mn}(\hat{\mathbf{k}}) \right], \\ \tilde{\phi}(\mathbf{r}, \mathbf{r}') &= \sum Q_n^m \left[\mathbf{M}_{mn}^3(k, \mathbf{r}) \mathbf{M}_{-mn}^1(k, \mathbf{r}') + \mathbf{N}_{mn}^3(k, \mathbf{r}) \mathbf{N}_{-mn}^1(k, \mathbf{r}') \right], \quad r > r', \\ \sum &\equiv \sum_{n=1}^{\infty} \sum_{m=-n}^n, \quad Q_n^m = \frac{(2n+1)(-1)^m}{n(n+1)}, \end{aligned} \quad (10)$$

where \mathbf{C} and \mathbf{B} are vector spherical harmonics. We use the definitions of these functions as given in [12] except that complex exponentials are used instead of even (cosine) and odd (sine) forms. The normalization of the spherical harmonics Y_n^m used here follows [11]. When $r < r'$, the corresponding vectors in the second eq. in (10) are interchanged.

The interior and radiated fields have the forms

$$\begin{aligned} \tilde{\psi}_{in}[\mathbf{r}, \hat{\mathbf{k}}] &= \sum \left\{ \mathbf{M}_{mn}^1(K, \mathbf{r}) \mathbf{a}_n^m[\hat{\mathbf{k}}] + \mathbf{N}_{mn}^1(K, \mathbf{r}) \mathbf{b}_n^m[\hat{\mathbf{k}}] \right\}, \\ \tilde{u}[\mathbf{r}, \hat{\mathbf{k}}] &= \sum \left\{ \mathbf{M}_{mn}^3(K, \mathbf{r}) \mathbf{c}_n^m[\hat{\mathbf{k}}] + \mathbf{N}_{mn}^3(K, \mathbf{r}) \mathbf{d}_n^m[\hat{\mathbf{k}}] \right\}, \\ \tilde{\psi}_{in}(\mathbf{r}, \mathbf{r}') &= \sum \left\{ \mathbf{M}_{mn}^1(K, \mathbf{r}) \mathbf{a}_n^m(\mathbf{r}') + \mathbf{N}_{mn}^1(K, \mathbf{r}) \mathbf{b}_n^m(\mathbf{r}') \right\}, \\ \tilde{u}(\mathbf{r}, \mathbf{r}') &= \sum \left\{ \mathbf{M}_{mn}^3(K, \mathbf{r}) \mathbf{c}_n^m(\mathbf{r}') + \mathbf{N}_{mn}^3(K, \mathbf{r}) \mathbf{d}_n^m(\mathbf{r}') \right\}, \end{aligned} \quad (11)$$

where $k = k(\epsilon_0, \mu_0)$ and $K = K(\epsilon, \mu)$ is the interior wave number. In general, the transition conditions at an interface, where the normal is denoted by $\hat{\mathbf{n}}$, require that

$$\hat{\mathbf{n}} \times (\tilde{\phi} + \tilde{u}) = \hat{\mathbf{n}} \times \tilde{\psi}_{in}, \quad \hat{\mathbf{n}} \times \nabla \times (\tilde{\phi} + \tilde{u}) = B \hat{\mathbf{n}} \times \nabla \times \tilde{\psi}_{in}, \quad (12)$$

where $B = \mu_0/\mu$ if $\tilde{\phi}$ represents an electric field and ϵ_0/ϵ if $\tilde{\phi}$ is taken to be a magnetic field.

For a sphere of radius a , the scattering coefficients are given by

$$\begin{aligned} \mathbf{a}_n^m[\hat{\mathbf{k}}] &= i^n \sqrt{n(n+1)} Q_n^m \mathbf{C}_{-mn}(\hat{\mathbf{k}}) a_n, & \mathbf{a}_n^m(\mathbf{r}') &= Q_n^m \mathbf{M}_{-mn}^1(k, \mathbf{r}') a_n, \\ \mathbf{b}_n^m[\hat{\mathbf{k}}] &= i^{n-1} \sqrt{n(n+1)} Q_n^m \mathbf{B}_{-mn}(\hat{\mathbf{k}}) b_n, & \mathbf{b}_n^m(\mathbf{r}') &= Q_n^m \mathbf{N}_{-mn}^1(k, \mathbf{r}') b_n, \\ \mathbf{c}_n^m[\hat{\mathbf{k}}] &= i^n \sqrt{n(n+1)} Q_n^m \mathbf{C}_{-mn}(\hat{\mathbf{k}}) c_n, & \mathbf{c}_n^m(\mathbf{r}') &= Q_n^m \mathbf{M}_{-mn}^1(k, \mathbf{r}') c_n, \\ \mathbf{d}_n^m[\hat{\mathbf{k}}] &= i^{n-1} \sqrt{n(n+1)} Q_n^m \mathbf{B}_{-mn}(\hat{\mathbf{k}}) d_n, & \mathbf{d}_n^m(\mathbf{r}') &= Q_n^m \mathbf{N}_{-mn}^1(k, \mathbf{r}') d_n, \end{aligned} \quad (13)$$

where the constants a_n , b_n , c_n , and d_n are the appropriate set of Mie coefficients found in [3]. Series for the scattering amplitudes may be obtained by substituting large kr forms for the Hansen's functions in (11),

$$\begin{aligned} \tilde{g}[\hat{\mathbf{r}}, \hat{\mathbf{k}}] &= \sum n(n+1) Q_n^m \left[c_n \mathbf{C}_{mn}(\hat{\mathbf{r}}) \mathbf{C}_{-mn}(\hat{\mathbf{k}}) + d_n \mathbf{B}_{mn}(\hat{\mathbf{r}}) \mathbf{B}_{-mn}(\hat{\mathbf{k}}) \right], \\ \tilde{g}(\hat{\mathbf{r}}, \mathbf{r}') &= \sum \sqrt{n(n+1)} i^{-n} Q_n^m \left[c_n \mathbf{C}_{mn}(\hat{\mathbf{r}}) \mathbf{M}_{-mn}^1(k, \mathbf{r}') + i d_n \mathbf{B}_{mn}(\hat{\mathbf{r}}) \mathbf{N}_{-mn}^1(k, \mathbf{r}') \right], \end{aligned} \quad (14)$$

and may be used for the electric or magnetic fields given the same was chosen as the incidence after multiplication by appropriate constants. The remaining fields may be found by first interchanging those M's and N's in \tilde{u} or C's and B's in \tilde{g} which are functions of \hat{r} . Solutions \tilde{u} and \tilde{g} for magnetic fields when $\tilde{\phi}$ is taken to be an electric field are then obtained by multiplication by $\gamma = -i\sqrt{\epsilon_0/\mu_0}$; use $1/\gamma$ for the remaining situation.

Consider a fixed configuration of N scatterers. Each has its "center" located at \mathbf{b}_s , $s = 1, 2, \dots, N$. The total field for plane wave excitation may be written as

$$\tilde{\Psi}[\mathbf{r}, \hat{\mathbf{k}}] = \tilde{\phi}[\mathbf{r}, \hat{\mathbf{k}}] + \tilde{U}[\mathbf{r}, \hat{\mathbf{k}}], \quad \tilde{U}[\mathbf{r}, \hat{\mathbf{k}}] = \sum_s \tilde{U}_s[\mathbf{r}_s, \hat{\mathbf{k}}] e^{i\hat{\mathbf{k}} \cdot \mathbf{b}_s} \sim h_0^{(1)}(kr) \tilde{G}[\mathbf{r}, \hat{\mathbf{k}}], \quad \mathbf{r}_s = \mathbf{r} - \mathbf{b}_s, \quad (15)$$

where \tilde{U}_s is the scattered field from the scatterer at \mathbf{b}_s as if it was located at the origin. Forms similar to those obtained for an isolated scatterer,

$$\tilde{U}_s[\mathbf{r}_s, \hat{\mathbf{k}}] = \frac{1}{2\pi} \int d\Omega(\hat{\mathbf{r}}_c) e^{i\hat{\mathbf{k}} \cdot \mathbf{r}_s} \tilde{G}_s[\hat{\mathbf{r}}_c, \hat{\mathbf{k}}] \sim h_0^{(1)}(kr_s) \tilde{G}_s[\hat{\mathbf{r}}, \hat{\mathbf{k}}], \quad \tilde{G}_s[\hat{\mathbf{r}}, \hat{\mathbf{k}}] = \{(\tilde{\mathbf{I}} - \hat{\mathbf{r}}\hat{\mathbf{r}}) e^{-i\hat{\mathbf{k}} \cdot \mathbf{r}_s}, \tilde{U}_s[\mathbf{r}_s, \hat{\mathbf{k}}]\}, \quad (16)$$

where $\hat{\mathbf{r}}_s \sim \hat{\mathbf{r}}$ as $r \sim \infty$, are also valid here. Taking phase differences into account, we have

$$\tilde{G}[\hat{\mathbf{r}}, \hat{\mathbf{k}}] = \sum_s e^{i\hat{\mathbf{k}} \cdot (\hat{\mathbf{r}} - \hat{\mathbf{r}}_s) \cdot \mathbf{b}_s} \tilde{G}_s[\hat{\mathbf{r}}, \hat{\mathbf{k}}] \quad (17)$$

Twersky [10] obtained a coupled set of integral eqs. for $\tilde{G}_s[\hat{\mathbf{r}}, \hat{\mathbf{k}}]$ in terms \tilde{g} ,

$$\tilde{G}_s[\hat{\mathbf{r}}, \hat{\mathbf{k}}] = \tilde{g}_s[\hat{\mathbf{r}}, \hat{\mathbf{k}}] + \frac{1}{2\pi} \sum_{t \neq s} \int d\Omega(\hat{\mathbf{r}}_c) e^{i\hat{\mathbf{k}} \cdot (\hat{\mathbf{r}}_c - \hat{\mathbf{k}}) \cdot \mathbf{b}_{st}} \tilde{g}_s[\hat{\mathbf{r}}, \hat{\mathbf{r}}_c] \cdot \tilde{G}_t[\hat{\mathbf{r}}_c, \hat{\mathbf{k}}], \quad \mathbf{b}_{st} = \mathbf{b}_s - \mathbf{b}_t. \quad (18)$$

Recall that \tilde{G}_s is related to \tilde{U}_s , which is written in local coordinates \mathbf{r}_s . Operating on (18) with the integral $(2\pi)^{-1} \int d\Omega(\hat{\mathbf{k}}) \exp[-i\hat{\mathbf{k}} \cdot (\mathbf{r}' - \mathbf{b}_s)]$ yields

$$\tilde{G}_s(\hat{\mathbf{r}}, \mathbf{b}'_s) = \tilde{g}_s(\hat{\mathbf{r}}, \mathbf{b}'_s) + \frac{1}{2\pi} \sum_{t \neq s} \int d\Omega(\hat{\mathbf{r}}_c) e^{i\hat{\mathbf{k}} \cdot \mathbf{b}_{st}} \tilde{g}_s[\hat{\mathbf{r}}, \hat{\mathbf{r}}_c] \cdot \tilde{G}_t(\hat{\mathbf{r}}_c, \mathbf{b}'_t), \quad \mathbf{b}'_s = \mathbf{r}' - \mathbf{b}_s. \quad (19)$$

When the particle separations are large compared to wavelength, the integral in (19) may be evaluated asymptotically. A convenient method [10] to do this exists whenever the kernel, aside from the exponential, can be expanded in a series of vector spherical harmonics. Iterating while retaining an appropriate number of terms in the asymptotic series will generate a consistent asymptotic expansion for \tilde{G}_s . Exactly the same expansion as given in [10] will work for (19) except that $\tilde{G}[\]$ is replaced by $\tilde{G}(\)$. Retaining only the leading term in the integral, gives

$$\tilde{G}(\hat{\mathbf{r}}, \mathbf{b}'_s) \sim \tilde{g}_s(\hat{\mathbf{r}}, \mathbf{b}'_s) + \sum_{t \neq s} h_0^{(1)}(kb_{st}) \tilde{g}_s[\hat{\mathbf{r}}, \hat{\mathbf{b}}_{st}] \cdot \tilde{G}_t(\hat{\mathbf{b}}_{st}, \mathbf{b}'_t) \quad (20)$$

A set of algebraic eqs. may be obtained by substituting (14) and

$$\tilde{G}_s(\hat{\mathbf{r}}, \mathbf{b}'_s) = \sum [C_{mn}(\hat{\mathbf{r}}) \mathbf{C}_{mn}^s(\mathbf{b}'_s) + \mathbf{B}_{mn}(\hat{\mathbf{r}}) \mathbf{D}_{mn}^s(\mathbf{b}'_s)] \quad (21)$$

into (19) and using orthogonality. Similar to [10], we obtain

$$\begin{aligned}
\mathbf{C}_{mn}^s &= \sqrt{n(n+1)}i^{-n}c_n^s Q_n^m \mathbf{M}_{-mn}^1(k, \mathbf{b}_s') + n(n+1)Q_n^m c_n^s \sum_{t=s} \sum_{q,p} [E_{-mn}^{qp}(\mathbf{b}_{st}) \mathbf{C}_{qp}^t + F_{-mn}^{qp}(\mathbf{b}_{st}) \mathbf{D}_{qp}^t] \\
\mathbf{D}_{mn}^{st} &= \sqrt{n(n+1)}i^{-n}d_n^s Q_n^m \mathbf{N}_{-mn}^1(k, \mathbf{b}_s') + n(n+1)Q_n^m d_n^s \sum_{t=s} \sum_{q,p} [-F_{-mn}^{qp}(\mathbf{b}_{st}) \mathbf{C}_{qp}^t + E_{-mn}^{st}(\mathbf{b}_{st}) \mathbf{D}_{qp}^t] \\
E_{-mn}^{qp}(\mathbf{b}_{st}) &= \frac{1}{2\pi} \int d\Omega(\hat{\mathbf{r}}_c) e^{ik\hat{\mathbf{r}}_c \cdot \mathbf{b}_{st}} \mathbf{C}_{-mn}(\hat{\mathbf{r}}_c) \cdot \mathbf{C}_{qp}(\hat{\mathbf{r}}_c) = \frac{1}{2\pi} \int d\Omega(\hat{\mathbf{r}}_c) e^{ik\hat{\mathbf{r}}_c \cdot \mathbf{b}_{st}} \mathbf{B}_{-mn}(\hat{\mathbf{r}}_c) \cdot \mathbf{B}_{qp}(\hat{\mathbf{r}}_c), \\
F_{-mn}^{qp}(\mathbf{b}_{st}) &= \frac{1}{2\pi} \int d\Omega(\hat{\mathbf{r}}_c) e^{ik\hat{\mathbf{r}}_c \cdot \mathbf{b}_{st}} \mathbf{C}_{-mn}(\hat{\mathbf{r}}_c) \cdot \mathbf{B}_{qp}(\hat{\mathbf{r}}_c) = -\frac{1}{2\pi} \int d\Omega(\hat{\mathbf{r}}_c) e^{ik\hat{\mathbf{r}}_c \cdot \mathbf{b}_{st}} \mathbf{B}_{-mn}(\hat{\mathbf{r}}_c) \cdot \mathbf{C}_{qp}(\hat{\mathbf{r}}_c),
\end{aligned} \tag{22}$$

where the scalars E and F can be evaluated in terms of special functions.

In a cubic cloud 10 km on a side, there are approximately 10^{20} drops. For such large systems, a simple approach as suggested in (20) may be appropriate. Sufficiently far from the source, each drop in a small sub-volume of the cloud experiences essentially the same initial excitation. All of the drops in this sub-volume can be considered as a "compound" scatterer. Its scattering amplitude may be determined by (17). It will then be possible to consider fewer particles making up the cloud. Presumably, the procedure of obtaining $\tilde{\mathbf{G}}$ from $\tilde{\mathbf{G}}$, considering $\tilde{\mathbf{G}}$ as a "compound" $\tilde{\mathbf{G}}$, and working with a distribution of "compound" scatterers can be repeated to obtain a result which is amenable to numerical computations.

The author would like to express his appreciation to W. Koshak, R. Blakeslee, H. Christian, and D. Phanord for their help and acknowledge the assistance of F. Six, L. Freeman, G. Karr, S. Novy and T. Shurtz.

REFERENCES

1. Thomason, L. and Krider, P., "The effect of clouds on the light produced by lightning", *J. Atmos. Sci.* 39 (1982) 2051-2065.
2. Phanord, D., "Analytical optical scattering in clouds", NASA Report NASA CR-184044 xxxvi (1990).
3. Solakiewicz, R., "Electromagnetic scattering in clouds", NASA Report xlviii (1992).
4. Solakiewicz, R., "Transport of photons produced by lightning in clouds", NASA Report NGT-TT-0100802 (1991).
5. Koshak, W., et al, "A diffusion model for lightning radiative transfer", To appear in *J. Geophys. Res.* (1994).
6. Twersky, V., "On scattering of waves by random distributions - 1", *J. Math. Phys.* 3 4 (1962) 700-715.
7. Twersky, V., "On scattering of waves by random distributions - 2", *J. Math. Phys.* 3 4 (1962) 724-734.
8. van de Hulst, H., *Multiple Light Scattering, Tables, Formulas, and Applications*, Academic Press, NY (1980).
9. Foldy, L., "The multiple scattering of waves - 1", *Phys. Rev.* 67 3&4 (1945) 107-119.
10. Twersky, V., "Multiple scattering of electromagnetic waves by arbitrary configurations", *J. Math. Phys.* 8 3 (1967) 589-610.
11. Sommerfeld, A., *Partial Differential Equations in Physics*, Academic Press, NY (1949).
12. Morse, P. and Feshbach, H., *Methods of Theoretical Physics*, Vol. 2, McGraw-Hill, NY (1953).

112592

N95-19007

1994

352856

3410
p-6

NASA/ASEE SUMMER FACULTY FELLOWSHIP PROGRAM

**MARSHALL SPACE FLIGHT CENTER
THE UNIVERSITY OF ALABAMA**

**MICROSTRUCTURAL ANALYSIS OF CRACKS GENERATED DURING
WELDING OF 2195 ALUMINUM-LITHIUM ALLOY**

Prepared By: George E. Talia, Ph.D.
Academic Rank: Associate Professor
Institution and Department: The Wichita State University
Department of Mechanical Engineering

NASA/MSFC:

Laboratory: Materials and Processes
Division: Metallic Materials and Processes
Branch: Metallurgical Research

MSFC Colleague: Arthur C. Nunes, Jr., Ph.D.

Introduction:

This research paper summarizes a series of studies conducted at Marshall Space Flight Center to characterize the properties of 2195 Al-Li alloy. 2195 Al-Li alloy, developed by Martin Marietta laboratories is designated as a replacement of 2219 Al-Cu alloy for the External Tank (E.T.) of the space shuttle. 2195 Al-Li alloy with its advantage of increased strength per weight over its predecessor 2219 Al-Cu alloy, also challenges current technology. 2195 Al-Li has a greater tendency to crack than its predecessor.

The present study began with the observation of pore formation in 2195 Al-Li alloy in a thermal aging process. In preliminary studies, Talia and Nunes found that most of the two pass welds studied exhibited round and crack-like porosity at the weld roots. Furthermore, the porosity observed was associated with the grain boundaries. The porosity level can be increased by thermal treatment in the air. A solid state reaction proceeding from dendritic boundaries in the weld fusion zone was observed to correlate with the generation of porosity.

These findings led Talia and Nunes to investigate further on the same lines, which resulted in this research. Particular emphasis was placed on the mechanisms of crack formation/propagation generated by VPPA welding process. The micro/macro structures of cracks were characterized by extensive optical and scanning electron microscope (SEM) observations. Differential Thermal Analysis (DTA), Thermal Gravimetric Analysis (TGA), and Energy Dispersive Spectrometry (EDS) investigations of the 2195 Al-Li alloy weldments were carried out in order to identify the nature of the dendritic reaction, porosity, and cracking. At the time of this writing a complete understanding of the nature of pores and cracking tendency of the 2195 Al-Li alloy is lacking. A model, explaining the different facets of the problem in accordance with the observations, is hence proposed.

Experimental Procedure

A series of experiments were performed during the course of this study to explain cracking of VPPA weldments at in 2195 Al-Li alloy. The plate thickness of the test specimens used during the experiments and analysis was 0.2 inches. Welds were performed both with and without filler metal. The welds were carried out in two sequential passes, a root and a cover pass. Samples were prepared for metallographic examination using standard polishing preparation technique and Kellers reagent etch. Optical microscopy observations were performed on a Nixon inverted microscope. One pass autogenous welds samples (no filler material) were selected for further thermal processing, i.e., heat treatment at different temperatures in air, oxygen, nitrogen and helium and vacuum. Extensive SEM fractographic analysis of the repair crack morphology was carried out on a Philips 515 SEM. Some of the

cracks were opened in tension mode for analysis of the inner surface. Furthermore, the appearance of tiny surface blisters on weld surface and on the fractured surface indicates an outgassing phenomenon linked to porosity, were also studied. X-ray microanalysis was carried out by EDAX (Energy Dispersive X-Ray System) attached to the Philips 515 SEM. EDAX performs the quantitative X-Ray microanalysis with the help of Super net X-Ray package. This software processes a spectrum to obtain net X-Ray intensities. The subjects of these analyses were of peculiar nature including crack interiors, supposed material "eruptions" from cracks, blisters and their morphology and the presence of magnesium rich "smut"/"snow" and oxides. All counts were taken at of 30 kv. Most of the SEM observations were accompanied by the X-Ray microanalysis.

To learn more about the dendritic or grain boundary reaction observed in the preliminary studies, Differential Thermal Analysis (DTA) and Thermal Gravimetric Analysis (TGA) were carried out. A systematic DTA analysis of the autogenous weld samples and parent metal was performed in air, nitrogen, helium and oxygen atmosphere. The analysis was performed on a DuPont 1090 system. The resulting thermograms were generated by General Analyser VI.0. The furnace and sample block temperature were increased at a linear rate of 10 and 20 °C/min and the sample weights were from 10 to 20 mg. A comparative TGA study was performed for 2195 Al-Li alloy and Al 2219 as control samples. PERKINS-ELMER 7 Series Thermal Analysis System was used for the analysis where the systems temperature was increased at a linear rate of 20 °C/min. The sample weight had a range from 70 to 95 mg. All the TGA experiments were performed under a dry nitrogen atmosphere.

Results and Discussion:

Repairs of defective welds sometimes produce new cracks, to be designated as "repair induced cracks." For subsequent SEM observations, repair induced cracks were torn open in a tensile mode. Figure 1(a) presents a view of "repair induced crack" fracture surface, indicating a ductile fracture, where the surface shows a combination of "melting" and "tearing" areas. Figure 1(b) illustrates another portion of the fracture surface, where melting is predominant. EDS microanalysis observations show that the melted areas present less copper and more nitrogen and oxygen than the tearing areas. The above fractographic observations revealed internal porosity with additional evidence of melting and gas pressure.

"Smut" outside the "repair induced crack," is shown in Figure 2. Its presence suggests fluid eruption from inside the crack. A high content of oxygen and nitrogen in the smut suggests a reaction inside the crack between nitrogen/oxygen/air and the crack wall. This reaction may generate gas pressure responsible of the eruption of low melting point smut outside the crack.

During the course of the study, a few samples of 2195 Al-Li welded specimens accidentally welded without the back shielding were examined. Air-contamination resulted in pore and blister formation. Typical SEM observations of the surface are presented in Figure 3. The root surface exhibits large and small blisters, and evidence of melting. The blisters are surrounded by matter as if matter erupted from inside, similar to the smut observed previously. It is conjectured that presence of a nitrogen/oxygen/air reaction causes melting and generates enough gas pressures in these blisters to cause eruption of melted matter to smut. In the interior of the blister, high nitrogen, magnesium, and oxygen, and decreased copper is measure. An optical micrograph cross section is presented in Figure 4, showing internal blister formation, and evidence of melting or partial melting induced by air contamination. The spherical form of the pore/blister indicates gas pressure acting.

To learn more about the dendritic or grain boundary reaction observed in the preliminary studies, DTA was performed on 2195 welds and parent metal. The analyses were carried out under atmospheres of air, oxygen, helium, and nitrogen.

During the DTA, for the parent metal no reactions were detected below the melting temperature of aluminum. However, all the weld samples exhibited a small endothermic transformation at about 530 °C, while those heated in nitrogen or air also exhibited exothermic transformations at about 360 °C. These features may be interpreted as indicating a nitrogen reaction that takes off and then saturates around 360 °C and, perhaps, partial melting at grain/dendrite boundaries at about 530 °C. During the TGA experiments in a dry nitrogen atmosphere at constant temperature and constant rate rising temperature, a weight gain of the samples was measured for 2195 Al-Li alloy. Since nitrogen is practically insoluble in the components of the alloy, it is inferred that a chemical reaction took place between the elements of the alloy and nitrogen. The reaction produced a brown film on the surface of the specimen. The film attacked the platinum crucible used to hold the specimen as the temperature moves into the neighborhood of the alloy liquidus. These features are characteristic of Li_3N .

Conclusions:

2195 weld metal exhibits evidence of surface melting on fracture surfaces an endothermic phase transformation at about 530 °C that would be consonant with grain boundary liquation. Nitrogen reacts with 2195 alloy at temperatures above 360 °C. Its is speculated that the solid state nitrogen reaction induces grain boundary melting while generating a pressurized gaseous phase that flashes out the melted matter at the free surfaces. In this way internal cracks, porosity, and surface blisters with surrounding exudates are formed.



(a)



(b)

Figure 1.- Fractographs of a repair induced crack presenting (a) ductile fracture and (b) evidence of grain boundary melting.

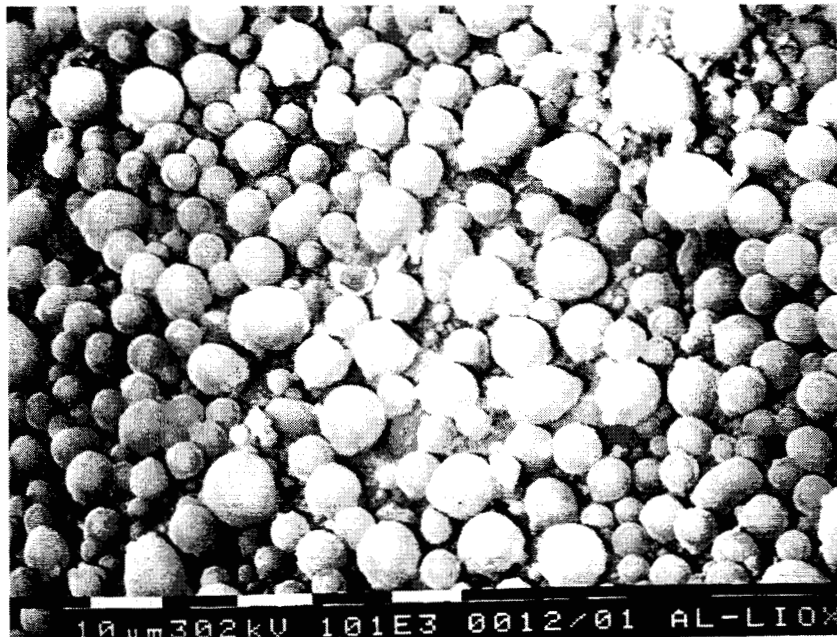


Figure 2.- SEM micrographs showing "smut" observed near the repair crack.



Figure 3.- Blisters on the free surface of a contaminated weld showing evidence of surface melting and gas pressure.

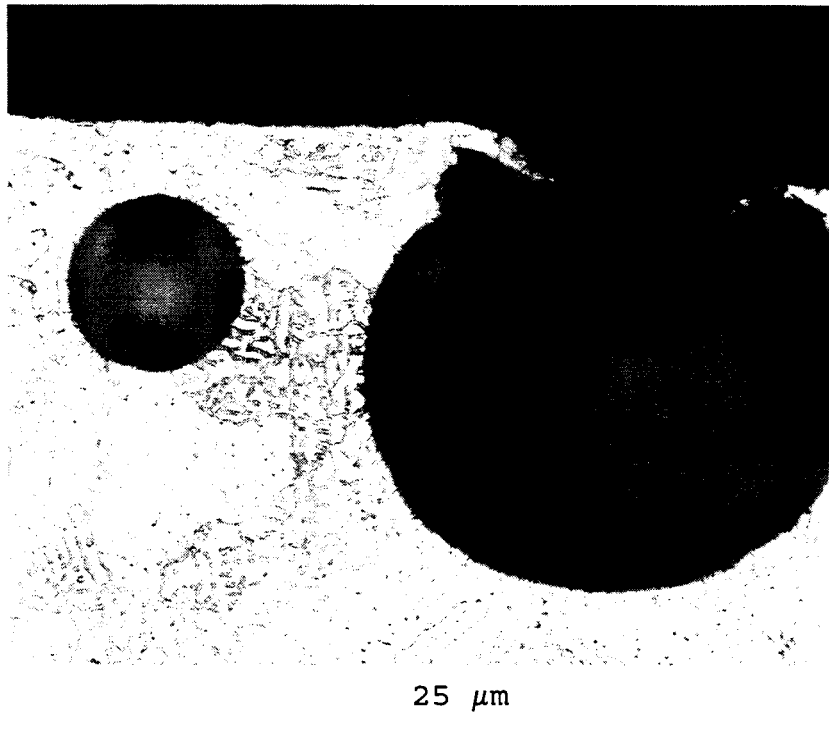


Figure 4.- Internal and external blistering in a 2195 alloy weld bead caused by air contamination.

112593

352857
N95-19008

30931
p. 9

1994

NASA/ASEE SUMMER FACULTY FELLOWSHIP PROGRAM

**MARSHALL SPACE FLIGHT CENTER
THE UNIVERSITY OF ALABAMA**

**QUALITY OPTIMIZATION OF THERMALLY SPRAYED COATINGS PRODUCED BY
THE JP-5000 (HVOF) GUN USING MATHEMATICAL MODELING**

Prepared By:	Hazem Tawfik, Ph.D., P.E., CMfgE
Academic Rank:	Professor and Director
Institution and Department:	State University of New York at Farmingdale Manufacturing and Mechanical Research
NASA/MSFC:	
Laboratory:	Materials & Processes Laboratory
Division:	Metallic Materials Division
Branch:	Metals Processes Branch
MSFC Colleagues:	Frank Zimmerman

INTRODUCTION

Thermal spray coatings have become increasingly important as one of the most advanced coating technologies in modern industry. Production of protective coatings from mechanical wear, excessive heat, and corrosion/oxidation applications has been the goal of thermal spray coatings for a number of years. In particular, the past decade has seen an increased use of various thermally sprayed metal matrix, ceramics and composite coatings. Currently, thermal barrier coatings (TBC) of gas-turbine blades and similar applications have centered around the use of zirconia as a protective coating for such a high thermal application. The advantages of zirconia include low thermal conductivity and good thermal shock resistance, Lugscheider and Rass¹. Moreover, thermally sprayed tungsten carbide hardface coatings are used for a wide range of applications spanning both the aerospace and other industrial markets. Major aircraft engine manufacturers and repair facilities use hardface coatings for original engine manufacture (OEM), as well as in the overhaul of critical engine components. The principle function of these coatings is to resist severe wear environments for such wear mechanisms as abrasion, adhesion, fretting, and erosion, Nerz et al².

The (JP-5000) thermal spray gun is the most advanced in the High Velocity Oxygen Fuel (HVOF) systems. Recently, the (JP-5000) has received considerable attention because of its relative low cost (\$50,000) and its production of quality coatings that challenge the very successful but yet relatively expensive (\$1.5 million) Vacuum Plasma Spraying (VPS) system. The quality of the thermal spray coatings is enhanced as porosity, oxidization, residual stresses, and surface roughness are reduced or minimized. Similarly, higher densification, interfacial bonding strength, hardness and wear resistance of a coating are definitely desirable features for quality improvement. The thermal spraying industry of today is aware of the necessity of well understood, optimized and reproducible coating processes. Therefore, it is essential to progress in the many fields of thermal spray technologies to efficiently determine the set of optimal spraying parameters, Knotek and Schnaut³.

Like all coating processes, HVOF thermal spraying has to be regarded as a system consisting of the substrate, coating material, and coating process (Figures 1,2). All components of the system and their interactions have to be optimized to obtain suitable coatings, Lugscheider et al⁴. The powder characteristics influence the spraying process and the resulting coating properties; two of the most important powder characteristics are flow behavior and particle grain size range. A powder that flows well results in a powder being fed continuously into the HVOF without intermittent or pulsating flow. A narrow particle size range provides homogeneous melting of the particles in the gun barrel. As well, the splat architecture, microstructure, diffusion, phase distribution, and phase transformation at the interface region are of considerable importance to the coating quality and the fundamental understanding of the deposition process, Zimmerman et al⁵. Mathematical modeling of the HVOF process gasdynamics is used to numerically evaluate the particle velocity and temperature immediately before impacting the substrate. These parameters are of prime influence on the coating formation and therefore the coating properties and quality. Numerical solutions and modeling techniques are evidently gaining more importance as tools for optimization of processes, especially in thermal spraying.

The reason is not only their cost effectiveness, but these simulation models are an efficient time saver and provide more insight in the subject matter as compared to the known statistical methods such as Design of Experiments and Taguchi methods, Regression analysis, Knotek and Schnaut³.

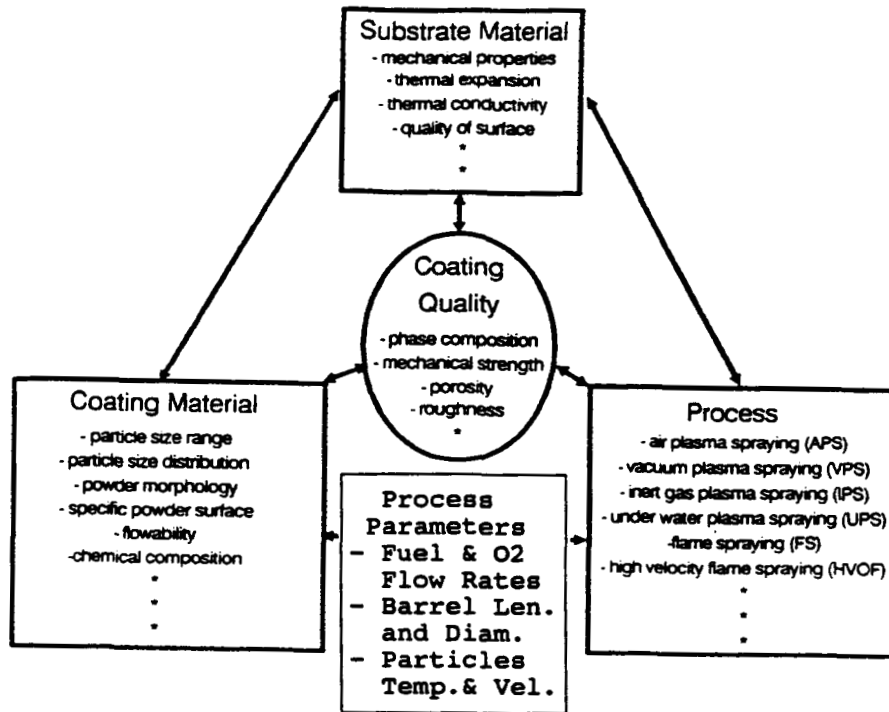


Figure 1: Thermal Coating Quality Diagram

MATHEMATICAL MODEL AND NUMERICAL SOLUTION

A one dimensional single phase flow of combustion gases was assumed in the combustion chamber, conversion-divergent nozzle, and gun barrel. The powder injection at the beginning of the barrel (Fig. 2) represented 10% [powder to (powder + gas), by weight ratio] and negligible volume ratio. For an initial study the effect of the powder on the flow properties was not considered.

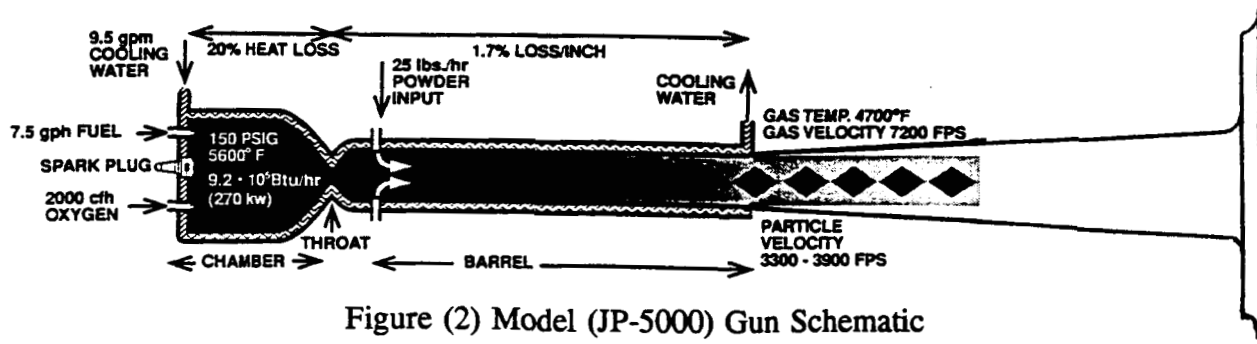


Figure (2) Model (JP-5000) Gun Schematic

Cooling Water Temperature Calculation at the Exit Section:

The model predictions of the cooling water exit temperature from the gun were in good agreement with the measured data provided by Rocketdyne Division. It was assumed that the cooling water absorbed 20% of the kerosene heat value in the combustion chamber and 1.7% of the same amount per unit length of the barrel Fig.(2), Thorpe and Richter⁶.

Modeling of the Combustion Chamber:

The combustion chamber C.C. was modeled through a heat balance equation as described in the following:

Total Heat input to the C.C. = Total Enthalpy Input of Oxygen and Kerosene to C.C. + Low Heat Value of Kerosene - Heat of Evaporation of Kerosene

Total Heat Output From The C.C. = Gases Temp x Gases Sp. Heat x Gases Weight Flow Rate - Heat absorbed by Cooling Water

The weight fractions of the combustion gases were obtained by Chemical Equilibrium with Transport Properties Computer Code, McBirde et al⁷. They were found to read as follows:

CO = 24.5% , O₂ = 12.6% , CO₂ = 16.8% , H₂ O = 27.9% , OH = 9.4% , H₂ = 8.8%

The gas mixture sp. heat was evaluated based on the weighted average of each gas sp. heat using the weight fractions shown above. The sp. heat of each gas was obtained from a correlation as a function of temperature. Due to the dependence of gas sp. heat on temperatures, iteration was necessary to solve for the temperature of the combustion chamber. For the gun specifications and geometry shown in (Fig. 2) a computer program written in the Basic language was developed and the temperature of the (C.C.) was evaluated by this program to read 4440.17 °F which indicated an excellent agreement with the gun manufacturer experimentally measured data.

Modeling of the Convergent-Divergent Nozzle:

Because of the symmetry and small width to length ratio of the HVOF configuration, one-dimensional, friction, diabatic, and steady state flow analysis was considered. The general differential model developed by Shapiro⁸ was modified to allow for four independent variables, namely, Cross-Sectional Area of flow (A), Heat Rejection (Q), Friction (f), and Sp. Heats Ratio (k). The model also incorporated another three dependent variables, they are as follows: Mach No. (M), Temperature (T), and Pressure (P). The working system of differential equations as applied to the control surface defined in Figure (3) is briefly described in Table (1) and in the following equations:

From the convergent-divergent nozzle geometry; $D_{n+1} = D_n - 1.3386 dx$ and $D_{n+1} = D_n +$

0.251 dx respectively.

The amount of heat absorbed by the cooling water per unit mass of the gaseous flow (dQ) is evaluated as 1.7% of the total heat value of kerosene per unit inch of the gun length, Thorpe and Richter⁶. Thus, $dQ = -0.017 \times$ kerosene flow rate \times (kerosene heat value - kerosene heat of evaporation) dx / gas weight flow rate. The friction coefficient (f) for subsonic and super sonic flow was given the value of 0.003 and 0.005 respectively.

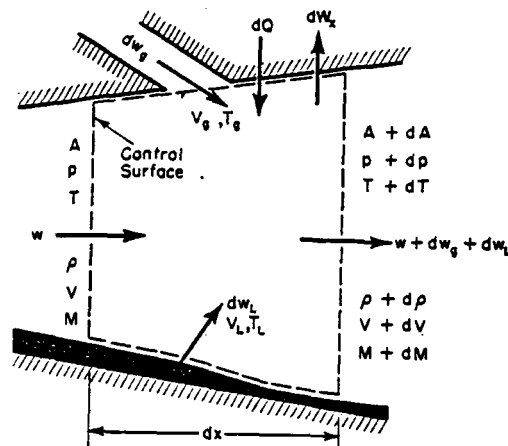


Figure (3) Control Surfaces Definitions

$$\frac{p_2}{p_1} = \frac{w_2 A_1 M_1}{w_1 A_2 M_2} \sqrt{\frac{T_2}{T_1}} \sqrt{\frac{k_1 W_1}{k_2 W_2}}$$

Table(1) INFLUENCE COEFFICIENTS FOR VARIABLE SPECIFIC HEAT AND MOLECULAR WEIGHT

	$\frac{dA}{A}$	$\frac{dQ - dW_x + dH}{cpT}$	$4f \frac{dx}{D} + \frac{dK}{\frac{1}{2} k p A M^2} - 2v \frac{dw}{w}$	$\frac{dw}{w}$	$\frac{dW}{W}$	$\frac{dk}{k}$
$\frac{dM^2}{M^2}$	$-\frac{2 \left(1 + \frac{k-1}{2} M^2\right)}{1 - M^2}$	$\frac{1 + kM^2}{1 - M^2}$	$\frac{kM^2 \left(1 + \frac{k-1}{2} M^2\right)}{1 - M^2}$	$\frac{2(1 + kM^2) \left(1 + \frac{k-1}{2} M^2\right)}{1 - M^2}$	$-\frac{1 + kM^2}{1 - M^2}$	-1
$\frac{dT}{T}$	$\frac{(k-1)M^2}{1 - M^2}$	$\frac{1 - kM^2}{1 - M^2}$	$-\frac{k(k-1)M^2}{2(1 - M^2)}$	$-\frac{(k-1)M^2(1 + kM^2)}{1 - M^2}$	$\frac{(k-1)M^2}{1 - M^2}$	0

NOTES: (1) Each influence coefficient represents the partial derivative of the variable in the left-hand column with respect to the variable in the top row; for example

$$\frac{dM^2}{M^2} = -\frac{2 \left(1 + \frac{k-1}{2} M^2\right)}{1 - M^2} \frac{dA}{A} + \frac{1 + kM^2}{1 - M^2} \frac{dQ - dW_x + dH}{cpT} + \dots - \frac{dk}{k}$$

NUMERICAL INTEGRATION SCHEME

Because of the high nonlinearity of this system of differential equations a numerical integration scheme was conducted to evaluate the flow velocity, temperature, and pressure at various cross-sections of the gun. Both the mach number and temperature differential equations given in Table (1) were modified and integrated over a small element bounded by sections n, n+1 as shown in the following:

$$\int_{T_n}^{T_{n+1}} \frac{dT}{T} = FAT_n \int_{A_n}^{A_{n+1}} \frac{dA}{A} + \frac{FQT_n}{c_p T_n} \int_{Q_n}^{Q_{n+1}} dQ + 4f \frac{FFT_n}{D_n} \int_{x_n}^{x_{n+1}} dx$$

$$\int_{M_n^2}^{M_{n+1}^2} \frac{dM^2}{M^2} = FAM_n \int_{A_n}^{A_{n+1}} \frac{dA}{A} + \frac{FQM_n}{c_p T_n} \int_{Q_n}^{Q_{n+1}} dQ + FFM_n \frac{4f}{D_n} \int_{x_n}^{x_{n+1}} dx - \int_{k_n}^{k_{n+1}} \frac{dk}{k}$$

All the influence coefficients were considered constant with their section (n) values in the elements between sections (n), (n+1). Further manipulation and re-arrangement of the last two eqn(s) were performed and an approximate numerical solution was achieved, it read as follows:

$$M_{n+1}^2 = e^{\ln M_n^2 + FAM_n (\ln A_{n+1} - \ln A_n) + FQM_n \frac{\Delta Q}{c_p T_n} + FFM_n \frac{4f \Delta x}{D_n} - (\ln k_{n+1} - \ln k_n)}$$

Similarly

$$T_{n+1} = e^{\ln T_n + FAT_n (\ln A_{n+1} - \ln A_n) + FQT_n \frac{\Delta Q}{c_p T_n} + FFT_n \frac{4f \Delta x}{D_n}}$$

NUMERICAL ITERATION SCHEME

To enhance the accuracy of the numerical integration and hamper the instability of the solution due to the discontinuity in the sonic speed at the throat cross-section, a numerical iteration scheme was developed. This iteration scheme was based on the assumption of linear variation of the coefficients and flow properties within the small integration elements. Therefore each influence coefficient and flow property were considered to be at their average value at the (n+0.5) cross section. The iteration scheme to minimize the errors in the temperature (ET) and Mach No. (EM) is described as shown in the following:

$$EM = \ln M_n^2 - \ln M_{n+1}^2 + FAM_{n+.5} (\ln A_{n+1} - \ln A_n) + FQM_{n+.5} \frac{\Delta Q}{c_p T_{n+.5}} + FFM_{n+.5} \frac{4f \Delta x}{D_{n+.5}} - (\ln k_{n+1} - \ln k_n)$$

$$ET = \ln T_n - \ln T_{n+1} + FAT_{n+.5} (\ln A_{n+1} - \ln A_n) + FQT_{n+.5} \frac{\Delta Q}{c_p T_{n+.5}} + FFT_{n+.5} \frac{4f \Delta x}{D_{n+.5}}$$

The numerical solution was carried out by dividing the convergent and divergent parts of the nozzle and the barrel to a total of 280 small increments. They were distributed as 40,40, and 200 respectively.

RESULTS AND ANALYSIS

The obtained results from the computer program for the flow's gas dynamics properties, pressure, velocity, and temperature calculated at different sections along the gun X-axis were exhibited in table (2). The pressure showed considerable expansion and sharp drop along the nozzle. Meanwhile, the gas velocity reached Mach No. of 1.9 or 8507 FPS, and the temperature dropped from 4440 °R at the C.C. to 3066 °R at the exit of the nozzle. The flow also showed a slight increase in pressure and decrease in velocity in the barrel due to friction. These changes were accompanied with a moderate decrease in temperature due to the cooling water effect.

Table(2) Computer Program Predictions of Flow Gas Dynamics Properties

X - Axis inches	Pressure psi	Velocity Feet/sec	Temperature Degrees R	Comments
0.0	100	194	4440	Comb. Chamber
3.4	100	194	4440	Exit of C.C.
4.28	65.26	4785	4193	Throat
4.78	17.9	8507	3052	Exit of Nozzle
6.78	18.76	8153	3066	Barrel Sec. @ 1.5"
8.78	19.50	7815	3067	Barrel Middle Sec.
10.78	20.34	7493	3055	Barrel Sec. @ 4.5"
12.78	21.05	7181	3031	Barrel Exit Sec.

CONCLUSIONS

- (1) The current model predicted the cooling water exit temperature as well as the gas flow properties, velocity, pressure, and temperature along the X-axis of the JP-5000 Thermal Spray Gun with an overall numerical accuracy of 96%.
- (2) These predictions are in excellent agreement with measurements at the combustion chamber and the barrel exit section.
- (3) The developed numerical iteration scheme succeeded to hamper the brief model instability due to the discontinuity of the sonic speed in the near vicinity of the throat cross-section.
- (4) In the area of thermal spray, the current model presented a unique and a successful beginning towards a more comprehensive simulation model of the JP-5000 to yield the necessary information for the control of the gun parameters on a real time basis to continuously provide optimum quality coatings

WHAT SHOULD BE DONE?

Recommendation #1:

Further development of the current model is recommended to account for the powder (10% by weight) flow in the barrel and in the free plume before impacting the substrate. The study and simulation of such a two phase gas-particle flow will enhance the model prediction accuracy.

Recommendation #2:

Further analysis is recommended to rectify the slight numerical instability in the current model in the very closed vicinity of the throat due to the discontinuity of the speed of sound in this area.

Recommendation #3:

After the incorporation of recommendations #1 and #2 above, the current simulation model should be used to conduct a detailed and comprehensive study on the influence of the thermal spray system parameters on the coatings quality. This model should then be used in cooperation with a neural network system to provide active and real time control on the coatings quality and provide a complete optimization of the HVOF thermal spray process.

REFERENCES

1. Lugscheider, E., and Rass, A., "Underwater Plasma Processing of Stabilized Zirconia for Thermal Barrier Coatings", Thermal Spray Technology, Vol. 1:No. 1, pp. 49-55, 1992.
2. Nerz, J., Kushner, b., and Rotolico, A., "Microstructural Evaluation of Tungsten Carbide-Cobolt Coatings", Thermal Spray Technology, Vol. 1:No. 2, pp. 147-152, 1992.
3. Knotek, O., and Schnaut, U., "Numerical simulation of the Influences of HVOF Spraying Parameters on Coating Properties", Thermal Spray Conference, Anaheim, CA, 7-11 June 93
4. Lugscheider, E., Knepper, M., and Gross, K.A., "Production of Spherical Apatite Powders - The First Step For Optimized Thermal-Sprayed Apatite Coatings", Thermal Spray Technology, Vol. 1:No. 3, pp. 215-221, 1992.
5. McKechnie, T. N., Zimmerman, F.R., and Bryant, M.A., "Vacuum Plasma Spray Applications on Liquid Fuel Rocket Engines", AIAA 92-3527, pp. 1-12, 1992
6. Thorpe, M.L., and Richter H.J., "A Pragmatic Analysis and Comparison of HVOF Process", Thermal Spray Technology, Volume 1(2), pp.161-170, 1992
7. McBirde, B., Gordon, S., Reno, M., "Chemical Equilibrium with Transport Properties, cosmic program # LEW-16017 - 1993.
8. Shapiro, A.H., "Compressible Fluid Flow", The Ronald Press Comp., New York, 1953

350858

112594

517 111
N95-19009

30732

P.6

1994

NASA/ASEE SUMMER FACULTY FELLOWSHIP PROGRAM

**MARSHALL SPACE FLIGHT CENTER
THE UNIVERSITY OF ALABAMA**

PRISM PROJECT OPTICAL INSTRUMENT

Prepared By: Charles R. Taylor, Ph.D.

Academic Rank: Assistant Professor

Institution and Department: Pacific University
Department of Physics

NASA/MSFC:

Laboratory: Space Sciences
Division: Physics and Astronomy
Branch: Astrophysics

MSFC Colleague: Charles M. Telesco

INTRODUCTION

The scientific goal of the PRISM (Passively-cooled Reconnaissance of the InterStellar Medium) project is to map the emission of molecular hydrogen at 17.035 μm and 28.221 μm . Since the atmosphere is opaque at these infrared wavelengths, an orbiting telescope is being studied. My role has been to work on the optical design of the instrument.

The availability of infrared focal plane arrays enables infrared imaging spectroscopy at the molecular hydrogen wavelengths. The array proposed for PRISM is 128 pixels square, with a pixel size of 75 μm . In order to map the sky in a period of six months, and to resolve the nearer molecular clouds, each pixel must cover 0.5 arcminutes. This sets the focal length of the instrument at 51.6 cm. In order for the pixel size to be half the diameter of the central diffraction peak at 28 μm would require a telescope aperture of 24 cm; an aperture of 60 cm has been selected for the PRISM study for greater light gathering power. This sets the focal ratio at $f/0.86$.

In order to find the emission lines in the background continuum, and to allow for Doppler shifts of the lines at radial speeds on the order of several hundreds of kilometers per second requires spectral resolution of at least 3000. Thus it would appear that two imaging spectrometers are required, one for each line.

PRELIMINARY DESIGN

A 370 cm focal length Cassegrain telescope has been designed by John Jackson. A preliminary spectrometer design by Russell Chipman of the University of Alabama in Huntsville is based on a 360 cm focal length telescope followed by a prism monochromator and a grating spectrograph. The monochromator is used to select the two wavelengths of interest. The grating spectrograph is used in fifth order at 17 μm and third order at 28 μm . With this design, a single spectrometer can place both wavelengths of interest on a single focal plane array. The version of the spectrometer design I have seen does not yet give the correct scale on the array in the imaging direction.

My suggestion is that the instrument consist of the four stages listed below.

1. Cassegrain telescope. This stage gathers infrared radiation over a large aperture and forms an image of the sky at the Cassegrain focus.
2. Grating monochromator. The entrance slit selects a strip of the sky for spectroscopic analysis. The grating disperses light along the strip by wavelength, and the exit slits select two wavelength bands for further analysis.
3. Grating spectrograph. Light in each of the two bands is further dispersed by wavelength.
4. Final reimager. The spectrograph output is rescaled to fit on the very small focal plane array.

I have chosen a 284 cm focal length Cassegrain telescope in order to shorten the instrument for improved passive cooling. The telescope is shown in Fig. 1a, including a flat

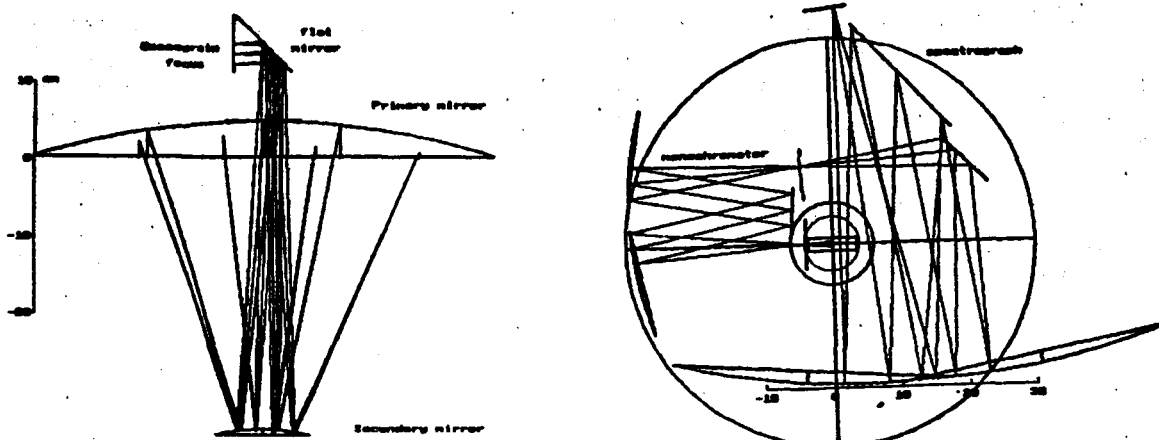


Figure 1a (left). 284 cm focal length Cassegrain telescope. 18 rays from three directions are shown. Figure. 1b (right). Grating monochromator and spectrograph. The 60-cm diameter circle is the outline of the primary mirror and the edge of the instrument volume. Three rays at $17 \mu\text{m}$ are shown.

mirror to redirect the light into the plane of the spectrometer. The distance between the primary and secondary mirrors is 40 cm, half the distance in Jackson's design.

I have chosen a grating monochromator because of the difficulty in finding a suitable prism material, and in order to avoid extreme curvature of the monochromator output slit.

A monochromator and spectrograph are shown in Fig. 1b. The four mirrors are paraboloids. The monochromator entrance slit is at the Cassegrain focus of the telescope. The monochromator grating is used in first order, and the two wavelengths are selected with two parallel exit slits. The spectrograph grating is used in fifth order at $17 \mu\text{m}$ and third order at $28 \mu\text{m}$ as in Chipman's design.

The design of the final reimager is yet to be completed. The optical parameters of the design are listed in Table 1.

PERFORMANCE OF THE PRELIMINARY DESIGN

The diameters of the central diffraction peaks for a 60 cm circular aperture are $196 \mu\text{m}$ for $17 \mu\text{m}$ and $326 \mu\text{m}$ for $28 \mu\text{m}$ at the monochromator slits, and $36 \mu\text{m}$ and $59 \mu\text{m}$ on the array. Thus diffraction should not cause significant loss of light at the slits or blurring of the image.

Aberrations must be minimized at the monochromator entrance and exit slits and at the final focus. The telescope optics determine the aberrations at the entrance slit. Conic surfaces optimized only in shape lead to the spot diagrams of Fig. 2. The spots are near the required size of 0.0413 cm ; the remaining aberrations could be reduced by further optimization.

Parameter	units	value
Effective focal length	cm	284.00
Primary mirror focal length	cm	49.36
Secondary mirror focal length	cm	-11.33
Primary/secondary separation distance	cm	40.00
Secondary/Cassegrain focus distance	cm	53.84
Primary mirror diameter	cm	60.00
Secondary mirror diameter	cm	12.12
Monochromator entrance slit width	μm	413
Monochromator collimator and reimager focal lengths	cm	25.00
Spectrograph collimator and reimager focal lengths	cm	55.00
Deviation by off-axis paraboloids	degrees	12
Monochromator grating groove density	mm^{-1}	9.5
Monochromator incidence angle	degrees	16.27
Monochromator diffraction angle, 17 μm	degrees	-6.79
Monochromator diffraction angle, 28 μm	degrees	-0.69
Spectrograph grating groove density	mm^{-1}	11.0
Mean spectrograph incidence angle	degrees	38.31
Mean spectrograph diffraction angle	degrees	18.31

Table 1. Instrumental parameters.

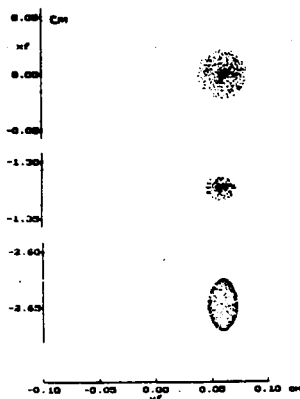


Figure 2. Spot diagrams at the Cassegrain focus/monochromator entrance. The center of the field is at the top and the edge of the field is at the bottom. Required spot diameter is 0.0413 cm.

The monochromator exit slit widths determine the widths of the spectral bands passed to the spectrograph. In order for each band to cover 32 pixels on the array, the widths are 0.043 cm

for $17\ \mu\text{m}$ and $0.071\ \text{cm}$ for $28\ \mu\text{m}$. Spot diagrams at the monochromator exit slits are shown in Fig. 3a. The required spot sizes are not quite achieved, particularly at the edge of the field. The consequence is that if this design were used, there would be a loss of signal at the exit slits, in an amount which increases toward the edge of the image. There would not be significant blurring of the image, for the aberrations of the monochromator are compensated by the spectrograph.

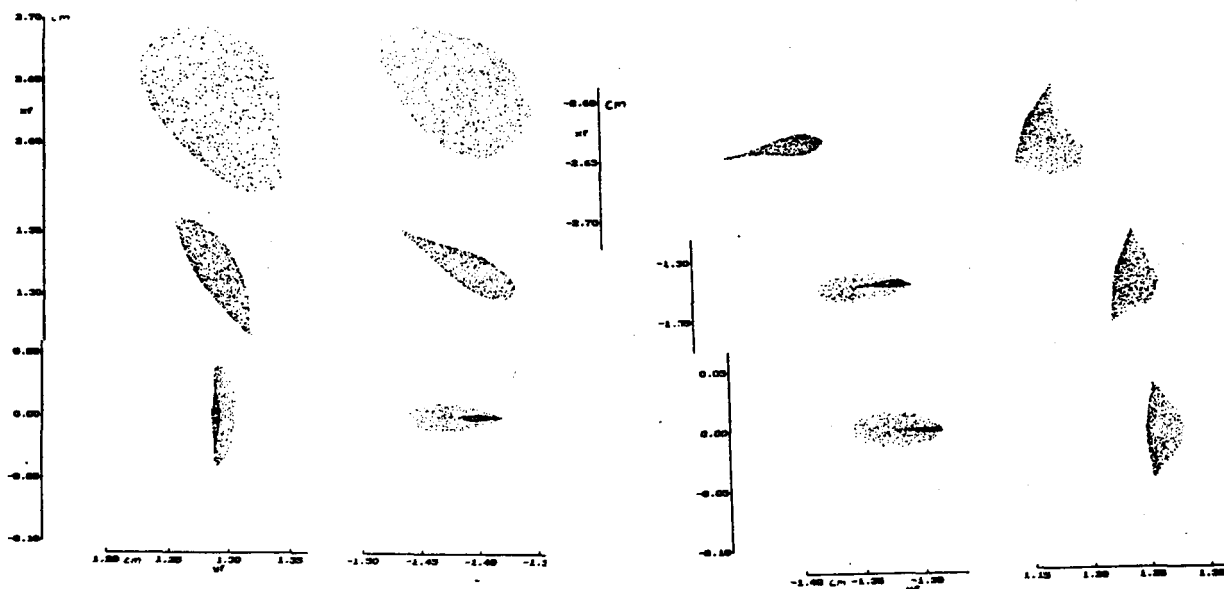


Figure 3a (left). Spot diagrams at the monochromator exit. The center of the field is at the bottom and the edge of the field is at the top. $17\ \mu\text{m}$ is on the left and $28\ \mu\text{m}$ is on the right. Required spot diameters are $0.043\ \text{cm}$ for $17\ \mu\text{m}$ and $0.071\ \text{cm}$ for $28\ \mu\text{m}$. Figure 3b (right). Spot diagrams at the spectrograph output. Organized as in Fig. 3a. Required spot diameter is $0.0413\ \text{cm}$.

An acceptable final reimager has not been designed, but the spectrograph output has been analyzed. Spot diagrams are shown in Fig. 3b. The spots generally are within the required size of $0.0413\ \text{cm}$, so the reimager will only need to maintain the quality of the spectrograph output.

Three attempts to achieve the scale of the final image have so far not met with success. The first was to change the focal length in the monochromator or spectrograph by using different focal lengths for the off-axis paraboloidal mirrors. With this approach I was not able to reduce the aberrations to acceptable levels. The second effort was to design a reimaging lens or pair of lenses of the same materials, either CsI or KRS-5. With this effort I was not able to overcome the chromatic aberration between $17\ \mu\text{m}$ and $28\ \mu\text{m}$. The third approach was to use a centered pair of mirrors, essentially a small Cassegrain telescope. So far I have not been able to reduce the aberrations to an acceptable level with components small enough to fit inside the instrument volume. Probably a third mirror, correcting plate, or meniscus lens is needed.

The throughput is limited primarily by the obstruction of the Cassegrain telescope and the efficiencies of the two gratings. My telescope design has only a 4.1 % obstruction by the secondary mirror. Grating efficiencies are limited to less than 91 % since 9% must go into secondary diffraction peaks between the principle peaks. Efficiencies must be calculated by electromagnetic theory, but I have made crude estimates based on scalar diffraction theory for the gratings in my design. The monochromator grating, if blazed at 5.7 degrees, should have efficiencies of about 70 % and 73 % for 17 μm and 28 μm , respectively. The spectrograph grating, if blazed at 52 degrees, should have efficiencies of about 46 % and 70 % respectively. Allowing for 99 % efficiency at each of 8 mirrors, the efficiencies of my design are about 28 % and 45 % for 17 μm and 28 μm , respectively.

The efficiency estimates above do not take into account the losses at the monochromator exit slit implied by the spot diagrams of Fig. 3a. There will also be losses in the final reimager, and reflection losses from the array. It should, however, be possible to antireflection coat the array¹ and any refractive surfaces in the final reimager, because of the coincidence noted by Chipman, that 5/4 of 17 μm is nearly equal to 3/4 of 28 μm .

In the spectrograph output, one-half arcminute on the sky is imaged onto 413 μm , and the entire field of 64 arcminutes is imaged onto a 5.3 cm line. The spectral lines are separated by a convenient distance of about 2.5 cm. The spectral lines are curved such that the top is displaced from the center by about 0.10 cm. The dispersion indicated by ray tracing is close to the amount I estimated for the design, so that after reimaging each pixel will cover 5.5 nm at 17 μm and 10.3 nm at 28 μm . The resolving powers are 3000 and 2700, respectively, and the velocity resolutions are 100 km/s and 111 km/s, respectively. I have not analyzed instrumental spectral linewidths.

The aberrations in the monochromator should be reduced. One way of doing this is to increase the focal lengths of the mirrors, but this will cause difficulties with packaging. Another approach is to improve upon the collimation and reimaging by using off-axis ellipsoids or other surfaces instead of paraboloids. My preliminary efforts indicate that ellipsoids can give improved collimation, but I have not yet incorporated them into the design.

The packaging of my design is very near to fitting within the instrument volume, which is a cylinder 60 cm in diameter and 20 cm tall. Fine tuning must be done to insure that components fit exactly within the allotted volume and that no rays intersect the wrong surfaces. The final reimager needs to be packaged as well.

The greatest problem is to reduce the spectrograph output to fit on the very small array. This problem would be alleviated if a larger array could be used.

REFERENCE

1. Rudisill, J. Earl and Hue Thi-Bach Nguyen, "Thin film coatings for improved IR detector performance", in Infrared Thin Films, Ric P. Shimshock, ed., pp. 141-55, 1992.

112595

N95-19010

350859

50933

p. 6

1994

NASA/ASEE SUMMER FACULTY FELLOWSHIP PROGRAM

**MARSHALL SPACE FLIGHT CENTER
THE UNIVERSITY OF ALABAMA**

**THE PROBABILITY OF FLAW DETECTION AND THE PROBABILITY OF FALSE
CALLS IN NONDESTRUCTIVE EVALUATION EQUIPMENT**

Prepared By: Enoch C. Temple, Ph.D.
Academic Rank: Associate Professor
Institution and Department: Alabama A&M University
Mathematics Department

NASA/MSFC:

Laboratory: Materials and Processes
Division: Engineering Physics
Branch: Nondestructive Evaluation

MSFC Colleague: Sam Russell, Ph.D.

1. INTRODUCTION

The space industry has developed many composite materials that have been designed to have high durability in proportion to their weights. Many of these materials have a likelihood for flaws that is higher than in traditional metals. There are also material coverings (such as paint) that develop flaws that may adversely affect the performance of the system in which they are used. Therefore, there is a need to monitor the soundness of composite structures. To meet this monitoring need, many nondestructive evaluation (NDE) systems have been developed. An NDE system is designed to detect material flaws and make flaw measurements without destroying the inspected item. Also, the detection operation is expected to be performed in a rapid manner in a field or production environment.

Within the last few years, several video-based optical NDE methodologies have been introduced. Some of the most recent of these methodologies are shearography, holography, thermography, and video image correlation. A detailed description of these may be found in Chu et al. (1985), Hung (1982), and Russell and Sutton (1989).

The NDE Branch of the Materials and Processes Laboratory at Marshall Space Flight Center has contracted to purchase video optical NDE equipment. Therefore, that Branch is now interested in qualifying the performance capability of this equipment. Qualification standards are found in MIL-STD (1989, draft No. 2) which gives the probability of detection (POD) curve as the primary qualification measurement. This curve summarizes the POD of a particular equipment type for a wide range of flaw sizes.

Section 2 will discuss what techniques are now available to estimate the POD curve from sample data. Section 3 will develop needed extensions for shortcomings in POD analysis. Section 4 shows how these extensions may be used to solve problems in the NDE Branch.

2. METHODS FOR COMPUTING POD

Figure 1 shows an example of a POD curve along with a lower 95-percent confidence boundary. The horizontal axis represents flaw size a and the vertical axis expresses probability as a percentage. As expected, the POD increases with flaw size. The darker curve is labeled POD and is sometimes called the 50-percent confidence boundary or the estimated mean POD. The lower lighter curve is called (in this figure), the lower 95-percent confidence boundary.

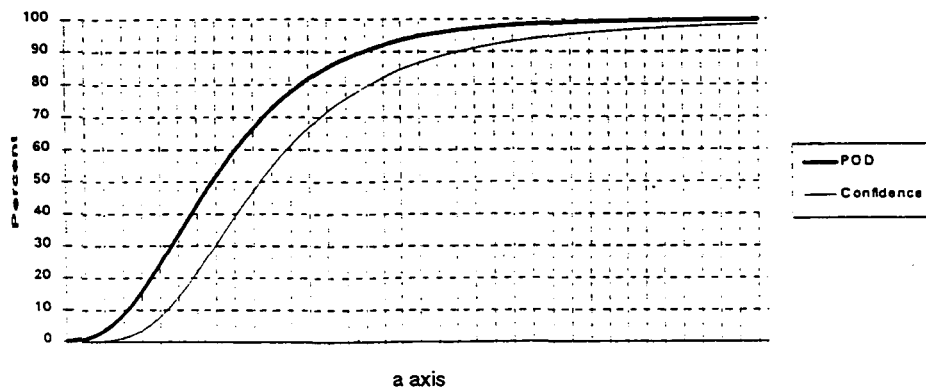


Figure 1

When qualifying an NDE equipment system, two major tasks must be performed. They are: (a) use sample data (perhaps from a demonstration test) to estimate the POD curve, and (b) determine a confidence boundary on the estimated POD curve. MIL-STD specifies a 95-percent confidence boundary.

Researchers have always classified POD(a) as a random variable that depends on a . This classification means that if the probability distribution of POD(a) is known, then mean POD and confidence boundaries are easily computed. Direct approaches used to identify the probability distribution of POD(a) have met with varying degrees of success. At least three different direct approaches are discussed by Berens and Hovey (1984). They also described alternative approaches that avoid the difficulties normally encountered with direct POD(a) distribution identification procedures. One is the pass/fail method and the other is labeled as the a -hat method.

Pass/Fail Method

The first method used to estimate the POD curve is described in Packman et al. (1976) and is based on the binomial distribution. To describe this method, let us assume that there are N_i identically fabricated flaws for each fixed flaw size a_i . An NDE system examines the N_i flaws and detects n_i of them. Binomial theory tells us that $P_i = \frac{n_i}{N_i}$ is an estimate of POD for flaw size a_i . Packman uses a slightly different definition for P_i and uses a collection of P_i 's, $i = 1, 2, \dots, k$, to estimate a POD curve and its confidence boundary. A NASA supported study (Yee et al. (1976)) improves Packman's method by using a smoothing procedure. The improved method appears in the USAF POD software system as subroutine FF. The NDE Branch at MSFC uses this software system (see Berens et al. (1988)).

A-hat Method

An alternative to the direct characterization of the distribution of POD(a) is to find a probability distribution for the output signal of the NDE equipment. In fact, if we let \hat{a} denote equipment response to the examination of a flaw of size a , experimentation by Berens et al. (1984) has shown that \hat{a} and a are related by

$$\ln \hat{a} = \alpha_0 + \alpha_1 \ln a + \varepsilon , \quad (2.1)$$

where ε denotes a random error term.

Berens also showed that $\ln \hat{a}$ has an approximate normal probability distribution. Hence, to summarize the probability behavior of equation (2.1), we say that $\varepsilon \sim N(0, \sigma^2)$, $\ln \hat{a} \sim N(\mu(a), \sigma^2)$ where $\mu(a) = \alpha_0 + \alpha_1 \ln a$ and $N(\cdot)$ denotes the normal distribution. The value of POD(a) is computed by

$$\text{POD}(a) = P(\ln \hat{a} > a_{th}) , \quad (2.2)$$

where a_{th} is called a threshold value and

$$a_{th} = \mu(a) + Z_p \sigma . \quad (2.3)$$

Here, Z_p is the Pth percentile of the standard normal distribution.

From sample to sample, sample estimates $\hat{\mu}(a)$ and $\hat{\sigma}$ of parameters in equation (2.3) change in a random manner. The random behavior of $\hat{\mu}(a)$ and $\hat{\sigma}$ makes POD(a) a random variable. (It appears that a_{th} changes from sample to sample. Actually, the probability distribution changes relative to a_{th} where a_{th} is fixed.) Hence, POD(a) as defined in equation (2.2) has a probability distribution which, if known, may be used to determine a confidence boundary for POD(a). However, Cheng and Iles (1983) showed that if $\mu(a)$ and σ are estimated and their confidence region determined, a corresponding confidence boundary for POD(a) may be determined without actually knowing the probability distribution of POD(a). Their approach used Lagrange multipliers to find maximum and minimum values of a_{th} where α_0 , α_1 , and σ are restricted to some confidence region. The maximum and minimum values of a_{th} are used to find corresponding confidence boundaries for POD(a).

3. SHORTCOMING OF POD

The probability of false calls (POF) is the probability that an NDE system will indicate the presence of a flaw when a flaw does not exist. The POD(a) curve does not assess this situation. In fact, MIL-STD (1989) left POF evaluation as an open question. The next section uses the relationship in equation (2.1) to recommend a computation procedure for POD and POF.

4. GENERAL SOLUTION FOR POD, POF

Let $y = \ln \hat{a}$ where \hat{a} is the output of NDE equipment when a flaw exists. Let $X_1 = \ln a$ where a is actual flaw size. Assume

$$y = f(X_1, \alpha_1) + \varepsilon_1 , \quad (4.1)$$

where y is normal, X_1 is a vector that contains x_1 as a first component, and $\varepsilon_1 \sim N(0, \sigma)$. In a similar manner, let w denote the logarithm of the output of NDE equipment when flaw does not exist. Assume $w = g(X_1, \alpha_2) + \varepsilon_2$ where w has normal distribution and $\varepsilon_2 \sim N(0, \sigma^2)$. In functions f and g , parameters α_1 , α_2 , and σ are to be estimated from sample data. POD and POF are based on equation (2.2). That is

$$\text{POD}(a) = P(y > a_{th}) , \quad (4.2)$$

and

$$\text{POF}(a) = P(w > a_{th}) . \quad (4.3)$$

After parameters are estimated, confidence bounds for POD(a) and POF(a) may be determined by procedures outlined in section 2.

Problem

Qualification standards require that the camera used in video optical equipment be qualified at a fixed distance between the camera lens and the object being examined. However, the NDE Branch of the Materials and Processes Laboratory is interested in the POD performance of this equipment at the tested distance as well as at untested distances. The solution to this problem requires the use of equation (4.2) which has the ability to predict POD performance of NDE equipment.

5. RECOMMENDATION

A solution to the problem posed above may be obtained by using equations (4.1) and (4.2). In this discussion, original variables of equation (2.1) will be used instead of the general vector variables of equation (4.1). That is, using equation (2.1) along with d which represents the distance of the camera lens from the examined object, \hat{a} may be related to a and d by

$$\ln \hat{a} = \alpha_0 + \alpha_1 \ln a + \alpha_2 d + \varepsilon_1 = f_1(a, d) + \varepsilon_1 \quad , \quad (5.1)$$

or

$$\ln \hat{a} = \alpha_0 + C_1 d \ln a + \varepsilon_2 = f_2(a, d) + \varepsilon_2 \quad . \quad (5.2)$$

Data inspection will provide a more realistic relationship. Furthermore, analysis of experimental data will determine if d in equations (5.1) or (5.2) is a significant predictor of $\ln \hat{a}$. If d is judged to be a significant variable, then POD(a) and its confidence bounds may be determined for any fixed distance d . Confidence boundaries are determined as discussed in section 2. However, if the functions f_1 or f_2 are nonlinear in their parameters, the confidence boundary computation procedure will depend on the nonlinear function. Actual data for this problem will be analyzed at a later date.

REFERENCES

1. Berens, A. P., and Hovey, P. W. (1984), "Flaw Detection Reliability Criteria," vol. 1, Method and Results, AFWAL-TR-84-4022, Air Force Aeronautical Labs.
2. Berens, A. P., Hovey, P. W., Donahue, R. M., and Craport, W. N. (1988), "User's Manual for Probability of Detection Software System," UDR-TR-88-12, University of Dayton Research Institute.
3. Cheng, R. C. H., and Iles, T. C. (1983), "Confidence Bands for Cumulative Distribution Functions of Continuous Random Variables," *Technometrics*, pp. 77-86.
4. Chu, T. C., Ranson, W. F., Sutton, M. A., and Peters, W. H. (1985), "Applications of Digital Image Correlation Techniques to Experimental Mechanics," *Experimental Mechanics*, pp. 232-244.

5. Hovey, P. W., and Berens, A. P. (1988), "Statistical Evaluation of NDE Reliability in the Aerospace Industry," *1988 Review of Progress in Quantitative NDE*, Williamsburg, VA.
6. Hung, Y. Y. (1982), "A New Optical Method for Strain Measurement and Nondestructive Testing," *Optical Engineering*, pp. 391-395.
7. MIL-STD (1989, Draft No. 2).
8. Packman, P. F. et al. (1976), "Reliability of Flaw Detection by Nondestructive Inspection," *ASM Metal Handbook*, vol. 11, 8th edition, pp. 214-224.
9. Russell, S. S., and Sutton, M. A. (1989), "Strain Field Analysis Acquired Through Correlation of X-Ray Radiographs of Fiber Reinforced Composite Laminates," *Experimental Mechanics*.
10. Yee, B. G. et al. (1976), "Assessment of NDE Reliability Data," NASA CR-134991.

112596

352860
N95-19011

30924
p. 6

1994

NASA/ASEE SUMMER FACULTY FELLOWSHIP PROGRAM

**MARSHALL SPACE FLIGHT CENTER
THE UNIVERSITY OF ALABAMA**

**THE EFFECT OF FABRICATION ON CORROSION
IN ALUMINUM 2195
ENVIRONMENTAL AND MICROSTRUCTURAL CONSIDERATIONS**

Prepared by: Daniel W. Walsh, Ph.D.
Academic Rank: Professor
Institution and Department: California Polytechnic State University
Department of Materials Engineering
NASA/MSFC:
Laboratory: Materials and Processes Laboratory
Division: Metallic Materials
Branch: Metallurgy Research
MSFC Colleague: Merlin D. Danford, Ph.D.

INTRODUCTION

Aluminum alloys containing lithium are particularly attractive to the aerospace structural designer. Lithium's density is only 0.53 g/cc, thus an addition of one weight percent lithium not only increases yield strength, but decreases the density by almost three percent while increasing the modulus by over six percent. The fact that lithium improves these physical properties simultaneously has led to intense study and development of the alloy system. Heretofore, problems in large scale alloy production have retarded commercial development. During the last fifteen years, advances in production technology have rekindled interest in Al - Li alloys, and aluminum suppliers have developed many candidate aerospace materials. However, if these alloys are to be employed successfully, a more complete understanding of their nonequilibrium metallurgy is required. Peel and Starke have each pointed out that an understanding of the weldability of these alloys is a critical step in their implementation. This study addresses the critical lack of information on the environmental compatibility of welded Al 2195 components. Corrosion data for these systems is incomplete, particularly for welded materials exposed to sea water or sea water condensate.

OBJECTIVES

One objective of this investigation was to measure the corrosion rates of welded and as-received Al 2195 samples in 3.5% NaCl and in mild corrosive water (148 mg/l sodium sulfate, 165 mg/l sodium chloride, 138mg/l Sodium carbonate) and to correlate the corrosion rates observed to material microstructure. A parallel set of Al 2219 samples was used to develop a corrosion benchmark. A second objective of this study was to determine the efficiency of organic and inorganic primers for aerospace aluminum alloys.

PROCEDURE

Electrochemical methods were used to determine the corrosion rates in various samples of Alloy 2219 and Alloy 2195. These electrochemical measurements were correlated to surface morphology and base/weld metal microstructures as observed by optical microscopy, scanning electron microscopy, electron microprobe analysis and environmental scanning electron microscopy. Al-2219 and Al 2195 samples, welded and unwelded, were exposed to sterile 3.5% NaCl solutions and solutions of mild corrosive water. These samples were monitored using the polarization resistance technique. In addition, Al 2219 samples coated with organic and inorganic primers were exposed to 3.5% NaCl solutions, and studied by AC impedance spectroscopy and polarization resistance techniques. Primer coated samples were also studied as galvanic couples with bare, grit-blasted Al 2219 surfaces.

Measurements of corrosion potential and corrosion rates were made over a period of twenty-five days. Sample discs 1.5 cm in diameter and 0.16 cm thick were used in testing the Al 2195 material as well as the Al 2219 baseline material. These samples were degreased and wiped with alcohol; samples were placed in a holder for exposure to corrosive media. A saturated calomel reference electrode was used in all electrochemical measurements. Primer coated samples were 1/8" X 2" X 5" plates. These samples were exposed in flat cells, both polarization resistance and AC impedance information was collected from these samples.

AC impedance and DC polarization resistance measurements were made on alternate days for the entire test period. AC impedance techniques apply a small amplitude signal of varied frequency to the sample. Electrochemical processes occurring at the surface are modeled as electrical circuits, fourier analysis of the data generated allows the determination of fundamental parameters of the system. The AC impedance data were taken in three sections. The first two sections, beginning at 0.001 Hz and 0.1 Hz, respectively were obtained using the fast fourier transform technique. The last section, ranging from 6.25 to 40,000 Hz was collected using the lock-in amplifier technique. The sequencing was performed automatically using program software, and all data were merged to a single set for each three hour run. After collection the data were processed and analyzed using a personal computer using the model developed by Danford.

Values of the corrosion potential, E_{corr} and the corrosion current, I_{corr} were obtained using the polarization resistance method - the small currents involved disturbed the samples only slightly, and made repeated examination possible. The polarization technique is based on the observation that near E_{corr} the slope of the current - potential graph is nearly constant. The slope is termed the polarization resistance, and is an indicator of the chemical activity in the cell. Stearn and Geary provide an excellent theoretical basis for this technique. One problem with the polarization resistance technique is that it does not indicate whether or not the corrosion is localized. However, in this study, subsequent examination of the sample allowed this to be determined. Polarization resistance data were collected at 0.5 mV intervals at a scan rate of 0.1 mV per second. The measurement range for all determinations was -20 to +20 mV with respect to E_{corr} , with all data corrected for IR drop. Data for all polarization resistance scans were analyzed using a commercial program, with a preliminary curve fitting technique as modified by Danford.

RESULTS AND DISCUSSION

Aluminum is a particularly reactive metal - it persists at room temperature because it forms a tenacious oxide film (passivates). An examination of the Pourbaix diagram for aluminum in water indicates that the film is stable in the pH range 4.5 to 8.5. This stability is limited at actual metal surfaces where the film is attacked by anions in solution, local variations in pH and local changes in oxygen concentration. The presence of second phases, as are found in both Al 2219 and Al 2195 often detract from the stability of passivating films.

Alloy 2219 is basically a binary alloy of aluminum and copper - an age hardening material. Its predecessors, 2014 and 2024 are Al-Cu materials with substantial Mg and Zn added to enhance aging kinetics at low temperatures. Alloy 2219, heat treated in an equivalent fashion is not as strong as 2014 or 2024 at low temperatures, but has superior high temperature strength and weldability. Improved weldability is won by increasing the copper content in the alloy past the limit of solid solubility. Enhanced weldability is promoted by an increased volume fraction of liquid present during critical stages of solidification; cracks form but are backfilled by the plentiful eutectic fluid present. Al 2195 is stronger, lighter and stiffer than Al2219, however it is more difficult to weld, and the character of the weld and HAZ region lead to problems with localized corrosion, particularly with autogenous welds.

Welding is an inherently nonequilibrium process, the severe thermal cycle associated with welding redistributes solutes, engenders transient stress in the weld vicinity, and changes base metal microstructure. The corrosion susceptibility of the Al 2195 alloy can be correlated to the solute redistribution associated with the welding process, and parallels the hot cracking susceptibility of the material in this study. Weld solidification cracking in the aluminum alloys depends upon alloy composition, the solidification temperature range, and the amount and character of the terminal eutectic constituent. At low solute contents, the solidification temperature range is small, and little eutectic forms in the structure. As the solute content increases, the solidification range expands, and the amount of eutectic constituent increases to a level that provides for a thin liquid coating in interdendritic and solidification grain boundaries. Under equilibrium conditions, a maximum cracking propensity is reached at the limit of solid solubility. At compositions in excess of the limit of solid solubility, the solidification range again decreases, and more eutectic is present during the latter stages of solidification. Stresses in the solidifying matrix diminish and if flaws occur, they can backfill with excess eutectic. During welding, the amount of eutectic fluid produced at lower solute contents increases, and the maximum crack susceptibility occurs at solute contents below the limit of maximum solid solubility. Under conditions of equilibrium, the amount of eutectic fluid can be estimated by using the lever law, $C_S F_S + C_L F_L = C_0$. The amounts of eutectic under nonequilibrium conditions can be estimated using the Scheil equation, $C_L = C_0 F_L^{(k-1)}$. Using these equations we can show that Al 2219, essentially a binary alloy of Al and Cu, would have 2.5% eutectic under equilibrium conditions, but has over 13% terminal eutectic fluid under nonequilibrium conditions. Al 2195, is a true ternary alloy and it is more difficult to estimate the amounts of terminal fluid. However, upper limits for the amount of fluid can be estimated as < 1% in the equilibrium case and , < 6% in the nonequilibrium case.

Al 2219 is essentially saturated with copper rich second phase materials, particularly in the weld region. On a microscopic scale, myriad anode cathode pairs exist and corrosion proceeds at many locations simultaneously. Al 2195, however exhibits regions of pronounced depletion adjacent to solute rich regions. Moreover, the depleted regions are often subject to microfissuring, providing preferred sites for localized corrosion. The transient stresses associated with the welding thermal cycle produce a macroscopic segregation of microconstituents through a "squeezing" mechanism during the welding cycle as described by Walsh and Nunes. This region can be identified on the surface of welds in both Al2219 and Al 2195, which exhibit narrow bands of exuded material in the fusion line region. The fine equiaxed region in Al 2195, an unmixed region, is enriched in terminal transient. The extensive adjacent PMZ is often starved of eutectic liquid, and is subject to hot cracking during the welding process. This location was found to be particularly sensitive to localized attack.

Table 1 provides a summary of the corrosion data gathered during this investigation. Figures 1 and 2 show typical histories for particular samples.

TABLE 1 CORROSION SUMMARY

MATERIAL	CONDITION	MEDIUM	AVERAGE	MAXIMUM	SLOPE
2195	BM	MC BIO	0.965	3.709	0.14
2219	HW	MC	0.535	1.36	0.012
2195	HW	MC	0.476	1.59	0.0195
2195	AW	MC	0.461	1.123	0.0221
2219	AW	MC	0.255	0.439	-0.004
2195	BM	SLT	0.250	0.8583	-0.0158
2195	BM	MC	0.245	0.6943	0.0266
2219	BM	SLT	0.221	0.6335	-0.0068
2219	BM	MC	0.204	0.4059	0.0004
2195A	BM	MC	0.200	0.3651	0.0266

CONCLUSIONS

Results indicate that for base metal samples, corrosion in mild corrosive water was more severe than corrosion in salt water, examination of test samples indicated that a uniform layer of passivating coating formed over the sample during the early stages of exposure and no stable pits developed in either alloy. High initial rates in both Al 2219 and Al 2195 indicates that corrosion was occurring at many locations over the surface, no preferred locations or stabilized pits developed, and a passivating coating formed over the surface. In mild corrosive water however, initial corrosion rates were lower and preferred sites developed. Welding was found to increase the corrosion rate in Al 2195 and Al 2219, creating strong local galvanic couples on the microscopic scale. More importantly, welding causes severe localized pitting in Al 2195 samples. Figure 3 shows severe localized pitting along the PMZ in a Al 2195 weld. Note the fine equiaxed region with the extensive amount of cathodic second phase adjacent to the severely corroded PMZ. Note the attack proceeding into the base material and the textured pancake structure. This localized attack was typical of Al 2195 welds and was not observed in Al 2219. Figure 4 shows the HAZ region in Al 2195. Note the hot cracking and porosity. Autogenously welded Al 2195 samples were more susceptible to attack than heterogeneously welded Al 2195 samples because there were microtears in the partially melted zone of autogenous samples. Autogenously welded Al 2219 samples were less susceptible to corrosion than autogenously welded Al 2195 samples because alloy 2219 is designed to "backfill" any flaws that form with copious amounts of eutectic liquid. Heterogeneously welded samples in both materials had high corrosion rates, but only the Al 2195 material was subject to localization of attack. The partially melted zones of Al 2195 samples were subject to severe, focused attack. In all cases, interdendritic constituents in welded areas and intergranular constituents in base material were cathodic to the Al rich matrix materials. Al 2219 samples were subject to crevice corrosion. Biologically active media (an inoculation of 30 cc of KFC water in a 1000cc mild corrosive water test unit) greatly increased the corrosion rate in the single 2195 sample studied. Galvanic studies show both organic and inorganic zinc primers protect grit blasted Al 2219. The inorganic zinc

primer studied was very sensitive to coating procedure. AC Impedance studies show that the pore resistance (r_p) and charge transfer resistance (r_t) of the organic zinc coating increase rapidly with time.

REFERENCES

- 1) C. J. Peel, The Development of Aluminum-Lithium Alloys: An Overview, Conference Proceedings, Fifth International Aluminum-Lithium Conference.
- 2) Starke, E.A. Jr. and Quist, William E., The Microstructure and Properties of Aluminum-Lithium Alloys, Conference Proceedings, Fifth International Aluminum-Lithium Conference.
- 3) Y. A. Chang and S.W. Chen, Microsegregation in Solidification for Ternary Alloys, Met. Trans. A, Volume 23A, march 1992.
- 4) Y.A. Chang et. al., Calculation of Phase Diagrams and Solidification Paths of Al Rich Al-Li-Cu Alloys, Met. Trans. A, Volume 2A, December 1991.
- 5) K. Moore et. al., Effect of Copper Content on the Corrosion and Stress Corrosion Behavior of Al-Cu-Li Weldalite Alloys, Aluminum-Lithium Alloys, Vol III
- 6) R.G. Buchheit, F.D. Wall and J.P. Moran, An Anodic Dissolution Based Mechanism for the rapid cracking Pre-Exposure Phenomenon Demonstrated by Al-Li-Cu Alloys, NACE, Corrosion 94, Baltimore, MS. Paper #623.
- 7) M. Stern, Theoretical Basis of the Polarization Resistance Technique, Corrosion, Vol. 14, 1958, p 410t.
- 8) D. S. Gnanamuthu, R.J. Moore, LASER Welding of 8090 Al-Li Alloy, Proceedings of International Power Beam Conference, San Diego, CA May 2-4, 1988.
- 9) T.A. Marsico, R. Kossowski, Physical properties of Laser Welded Al alloy 2090. Conference Proceedings, Fifth International Aluminum-Lithium Conference, Williamsburg Va., March, 1989.
- 10) P. Bourgwasser, et. al., Intergranular Fracture of Al-Li-Cu-Mg Alloy Resulting from Non-equilibrium Eutectic Melting During Solution Treatment. Materials Science and Technology, Vo1 5, 1989.

Figure 1

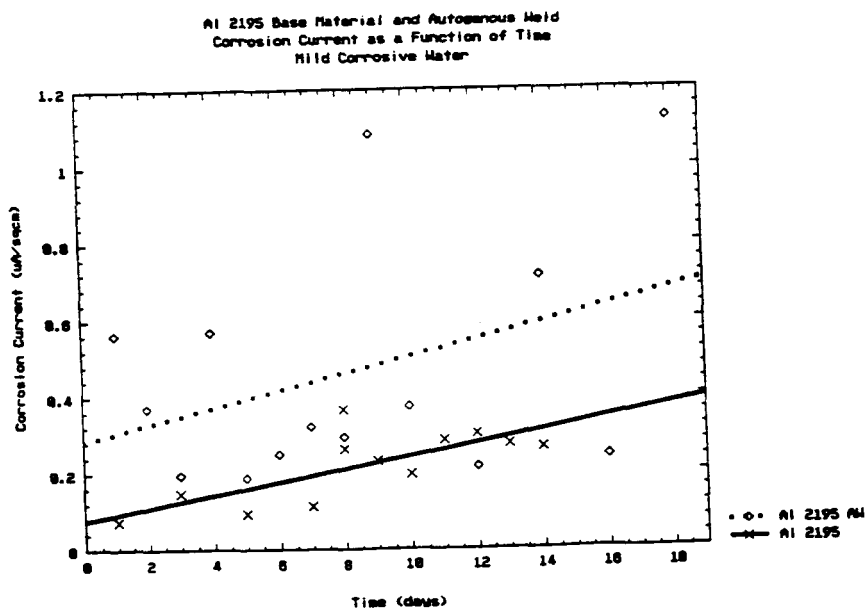


Figure 2
 Al 2219 and Al 2195
 Corrosion Current as a Function of Time
 3.5% NaCl

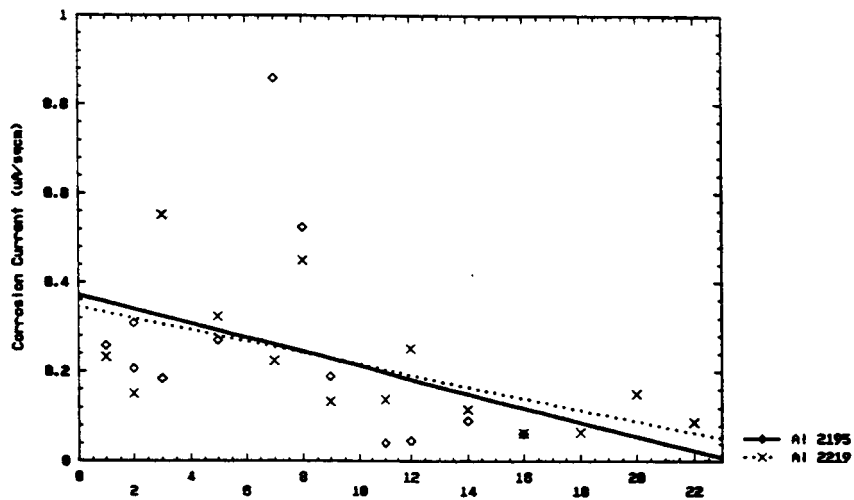


Figure 3. Localized PMZ Attack

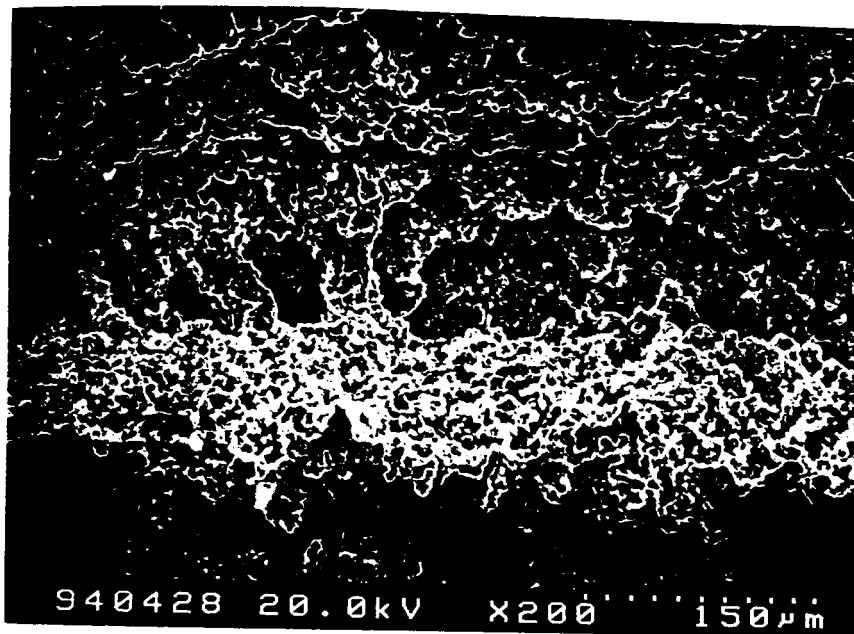
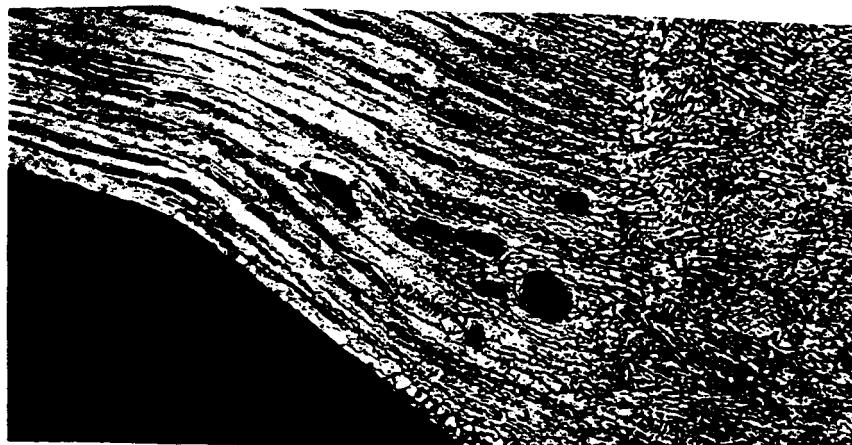


Figure 4. HAZ of Al 2195 Weldment



112597

N95-19012-5

352861

30930

p. 6

1994

NASA/ASEE SUMMER FACULTY FELLOWSHIP PROGRAM

**MARSHALL SPACE FLIGHT CENTER
THE UNIVERSITY OF ALABAMA**

**NUMERICAL FORMULATION OF COMPOSITION SEGREGATION AT CURVED
SOLID-LIQUID INTERFACE DURING STEADY STATE SOLIDIFICATION
PROCESS**

Prepared By: Jai-Ching Wang, Ph.D.

Academic Rank: Associate Professor

**Institution and
Department:** Alabama A&M University
Department of Physics

NASA/MSFC

Office: Space Science Laboratory
Division: Microgravity Science & Application Division/ES
71
Branch: Electronic & Photonic Materials Branch/ES 75

MSFC Colleague(s): Sandor L. Lehoczky, Ph D.
Frank Szofran, Ph.D
Dale Watring

XLV

INTRODUCTION

The lateral solute segregation that results from a curved solid-liquid interface shape during steady state unidirectional solidification of a binary alloy system has been studied both analytically and numerically by Coriell, Boisvert, Rehm, Sekerka (1). The system under their study is a two dimensional rectangular system. However, most real growth systems are cylindrical systems. Thus, in a previous study(2) we have followed Coriell etc. formalism and obtained analytical results for lateral solute segregation for an azimuthal symmetric cylindrical binary melt system during steady state solidification process. The solid-liquid interface shape is expressed as a series combination of Bessel functions. In this study a computer program has been developed to simulate this lateral solute segregation.

FORMALISM

In this section we present the basic equation and boundary condition used in this calculation. The diffusion equation for an azimuthal system is

$$D \frac{\partial^2 c'(r',z')}{\partial r'^2} + \frac{1}{r'} \frac{\partial c'(r',z')}{\partial r'} + \frac{\partial^2 c'(r',z')}{\partial z'^2} + V \frac{\partial c'(r',z')}{\partial z'} = 0 \quad \text{---(1)}$$

Where D is diffusivity of solute in the liquid, V is the velocity of solidification, c', r', z', w' are dimensional solute concentration, radial and axial coordinates, and interface thickness. The boundary conditions are

$$V c'_{,z} (k-1) = D \left(\frac{\partial c'(r',z')}{\partial r'} - \frac{\partial c'(r',z')}{\partial z'} \frac{\partial w'(r')}{\partial r'} \right) \quad \text{---(2)} \quad c'(r',z') = c_0 \quad \text{---(3)}$$

$$\frac{\partial c'(r',z')}{\partial r'} = 0 \quad \text{at } r' = R \quad \text{---(4)}$$

Where k is distribution coefficient. The variables can be nondimensionalized by letting $c=c'/c_0$, $r=r'/R$, $z=z'/R$, $w=w'/R$ and $\beta=VR/D$ where R is radius of the ampule. The diffusion equation and the boundary conditions become

$$\frac{\partial^2 c(r,z)}{\partial r^2} + \frac{1}{r} \frac{\partial c(r,z)}{\partial r} + \frac{\partial^2 c(r,z)}{\partial z^2} + \beta \frac{\partial c(r,z)}{\partial z} = 0 \quad \text{-----(5)}$$

$$\beta C_I(k-1) = \frac{\partial C(r,z)}{\partial z_I} - \frac{\partial C(r,z)}{\partial r_I} \frac{\partial w(r)}{\partial r} \quad \text{-----(6)}$$

$$c(r, z=\infty) = 1 \quad \text{-----(7)} \quad \frac{\partial C(r,z)}{\partial r} = 0 \quad \text{at } r=1 \quad \text{-----(8)}$$

In the limits of very small β , by using variable separation method, equation (5) can be solved to give

$$c(r,z) = A J_0(ar) e^{-\frac{b}{2} [1 + [1 + (2a/b)^2]^{1/2}] z} + A' \quad \text{-----(9)}$$

From boundary condition $c(r, z=\infty) = 1$, We have $A' = 1$

$$\text{From boundary condition } \frac{\partial C(r,z)}{\partial r} = 0 \quad \text{at } r=1, \text{ We have}$$

$$\frac{\partial J_0(ar)}{\partial r} = -a J_1(ar) = 0 \quad \text{-----(10)}$$

let u_n be the zeros of $J_1(\alpha)$, where $n=1$ to infinite.

By using $p(n)$ to denote $[1 + (\frac{2u_n}{\beta})^2]^{1/2}$. The general solution is

$$C(r,z) = 1 + \frac{1-k}{k} e^{-\beta(z-w_0)} + \sum_{n=1}^{\infty} A_n J_0(u_n r) e^{-\frac{\beta}{2} [1+p(n)]^{1/2} z} \quad \text{-----(11)}$$

There is another boundary condition which needs to be satisfied, i.e.

$$\beta C_I(k-1) = \frac{\partial C(r,z)}{\partial z_I} - \frac{\partial C(r,z)}{\partial r_I} \frac{\partial w(r)}{\partial r'} \quad \text{-----(12)}$$

The solid-liquid interface shape is assumed to be parabolic δr^2 and is expressed as a series combination of Bessel function, i.e.

$$w(r) = w_0 + \sum_{n=1}^{\infty} \delta(n) J_0(u_n r) \text{-----(13)}$$

Assume both $w(r)$ and $\frac{dw(r)}{dr}$ to be small, We obtain the solute concentration at the interface to be

$$c_I(r, z) = \frac{1-\beta}{k} \frac{(1-k)}{k} \sum_{n=1}^{\infty} \frac{\delta(n) J_0(u_n r)}{1+2k/[p(n)-1]} \text{-----(14)}$$

$$c_{S_I}(r, z) = k c_I$$

$$= 1-\beta(1-k) \sum_{n=1}^{\infty} \frac{\delta(n) J_0(u_n r)}{1+2k/[p(n)-1]} \text{-----(15)}$$

This shows that the solute concentration in the solid at the interface is a function of $w(r)$, β and k .

NUMERICAL CALCULATIONS AND RESULTS

The results obtained from these calculations show that

- (1) The solute concentration at the interface at $r = 0.7$ which were calculated by using the general expression eq (11). with n from 1 to i is denoted by C^3_j . The same value calculated by using the approximate expression eq(15). with n from 1 to i is denoted by C^4_j . The results in figure 1 show that if we have include more than 40 terms in the calculations, the two expressions give almost exact results.
- (2) .The solute concentration in the solid at the interface obtained analytically show that the compositional segregation in the solid is proportional to the deviation of the interface from planarity. The proportional factor being the product of β and $(1-k)$. The solute concentration at the interface $C_{si}(x)$ calculated by using the general expression and by using the approximate expression for a small β limit agree very well. The results for $\beta = 0.173$, $k=4$ and $\delta = 0.05, 0.1, 0.2, 0.375$ and 0.4 are calculated and the result for $\delta = 0.375$ is shown in figure 2. The results of C^1_j were calculated by using the general expression eq (11) with n from 1 to 89, while the results of C^2_j were calculated by using the approximate

expression eq(15) with n from 1 to 89.

3. The results in figure 3 show that the solute concentration at the interface $C_{si}(x)$ is linearly proportional to the amplitude of the interface shape deviation at both $x=0$, the center of the interface and $x=1$, the edge of the interface for $\beta = 0.1256637$, 1.256639 and 12.56637 . These results are calculated by using the approximate expression eq(15) which is valid for small β . The results for $\beta = 12.56637$ need to be reconsidered.
4. The results in figure 4 show that the solute concentration at the interface $C_{si}(x)$ for different interface amplitudes all have the same shape as a function of its radius.
5. In table 1, for various values of k , β , and δ , we give the solute concentration at the interface $C_{si}(x)$ in the solid at $x=0$ and $x=1$. These results have similar β and k dependence as that in table 1 in ref 1.

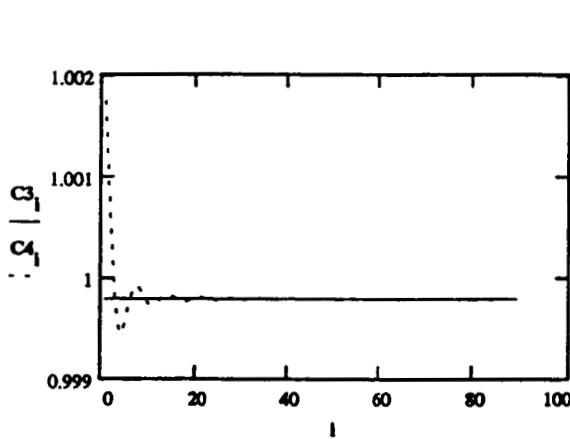


Figure 1. Caption see text.

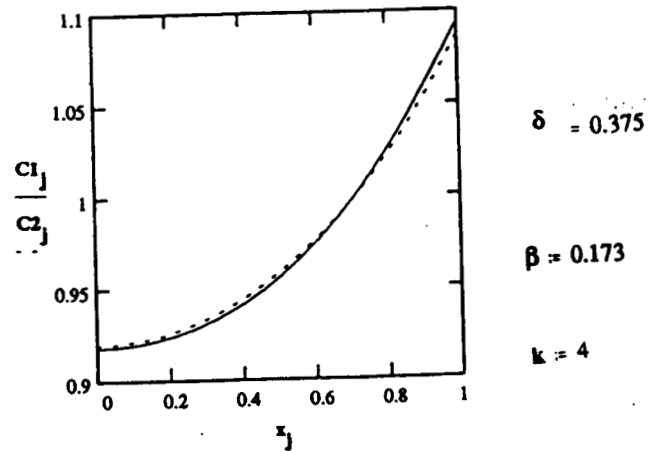


Figure 2. Caption see text.

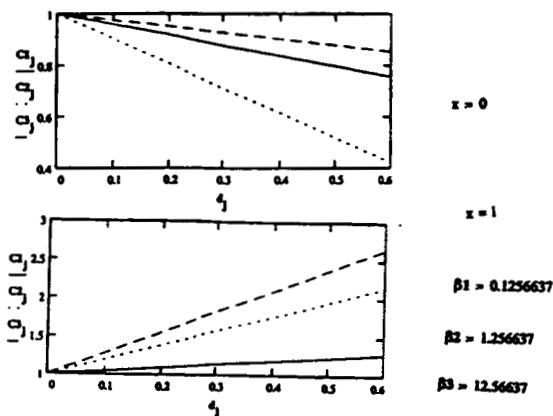


Figure 3. Caption see text.

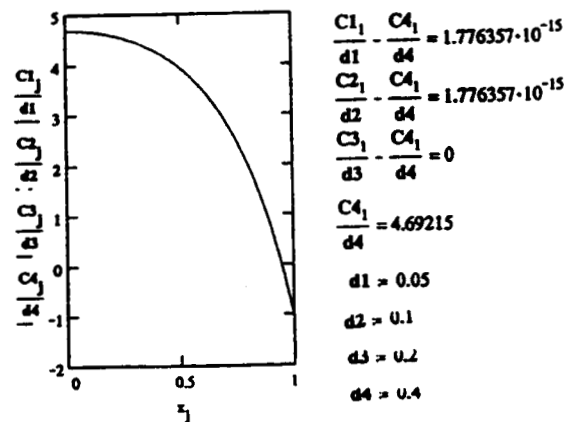


Figure 4 Caption see text.

k	$\frac{\beta}{4 \cdot 3.14}$	δ	$C_{sl(0)}$	$C_{sl(1)}$
0.1	0.01	0.05	0.9972	1.003
0.1	0.01	0.1	0.9944	1.006
0.1	0.01	0.2	0.9887	1.011
0.1	0.01	0.3	0.9831	1.017
0.1	0.01	0.4	0.9775	1.022
0.1	0.01	0.5	0.9719	1.028
0.1	0.01	0.6	0.9662	1.034
0.1	0.01	0.7	0.9606	1.039
0.1	0.01	0.8	0.95498	1.045
0.1	0.01	0.9	0.9494	1.05
0.1	0.01	1.0	0.9437	1.056

k	$\frac{\beta}{4 \cdot 3.14}$	δ	$C_{sl(0)}$	$C_{sl(1)}$
2	0.01	0.05	1.0029	0.997
2	0.01	0.1	1.0058	0.994
2	0.01	0.2	1.0117	0.988
2	0.01	0.3	1.0175	0.982
2	0.01	0.4	1.0233	0.976
2	0.01	0.5	1.0292	0.97
2	0.01	0.6	1.0350	0.964
2	0.01	0.7	1.0408	0.958
2	0.01	0.8	1.0467	0.952
2	0.01	0.9	1.0525	0.946
2	0.01	1.0	1.0583	0.94

k	$\frac{\beta}{4 \cdot 3.14}$	δ	C	$C_{sl(1)}$
2	0.1	0.05	1.01	0.979
2	0.1	0.1	1.0326	0.958
2	0.1	0.2	1.0652	0.916
2	0.1	0.3	1.1078	0.873
2	0.1	0.4	1.15045	0.831
2	0.1	0.5	1.163	0.789
2	0.1	0.6	1.1957	0.747
2	0.1	0.7	1.2283	0.705
2	0.1	0.8	1.2609	0.663
2	0.1	0.9	1.2935	0.62
2	0.1	1.0	1.3261	0.578

k	$\frac{\beta}{4 \cdot 3.14}$	δ	$C_{sl(0)}$	$C_{sl(1)}$
0.1	0.1	0.05	0.973	1.027
0.1	0.1	0.1	0.9459	1.055
0.1	0.1	0.2	0.8918	1.109
0.1	0.1	0.3	0.8378	1.164
0.1	0.1	0.4	0.7837	1.218
0.1	0.1	0.5	0.7296	1.273
0.1	0.1	0.6	0.67553	1.328
0.1	0.1	0.7	0.62145	1.382
0.1	0.1	0.8	0.5674	1.437
0.1	0.1	0.9	0.5133	1.491
0.1	0.1	1.0	0.4592	1.546

k	$\frac{\beta}{4 \cdot 3.14}$	δ	$C_{sl(0)}$	$C_{sl(1)}$
10	0.01	0.05	1.0204	0.977
10	0.01	0.1	1.0408	0.954
10	0.01	0.2	1.0815	0.908
10	0.01	0.3	1.1223	0.862
10	0.01	0.4	1.163	0.817
10	0.01	0.5	1.2038	0.771
10	0.01	0.6	1.2445	0.725
10	0.01	0.7	1.2853	0.679
10	0.01	0.8	1.3260	0.633
10	0.01	0.9	1.3668	0.587
10	0.01	1.0	1.4076	0.542

k	$\frac{\beta}{4 \cdot 3.14}$	δ	$C_{sl(0)}$	$C_{sl(1)}$
10	0.1	0.05	1.0481	0.905
10	0.1	0.1	1.09627	0.809
10	0.1	0.2	1.1925	0.619
10	0.1	0.3	1.2888	0.428
10	0.1	0.4	1.385	0.237
10	0.1	0.5	1.4814	0.047
10	0.1	0.6	1.5776	-0.144
1.0	0.1	0.7	1.6739	-0.335
10	0.1	0.8	1.7701	-0.525
10	0.1	0.9	1.8664	-0.716
10	0.1	1.0	1.9627	-0.907

Table 1. Solute segregation for solid-liquid interface shape $w(r) = \delta r^2$ for various values of k , β , and δ

REFERENCES

1. Coriell, S. R., F. Boisvert, R. G. Rehm, and R. F. Sekerka, "Lateral Solute Segregation During Unidirectional Solidification of a Binary Alloy with a Curved Solid-Liquid interface", Journal of Crystal Growth 54, 167, 1981
2. Wang, J. C., "Investigation of Compositional Segregation During Unidirectional Solidification of Solid Solution Semi-Conducting Alloy", NASA CR 162051, ed. by Karr, G. R., Barfield, J., and Kent, M., pXLI 1-20, Aug. 1982.

112598

N95-19013

352862

30936

P-9

1994

NASA/ASEE SUMMER FACULTY FELLOWSHIP PROGRAM

**MARSHALL SPACE FLIGHT CENTER
THE UNIVERSITY OF ALABAMA**

**EFFECTS OF VIBRATION
(G-JITTERS)
ON CONVECTION IN MICRO-GRAVITY**

Prepared By: Francis C. Wang, Ph.D.
Academic Rank: Senior Research Engineer
Institution: University of Alabama in Huntsville
Research Institute

NASA/MSFC:

Laboratory: Space Sciences Laboratory
Division: Microgravity Science & Applications Division
Branch: Crystal Growth & Solidification

MSFC Colleagues: Charles R. Baugher, MSFC Colleague
N. Ramachandran, Ph.D., USRA Colleague

INTRODUCTION

To obtain high quality crystals, it is desirable to maintain a diffusion-limited transport process and a planar solidification surface between the solid and the melt during the crystal growth process. Due to the presence of buoyancy-driven convection, however, this situation is difficult to maintain on Earth. The microgravity environment of an orbiting space laboratory presents an alternative worth pursuing. With reduced gravity, convection is very much suppressed in a space laboratory, making the environment more conducive for growing crystals with better quality.

However, a space laboratory is not immune from any undesirable disturbances. Non-uniform and transient accelerations such as vibrations, g-jitters, and impulsive accelerations exist as a result of crew activities, space vehicle maneuvering, and the operations of on-board equipment. Measurements conducted on-board a U. S. Spacelab mission showed the existence of vibrations in the frequency range of 1 to 100 Hz. (See Ramachandran, Baugher, and Rogers, "Acceleration Environment on the Space Shuttle and Its Impact On Thermo-Solutal Fluid Mechanics," ASME Winter Annual Meeting, 1993). It was reported that a dominant mode of 17 Hz and harmonics of 54 Hz were observed and these were attributed to antenna operations. The vibration is not limited to any single plane but exists in all directions. Some data from the Russian MIR space station indicates the existence of vibration also at this frequency range.

It is known [Refs. 1-10] that vibration can exert substantial influence on the fluid flow and heat transfer characteristics, such as changing the local or total heat transfer rate, affecting the transition from conduction heat transfer to convection, and from laminar flow to turbulent flow. It can also change the boundary layer thickness thus affecting mass transfer. Hence the presence of vibration will have negative impact on achieving the diffusion-limited process in a space laboratory.

This report summarizes the work conducted at NASA MSFC during the tenure of the 1994 Summer Faculty Fellowship Program. It consists of two parts: a brief summary of an extensive literature search and review on vibration convection; and the results of a numerical study of vibration convection in an enclosure under zero gravity.

REVIEW OF LITERATURE ON VIBRATION CONVECTION

An extensive literature search has been conducted on vibration convection studies conducted for the past three decades. Although most works reported in the open literature are included, the emphasis has been on works conducted in the former Soviet Union. It was found that the Russians have conducted quite extensive studies, and an analytical method has been developed for studying high frequency vibration convection. A brief summary of the review is given below. Two areas covered in this summary are the effects of vibration on fluid stability, and vibration effects on convection in fluid-filled enclosures.

Stability of Fluid Layer

Stability of fluid layers subject to vibration modulation has been the subject of analytical and experimental studies for many years. Most analyses were conducted using the linear perturbation method. In the Russian studies, a time-averaged method has been used for flows with high frequency vibrations. This method, first proposed by Zenkovskaya and Simonenko [Ref. 11], utilizes a time-averaged quantity to represent the effects of vibration acceleration. Closed form solutions were obtained under certain conditions. Problems studied include vibration convection in a rectangular cavity [Ref. 12], vibration convection in a cylindrical cavity [13], flow about a uniformly heated cylinder [14] and others. It was found that vibration modulation can alter the stability criteria. Implications to fluid behaviors under zero gravity were also made. Detailed description of this method, its development and application can be found in the treatises of Refs. 15 & 16.

Experimental studies of stability were conducted by Zavarykin et al. [Refs. 17, 18] for fluid layers subject to heating and vibration. In their experiments, the stability of a vertical and a horizontal fluid layer were studied when subject to vibrations. Results indicate that vertical vibration can suppress convection instabilities in fluid layers that are vertically stratified in temperature. The results also indicate that vibration excitations in the horizontal direction can destabilize the fluid. These results support the predictions obtained from analyses.

Vibration Convection In An Enclosure

Early experiments conducted by Forbes, Carley and Bell [Ref. 4] showed that heat transfer rate for a liquid-filled vertical rectangular enclosure is enhanced when sinusoidal vibration is applied. Their experiments indicated the existence of a resonant frequency, near which the enhancement is the strongest. Similarly, Ivanova and Kozlov [19] applied vibrations to a horizontal cylindrical layer under convection and reported the existence of three flow regimes based on vibration intensity. Effects of transient vibrations were studied by Ivanova who conducted an experiment to study cooling of fluids between two concentric cylinders [Ref. 20].

As the frequency of vibration reaches a certain range, phenomena such as resonance and the change of heat transfer modes may occur. These phenomena, usually transient and highly non-linear, cannot be analyzed using the linearized methods. Full equations must be used and numerical solutions are usually required. Studies of vibration convection in an enclosure have provided significant insight into these complex phenomena. Heat transfer rate across the enclosure walls, given in terms of the average Nusselt number, has been used as a direct measure of the intensity of interactions between vibration and convection.

The existence of synchronous, sub-harmonic and relaxation oscillations which resulted from the non-linear interaction of vibration and convection has been studied by Gresho and Sani [6]. Numerical studies of this phenomenon were conducted by Yurkov [Refs. 21, 22], by Biringen & Danabasoglu [23] and others. Most recently, a numerical simulation of vibration convection in a two-dimensional cavity was conducted by Fu and Shieh [24] which covered a wide range of vibration frequencies. Their study also covered several different values of residual gravity

including zero gravity. Their results showed the existence of different flow regimes confirming the findings of the Russians [Ref. 25]. A summary of these results are given below:

- The key parameters of vibration convection are the Prandtl number, the vibration frequency, and the Grashof number (G).
- The effect of vibration is more prominent in frequency variations than in amplitude variations.
- The effect of vibration reaches an asymptote at high frequencies.
- There exists a resonance regime for which heat and mass transfer are greatly enhanced.

Figure 1. shows the variation of the average Nusselt number vs. vibration frequency for a fluid-filled cavity subject to sinusoidal vibrations in the direction normal to the temperature gradient. Figure 1(a) is from [Ref. 25], while figure 1(b) is from [Ref. 24]. A quick analysis of the data from Ref. 24, indicates that the resonance frequency could be in the range of 1 to 100 Hz.

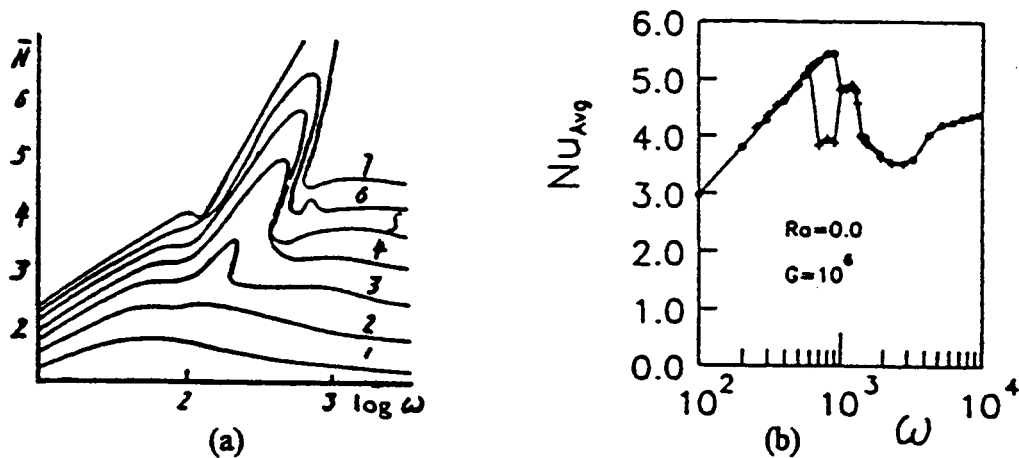


Figure 1. Results of Past Studies

A NUMERICAL STUDY OF VIBRATION CONVECTION

To demonstrate the effects of vibration on convection in a weightlessness environment, a numerical simulation of a crystal growth cell was conducted using a two-dimensional fluid-filled cell. This cell is subjected to a lateral temperature gradient and a vertical sinusoidal vibration. Fluid flow and heat transfer rates were obtained for a wide range of vibration frequencies. Results of the numerical simulation demonstrate the complex processes occurring inside the cell, and supports the existence of resonance regime and the high frequency asymptotes as were reported in Refs. 24 and 25.

Non-Dimensional Equations

The basic equations for analysis are the equations for an incompressible fluid with Boussinesq approximation. Casting in non-dimensional form using a characteristic velocity based on thermal diffusion, α , and the length of the cell, L , we obtain the following equations

$$\frac{\partial U}{\partial X} + \frac{\partial V}{\partial Y} = 0 \quad (1)$$

$$\frac{\partial U}{\partial \tau} + U \frac{\partial U}{\partial X} + V \frac{\partial U}{\partial Y} = -\frac{\partial P}{\partial X} + \text{Pr} \nabla^2 U \quad (2)$$

$$\frac{\partial V}{\partial \tau} + U \frac{\partial V}{\partial X} + V \frac{\partial V}{\partial Y} = -\frac{\partial P}{\partial Y} + \text{Pr} \nabla^2 V \quad (3)$$

$$+ \text{Pr}[Ra + G\omega \sin(\tau\omega)]\theta$$

$$\frac{\partial \theta}{\partial \tau} + U \frac{\partial \theta}{\partial X} + V \frac{\partial \theta}{\partial Y} = \frac{\partial^2 \theta}{\partial X^2} + \frac{\partial^2 \theta}{\partial Y^2} \quad (4)$$

Here θ , P , U , V , and τ are non-dimensional variables. Other parameters are Pr the Prandtl Number, Ra the Rayleigh number, G the Grashof Number, and ω the non-dimensional circular frequency. Here we have assumed that the sinusoidal vibration is imposed in the vertical (Y) direction, same as the residual acceleration. Figure 2 depicts the domain of calculations.

Solution Method

Equations (1-4) are solved numerically using the NASA developed two-dimensional Finite Difference Navier-Stokes solver (FDNS2D). A finite difference mesh of 31 by 31 are used to calculate flow properties in the interior of the cavity. The quasi-static condition was used as the initial condition and transient solutions were obtained for different vibration frequencies using a time marching technique. Iterations at each time step is used to ensure convergence.

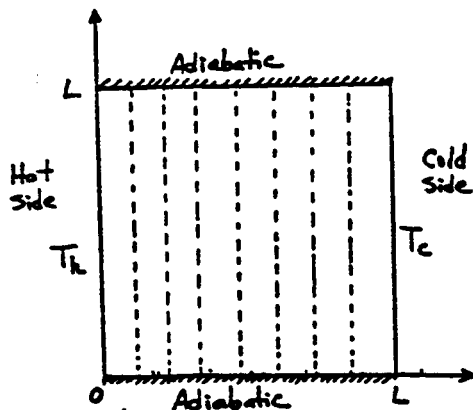


Figure 2. Rectangular Cavity

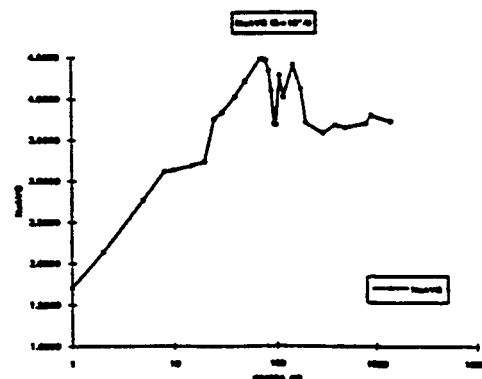


Figure 3. Results of Current Study

RESULTS & DISCUSSIONS

Numerical calculations were conducted for air ($Pr = 0.7$) in a cavity of 1 cm squared in a zero gravity environment ($Ra = 0$). The vibration acceleration is applied in the Y-direction while a temperature difference of 100 k is maintained between the walls at $X=0$, and $X=1$ as shown in Figure 2. Results of numerical calculations are shown in Figures 3 through 5 for the case of $G = 10^{+4}$. From the variation of Nusselt number as shown in Figure 3, it is evident that several different flow regimes exist as vibration frequency changes. This variation follows the same trend as shown in Figure 1, supporting the findings of previous studies. The resonance frequency obtained here is within the range as predicted in Ref. 24.

Figure 4 shows the variation of the average Nusselt number as a function of time for six different vibration frequencies. These curves showed the strong interactions between convection and vibration at different frequencies. At low vibration frequencies, as shown in Fig. 4 (a), the flow is oscillatory at twice the vibration frequency. At intermediate vibration frequencies, shown in Fig. 4 (b), instability has set in and multiple frequencies showed up. As the frequency increases further resonance is reached. As shown in Fig. 4 (c), the flow showed large variations in Nusselt number. At even higher frequencies, as shown in Figs. 4(d) and (e), a transition period occurred with oscillations of multiple frequencies. At extremely high frequencies, as shown in Fig. 4(f), high frequency vibration convection is established. The flow settles rapidly after an initial response to the vibration. The Nusselt number peaked first then levels off to its asymptote.

Details of the flow field can be shown by plotting the stream functions, the isotherms, and the velocity vectors at different stages of its development. Shown in Figure 5 are the plots for a high frequency vibration convection ($\omega = 1400$). Figure 5(a) shows the stream functions (left row), the isotherms (middle row), and the velocity vectors (right row) of the first two cycles. Figure 5(b) shows the same after 10 cycles of vibrations. Notice the thin thermal boundary layers near the isothermal walls which cause the Nusselt number to peak. Figure 5(c) shows the fully developed flow which has reached the asymptote.

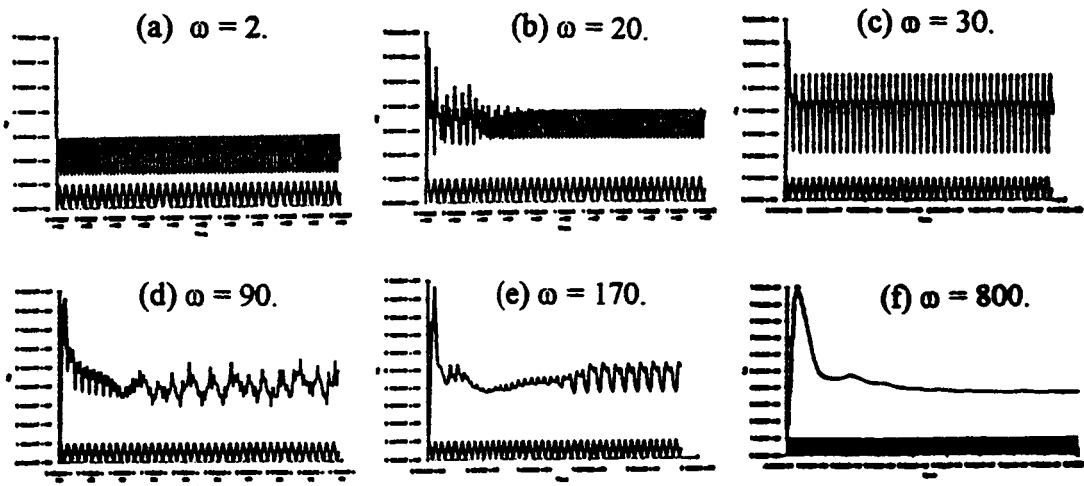


Fig. 4. Time Variation of Nusselt Number at Different Frequencies

Results of this study strongly support the findings of other researchers. To assess the impact of vibration on crystal growth on orbit, quantitative information would be needed. It is recommended that further studies be conducted covering a wider range of Grashof number; that properties of a typical liquid metal be used; and that non-zero residual gravity be added. This will not only provide better understanding of the behavior of liquid melt in space but also provide necessary guidelines for the planning of ground experiments. Theoretical studies of the resonance phenomenon will also add to our understanding of this interesting and complex phenomenon.

REFERENCES

1. Richardson, P.D., "Effects of Sound and Vibration on Heat Transfer," Applied Physics Review, Vol. 20, 201-217, March, 1967.
2. Pak, H.Y., Winter, E.R.F., and Schoenals, R.J., "Convection Heat Transfer in a Contained Fluid Subject to Vibration," In *Augmentation of Convective Heat and Mass Transfer*, edited by A.E. Bergles and A.L. Webb, ASME, New York, 158, 1970.
3. Gebhart, B., "Random Convection Under Conditions of Weightlessness," AIAA Journal, Vol. 1, 380-383, 1963.
4. Forbes, R.E., Carley, C.T., and Bell, C.J., "Vibration Effects on Convective Heat Transfer in Enclosures," Journal of Heat Transfer, Vol. 92, Ser. C, 429-438, March 1970.
5. Gershuni G.Z., Zhukhoviskii, E.M., and Yurkov, I.S., "On Convective Stability in the Presence of a Periodically Varying Parameter," PMM, Vol. 34, 470-480, 1970.
6. Gresho, P.M., and Sani, R.L., "The Effect of Gravity Modulation on the Stability of Heated Fluid Layers," Journal of Fluid Mechanics, Vol. 40, 783-806, June 1970.
7. Donnelly, R.J., Reif, F., and Suhl, H., "Enhancement of Hydrodynamic Stability by Modulation," Physical Review Letters, Vol. 9, 363-364, March 1962.
8. Kezios, S.P. and Prasanna, K.V., "Effect of Vibration on Heat Transfer from a Cylinder in Normal Flow," ASME Paper 66-WA/HT-43, 1966.
9. Bloor, M.S., "The Transition in the Wake of a Circular Cylinder," Journal of Fluid Mechanics, Vol. 19, 290-301, February 1964.
10. Carruthers, J.R., "Crystal Growth from the Melt," In *Treatise on Solid State Chemistry*, Vol. 5, 325-406, edited by N.B. Hannay, Plenum Press, New York 1975.
11. Zenkovskaya, G.Z. and I.B. Simonenko, "Effect of High Frequency Vibration on Convection Initiation," Izv. AN SSSR, Mech. Zhidk. Gaza 1(5), 51-55, 1966.

12. Gershuni G.Z., Zhukhoviskii, E.M., and Yurkov, Y.S., " Vibration Thermal Convection in a Rectangular Cavity," Izv. AN SSSR, Mech. Zhidk. Gaza 4, 94-99, 1982.
13. Sharifulin, A.N., "Supercritical Vibration-Induced Thermal Convection in a Cylindrical Cavity," Fluid Mechanics - Sov. Res. 15(2), 335-338, 1986.
14. Siraev, R.R., "Vibration Thermal Convection about a Uniformly Heated Cylinder," Izv. AN SSSR, Mech. Zhidk. Gaza, No. 3, 23-26, 1989.
15. Gershuni G.Z., Zhukhoviskii, E.M., *Convective Stability of Incompressible Fluids*, 1976.
16. Gershuni G.Z., Zhukhoviskii, E.M., A. Napomniashi, *Stability of Convective Flows*, Nauka, Moscow, 1989.
17. Zavarykin, M.P., S.V. Zorin, and G.F. Putin, "Experimental Study of Vibrational Convection," Dokl. Akad. Nauk SSSR, 281, 815-816, 1985.
18. Zavarykin, M.P., S.V. Zorin, and G.F. Putin, " Convective Instability in a Vibrational Field," Dokl. Akad. Nauk SSSR, 299, 309-312, 1988.
19. Ivanova, A.A., and Kozlov, V.G., "Vibrationally Gravitational Convection in a Horizontal Cylindrical Layer," Heat Transfer-Sov. Res. 20, 235-247, 1988.
20. Ivanova, A.A., "Influence of Vibrations of the Unsteady-State Convective Heat Transfer in a Cylindrical Cavity," Heat Transfer-Sov. Res. 20, 248-251, 1988.
21. Yurkov, Yu.S., "Vibration-Induced Thermal Convection in a Square Cavity in Weightlessness at Arbitrary Frequencies," In *II Vsesoyuznyye seminar po gidromekhanike i teplomassoobmemu V nevesomosti* [Tezisy dokladov], Perm, 36-37, 1981.
22. Yurkov, Yu.S., "Vibration-Induced Thermal Convection in a Square Cavity in Weightlessness (Finite Frequencies)" In *Konvektivnyye techeniya*, Convective Perm Teachers' Institute, Perm, . 98-103, 1981.
23. Biringen, S. and Danabasoglu, G., "Computation of Convective Flow with Gravity Modulation in Rectangular Cavity," J. Thermophys. 4, 357-365, 1990.
24. Fu, W.S., and Shieh, W.J., " A Study of Thermal Convection in an Enclosure Induced Simultaneously by Gravity and Vibration," Intl. J. Heat Mass Transfer, 35, 7, 1695-1710, 1992.
25. Gershuni G.Z., Zhukhoviskii, E.M., "Vibration-Induced Thermal Convection in Weightlessness," Fluid Mechanics-Soviet Research, 15, 1, Jan/Feb, 1986. Translation from *Gidromekhanika i Protsessy Perensa v Nevesomosti*, 86-105, 1983.

112599

N95-19014

1994

352863 ~~30939~~
p-5

NASA/ASEE SUMMER FACULTY FELLOWSHIP PROGRAM

**MARSHALL SPACE FLIGHT CENTER
THE UNIVERSITY OF ALABAMA**

**CAPILLARY ELECTROPHORESIS: BIOTECHNOLOGY FOR SEPARATION
OF DNA AND CHROMOSOMES**

Prepared By: George O. Williams, Jr.
Academic Rank: Instructor
Institution and Department: Calhoun Community College
Department of Natural Sciences
NASA/MSFC
Laboratory: Space Science
Division: Microgravity Science and Applications
Branch: Biophysics
MSFC Colleagues: Percy Rhodes
Robert Snyder
David Donovan

Introduction

Electrophoresis has been used for the separation of particles, ions and molecules for a number of years. The technology for separation and detection of the results has many applications in the life sciences. One of the major goals of the scientific community is to separate DNA molecules and intact chromosomes based upon their different lengths or number of base pairs. This may be achieved using some of the commercially available and widely used methods, but these processes require a considerable amount of time. The challenge is to achieve separation of intact chromosomes in a short time, preferably in a matter of minutes.

The Biophysics Branch of the Marshall Space Flight Center has been doing electrophoresis research for several years. Recently the research effort has focused on macromolecules, particularly DNA. Electrophoretic mobilities of various DNA molecules have been determined using new technology. The research team has worked with agarose and polyacrylamide gels; chambers made from microslides, glass, and plastics; various buffer systems; ac and dc fields; and advanced technology for imaging and videotaping of various sizes of DNA in Brownian motion and under the effects of an electric field. This has been accomplished by using epifluorescence, a CCD camera with an image intensifier, an image analysis system, and a research microscope (1).

The technology for capillary electrophoresis (CE) has developed rapidly and has many advantages over more conventional methods. Separation of DNA and chromosomes has required the use of gels. A large portion of the science of modern electrophoresis is devoted to understanding and controlling the formation of types of gels. However, the use of these gels has not been easily adapted to on-line sample applications, detection, quantification or automated operation. This type of electrophoresis has been for a number of years a powerful but manual-intensive methodology (2).

Capillary electrophoresis has been used to separate various types of biologicals including purine bases and nucleosides (3), drug related impurities (4), amino acids, human urine, peptides from the tryptic digestion of egg white lysozyme, and the components of a one kilobase ladder of DNA in agarose solutions (5). Entangled polymer solutions have been employed as a mesh for separating DNA restriction fragments ranging in size from 72 to 1353 base pairs (6). Grossman and Soan have used CE to study the orientation effects on the electrophoretic mobility of the tobacco mosaic virus in free solution (7). This brings us to a brief discussion of the advantages of capillary electrophoresis and, therefore, the technique of choice for this research. Some of these advantages are as follows: sample requirements of only 2 to 4 nL; time requirements of only 10 to 40 minutes; high resolution of sample species; reproducibility is greatly enhanced with only about 0.5 percent error; sensitivity in the picomoles range; no molecular weight limitations enabling separation of smaller substances from complex macromolecules; capillary conditions may be mild with the use of mobile phases usually ranging from slightly acidic to slightly basic buffers and certain organic solvents and denaturing agents may be added; compatibility with biological systems provides for recovery of more than 95 percent of original enzymes and their immunological activities; instrumentation for CE may be programmed for semi-automated or fully automated operation; complete spectrum may be measured after a single injection; and minimal reagent consumption is a decided advantage(8).

Experimental Section

The current task at MSFC and the Biophysics Branch has focused on the type of instrumentation, safety, power requirements, systems interface, detection methods, sample injection methodology, buffer systems, sample handling, and recording of results for capillary electrophoresis studies. A Model 785A absorbance detector was obtained from Applied Biosystems, Inc. A high sensitivity optical cell assembly supplied by L.C. Packings, San Francisco, CA, includes a CE cell, a fused silica capillary, 75 μm inside diameter and 280 μm outside diameter, coated externally with polyimide, and a reference cell. The analytical length of the capillary is 122 cm, 100 cm from the injection end to the detector cell and 22 cm to the outlet buffer. The Z-cell has a light path of three millimeters. The KSI 1000 Series 100-5 power supply is capable of delivering 100 kV of dc power and is connected to the anode by using standard sparkplug wires and terminals. These terminals on the anode side were mounted into a custom one-quarter inch plexiglass capillary holder especially designed to hold the capillary in place under load. Since power requirements may range up to 40 kV and 90 μA , a plexiglass cover for the entire terminal and connection assembly was designed and custom built for safety shielding at the inlet buffer electrode. The capillary holder, connectors, terminals and safety shielding assemblies were designed by Percy Rhodes and David Donovan and built by Campbell Engineering of Huntsville, AL. Grounding is provided by direct mount to the absorbance detector chassis and by connection directly into the laboratory electrical system ground. A Fluke model 87 multimeter was connected for in-line monitoring of the system. A Kipp and Zonen chart recorder was connected to the detector output for recording results.

Conditioning of the capillary was required before system interfacing and full operation of the unit could be tested. To reduce the amount of direct handling of the capillary and possible breakage, two to three centimeters of a glass capillary was epoxy-welded as a sleeve over both ends. The glass sleeve allowed us to attach a piece of small rubber tubing between an eighteen gauge hypodermic needle on the syringe and the fused silica capillary. The capillary was purged by pumping 1M NaOH for thirty minutes with a syringe pump. The operating buffer of choice, 0.1 M Tris-HCl (pH 8.05, conductivity = $\sim 4800 \mu\text{mhos}$), was then flushed through the capillary. Tests for absorbance detection were made using 20 mM sodium phosphate at pH 2.5. Before the system could be fully operational and brought under load, further cell conditioning was necessary. The cell optics in the detector were burned in by illumination with the deuterium lamp for forty-eight hours at a wavelength of 200 nanometers.

Buffer preparation was carefully controlled by using distilled water and filtration with a 0.22 μm pore size. All fluids were filtered before introduction into the capillary. Sample injection was achieved by using 10 kV of power to enable the sample to flow into the tube on the anode side by electroosmosis. A biotinylated protein molecular weight standard which is prepared for use with gel electrophoresis was used initially for detection. In addition, egg white lysozyme was prepared and run in the CE system. A Hewlett-Packard Model 8452 UV-VIS Spectrophotometer with computer interface was used to provide electropherograms of the buffers and sample prior to the CE runs.

Results and Discussion

We fully expected to experience a "learning curve" with these experiments, but, overall, the results have been somewhat disappointing. Over a period of about three weeks we have experienced several problems relative to the detection equipment and the system as a whole, but particularly with the CE-cell. Some of the problems are listed below.

1. initial filling of the capillary
2. erratic results with absorbance detection
3. current unstable
4. amount of current inconsistent with calculated theoretical values
5. small current spike
6. baseline drift
7. electropherograms show unreliable and inconsistent results
8. possible thermal problems
9. bubbles in the capillary under load
10. sample injection methodology

The first attempt at filling the capillary provided evidence of a problem with the CE-cell. Initial tests of the capillary system under load of 20kV produced a current of between 0.9 μ A to 29.0 μ A. These results were inconsistent with the calculated values of 60-80 μ A while using the high conductivity Tris-HCl. Upon examination of the capillary with a dissecting microscope, an obstruction was observed about ten centimeters from the inlet buffer end. This section of the capillary was sacrificed and the system was tested again under load. Subsequent tests provided excellent results which were consistent with the calculated theoretical values. We were able to run the protein molecular weight standard and record the results on the chart recorder. However, the results of several experiments conducted under the same conditions were unacceptable. Changes in the buffers and sample injection were made. There was some evidence of bubbles in the system. Degassing of all buffers and sample is now standard operating procedure. These precautions eliminated some of the problems we were experiencing, however, the baseline noise or drift continued to be a serious area of concern. Finally, we determined that the CE-cell was defective. At the time of this report the cell has been returned and a new one is being provided by the company.

Recommendations for Further Research

Sample injection may be accomplished in a number of ways, but the recommendation is the one used by Grossman and Soan. A vacuum of 5 in Hg is applied to the cathodic electrode reservoir for two or three seconds while the inlet end of the capillary is immersed in the sample solution (6). On-column detection seems to be the method of choice for high resolution electropherograms (5) (9) (10). Strege and Lagu have also obtained higher resolution electropherograms with the use of coatings of polyacrylamide on the inner surface of the capillary (11). Various buffer systems may be used for better results and cooling of the capillary will eliminate problems which may be thermally induced. Finally, we recommend tests with various samples including the tobacco mosaic virus, lambda DNA, DNA ladders, deproteinated chromosomes of the yeast *S. cerevisiae* and intact chromosomes of *S. pombe*.

References

1. Song, Lu, and Maestre, Marcos F., "Observation of DNA Molecules Undergoing Capillary Electrophoresis," *J. of Biomolecular Structure and Dynamics*. Vol. 9, No. 3, pp. 525-535, 1991.
2. Jorgenson, James W., and Lukacs, Kryn DeArman. "Capillary Zone Electrophoresis," *Science*, Vol. 222, pp. 265-272, 1983.
3. Grune, Tilman, Ross, Gordon, Schmide, Heike, Siems, Werner and Perrett, David. "Optimized separation of purine bases and nucleosides in human cord and plasma by capillary zone electrophoresis," *J. of Chromatography*, Vol. 636, pp. 105-111, 1993.
4. Altria, K.D., "High speed determination of drug related impurities by capillary electrophoresis employing commercial instrumentation," *J. of Chromatography*, Vol. 636, pp. 125-132, 1993.
5. Boeck, Petr, and Chrambach, Andreas. "Capillary Electrophoresis of DNA in Agarose Solutions at 40 degrees C," *Electrophoresis*, Vol 31, pp. 1221-1228, 1991.
6. Grossman, Paul D., and Soane, David S. "Experimental and theoretical studies of DNA separations by capillary electrophoresis in entangled polymer solutions," *Biopolymers*, Vol 31, pp. 1221-1228, 1991.
7. Grossman, Paul D., and Soan, David S., "Orientation effects on the electrophoretic mobility of rod-shaped molecules in free solution," *Analytical Chemistry*, Vol. 62, No. 15, pp. 1592-1596, 1990.
8. Guzman, Norberto A., Hernandez, Luis, and Hoebel, Bartley G., "Capillary Electrophoresis: A New Era in Microseparation," *BioPharm.* pp. 22-37, 1989.
9. Gordon, Manuel, Huang, Xiaohua, Huang, Pentoney, Stephen L., Jr., and Zare, Richard. "Capillary Electrophoresis," *Science*, Vol. 242. pp. 224-228, 1988.
10. Vespalec, Radim, Gebauer, Petr, and Bocek, Petr. "Identification of peaks in capillary zone electrophoresis based on actual mobilities", *Electrophoresis*, Vol. 13, pp. 677-682, 1992.
11. Strege, Mark and Lagu, Avinash, "Separation of DNA restriction fragments by capillary electrophoresis using coated fused silica capillaries," *Analytical Chemistry*, Vol. 63, No. 13, pp. 1233-1236, 1991.

5 - 111
N95-19015

112 600

1994

352804 30935
P-6

NASA/ASEE SUMMER FACULTY FELLOWSHIP PROGRAM

**MARSHALL SPACE FLIGHT CENTER
THE UNIVERSITY OF ALABAMA**

**SALT-INDUCED AGGREGATION OF LYSOZYME: IMPLICATIONS
FOR CRYSTAL GROWTH**

Prepared By: Lori J. Wilson
Academic Rank: Assistant Professor
Institution and Department: East Tennessee State University
Department of Chemistry

NASA/MSFC:
Laboratory: Space Science
Division: Microgravity Sciences
Branch: Biophysics

MSFC Colleagues: Marc L. Pusey
Lawana Adcock

Introduction

Crystallization of proteins is a prerequisite for structural analysis by x-ray crystallography. While improvements in protein crystals have been obtained in microgravity onboard the U.S. Space Shuttle [1], attempts to improve the crystal growth process both on the ground and in space have been limited by our lack of understanding of the mechanism(s) involved. Almost all proteins are crystallized with the aid of a precipitating agent. Many of the common precipitating agents are inorganic salts. An understanding of the role of salts on the aggregation of protein monomers is key to the elucidation of the mechanism(s) involved in protein crystallization. In order for crystallization to occur individual molecules must self-associate into aggregates. Detection and characterization of aggregates in supersaturated protein solutions is the first step in understanding salt-induced crystallization. Laser light scattering [2], and more recently neutron scattering [3], have provided evidence for the presence of aggregates supersaturated protein solutions. However, each of these methods is severely limited in their ability to make direct measurements of the concentration of discrete aggregate species present in a polydisperse solution. Light scattering experiments, costly in both equipment and time, are further impaired by their reliance upon clean solutions for accurate measurements. This is an impediment for protein crystal growth experiments, often requiring supersaturated solutions, by their very nature unstable and subject to particulate (i.e. crystalline) contaminations.

We have used a dialysis kinetic technique to study the role of sodium chloride on the aggregation process of hen egg white lysozyme. This dynamic dialysis technique is based upon the fact that the flux of protein molecules across a porous barrier is proportional to the size, diffusivity and the concentration difference across that barrier. By analyzing the flux at which protein molecules cross a semipermeable membrane the concentrations of discrete aggregates can be calculated. Using this method we have determined the aggregate distribution of lysozyme in supersaturated solutions of varying salt content. A model incorporating the unusual protein chemistry of lysozyme has been developed to model the aggregate distribution. The aggregate distributions of the solutions have been compared to face growth rate measurements allowing identification of the growth unit.

Materials and Methods

Materials. Hen egg white lysozyme was purchased from Calbiochem. All buffer components, except sodium phosphate monobasic (Fisher-Scientific Company), sodium chloride and 70% glutaraldehyde were all reagent grade from Sigma Chemical Company. Cellulose ester dialysis tubing was from Spectrum. Electrophoretic reagents, standards, and precast gels were from Pharmacia. Lysozyme was dissolved and dialyzed against distilled water

overnight to remove salts and buffers. It was then re-dialyzed against 1%(w/v) NaCl (0.1M NaAc, pH 4.0). All working solutions were stored in a water bath at 20°C until used. To prepare protein in 3%(w/v) NaCl (0.1M NaAc, pH 4.0), equal volumes of the working solution and 5%(w/v) NaCl (0.1M NaAc, pH 4.0). Lysozyme concentrations were determined using an A(1%, 281.5nm.)= 26.4 on a Varian DMS 200 UV-VIS spectrophotometer.

Cross-linking . The preparation of covalently cross-linked lysozyme was prepared by the addition of 200 mL of 70% glutaraldehyde to 5 mL of 20 mg/mL lysozyme in 3%(w/v) NaCl (0.1M NaAc, pH 4.0) was allowed to react for five minutes before it was loaded onto a 115 x 5 cm size exclusion column of G-50 Sephadex running at 0.2 mL/min. Fractions were collected and analyzed by sodium dodecyl sulfate polyacrylamide gel electrophoresis (SDS-PAGE) on Pharmacia's PhastSystem using the recommended protocols. The samples were dialyzed against distilled water and lyophilized for storage.

Dialysis Kinetics . The dialysis kinetics apparatus has been described previously [4 and 5] so only pertinent items will be discussed. Briefly, the polydisperse protein solution was placed inside of a custom made dialysis bag with a membrane with a molecular weight cut-off (MWCO). Aggregates with molecular weights larger than the MWCO cannot escape the bag. In order to overcome the osmotic back flow which results in buffer flowing inside of the bag during the first 10 minutes of a run pressure was kept on the bag using a syringe. The dialysis bag was placed inside of a thermostated beaker within which water was circulated, via a circulating bath, in order to maintain the temperature at 20°C. Approximately 115 mL of buffer, also kept at 20°C, was placed in the beaker for each run. The external buffer solution was circulated through an ISCO Model 229 UV-VIS detector monitoring the absorbance at 281.5 nm. The output voltage of the detector was recorded using an NB-MIO-16X multi-purpose acquisition board in a Macintosh II cx computer running LabView.

Results

Development of a dimerization model. In order for this technique to be successful we must be certain of which aggregates are retained in the dialysis bag and which can escape through the pores. Our approach was to prepare standard solutions of aggregates of hen egg white lysozyme. The aggregates were cross-linked with glutaraldehyde and then separated on a G-50 size exclusion chromatography column. The purity of the aggregates was checked with SDS-PAGE which separates proteins by their molecular weights. The flux of purified dimer from a 25K MWCO dialysis membrane was found to be 0.15 sec⁻¹ in 1% NaCl (pH 4.0, 0.1M NaAc). This is about 30% of the monomer flux rate of 0.50 sec⁻¹ in the same buffer.

Knowing this we constructed a model which describes the total flux, F_{tot} , from the membrane to be composed of monomer concentration, $[M]$, times the

flux of the monomer, F_{mono} plus the dimer concentration, $[D]$ times the flux of the dimer, F_{dimer} .

$$F_{\text{tot}} = [M]F_{\text{mono}} + [D]F_{\text{dimer}} \quad \text{Eq. 1.}$$

Since F_{mono} and F_{dimer} are known to be 0.50 sec^{-1} and 0.15 sec^{-1} respectively and F_{tot} can be measured we can get monomer and dimer concentrations from the following equilibrium:



where K_1 is equal to:

$$K_1 = \frac{[D]}{[M]^2} \quad \text{Eq. 3.}$$

Assuming that the total concentration is composed of monomers and dimers we can obtain K_1 estimates by measuring the total flux, F_{tot} , and using non-linear least squares regression analysis (MINSQ) to vary the monomer and dimer concentrations until an optimum fit is obtained.

Flux rate measurements and estimation of dimerization constant. The total flux from a 25K MWCO dialysis membrane was measured at four different salt concentrations. These flux measurements were found to vary significantly with the supersaturation level of the solution (Fig. 1).

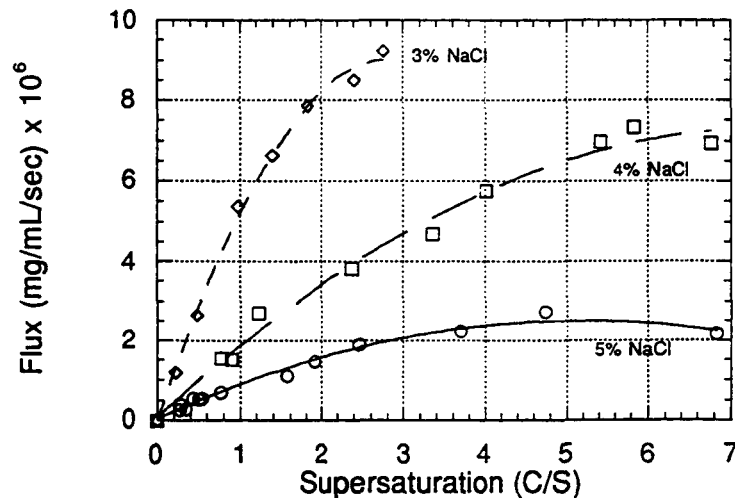


Figure 1. Flux measurements as a function of supersaturation.

Using the dimerization model the value of K_1 was estimated (Table 1) and the goodness of fit was tested by a graph of the calculated flux vs. the observed

flux. As expected the model fit the data well at low protein concentrations. However, at high concentrations the observed flux showed large curvature indicating the presence of higher ordered species. Since our initial model only allows for monomers and dimers we would not expect good agreement when higher aggregates are present.

Table 1. Equilibrium Constants for 1->2 Pathway

% NaCl	Solubility (mg/mL) [6]	K_1	R^2
1	>100	2.4844	0.99728
3	7.14	98.09	0.98719
4	2.43	290.39	0.98840
5	1.69	526.15	0.98012

There was a dramatic increase in K_1 at salt concentrations greater than 3% NaCl. Since the solubility of lysozyme decreases with increasing salt concentration the supersaturation levels are higher for higher salt concentrations. However, the increase in K_1 was not linear with the solubility or with the salt concentration. Instead it increased exponentially with salt concentration above 3% NaCl. The most obvious conclusion from the data in Table 1. is that the salt is driving the aggregation process.

Conclusions

The simple model we have used assumes that the first step in the aggregation process is the formation of a dimer from two monomers. Using this model we have determined equilibrium constants for this step which allows us to calculate monomer and dimer concentrations. When we compare how the dimer concentrations vary over a given supersaturation range we see an increase in the amount of dimer. In fact the profile of the dimer concentration parallels the profile of measured 110 face growth rates [7]. In contrast, the monomer concentrations level out at supersaturations wher the crystal is going at a significant rate. This leads one to assume that aggregates, and not monomers, are responsible for the growth of the crystals. Also, the high level of aggregated species in solutions which lead to crystal growth must affect both the nucleation and growth mechanisms.

It is recommended that future efforts be directed toward the development of a model which incorporates more aggregation steps. Of particular interest is the next step which could be a) the formation of trimers from a dimer and a monomer or b) the formation of tetramers from two dimers. Both of these scenarios have been seen in aggregating biological systems. In order to determine this critical next step it will be necessary to use a 50K MWCO membrane which allows trimers, if present, to escape.

Additional improvements in the purification of the cross-linked aggregates is necessary to allow characterization of dialysis membranes more easily and accurately. Knowing the escapable units for each MWCO is a requirement for development of appropriate models and determination of equilibrium constants for each step in the pathway up to a critical nucleus.

References

1. L. J. DeLucas, M.M. Long and K. M. Moore et. al., J. Crystal Growth 135 (1994) 183.
2. M. L. Pusey, J. Crystal Growth 110 (1991) 60.
3. F. Boue, F. Lefauchaux, M.C. Robert and I. Rosenman, J. Crystal Growth 133 (1993) 246.
4. L. J. Wilson, L.D. Adcock and M.L. Pusey, J. Phys. D. 26 (1993) B113.
5. L. J. Wilson and M. L. Pusey, J. Crystal Growth 122 (1992) 8.
6. E. Cacioppo and M.L. Pusey, J. Crystal Growth 114 (1991) 286.
7. E. Forsythe and M.L. Pusey, J. Crystal Growth 139 (1994) 89.

N95-19016

112601

1994

352865

~~30934~~
P 5

NASA/ASEE SUMMER FACULTY FELLOWSHIP PROGRAM

**MARSHALL SPACE FLIGHT CENTER
THE UNIVERSITY OF ALABAMA**

**A TECHNIQUE FOR DETERMINING CLOUD FREE VS CLOUD CONTAMINATED
PIXELS IN SATELLITE IMAGERY**

Prepared By: Richard A. Wohlman

Academic Rank: Instructor

Institution and Department: Western Carolina University
Department of Mathematics and Computer Science

NASA/MSFC:

Laboratory: Earth Sciences
Division: Earth System Science
Branch: Observing Systems

MSFC Colleagues: Gary J. Jedlovec, PhD.
Anthony R. Guillory

INTRODUCTION

Weather forecasting has been called the second oldest profession. To do so accurately and with some consistency requires an ability to understand the processes which create the clouds, drive the winds, and produce the ever changing atmospheric conditions. Measurement of basic parameters such as temperature, water vapor content, pressure, windspeed and wind direction throughout the three dimensional atmosphere form the foundation upon which a modern forecast is created. Modern technology in the form of automated observing stations, Doppler radar, and space borne remote sensing have provided forecasters the new tools with which to ply their trade.

One of the latest additions to the forecasters resources is found high over the earth, some in geosynchronous orbits above the equator. The newest of these Geosynchronous Operational Environmental Satellites (GOES) is GOES 8 which will become operational in October of 1994. It has the ability to scan the entire disk of the earth each half hour, producing imagery in both visible and infrared (IR) wavelengths. These images are familiar to anyone with a television, as they are shown during every weather segment of the local news to point out fronts, thunderstorms, and even areas of nice weather. For research scientists and professional meteorologists, imagery from all channels, not just visible, are of importance. The IR channels provide information about the location and amount of such atmospheric variables such as water vapor, ozone, and carbon dioxide. Of particular interest here, is water vapor. It is invisible to the naked eye, as it is to the visible channels of the meteorological satellites. But, water vapor content of the atmosphere is one of the variables that forecasters need to produce accurate forecasts. For example, the orientation, temperature, height and depth of the warm moist region of air flowing into a squall line is used to predict whether or not the squall line will generate severe weather and tornadoes. So, given its invisibility, how can we use satellite imagery to help determine the location and amount of the water vapor in the atmosphere?

THE PLANCK CURVE AND BASIC RADIATIVE TRANSFER

In 1901, Max Planck derived his famous function (the Planck function, of course) which for a blackbody at a given temperature relates radiance to wavelength. If you have a blackbody at a specific temperature, and are interested in the radiance at a particular wavelength, the Planck function gives it to you. If, however, you have the wavelength and the radiance, you can determine the blackbody temperature by manipulating the function.

In this manner, IR data is converted to temperature. Assume for a moment that there were no impediments to 'seeing' the radiance of the earth. Earth has a maximum radiance at about 15 microns because of its average temperature of 255°. So, if we had a sensor which viewed the earth at 15 microns, it would see some given radiance. Knowing the wavelength (15 microns) and the observed radiance, we could compute the skin temperature of the surface of the earth. The lower the radiance, the lower the temperature and vice versa. And this can be done for each wavelength because the relationship between wavelength and temperature is unique.

Unfortunately, there are contaminants in the atmosphere which act as impediments when observing the earth, and the energy which reaches the satellite is diminished by them. The atmosphere will tend to attenuate the radiance of the earth and this will yield artificially low temperatures. The attenuation can be corrected as the atmosphere, with a few noteworthy exceptions, is a fairly consistent mix of gasses. Water vapor is one of those exceptions and it absorbs mightily in the IR regions of the spectrum. There are some windows in this region, though, and sensors on the meteorological satellites take advantage of them. But even in these windows, attenuation due to water vapor occurs. The transmittance, or ability to transmit radiation, varies with the water vapor content: the more water vapor, the more attenuation. This relationship between attenuation and water vapor content, plus the varying effects of the water vapor content at different wavelengths can be used to determine the actual amount of water vapor in the atmosphere.

COLUMN-INTEGRATED WATER CONTENT

Many schemes have been proposed to determine the water content in a column of air as observed from space. One such scheme refined by Jedlovec¹ is known as the Physical Split Window (PSW) method. It makes use of the temperature values found in the 11.2 and 12.0 micron wavelengths, the so called Physical Split Window. While the wavelengths are very close together, they react differently when observing through water vapor. By comparing the resultant temperatures from these wavelengths to a first guess temperature, a determination of the derived column-integrated water content (IWC) can be made. Making use of the PSW method in data gathered experimentally over Florida and over the South Central United States, Guillory and Jedlovec² retrieved IWCs over the region, verifying their accuracy with values more conventionally determined.

Since GOES 8 carries sensors which observe in the same wavelengths, one should be able to use the same technique to determine IWC over large areas. Typically, water vapor content is determined from radiosonde data. However, the radiosonde launch rates are decreasing yearly due to budget constraints. Additionally, there are huge regions of the earth's surface which are covered by ocean that rarely if ever are probed by radiosondes. Using the PSW technique, reliance upon radiosonde data is greatly reduced. Because GOES 8 can produce soundings every half hour, IWC retrievals can be made almost anytime, anywhere.

Almost, because the PSW method requires clear cloud free line of sight from the sensor to the ground. Cloud contamination is a significant problem for several reasons. Thick clouds result in IWC retrievals from the top of the cloud to the top of the atmosphere (TOA), instead of from the ground to the TOA. Secondly, thin cirrus clouds absorb radiance from the ground, and radiate at colder temperature, artificially decreasing the radiance seen by the sensor. This in turn yields erroneous IWC values. Low fair weather cumulus fields whose clouds are smaller than sensor resolution produce erroneous values, but their deviation from actual values is not well known.

CLOUD FILTERING AND DATA COLLECTION

A scheme was needed to filter those cloud pixels from the image. Early in the research, we decided that only satellite data could be used, that is, no temperature fields (forecast or actual) were allowed in the cloud filtering method.

In a paper by Hayden³, a method for cloud filtering was suggested and was used as a starting point for the scheme. But first, data had to be gathered. Using McIDAS, imagery from several days was examined. Values for temperatures were made in three IR wavelengths: 3.9, 11.2 and 12.0 microns, the split window wavelengths. The first, 3.9 microns, is much less affected by the water vapor content of the atmosphere than are the split window wavelengths of 11.2 and 12.0 microns so can better give a reasonable surface temperature. In addition to the IR channel data, brightness counts in the visible channel were made. These data were collected at one hundred locations in the image and stored in a data file. The data file was then loaded into a spread sheet program, and examination began. In all, nine separate samples were made, three each from 26 July 1994 at 15Z, 18Z and 21Z.

RESULTS

After much manipulating and messaging, the data began to yield a pattern. It was noticed that the cirrus clouds could be detected if 11.2 micron temperature was less than 265°K. Mid level clouds could be found by using the difference in temperature between the 11.2 and the 12.0 microns, and applying an empirically derived threshold value. Finally, values were calculated for the difference between the temperature at 3.9 and 11.2 microns, and 3.9 and 12.0 microns. The difference of these values was related to the presence of cloud.

These data are represented in figure 1 below.

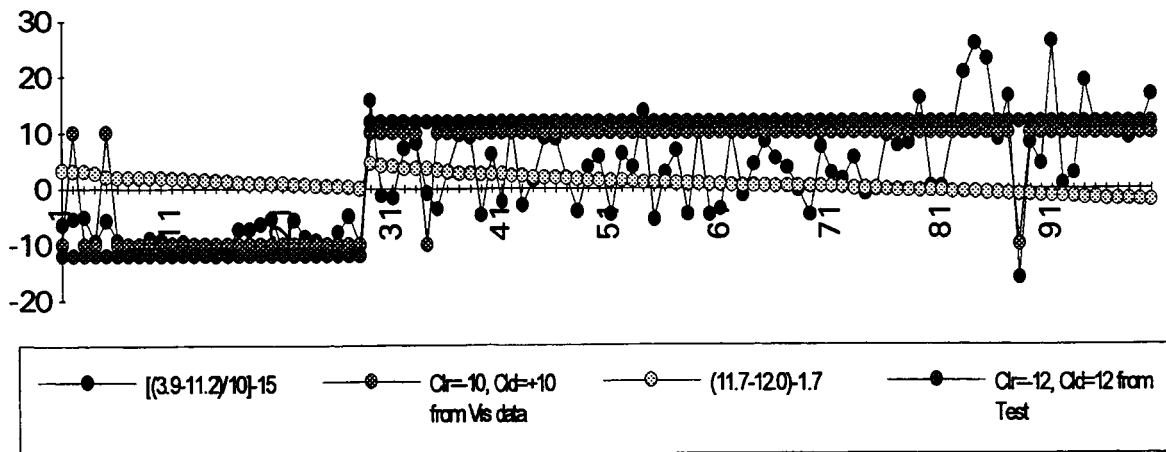


Figure 1.

Values which have a visible brightness counts greater than a threshold value of 80 are assumed cloudy, while those less than 80 are assumed clear. The cloudy pixels are given a value of 10, while the clear pixels are valued at -10 (the second data points). The difference temperatures between 3.9 and 11.2 microns (first points in the key) vary greatly ranging from -15 to +25, while the difference temperatures between 11.2 and 12.0 (third set of data points) vary only slightly between about -3 to +4. Note that the key indicates that there is an arbitrarily selected scalar subtracted from each of these difference temperature values. This shifts the curve downwards in the graph for esthetic reasons so that the clear/cloudy determination follows the convention of the visible brightness values- that is clear is negative, cloudy positive.

The last set of points is the test selection criteria using the cloud filtering scheme. The test works as follows:

The pixel is determined to be a cloud if any of the following are true:

- Temperature at 11.2 microns is colder than 275°K
- Difference between 3.9 and 11.2 micron temperature > -5
- Difference between 11.2 and 12.0 micron temperature is <0

Otherwise, the pixel is clear.

These values are depicted as the last data point, and given a value of -12 if clear, and +12 if cloudy.

Once the test was applied to the data in the spreadsheet, any conflicts between what the test determined and what the visible imagery said was clear or cloud was examined in the original imagery. Pixel addresses were saved along with data, and these allowed a close inspection of the data point in question. Occasionally, some of the visible imagery data was determined to be clear or cloudy contrary to the brightness value cutoff of 80. For example, thin cirrus over the water was rarely seen as cloudy at that cutoff value, because the underlying water was very dark. This had the effect of darkening the thin cirrus. In these cases, correct values (+10 or -10) were inserted into the database overruling the automatic cloud determination mechanism.

The test worked correctly in 96 of the 100 cases for this date and time group. This was consistent with the other eight cases. Errors occurred primarily in the ability of the test to determine low cumulus fields. The small cumulus clouds are quite frequently smaller than the resolution size of the imagery, which has the effect of raising its brightness count above the threshold value of 80. Since the cloud is low, the temperature in all of the IR channels is very close to that of the surface, and consequently is not selected in the test. Examination of figure 1 shows two such cases- visible data says that point 2 and point 5 are cloudy, while the test shows it to be clear. On the other hand, the test excelled in selecting cirrus clouds. Of all of the 'corrections' inserted into the original database, by far the greatest number were for cirrus and thin cirrus. The test correctly selected each case of thin cirrus clouds.

CONCLUSION AND FURTHER CONSIDERATIONS

The test seems to be able to determine clear or cloudy pixels with a consistency greater than 94% for these cases. By carefully selecting threshold values for use in the test it appears that automatic cloud filtering is possible.

Additional data needs to be examined, as there is a variability in the threshold values which appears dependent upon solar angle and consequently surface heating. This would also indicate that there should be significant seasonal variations for northern (southern) latitudes where solar insolation varies most extremely. Thus, seasonal data sets as well as different time of day data sets should be collected so that those threshold values can be determined.

Once those values are determined and verified to an acceptable level, construction may begin on a map which would act as a mask to overlay an image. This could allow a determination of areas which are clear or cloudy. Since a version of the PSW routine has been written for use with McIDAS, integration of such a mask in the routine could allow the retrieval of IWC without the need for careful time consuming individual pixel examination as is now required.

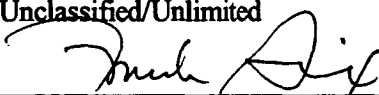
SELECTED REFERENCES

1. Jedlovec, G. J., "Precipitable Water Estimation from High-Resolution Split Window Radiance Measurements," *Journal of Applied Meteorology*, Vol. 39, pp. 863-876, 1990.
2. Guillory, A. R., and Jedlovec, G. J., "A Technique for Deriving Column-integrated Water Content Using VAS Split-Window Data," *Journal of Applied Meteorology*, Vol. 32, pp. 1226-1241, 1993.
3. Hayden, C. M., "GOES-VAS Simultaneous Temperature-Moisture Retrieval Algorithm," *Journal of Applied Meteorology*, Vol 27, pp. 705-733, 1988.

REPORT DOCUMENTATION PAGE

Form Approved
OMB No. 0704-0188

Public reporting burden for this collection of information is estimated to average 1 hour per response, including the time for reviewing instructions, searching existing data sources, gathering and maintaining the data needed, and completing and reviewing the collection of information. Send comments regarding this burden estimate or any other aspect of this collection of information, including suggestions for reducing this burden, to Washington Headquarters Services, Directorate for Information Operations and Reports, 1215 Jefferson Davis Highway, Suite 1204, Arlington, VA 22202-4302, and to the Office of Management and Budget, Paperwork Reduction Project (0704-0188), Washington, DC 20503.

1. AGENCY USE ONLY (Leave blank)		2. REPORT DATE October 1994	3. REPORT TYPE AND DATES COVERED Contractor Report	
4. TITLE AND SUBTITLE Research Reports - 1994 NASA/ASEE Summer Faculty Fellowship Program			5. FUNDING NUMBERS NGT-01-002-099	
6. AUTHOR(S) M. Freeman, R. Chappell, F. Six, G. Karr, Editors				
7. PERFORMING ORGANIZATION NAME(S) AND ADDRESS(ES) The University of Alabama, Tuscaloosa, Alabama and The University of Alabama in Huntsville			8. PERFORMING ORGANIZATION REPORT NUMBER	
9. SPONSORING / MONITORING AGENCY NAME(S) AND ADDRESS(ES) National Aeronautics and Space Administration Washington, D.C. 20546			10. SPONSORING / MONITORING AGENCY REPORT NUMBER NASA CR- 196533	
11. SUPPLEMENTARY NOTES				
12a. DISTRIBUTION / AVAILABILITY STATEMENT Unclassified/Unlimited  Date: 10-31-94 Dr. Frank Six, University Affairs Officer			12b. DISTRIBUTION CODE	
13. ABSTRACT (Maximum 200 words) For the 30th consecutive year, a NASA/ASEE Summer Faculty Fellowship Program was conducted at the Marshall Space Flight Center (MSFC). The program was conducted by the University of Alabama and MSFC during the period May 31, 1994 through August 5, 1994. Operated under the auspices of the American Society for Engineering Education, the MSFC program, as well as those at other NASA centers, was sponsored by the Higher Education Branch, Education Division, NASA Headquarters, Washington, D.C. The basic objectives of the programs, which are in the 31st year of operation nationally, are (1) to further the professional knowledge of qualified engineering and science faculty members; (2) to stimulate an exchange of ideas between participants and NASA; (3) to enrich and refresh the research and teaching activities of the participants' institutions; and (4) to contribute to the research objectives of the NASA centers. The Faculty Fellows spent 10 weeks at MSFC engaged in a research project compatible with their interests and background and worked in collaboration with a NASA/MSFC colleague. This document is a compilation of Fellows' reports on their research during the summer of 1994. The University of Alabama presents the Co-Directors' report on the administrative operations of the program. Further information can be obtained by contacting any of the editors.				
14. SUBJECT TERMS Astrionics; structures and dynamics; materials and processes; systems analysis and integration; propulsion; space sciences; mission operations; information systems; advanced spacecraft and payload systems; preliminary design; and technology transfer.			15. NUMBER OF PAGES 301	
			16. PRICE CODE NTIS	
17. SECURITY CLASSIFICATION OF REPORT Unclassified	18. SECURITY CLASSIFICATION OF THIS PAGE Unclassified	19. SECURITY CLASSIFICATION OF ABSTRACT Unclassified	20. LIMITATION OF ABSTRACT Unlimited	